DOE-ER-0313/45
Distribution
Categories
UC-423, -424

FUSION MATERIALS
SEMIANNUAL PROGRESS REPORT
FOR THE PERIOD ENDING

December 31, 2008

Prepared for
DOE Office of Fusion Energy Sciences
(AT 60 20 10 0)

DATE PUBLISHED: February 2009

Prepared by
OAK RIDGE NATIONAL LABORATORY
Oak Ridge, Tennessee 37831
Managed by
UT-Battelle, LLC
For the
U.S. DEPARTMENT OF ENERGY

FOREWORD

This is the forty-fifth in a series of semiannual technical progress reports on fusion materials science activity supported by the Fusion Energy Sciences Program of the U.S. Department of Energy. It covers the period ending December 31, 2008. This report focuses on research addressing the effects on materials properties and performance of exposure to the neutronic, thermal and chemical environments anticipated in the chambers of fusion experiments and energy systems. This research is a major element of the national effort to establish the materials knowledge base for an economically and environmentally attractive fusion energy source. Research activities on issues related to the interaction of materials with plasmas are reported separately.

The results reported are the product of a national effort involving a number of national laboratories and universities. A large fraction of this work, particularly in relation to fission reactor irradiations, is carried out collaboratively with partners in Japan, Russia, and the European Union. The purpose of this series of reports is to provide a working technical record for the use of program participants, and to provide a means of communicating the efforts of fusion materials scientists to the broader fusion community, both nationally and worldwide.

This report has been compiled under the guidance of F. W. (Bill) Wiffen and Renetta Godfrey, Oak Ridge National Laboratory. Their efforts, and the efforts of the many persons who made technical contributions, are gratefully acknowledged.

Barry Sullivan
Research Division
Office of Fusion Energy Sciences

TABLE OF CONTENTS

1 VANADIUM ALLOYS

1.1 MICROSTRUCTURAL EXAMINATION OF DEFORMATION IN IRRADIATED V-4Cr-4Ti COMPRESSION SPECIMENS – D. S. Gelles (Pacific Northwest National Laboratory) **1**

Microstructural examinations have been performed on a series of V-4Cr-4Ti cylindrical compression specimens in order to provide understanding of the observed deformation behavior. Compression testing showed that unirradiated specimens exhibited upper and lower yield points whereas following irradiation the yield stresses were much higher and no yield drop behavior was observed. Both conditions showed evidence of serrated yielding during testing at ~420°C. Microstructural examination of irradiated conditions revealed extensive precipitation making it difficult to observe dislocation structures. Interstitial Impurities were found to form a fine distribution of precipitates following irradiation at ~420°C. Interaction between these precipitates and glide dislocations is apparent.

1.2 ADDITIONAL CHARACTERIZATION OF V-4Cr-4Ti EXPOSED TO FLOWING Li – B. A. Pint (Oak Ridge National Laboratory) **11**

The high temperature tensile behavior of V-4Cr-4Ti specimens was evaluated at 500°C in vacuum with a strain rate of 10-3s-1 after exposure to flowing Li at 400°-700°C. Specimens exposed in the loop exhibited increased strength and decreased ductility and the effect increased with decreasing temperature at the various locations in the loop. Thus, the specimens from the bottom of the hot and cold legs of the loop with exposure temperatures near 450°C showed the highest tensile strength, lowest ductility and also the least dynamic strain aging. For comparison, the tensile behavior of unexposed as-annealed V-4Cr-4Ti specimens from the same batch of specimens also was measured as well as specimens (1) exposed to Li for 1000h at 800°C in a capsule and (2) annealed for 2,350h at 700°C in an evacuated quartz capsule. The present results were compared to similar studies in the literature.

2 CERAMIC COMPOSITE MATERIALS

2.1 DETAILED 3D STRUCTURE OF {111} TETRAHEDRAL VOIDS AND ITS UNIDIRECTIONAL FORMATION IN CUBIC SIC - S. Kondo, Y. Katoh, and L.L. Snead (Oak Ridge National Laboratory) **16**

The {111} tetrahedral voids induced by neutron-irradiation in 3C-SiC were found to be spatially oriented in only one of two possible directions. The tetrahedral shape was unexpected as the surface-to-volume ratio is larger than the alternative {111} octahedral void common in both metals and ceramics. From a geometric viewpoint, all faces of the observed voids are either Si- or C-terminated surfaces. By comparing the surface area with the octahedral void (composed of the both Si- and C-surfaces) of the same volume, the considerable difference of surface energy between the Si(111) and C($\bar{1}\bar{1}\bar{1}$) was implicated.

2.2 MECHANICAL CHARACTERIZATION OF SILICON CARBIDE COMPOSITES FOR HFIR-18J EXPERIMENT IN UNIRRADIATED CONDITION — Y. Katoh, K. Ozawa, L.L. Snead (Oak Ridge National Laboratory), Y.B. Choi (Hiroshima University), T. Hinoki (Kyoto University), and A. Hasegawa (Tohoku University) **21**

A suite of silicon carbide ceramics and composite materials were prepared in various specimen types for the purpose of evaluating irradiation performance at high to very high temperatures in the HFIR RB-18J experiment. Detailed information of the materials prepared is provided. Properties including tensile strength, dynamic elastic modulus, interlaminar shear strength, and trans-thickness tensile strength were determined in an unirradiated condition.

2.3 MODELING THE ELECTRICAL CONDUCTIVITY OF SiC$_F$/SiC FOR FCI-APPLICATION – **G. E. Youngblood and E. Thomsen (Pacific Northwest National Laboratory) **35

Using a combination 2/4-probe method to measure the electrical resistance across a disc-shaped CVD-SiC sample with evaporated gold electrodes, the average specific contact resistances at 200ºC and 500ºC were determined to be 12±2 and 7±1 Ωcm^2, respectively. The measured transverse electrical conductivity values for a high quality 2D-SiC/CVI-SiC composite made with Nicalon™ type S fabric were much lower than similar values measured for the same material with its SiC seal coat removed. This observation suggests that the pyrocarbon fiber coatings form an interconnected, highly conductive carbon network within the interior regions of the composite, and are largely responsible for the overall transverse electrical conductivity of the composite. At lower temperatures, the composite SiC seal coat should be an effective electrical insulator in the transverse direction across such 2D-SiC/SiC composites. However, the effectiveness becomes less as the temperature increases due to the rapidly increasing conductivity of SiC with increasing temperature. Nevertheless, the seal coat thickness (and type) can easily be adjusted during the composite fabrication to control the overall transverse electrical conductivity, an important parameter in the design of a FCI-structure. A simple three-layer series electrical conduction model fails to explain the unexpected low electrical conductivity values observed for the 2D-Nic S/CVI-SiC composite with a CVD-SiC seal coat. Importantly, up to 700ºC the transverse EC-values for a Nic S/CVI composite (with or without seal coat) appear to meet the desired criteria for FCI-application of < 20 S/m.

2.4 MECHANICAL PROPERTIES OF TRI-AXIALLY BRAIDED CARBON FIBER COMPOSITE - K. Ozawa, Y. Katoh, L.L. Snead, J.W. Klett (Oak Ridge National Laboratory), and W.E. Windes (Idaho National Laboratory) **43**

Tensile, inter-laminar shear and trans-thickness tensile properties of tri-axially braided carbon fiber-reinforced carbon matrix (C/C) composites were evaluated. The C/C composites exhibited the quasi-ductile behaviors with initial elastic behavior, second linear portion and non-linear region. Tensile properties of the C/C composites such as ultimate tensile strength, elastic tensile modulus, and proportional limit stress depended on the axial fiber volume fraction. Relatively low inter-laminar shear (2.2 MPa) and quite low trans-thickness tensile

3 FERRITIC/MARTENSITIC STEELS

3.1 RESULTS OF FRACTURE TOUGHNESS TESTS OF SEVERAL RAFM STEELS IRRADIATED IN JP-27 CAPSULE IN HFIR — M. A. Sokolov (Oak Ridge National Laboratory) **49**

Large number of 3-point bend multi-notch specimens of several RAFM steels was irradiated at 300°C and 400°C in capsule JP-27 up to ~22 dpa. These specimens were tested in the hot cell and results are reported here.

4 COPPER ALLOYS

No contributions this period

5 REFRACTORY METALS AND ALLOYS

No contributions this period

6 AUSTENITIC STAINLESS STEELS

6.1 PRECIPITATE EVOLUTION IN LOW-NICKEL AUSTENITIC STAINLESS STEELS DURING NEUTRON IRRADIATION AT VERY LOW DOSE RATES - Y. Isobe, M. Sagisaka (Nuclear Fuels Limited), F. A. Garner (Pacific Northwest National Laboratory) and T. Okita (University of Tokyo) **52**

Neutron-induced microstructural evolution in response to long term irradiation at very low dose rates was studied for a Russian low-nickel austenitic stainless steel designated X18H9 that is analogous to AISI 304. The irradiated samples were obtained from an out-of-core support column for the pressure vessel of the BN-600 fast reactor with doses ranging from 1.7 to 20.5 dpa generated at $3.8x10^{-9}$ to $4.3x10^{-8}$ dpa/s. The irradiation temperatures were in a very narrow range of 370-375°C. Microstructural observation showed that in addition to voids and dislocations, an unexpectedly high density of small G-phase precipitates was formed that are not usually observed at higher dpa rates in this temperature range.

A similar behavior was observed in a Western stainless steel, namely AISI 304 stainless steel, irradiated at similar temperatures and somewhat higher dpa rates in the EBR-II fast reactor, indicating that irradiation at low dpa rates for many years can lead to a different precipitate microstructure and therefore different associated changes in matrix composition than are generated at higher dpa rates. The contribution of such radiation-induced precipitation to changes in electrical resistivity was measured in the X18H9 specimens and was shown to cause significant deviation from predictions based only on void swelling.

7 FUNCTIONAL MATERIALS – INCLUDING MHD INSULATORS, COATINGS, INSULATING CERAMICS, AND OPTICAL MATERIALS

7.1 COMPATIBILITY OF MATERIALS EXPOSED TO ISOTHERMAL Pb-Li – B. A. Pint (Oak Ridge National Laboratory) **61**

Specimens from six Pb-Li capsule experiments exposed for 1000h at 700° or 800°C were further characterized to determine the extent of attack. The LiAlO2 reaction product appeared to spall in some cases, although this may be due to the Pb-Li cleaning process after exposure. The most unusual result was the large Al loss from the coating on Fe-9Cr-2W after 1000h at 700°C in Pb-Li. If this result indicates the rate of Al loss, it has strong implications for the coating lifetime at this temperature. Also, the mass loss from type 316 stainless steel and resulting microstructure were compared for commercial Pb-Li and high purity Pb-Li. The experimental plan is outlined for the next series of 1000h capsule experiments beginning in January 2009.

7.2 IRRADIATION EFFECTS ON DIELECTRIC MIRRORS IN INERTIAL FUSION POWER REACTOR APPLICATION - L. L Snead and K. Leonard (Oak Ridge National Laboratory), G. E. Jellison Jr. (Fusion Technology Institute), Mohamed Sawan (University of Wisconsin-Madison), and Tom Lehecka (Penn State University) **68**

This paper discusses the neutron exposure expected in the HAPL dielectric mirrors and an experimental program comprised of fabrication of advanced dielectric mirrors and testing of these mirrors exposed to prototypical irradiation environment. Specifically, three dielectric mirror types were fabricated to reflect in the KrF laser wavelength of 248 nm and these mirrors irradiated at ~ 175°C in the dose range of 0.001 to 0.1 x 10^{25} n/m^2 (E>0.1 MeV.) This dose range spans the range calculated with a recently developed 3-D Monte Carlo code. Mirrors were visually inspected following irradiation and reflectivity and laser induced damage threshold measured. All mirrors were intact following irradiation and did not appear to degrade significantly either in reflectivity or damage threshold. This finding is somewhat in contradiction to earlier work on dielectric mirrors, which suggested poor performance of dielectric mirrors at an order of magnitude lower neutron dose. Moreover, the current finding suggests the possibility for using dielectric mirrors to much high dose levels.

8 BREEDING MATERIALS

No contributions this period

9 RADIATION EFFECTS, MECHANISTIC STUDIES, AND EXPERIMENTAL METHODS

9.1 MODELLING THERMODYNAMICS OF ALLOYS FOR FUSION APPLICATION - A. Caro, P. Erhart, M. Serrano de Caro, B. Sadigh (Lawrence Livermore National Laboratory), S.G. Srinivasan, and C. Jiang (LANL). L. Malerba (Belgium), J. Wallenius (Sweden), A. Stukowski (Germany) **81**

We develop a strategy to model radiation damage in FeCr alloys, system in which magnetism introduces an anomaly in the heat of formation of the solid solution that is at the basis of its unique behavior. Magnetism has implications for the precipitation of excess Cr in the *a*' phase in the presence of heterogeneities. These complexities pose many challenges for atomistic (empirical) methods. To address such issues we develop a modified, many-body potential by rigorously fitting thermodynamic properties, including free-energy. Multi-million atom displacement Monte Carlo simulations in the transmutation ensemble, using both our new potential and our new MC code, are able to predict properties of non equilibrium processes like heterogeneous precipitation, and dislocation – precipitate interactions, enabling the study of hardening and embrittlement under irradiation.

9.2 ATOMISTIC STUDIES OF PROPERTIES OF HELIUM IN BCC IRON: COMPARISON OF FE–HE AND FE MATRIX POTENTIALS—David M. Stewart, Stanislav Golubov (Oak Ridge National Laboratory and the University of Tennessee), Yuri Ostesky, Roger E. Stoller, Tatiana Seletskaia, and Paul Kamenski (Oak Ridge National Laboratory) **92**

In fusion applications, helium caused by transmutation plays an important role in the response of RAFM steels to neutron radiation damage. We have performed atomistic simulations using a new 3-body Fe–He inter-atomic potential combined with the Ackland iron potential. The results are compared with older (Wilson) and more recent (Juslin-Nordund) Fe-He pair potentials, and with alternate iron matrices. With the ORNL potential, interstitial helium is very mobile and coalesces together to form interstitial clusters. We have investigated the mobility of these clusters. If the He cluster is sufficiently large the cluster can push out an Fe interstitial, creating a Frenkel pair. The resulting helium-vacancy cluster is not mobile. The ejected SIA is mobile, but is weakly trapped by the He–V cluster. If more helium atoms join the He–V cluster, more Fe interstitials can be pushed out, and they combine to form an interstitial dislocation loop. The reverse process is also studied. Multiple helium atoms can be trapped in a single vacancy, and if there are few enough, the vacancy can recombine with an Fe interstitial to create a helium interstitial cluster. These mechanisms are investigated together in larger simulations that examine the nucleation of He defects. Results are compared based on temperature, interatomic potentials used and helium concentration.

9.3 IMPLEMENTATION OF A Fe-He 3-BODY INTERATOMIC POTENTIAL - R. E. Stoller (Oak Ridge National Laboratory), S. I. Golubov (Oak Ridge National Laboratory and the University of Tennessee), P. J. Kamenski (University of Wisconsin, Madison), T. Seletskaia and Yu. N. Osetsky (Oak Ridge National Laboratory) **97**

The implementation of a recently-developed interatomic potential describing the interactions of helium in bcc iron is described. This He-Fe potential was based on an empirical fit to the results of *ab initio* calculations of both the formation and relaxation energies of small helium defect structures in iron. The fitting database included substitutional and interstitial helium, as well as small helium and helium-vacancy clusters. In contrast to previous He-Fe pair potentials, fitting the *ab initio* forces and energies required the use of a three-body interaction term. The implementation of this potential for atomistic simulations using molecular dynamics presented certain challenges which are discussed here to facilitate its further use in materials research, particularly to investigate the behavior of iron-based alloys that may be employed in fusion energy systems.

9.4 **STEADY-STATE SIZE DISTRIBUTION OF VOIDS IN METALS UNDER CASCADE IRRADIATION -** A.V. Barashev (The University of Liverpool), S.I. Golubov (Oak Ridge National Laboratory, University of Tennessee) 108

The steady state of the void population predicted by the theory under cascade-irradiation conditions has been analyzed. The following conclusions have been drawn.

1) The theoretical steady-state SDF of voids is described by a Gaussian distribution, which is quite narrow, in contrast to much bigger spread of void sizes observed.
2) At high void density, when $\alpha >> 1$, the irradiation dose required to reach the steady state is higher than those at which void lattices are observed. Hence, the void size saturation of randomly distributed voids and in the lattice are not related to each other.
3) At low void density, when $\alpha \leq 1$, the irradiation dose required to reach the steady state is relatively small and might be a reason for the incubation period of swelling frequently observed.

9.5 **KINETICS OF SELF-INTERSTITIAL CLUSTER AGGREGATION NEAR DISLOCATIONS AND THEIR INFLUENCE ON HARDENING -** Ming Wencor (University of California-Los Angeles), Akiyuki Takahashi (Tokyo Univ. of Science) and Nasr M. Ghoniem (University of California-Los Angeles) 114

Kinetic Monte Carlo (KMC) computer simulations are performed to determine the kinetics of SIA cluster "clouds" in the vicinity of edge dislocations. The simulations include elastic interactions amongst SIA clusters, and between clusters and dislocations. Results of KMC simulations that describe the formation of "SIA clouds" during neutron irradiation of bcc Fe and the corresponding evolution kinetics are presented, and the size and spatial distribution of SIA clusters in the cloud region are studied for a variety of neutron displacement damage dose levels. We then investigate the collective spatio-temporal dynamics of SIA clusters in the presence of internal elastic fields generated by static and mobile dislocations. The main features of the investigations are: (1) determination of the kinetics and spatial extent of defect clouds near static dislocations; (2) assessment of the influence of localized patches of SIA clouds on the pinning-depinning motion of dislocations in irradiated materials; and (3) estimation of the radiation hardening effects of SIA clusters. The critical stress to unlock dislocations from self-interstitial atom (SIA) cluster atmospheres and the reduced dislocation mobility associated with cluster drag by gliding dislocations are determined.

9.6 **LENGTH-SCALE EFFECTS IN CASCADE DAMAGE PRODUCTION IN IRON -** R. E. Stoller (Oak Ridge National Laboratory), P. J. Kamenski (University of Wisconsin, Madison) and Yu. N. Osetsky (Oak Ridge National Laboratory) 131

Molecular dynamics simulations provide an atomistic description of the processes that control primary radiation damage formation in atomic displacement cascades. An extensive database of simulations describing cascade damage production in single crystal iron has been compiled using a modified version of the interatomic potential developed by Finnis and Sinclair. This same potential has been used to investigate primary damage formation in nanocrystalline iron in order to have a direct comparison with the single crystal results. A statistically significant number of simulations were carried out at cascade energies of 10 keV and 20 keV and temperatures of 100 and 600K to make this comparison. The results demonstrate a significant influence of nearby grain boundaries as a sink for mobile defects during the cascade cooling phase. This alters the residual primary damage that survives the cascade event. Compared to single crystal, substantially fewer interstitials survive in the nanograined iron, while the number of surviving vacancies is similar or slightly greater than the single crystal result. The fraction of the surviving interstitials contained in clusters is also reduced. The asymmetry in the survival of the two types of point defects is likely to alter damage accumulation at longer times.

10 DOSIMETRY, DAMAGE PARAMETERS, AND ACTIVATION CALCULATIONS

No contributions this period

11 MATERIALS ENGINEERING AND DESIGN REQUIREMENTS

No contributions this period

12 IRRADIATION FACILITIES AND TEST MATRICES

12.1 TITAN TASK 2-3 SILICON CARBIDE BEND STRESS RELAXATION CREEP EXPERIMENT - Y. Katoh (Oak Ridge National Laboratory), Y.B. Choi (Hiroshima University), and T. Hinoki (Kyoto University) **140**

A study on transient irradiation creep deformation of silicon carbide is being undertaken as a part of Task 2-3 of the US/Japan TITAN collaboration on fusion materials and blanket technology. The Phase-IA program is the first of the two irradiation campaigns planned for studying the bend stress relaxation (BSR) creep of ceramics and composites under neutron irradiation. The objective of experiment is to gain understanding of the stress relaxation and transient creep behavior of SiC composites and constituents under neutron irradiation at elevated temperatures. The neutron irradiation will be performed using hydraulic and fixed rabbit facilities of the High Flux Isotope Reactor. The Phase-IA program irradiates 8 rabbit capsules; 5 in hydraulic and 3 in fixed facility. Target irradiation temperatures in the Phase-I are 300, 500, 800, and 1200ºC. The minimum number of rabbit capsules to be irradiated in entire Phase-I campaign will be 15. The present schedule assumes the initiation of irradiation in early 2009.

12.2 IRRADIATION EXPERIMENT DESIGN FOR TITAN RABBITS WITH FERRITIC STEEL, TUNGSTEN, AND NICKEL SPECIMENS - E. Popov, J. McDuffee, M. Sokolov, (Oak Ridge National Laboratory) **146**

Several designs of capsules for irradiating different specimens are described in this work. The specimens are of tensile, disk, or plate configurations from ferritic steels (FS), tungsten, and nickel. Some designs are complete, and others are still in the temperature evaluation phase. Two capsules (T9A1 and T9A2) are currently being irradiated in the hydraulic tube of HFIR as of January 2009

12.3 PULSED E-BEAM THERMO-FATIGUE SYSTEM (PETS)—Chad Duty, Lance Snead (Oak Ridge National Laboratory), John Sethian (Naval Research Laboratory) **155**

A unique pulsed electron beam system has been developed for the thermo-mechanical fatigue testing of potential first wall materials for inertial fusion energy program. The Pulsed E-beam Thermo-fatigue System (PETS) is a high perveance system that pulses a 70 kV, 74 A electron beam at rates up to 100 Hz. The pulse width ranges from 0.5 to 1.5 μs and is confined to an area of 1 cm^2. Following design and fabrication of the PETS system, it was installed at ORNL in the fall of 2007. Several technical challenges have precluded its use as a thermo-fatigue system, but plans are in place to resolve many of these issues and move toward a fully-operational system by the summer of 2009.

MICROSTRUCTURAL EXAMINATION OF DEFORMATION IN IRRADIATED V-4CR-4TI COMPRESSION SPECIMENS – D. S. Gelles (Pacific Northwest National Laboratory)[*]

OBJECTIVE

The objective of this effort is employ compression testing on irradiated vanadium alloys in order to better understand deformation behavior in this class of materials.

SUMMARY

Microstructural examinations have been performed on a series of V-4Cr-4Ti cylindrical compression specimens in order to provide understanding of the observed deformation behavior. Compression testing showed that unirradiated specimens exhibited upper and lower yield points whereas following irradiation the yield stresses were much higher and no yield drop behavior was observed. Both conditions showed evidence of serrated yielding during testing at ~420°C. Microstructural examination of irradiated conditions revealed extensive precipitation making it difficult to observe dislocation structures. Interstitial Impurities were found to form a fine distribution of precipitates following irradiation at ~420°C. Interaction between these precipitates and glide dislocations is apparent.

PROGRESS AND STATUS

Introduction

Compression testing allows measurement of deformation of low ductility materials to considerably higher strains than are possible by tensile testing. It also allows for stress relaxation test to identify deformation processes. If specimens are cylindrical and of sizes comparable to TEM disks, a simple process for preparing specimens for microstructural examination is possible, using slicing and electropolishing procedures. In previous reports on V-4Cr-4Ti compression testing of unirradiated materials, [1,2] two heats (NIFS-1 and 832665) were examined at three test temperatures (RT,~250 ~and ~420°C), and showed upper and lower yield points with strains to ~20%. Results are shown in Figure 1a with the coed CA designation the US heat (832665). More recently, tests have been performed on specimens from the MFE-RB-17J irradiation experiment in HFIR,[3,4] with those results reprocduced in Figure 1b.[5] It can be noted that compared to the unirradiated specimens, irradiated specimens are considerably stronger and do not show upper and lower yield pints. Also, testing at ~432°C of both unirradiated and irradiated speciments shows evidence for serrated yielding (specimens CA06, CJ87, CJ89, CA02 and CA05). The purpose of this report is to describe microstructural development in several of these samples of interest.

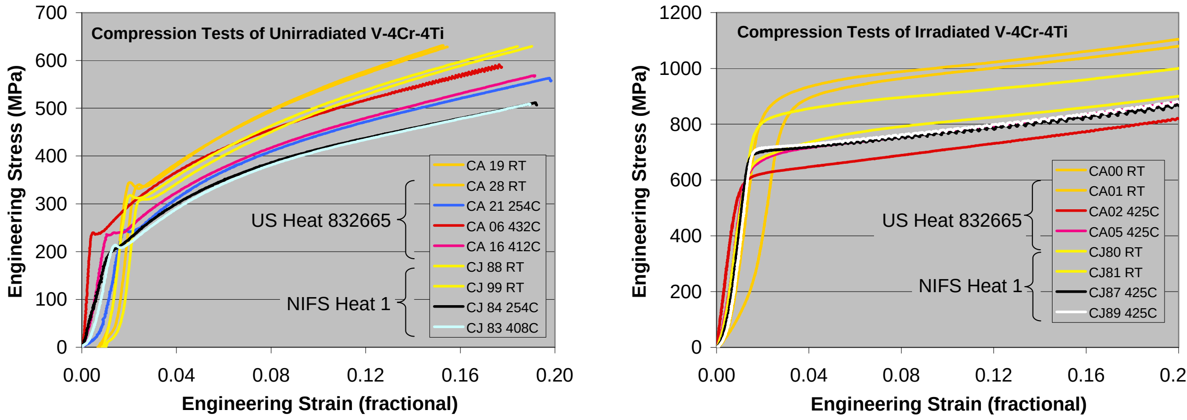

Figure 1. Compression test results of V-4Cr-4Ti for a) unirradiated and b) irradiated cylindrical samples.

---

[*] Pacific Northwest National Laboratory (PNNL) is operated for the U.S. Department of Energy by Battelle Memorial Institute under contract DE-AC06-76RLO-1830.

Experimental Procedure

Specimens selected for microstructural examination are listed in Table 1. These include specimens tested to ~20% as indicated in Figure 1 as well as one specimen, CA09, tested at RT to about 2% strain following irradiation and a second, CA10, untested following irradiation. Following compression testing, specimens tested to ~20% strain were barrel-shaped, indicating that strains were not completely uniaxial at the ends due to friction effects. Therefore, cylindrical specimens initially 3.0 mm in diameter were sectioned with a slow speed saw to provide only central slices ~.25 mm thick. Disks were then electrochemically thinned using standard procedures and examined in a JEM 2010F transmission electron microscope. This provided specimens for examination with the compression axis parallel to the electron beam when the sample was untilted. Images were collected digitally.

Table 1. Test conditions for specimens examined in this report.

Specimen ID	Test Temperature (°C)	~Strain (%)	Irradiation Dose (dpa)	Irradiation Temperature (°C)	Comments
CA19	RT	15			
CA16	412	18			
CJ88	RT	19			
CJ83	408	19			
CA10	Not tested	0	~2.5	425 [2]	
CA09	RT	2	~2.5	425	
CA00	RT	20	~2.5	425	

Results

Examinations are reported in the following order. The microstructure found in specimen CA09, a deformed sample of the US heat of V-4Cr-4Ti that was irradiated in the 17J test at 425°C to about 2.5 dpa and tested in compression at room temperature to approximately 2% strain, is compared with an undeformed duplicate, specimen CA10. Comparison is then made with specimen CA00, similar to CA09 but tested to ~20% strain. Finally, comparison is made with unirradiated conditions CA19 and CA16 tested at RT and 412°C, respectively and with CJ88 and CJ83, of the NIFS-1 heat, tested at RT and 408°C, respectively, all to ~20% strain.

The microstructure of as-irradiated V-4Cr-4Ti is complex, consisting of a high density of irradiation induced precipitates previously identified as [6-8] as "oxy-carbo-nitrides," and dislocation loops and line segments, despite the low dose of ~2.5 dpa. Examples of the microstructure, comparing undeformed material with the ~2% deformation condition in CA09 are given in Figure 2, using imaging conditions best suited for observation of dislocations, $\bar{g}$=011. The area for CA10 is thicker than for CA09, but both contain small dark "black spot" features typical of precipitates, small dislocation loops on the order of 30 nm in diameter and longer dislocation line segments. Some differences can be identified by comparing these images. Many of the precipitates appear in stronger contrast following deformation, perhaps indicating that precipitates are decorated with circular dislocation rings retained following a dislocation bypass mechanism or deformed by a dislocation cutting through the particle to an internal fault. Also, regions can be indentified on the orderof 30 nm wide and 100 to 200 nm long following deformation that contain no precipitate or dislocation images, perhaps cleared of microsturctual features by deformation. However, both observations may be a result of differences in specimen thickness. Alternatively, it can be noted that the imaging conditions used should only allow observation of half the dislocations present, and these "cleared regions" may appear because not all Burgers vectors are imaged.

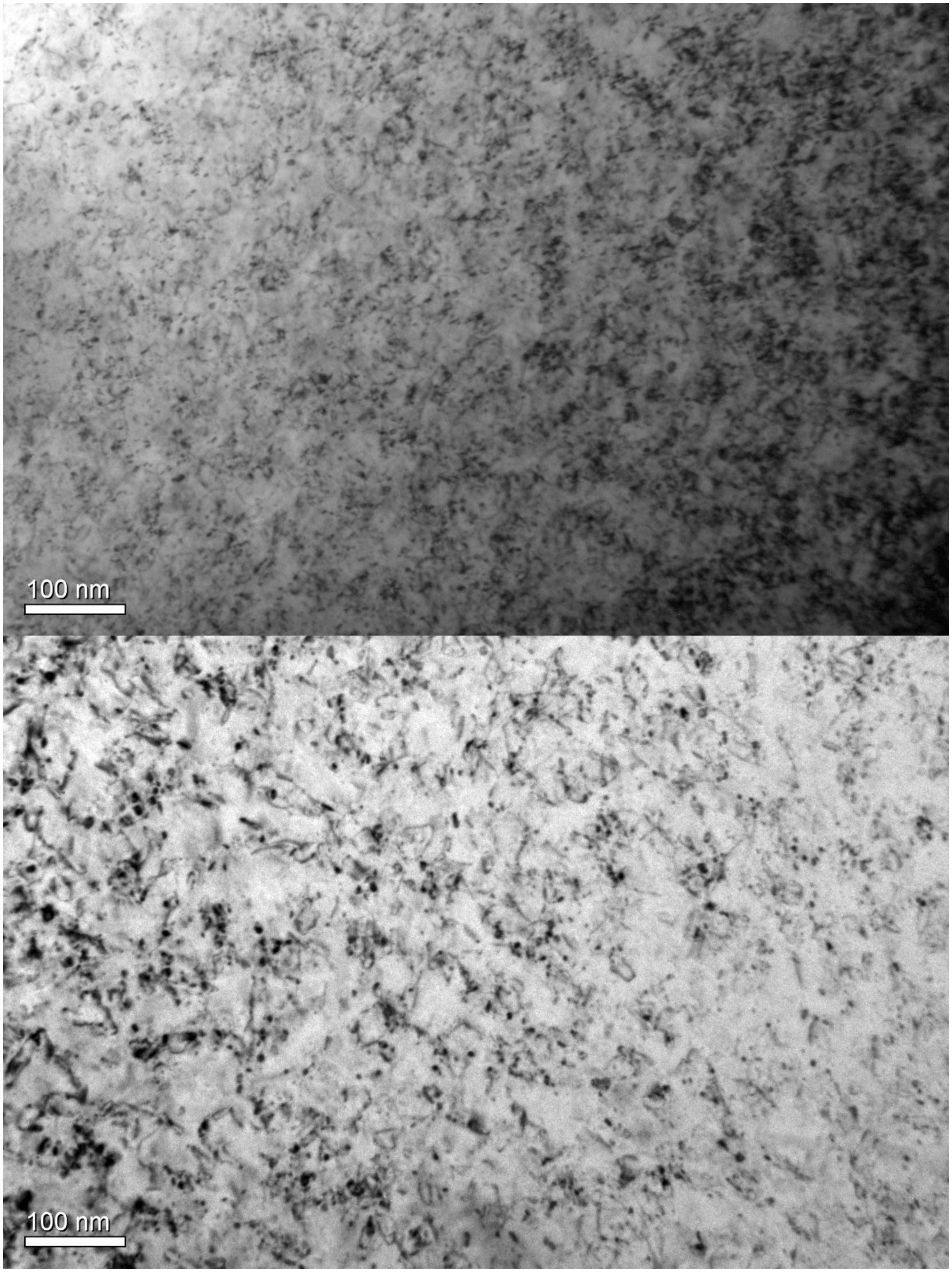

Figure 2. Comparison of microstructures in a) undeformed and b) deformed V-4Cr-4Ti, both irradiated at 425°C to ~2.5 dpa.

In order to ensure that deformation had indeed occurred following a strain of ~2%, attention was centered on a grain boundary area in each condition. Typically, a denuded zone develops free of irradiation-induced microstructure adjacent to grain boundaries during irradiation. Figure 3a shows such a boundary oriented from upper left to lower right in undefromed condition CA10. Denuded zones approximately 50 nm wide have developed on either side of the boundary. Figure 3b provides the comparison following deformation to ~2% strain in condition CA09, showing a typical grain boundary region oriented horizontally in dislocation contrast. Dislocations can be seen at several places, crossing the denuded zone adjacent to the boundary. Therefore, sufficient strain has been induced to cause dislocation slip bands to cross denuded zones in sample CA09 at a spacing of ~100 nm so that any typical region selected for examination can be expected to be deformed.

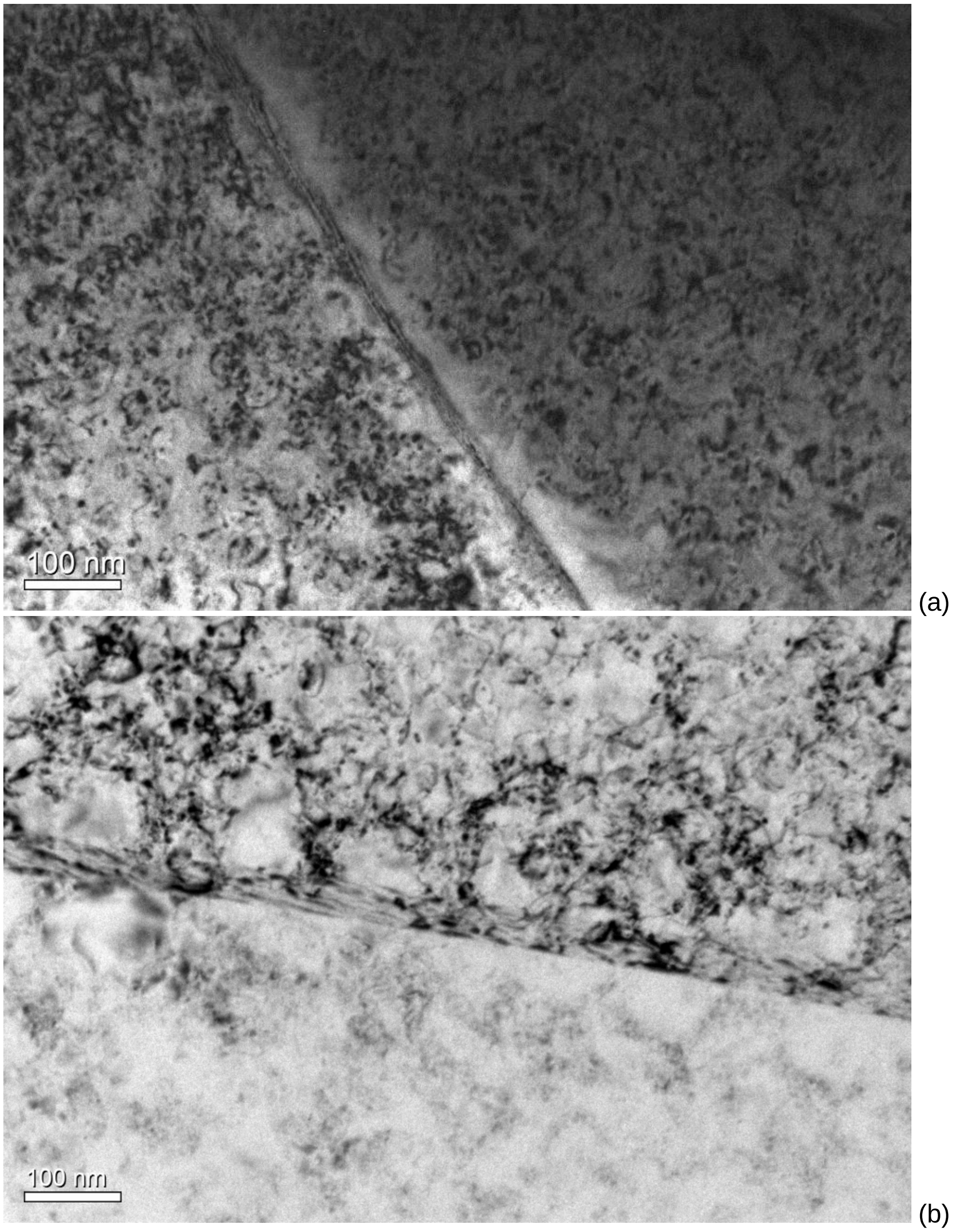

Figure 3. Dislocation structures near grain boundaries in conditions a) CA10, undeformed, and b) CA09, deformed to ~2%.

In an effort to better understand the microstructures due to deformation following irradiation, stereo pairs were taken of condition CA09 and are presented as anaglyphs, requiring the use of colored glasses for stereo observation. Figure 4 provides an anaglyph using $\bar{g}=011$ contrast showing the area in Figure 2b, and Figure 5 provides an anaglyph using weak beam $\bar{g}=200$ contrast, with the images inverted to better show the dislocation structures. Both images have been rotated to optimize stereo viewing, so that g is vertical. It can be noted that $\bar{g}=200$ imaging should show all dislocations present.

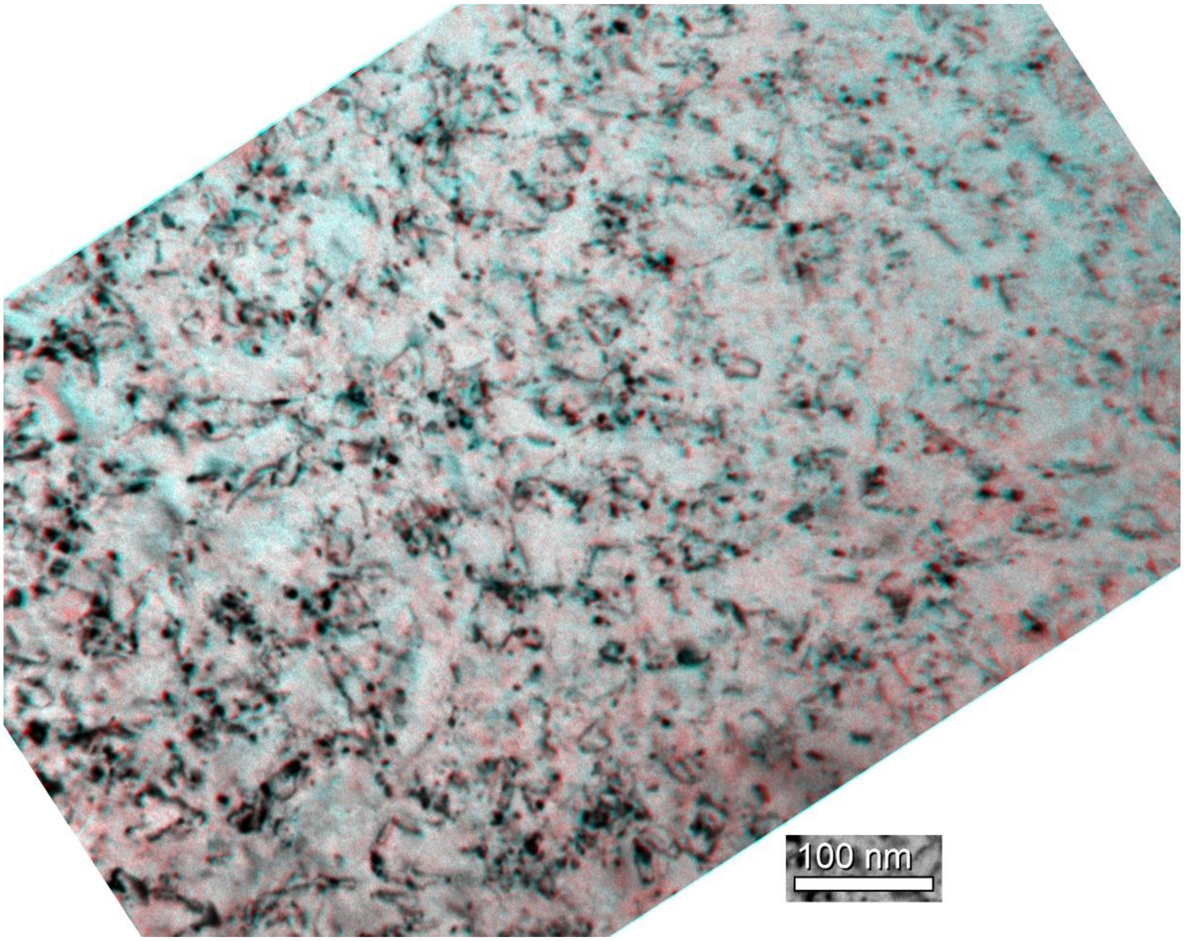

Figure 4. Anaglyph of dislocation structure in CA09 using $\bar{g}=011$ contrast for a foil near $(01\bar{1})$.

For those having difficulty seeing these images in stereo, a brief description will be provided based on standard viewing conditions with a red lens on the left. The stereo model for Figure 4 is only slightly inclined, with the thicker section on the right. Dislocation and precipitate features appear in vertical walls, often inclined to the vertical direction. A number of examples of (a/2)<111> loops on the order of 25 nm diameter or less can be identified with segments often obscured by overlying features, and both strongly contrasted and weakly contrasted “black spot damage” representing precipitates can be seen. The black spot features are describe as representing precipitates because two size distributions of loops are unlikely unless two different Burgers vectors are represented. This structure appears in patches, with intervening background of two shades, one grey and the other more white. It is possible to convince oneself that the white patches represent planar regions at a ~45° incline to the surface, and therefore they may define deformation bands. Also, examples can be found of straight dislocation segments, many of which are not associated with precipitate (black spot) decoration. The foil thickness is estimated, based on a convergent beam pattern for a nearby area is ~150 nm.

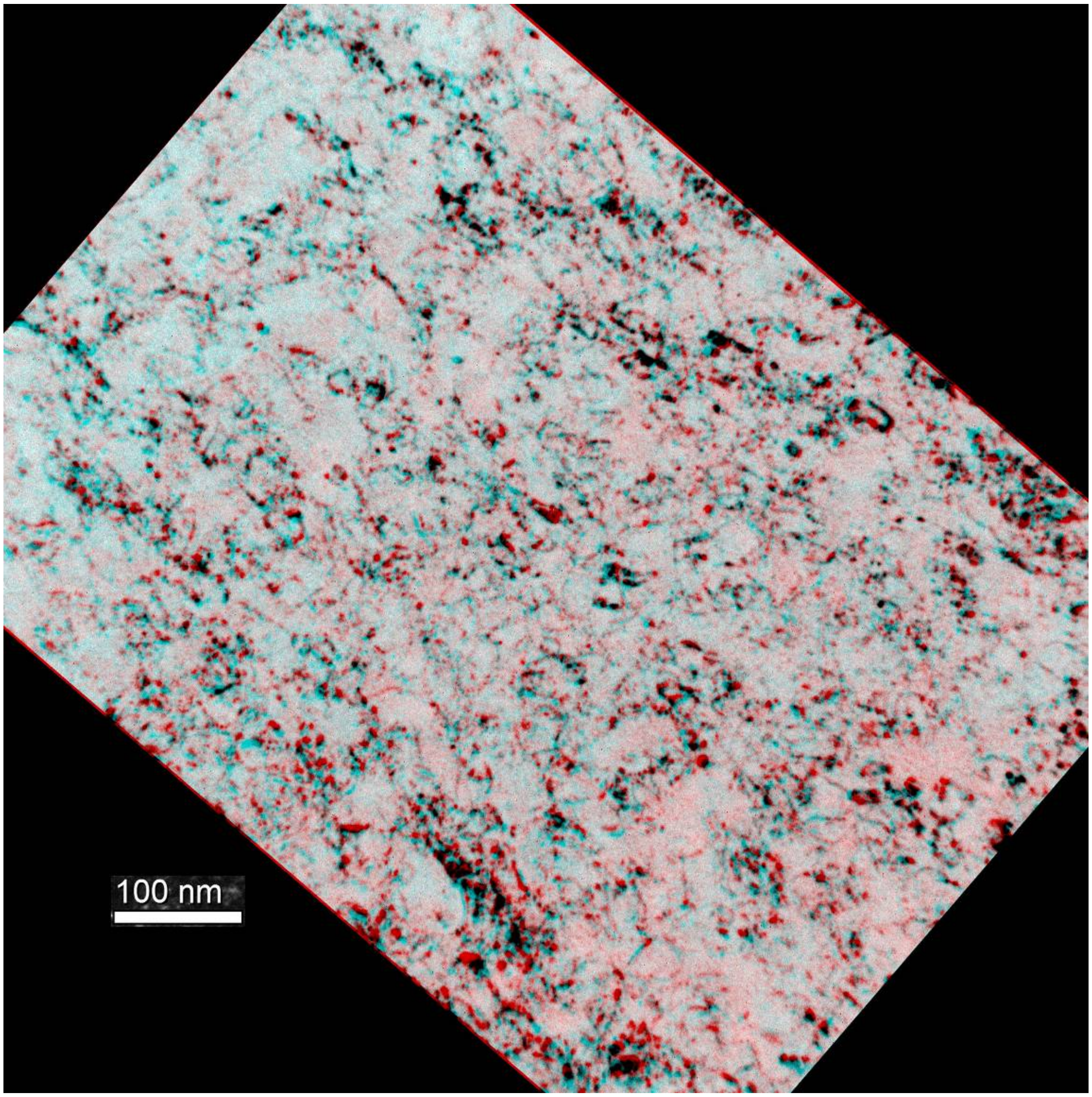

Figure 5. Anaglyph of dislocation structure in CA09 using $\bar{g}$=200 weak beam contrast with the image inverted for a foil near $(01\bar{1})$.

Figure 5 shows the same region using $\bar{g}$=200 contrast so that all (a/2) <111> dislocations can be seen. The stereo model is about three times deeper, and individual dislocation loops and line segments can be identified in weak contrast from top to bottom. Therefore the dislocation images are very narrow and weak, but in stereo, a dislocation network can be identified. Again, strongly and weakly contrasted “black spot damage” can be seen which tends to be clumped as a function of depth and structure is non-uniformly distributed, with some whiter background regions identifiable.

In order to better understand the consequences of much higher levels of deformation, Figure 6 has been prepared from specimen CA00 deformed ~20% following irradiation. The imaging conditions are the same as those in Figures 5 with the anaglyph image using inverted $\bar{g}$ =200 contrast with $\bar{g}$ vertical. The stereo model in this case is inclined with the lower left down and upper right up. Individual dislocations are difficult to identify, the structure appears to primarily consist of walls of clumped black spots or precipitates. Examples can be found in the central left area where black spots or precipitates are in linear arrays. Therefore, a much lower density of dislocations is apparent, probably because dislocations are masked by black spot features or at too high a density to be resolved. However, regions are again apparent where little structure is visible, defining a cell wall structure with no internal structure that probably originated from the irradiated microstructure.

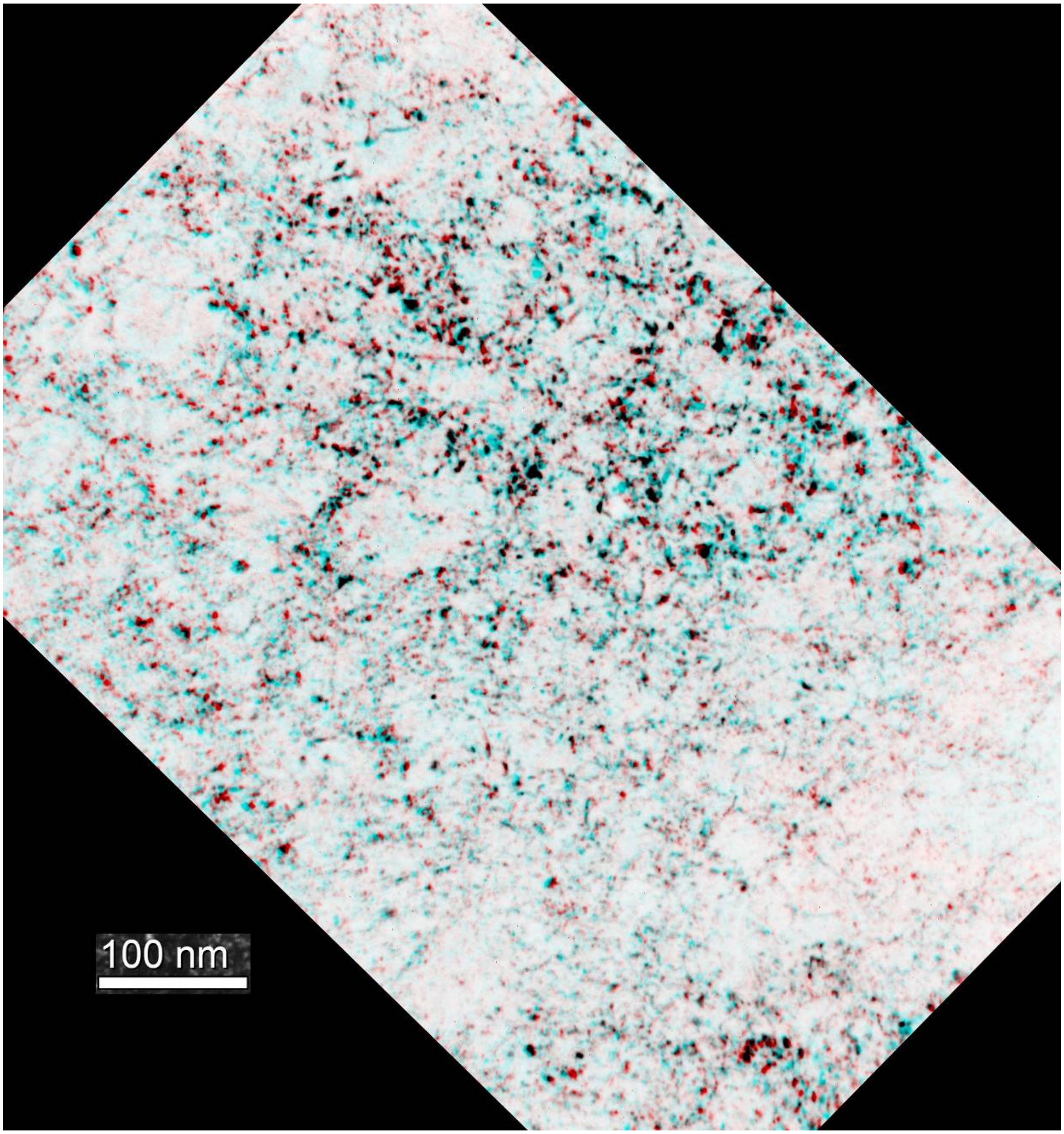

Figure 6. Anaglyph of dislocation structure in CA00 using $\bar{g}$=200 weak beam contrast with the image inverted for a foil near (001).

Figure 7 shows another example of the dislocation structure in CA00 in $\bar{g}$=011 contrast in order to provide comparison with Figure 2b (in part, for those unable to deal with the stereo images). The magnification is lower, so the dislocation density appears higher in CA00 than in CA09 and consisting of complex line segment networks. Of note is the fact that most precipitates appear in strong contrast whereas images of Ca09 and CA10 in Figures 2 and 3 show both precipitates appear in both strong and weak contrast. Appear at a higher density following deformation to 20% strain.

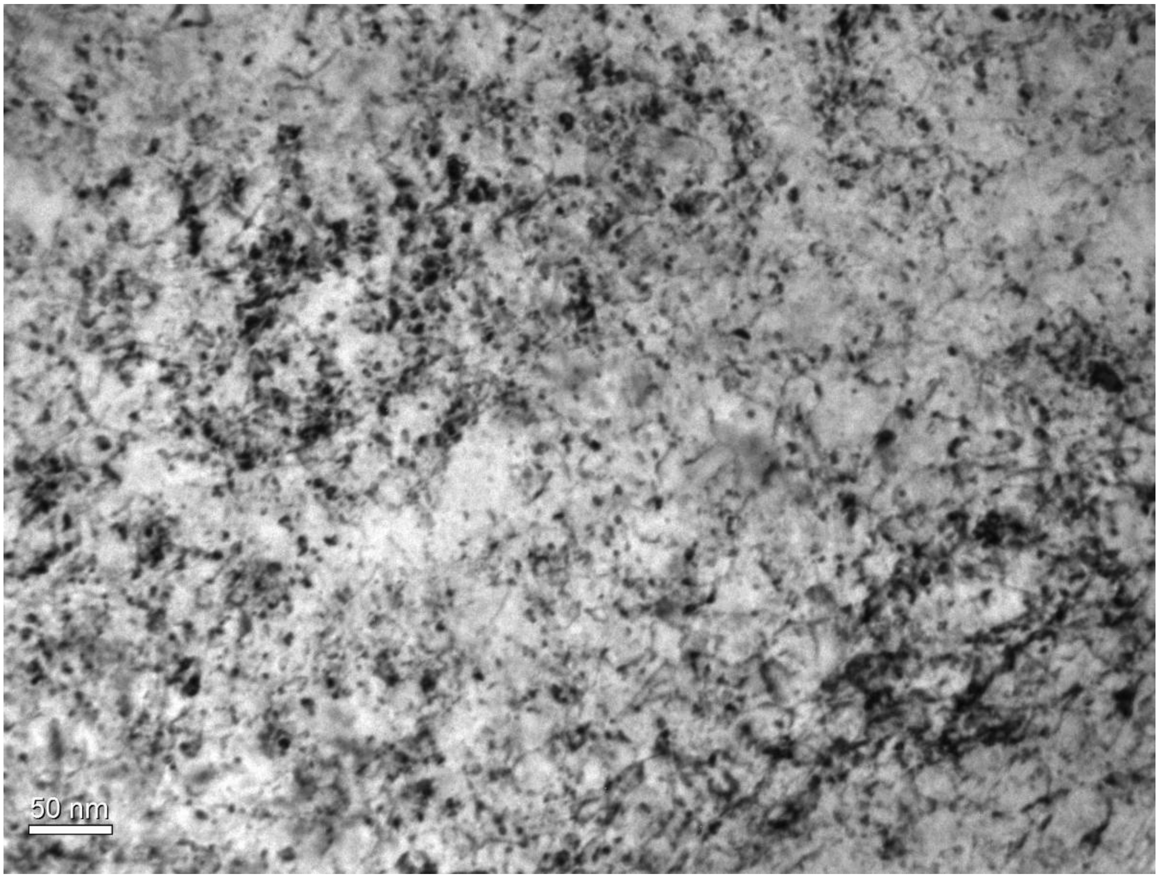

Figure 7. Dislocation and precipitate strictures in condition CA00 after irradiation at 425°C to ~2.5 dpa and ~20% strain.

Finally, examples are provided of microstructures in unirradiated conditions tested to ~20% strain. All images are for $\bar{g}$=110, with CA19, tested at RT in a), CA16, tested at 412°C in b), CJ88, tested at RT in c) and CJ83 tested at 408°C in d). Dislocations are clearly visible without precipitate particles do not appear to be present for the CA (or US heat) conditions, but surprisingly, a few precipitates can be seen for the CJ (or NIFS-1) heat conditions. The dislocation structure is less tangled following testing at the higher temperature, as expected. In comparison with the irradiated microstructures, the major difference is the precipitate (or black spot) density following irradiation.

Discussion

Microstructural studies have demonstrated that irradiation of V-4Cr-4Ti at temperatures around 425°C and below results in extensive precipitation of “oxy-carbo-nitrides” [6,7]. Higher irradiation temperatures do not show these features. Also, deformation tests on V-4Cr-4Ti following irradiation in this temperature range of 425°C, both in tension and compression, have repeatedly demonstrated significant hardening [5,9]. Furthermore, tensile and compression testing of both unirradiated and irradiated V-4Cr-4Ti demonstrate serrated yielding in the range 200 to 400°C [5,9,10]. It is apparent that the deformation properties of this material are dependent on the distribution and motion of interstitial oxygen, carbon and nitrogen present in the alloy and irradiation encourages precipitation.

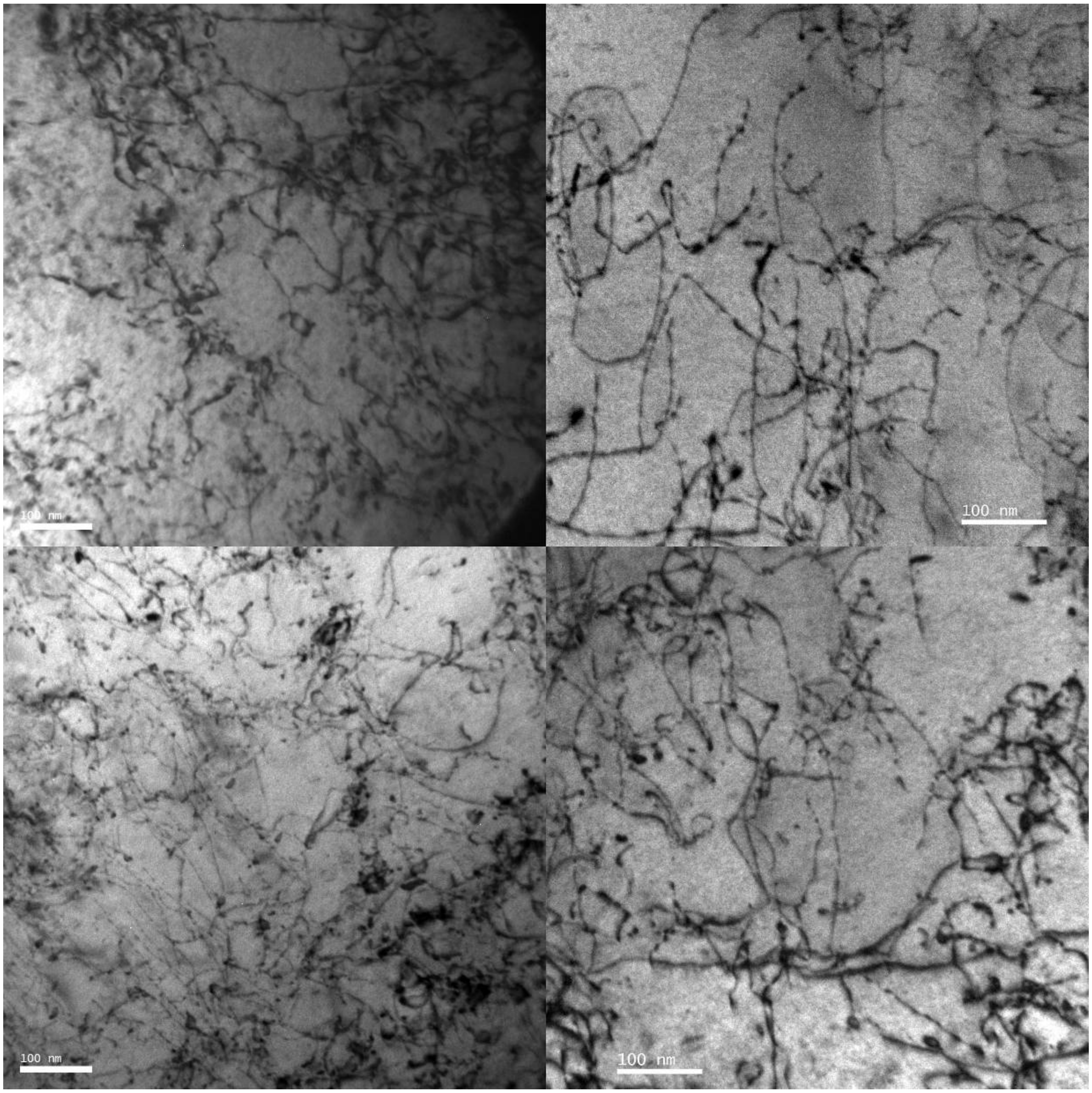

Figure 8, Microstructures in unirradiated conditions at ~20% strain with CA19, tested at RT in a), CA16 tested at 412° C in b), CJ88, tested at RT in c) and CJ83 tested at 408°C in d).

The present work confirms that irradiation induced dislocation structure is highly decorated with precipitation. In fact, several images taken in this study show precipitation localized into cell walls and in linear arrays indicating that precipitation is favored on growing dislocation loops, presumably by a solute segregation process. This can account for regions in the microstructure where precipitation is not prevalent because dislocations did not evolve there.

The dislocations formed in V-4Cr-4Ti are of the type (a/2)<111>, and if no obstacles exist and applied stresses are sufficiently high, they are free to glide on glide planes or cylinders that contain the Burger's vector. Irradiation at ~425°C to ~2.5 dpa raises yield strength by a factor of two. It is apparent from the microstructures presented here for specimens tested at RT following irradiation, and predicted by earlier work, that the irradiation induced precipitates are responsible for the hardening observed. We have not observed extensive planar slip band deformation except in denuded grain boundary regions, (and do not expect to see it in a microstructure containing high precipitate densities).

However, it is noted that serrated yielding was observed for several irradiated specimens tested in compression at ~425-500°C,[5,9]. As irradiation induced precipitation is understood to remove the oxy-carbo-nitrides that cause serrated yielding, this result is surprising. Either significant solute concentrations remain in solution following irradiation, or solute is released during deformation. Evidence for the latter can be noted based on the observation that the extent of serrated yielding increases with strain (or time at temperature.) [5,9] Further studies should be worthwhile, including stress relaxation tests, which may provide a measure of the solute in the vicinity of dislocations, as a function of hold time so as to differentiate between deformation-induced and thermal dissolution.

Conclusions

The mechanism controlling deformation at room temperature in V-4Cr-4Ti was shown to be extensive precipitation, in some measure due to solute segregation. No evidence for extensive planar slip band formation was found.

Future Work

The effort will be continued as opportunities become available.

References

[1] M. B. Toloczko and R. J. Kurtz, in DOE/ER-0313/36 (2004) 131.
[2] M. M. Fryd, M. B. Toloczko and R. J. Kurtz, in DOE/ER-0313/39 (2006) 11.
[3] D. K. Felde, A. L. Qualls, K. R. Thoms, D. W. Heatherly, R. G. Sitterson and R. L Wallace, in DOE/ER-0313/36 (2004) 120.
[4] D. K. Felde, and R. L Wallace, in DOE/ER-0313/38 (2005) 159.
[5] M. B. Toloczko, to be reported.
[6] D. S. Gelles, P. M. Rice, S. J. Zinkle and H. M. Chung, "Microstructural Examination of Irradiated V-(4-5%)Cr-(4-6%)Ti," *J. Nucl. Mater.* V 258-263 (1998) 1380.
[7] D. S. Gelles, "Microstructural Examination of V-(3-6%)Cr-(3-5%)Ti Irradiated in the ATR-A1 Experiment," *J. Nucl. Mater*. V 283-287 (2000) 344.
[8] H. M. Chung, M. C. Billone, and D. L. Smith, in DOE/ER-0313/22 (1998) 22.
[9] A. F, Rowcliffe, S. J. Zinkle and D. T. Hoelzer, J. Nucl. Mater., 283-287 (2000) 508.
[10] D. T. Hoelzer and A. F, Rowcliffe, J. Nucl. Mater., 307-311 (2002) 596.

ADDITIONAL CHARACTERIZATION OF V-4Cr-4Ti EXPOSED TO FLOWING Li – B. A. Pint (Oak Ridge National Laboratory)

OBJECTIVE

Characterize specimens exposed to flowing Li in a thermal gradient to evaluate the effects on V-4Cr-4Ti and a multi-layer electrically-insulating coating needed to reduce the magneto hydrodynamic (MHD) force in the first wall of a lithium cooled blanket.

SUMMARY

The high temperature tensile behavior of V-4Cr-4Ti specimens was evaluated at 500°C in vacuum with a strain rate of $10^{-3}\,s^{-1}$ after exposure to flowing Li at 400°-700°C. Specimens exposed in the loop exhibited increased strength and decreased ductility and the effect increased with decreasing temperature at the various locations in the loop. Thus, the specimens from the bottom of the hot and cold legs of the loop with exposure temperatures near 450°C showed the highest tensile strength, lowest ductility and also the least dynamic strain aging. For comparison, the tensile behavior of unexposed as-annealed V-4Cr-4Ti specimens from the same batch of specimens also was measured as well as specimens (1) exposed to Li for 1000h at 800°C in a capsule and (2) annealed for 2,350 h at 700°C in an evacuated quartz capsule. The present results were compared to similar studies in the literature.

PROGRESS AND STATUS

Introduction

One critical unresolved issue for the vanadium-lithium blanket concept[1,2] (and any liquid metal concept) in a deuterium/tritium fueled fusion reactor[3,4] is the pressure drop associated with the magnetohydrodynamic (MHD) effect of a conducting liquid flowing across the magnetic field lines One proposed solution is to decouple the structural wall from the liquid metal with an electrically insulating coating or flow channel insert (FCI).[5] This coating application requires a thin, crack-free,[6] durable layer with a relatively high electrical resistance.[7] While a "self-healing" layer is possible in corrosion where a re-passivation can occur by the re-formation of a surface oxide, this concept is not applicable to functional (i.e. electrically resistant) coatings because a defect that shorts the coating is unlikely to "heal". Therefore, a robust coating system or a FCI is needed for this application. Due to incompatibility between Li and virtually all candidate insulating oxides,[8-12] the current focus of the U.S. MHD coating program[10-12] is evaluating the compatibility of durable, multi-layer coatings[7,13] where a vanadium overlayer prevents direct contact between the insulating oxide layer and Li. This concept shifts the compatibility concern from the oxide layer to the thin vanadium overlayer. In order to verify that a thin, ~10μm, V layer is sufficiently compatible with Li to function in long-term service, a mono-metallic thermal convection loop was designed and built to expose specimens with thin V overlayers to flowing Li. The loop was operated at a peak temperature of ~700°C for 2,355h.[14,15] Initial characterization of the coatings and V-4Cr-4Ti specimens in the loop was previously reported.[15-17] Further progress with the characterization is reported here, focused on the effect of the flowing Li exposure on the 500°C tensile properties.

Experimental Procedure

Details of the thermal convection loop exposure have been presented previously.[14-16] The specimens consisted of miniature tensile specimens (type SS-3: 25 x 4 x 0.9mm), tab specimens and specimens with a dual layer MHD coating in a chain held together with V-4Cr-4Ti wire. The tensile specimens were annealed for 1h at 1050°C prior to exposure in Li. Specimens from four loop locations were selected for 500°C tensile testing in a vacuum with a base pressure of 10^{-6} Pa (10^{-8} Torr) and a strain rate of $10^{-3}\,s^{-1}$.

Two unexposed, annealed specimens also were evaluated at 500°C to provide a baseline. To further understand the role of flowing Li, tensile tests were performed on specimens that had been (1) annealed for 2,350h at 700°C and (2) exposed to Li in an isothermal 800°C capsule test. The anneal was conducted in an evacuated quartz ampoule to prevent oxidation and the time and temperature were selected to match the time and peak temperature of loop operation.[15] The capsule test was conducted by using a section of V-4Cr-4Ti tubing fabricated for the loop and welding on end caps of V-4Cr-4Ti sheet. The capsule contained 6g of Li and four V-4Cr-4Ti SS-3 tensile specimens from the same batch used in the loop. No microstructural characterization of these V-4Cr-4Ti tensile specimens has been conducted at this time.

Results and Discussion

Table I summarizes the results from nine tensile experiments conducted at 500°C and the mass change that occurred during loop exposure for each of the specimens. The mass loss for the specimen at the top of the hot leg was one of the smaller mass losses as this specimen was the eighth in the chain and saw a temperature of ~627°C based on a linear extrapolation of the thermocouple data.[15] The mass gain for the specimen at the bottom of the hot leg was only 0.02 mg/cm^2 which was lower than the 0.05-0.06 mg/cm^2 for surrounding specimens.

In general, the loop specimens all showed some increase in ultimate tensile stress (UTS) compared to the unexposed specimens and some decrease in ductility, Table 1. Figure 1 shows the 500°C tensile properties as a function of calculated exposure temperature for the four locations in the loop. Combining the hot and cold legs in one graph may be confusing the effect of temperature. In both the hot and cold leg, decreasing temperature resulted in a decrease in ductility and an increase in yield and ultimate stress. The loop locations in Figure 1 also include a total of [O]+[C]+[N] in parentheses which is detailed in Table 2. The chemical analyses of tab and tube specimens[15-17] consistently showed a decrease in the O content and an increase in the C and N contents. These changes in interstitial content are expected based on Li thermodynamics of gettering O, but low affinity, compared to vanadium, for C and N. The calculated temperatures in Table 2 are different because the tab specimens that were chemically analyzed were at different locations than the tensile specimens in Figure 1. Characterization work is needed to determine how the decrease in O and increase in C and N affected the precipitate composition and distribution.

In order to separate the effect of Li exposure, temperature gradient and simple temperature affects (e.g. grain coarsening), two additional exposures have been conducted: a Li capsule test at 800°C for 1000h and an anneal at 700°C for 2,350h. Table 3 summarizes the room temperature and 500°C tensile results

Table 1. Summary of 500°C tensile data for V-4Cr-4Ti specimens with $10^{-3}s^{-1}$ strain rate.

Location	Mass Gain (mg/cm^2)	Yield Stress (MPa)	Ultimate Stress (MPa)	Uniform Elong. (%)	Total Elong. (%)
As-annealed	N/A	218	384	25.3	25.6
As-annealed	N/A	194	379	23.8	24.9
Top Hot Leg, 627°C	-0.13	185	388	21.0	23.2
Top Cold Leg, 562°C	0.06	234	392	22.5	23.5
Bottom Cold Leg, 447°C	0.10	287	441	20.1	21.6
Bottom Hot Leg, 459°C	**0.02**	306	**465**	18.6	20.6
800°C Li capsule	-0.04	178	351	25.3	27.3
800°C Li capsule	-0.01	181	358	26.5	28.2
700°C anneal	0.01	220	371	21.9	23.6

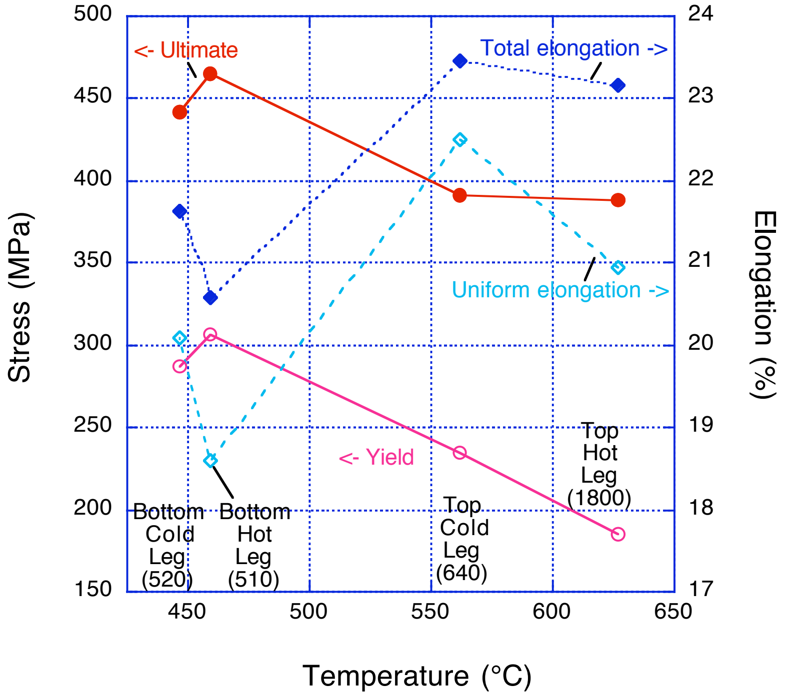

Figure 1. Tensile properties measured at 500°C for the loop-exposed specimens as a function of the calculated average exposure temperature for each specimen. At each general location, the interstitial total ([O]+[C]+[N] in ppmw) in a nearby specimen is shown in parentheses.

for these various conditions along with two conditions from the loop. The specimens exposed in the 800°C Li capsule showed a reduction in UTS and a slight change in ductility. This change is consistent with O removal from the specimen during the Li exposure at 800°C. However, in a previous study examining the effect of Li exposure at 700° and 800°C on mechanical properties of V-4Cr-4Ti,[18] O removal was not clearly observed, which is somewhat surprising. In that study, 500°C tensile testing showed an increase in UTS during exposure to Li for up to 1,000h and a larger decrease in room temperature ductility. One difference in the Li exposure in the previous study is that it was conducted in an Ar-filled glove box, nominally allowing a much greater contamination of the Li, particularly by O, than a capsule exposure where the V-4Cr-4Ti capsule also was gettering C and N from the Li and the C, N and O contents were

Table 2. Measured interstitial composition for tab specimens and the calculated temperature at each location.

Location	Calculated Temperature (°C)	Measured Composition (wppm)			
		O	N	C	Total
Top Hot Leg	657	20	1590	190	1800
Top Cold Leg	556	310	160	170	640
Bottom Cold Leg	423	320	110	90	520
Bottom Hot Leg	416	320	110	80	510
Starting average content:		360	80	70	510

Table 3. Summary of 500°C tensile data for V-4Cr-4Ti specimens with $10^{-3}s^{-1}$ strain rate.

Location	Ultimate Tensile Stress (MPa)		Total Elongation (%)	
	27°C	500°C	27°C	500°C
As-annealed*	466	381	35.7	25.2
Top Hot Leg	452	388	30.7	23.2
Bottom Hot Leg	597	465	24.8	20.6
800°C Li capsule*	432	354	33.5	27.7
700°C anneal	516	371	30.1	23.6

* average of 2-3 specimens

fixed in the capsule. Thus, the V-4Cr-4Ti tensile specimen from the capsule experiment likely had a lower O, C and N content than in the previous study. In the loop experiment, a major drop in O content was observed in the hot leg and all of the specimens showed some reduction, Table 2. The specimens from the 800°C capsule experiment will be chemically analyzed now that they have been tensile tested.

Figure 2 shows another comparison with the prior study,[18] the effect of these various exposures on the serrations in the stress-strain curve due to dynamic strain aging (DSA).[19,20] Compared to the behavior of the unexposed material, the specimens exposed in the loop showed a decrease in the serrations with

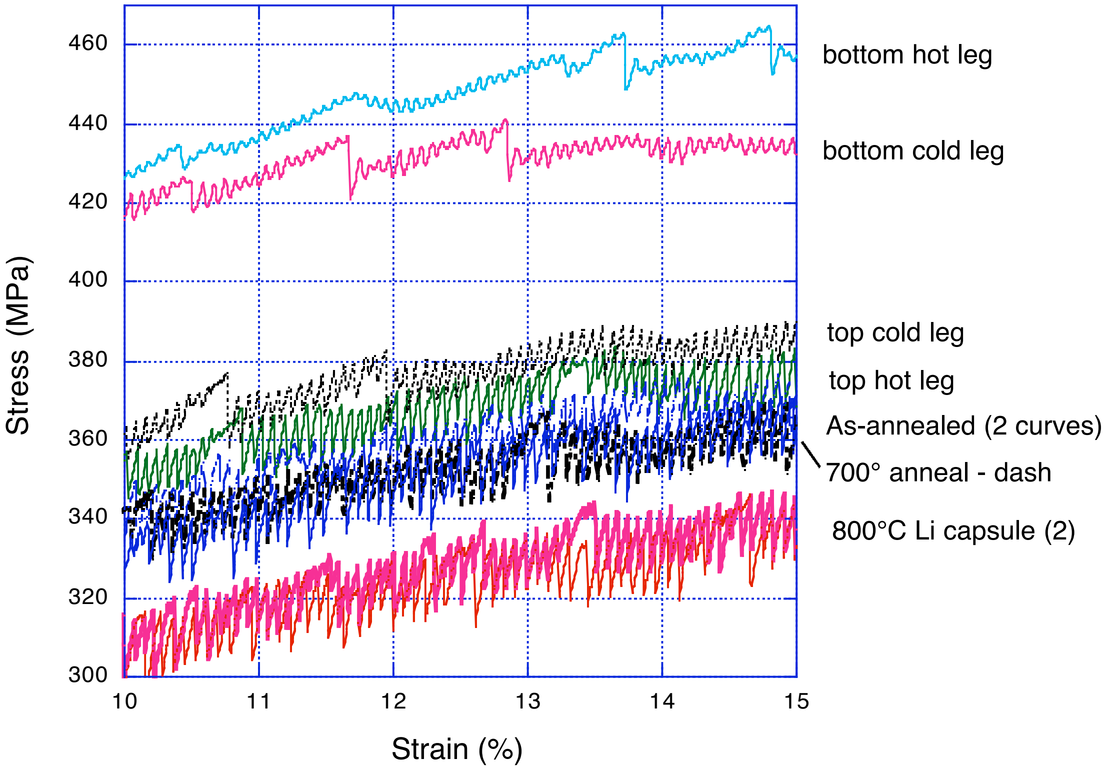

Figure 2. Expanded stress-strain curves of V-4Cr-4Ti specimens evaluated at 500°C in vacuum with a strain rate of $10^{-3}s^{-1}$ to show the dynamic strain aging behavior.

increasing hardness which is not unexpected. The 700°C anneal had almost no effect on the serration behavior (dashed line in Figure 2 on top of unexposed curves). The 800°C Li exposure resulted in a lower strength but similar serrations, essentially the opposite behavior of the previous Li study.[18] The conventional explanation for DSA is the interaction of dislocations with solute interstitials. Interpreting these results is complicated by the competing reduction in O with the increase in C and N, Table 2. A complete characterization of the microstructure of these specimens is needed to understand the mechanism. However, based on the thermodynamics, a large O reduction would be expected from the Li capsule exposure. Such a reduction suggests that O content is not critical to the observed DSA behavior.

References

[1] R. J. Kurtz, K. Abe, V. M. Chernov, D. T. Hoelzer, H. Matsui, T. Muroga and G. R. Odette, J. Nucl. Mater. 329-333 (2004) 47.
[2] T. Muroga, J. M. Chen, V. M. Chernov, K. Fukumoto, D. T. Hoelzer, R. J. Kurtz, T. Nagasaka, B. A. Pint, M. Satou, A. Suzuki and H. Watanabe, J. Nucl. Mater. 367-370 (2007) 780.
[3]. I. R. Kirillov, C. B. Reed, L. Barleon and K. Miyazaki, Fus. Eng. Design 27 (1995) 553.
[4] L. Barleon, V. Casal and L. Lenhart, Fus. Eng. Design 14 (1991) 401.
[5] S. Malang, H. U. Borgstedt E. H. Farnum, K. Natesan and I. V. Vitkovski, Fus. Eng. Design 27 (1995) 570.
[6] L. Bühler, Fus. Eng. Design, 27 (1995) 650.
[7] Y. Y. Liu and D. L. Smith, J. Nucl. Mat. 141-143 (1986) 38.
[8] J. E. Battles, Intern. Mater. Rev. 34 (1989) 1.
[9] T. Terai, et al., J. Nucl. Mater. 233-237 (1996) 1421.
[10] B. A. Pint, P. F. Tortorelli, A. Jankowski, J. Hayes, T. Muroga, A. Suzuki, O. I. Yeliseyeva and V. M. Chernov, J. Nucl. Mater. 329-333 (2004) 119.
[11] B. A. Pint J. L. Moser and P. F. Tortorelli, Fus. Eng. Des. 81 (2006) 901.
[12] B. A. Pint, J. L. Moser, A. Jankowski and J. Hayes, J. Nucl. Mater. 367-370 (2007) 1165.
[13] I. V. Vitkovsky, et al., Fus. Eng. Design, 61-62 (2002) 739.
[14] B. A. Pint, et al., DOE/ER-0313/42 (2007) 2.
[15] B. A. Pint, et al., J. Nucl. Mater. in press (2009).
[16] B. A. Pint, et al., DOE/ER-0313/43 (2007) 2.
[17] B. A. Pint, DOE/ER-0313/44 (2008) 10.
[18] M. M. Li and D. T. Hoelzer, J. Nucl. Mater. in press (2009).
[19] T. Nagasaka, T. Muroga, M. M. Li, D. T. Hoelzer, S. J. Zinkle, M. L. Grossbeck and H. Matsui, Fus. Eng. Des., 81 (2006) 307.
[20] A. F. Rowcliffe, S. J. Zinkle and D. T. Hoelzer, J. Nucl. Mater. 283-287 (2000) 508.

DETAILED 3D STRUCTURE OF {111} TETRAHEDRAL VOIDS AND ITS UNIDIRECTIONAL FORMATION IN CUBIC SIC

—— S. Kondo, Y. Katoh, and L.L. Snead (Oak Ridge National Laboratory)

OBJECTIVES

We report the detailed shape and distribution of the tetrahedral voids in SiC neutron irradiated at 1460˚C, contributing significantly to irradiation-induced swelling. The specific rules for the selection of faceted void surfaces formed in crystals with polar surfaces are discussed.

SUMMARY

The {111} tetrahedral voids induced by neutron-irradiation in 3C-SiC were found to be spatially oriented in only one of two possible directions. The tetrahedral shape was unexpected as the surface-to-volume ratio is larger than the alternative {111} octahedral void common in both metals and ceramics. From a geometric viewpoint, all faces of the observed voids are either Si- or C-terminated surfaces. By comparing the surface area with the octahedral void (composed of the both Si- and C-surfaces) of the same volume, the considerable difference of surface energy between the Si(111) and C($\bar{1}\bar{1}\bar{1}$) was implicated.

INTRODUCTION

Microscopic voids, which are essentially three-dimensional aggregates of vacancies, have been the subject of study in several fields of material science. Significant effort has been directed to understanding the phenomena of the irradiation induced voids and the associated dimensional instability of nuclear materials [1,2]. In semiconductor devices, the distribution and elimination of grown-in voids, which are responsible for the reduction of carrier mobility, has also been extensively investigated [3,4]. On the other hand, engineered three dimensional periodic arrays of voids with a uniform geometric configuration in semiconductor crystals, often referred to as defect engineering, may enable optoelectronic, photonic, and/or quantum electronic functions. Knowing the material-specific three dimensional morphology is one of the key features of voids to help understand fundamental crystal properties and to control the void microstructures. For a given volume, voids generally take a shape that minimizes the total surface free energy [5,6]. If the surface energies of the different family planes are sufficiently close, more than one facet type may emerge. Void formation in face centered cubic (FCC) metals and alloys are generally classified as {111} truncated octahedra of {100} faceting (or tetrakaidecahedron) [7]. In body centered cubic (BCC) crystals there is no consistent void morphology. However, {011} faceted voids have been observed in iron [8] and other BCC metals [9].

Cubic silicon carbide (3C-SiC) is considered as a promising structural material for nuclear applications [10], and electronic and optoelectronic devices [11], because of the high thermal stability, excellent resistance to chemical attack, high thermal conductivity, and high electron saturation drift velocity. In the work by Kondo et al., likely production of {111} tetrahedral voids was reported in the irradiated β-phase SiC (3C crystallographic structure), contributing significantly to irradiation-induced volume expansion above ~1400˚C [12]. The faceted voids were previously observed in neutron-irradiated SiC by Price without detailed structural analysis [13], which is the only one other work implying the tetrahedral feature. In most materials having {111} faceted voids, the void shapes are octahedral and/or {110} truncated octahedra because of their lower surface area than the tetrahedra for a given volume. The formation of uncommon tetrahedral voids may result from the specific rules in this material made of two group IV elements of different electronegativities. In the present work, we report the detailed void shape in SiC and discuss the specific rules for the selection of faceted void surfaces formed in crystals with polar surfaces.

PROGRESS AND STATUS

Experimental

The material used for this work was poly crystalline β-SiC which was produced by chemically vapor deposition by Rohm and Haas Advanced Materials. The CVD material is extremely pure, with typical total impurity concentration of less than 5 wppm. The grain size is between 5 and 10 μm in the plane parallel to the deposition substrate, with the grains elongated in the <111> growth direction perpendicular to the substrate. The material is typically free of micro cracks or other large flaws, but atomic layer stacking faults on the {111} planes are common. There is no porosity in CVD SiC, and the material is generally considered to be of theoretical density (approximately 3.21 g/cm^3). The specimen was irradiated to 5.8 × 10^{25} n/m^2 (>0.1 MeV) at 1460 ± 100 ˚C in the HFIR, Oak Ridge National Laboratory in an ultrahigh purity inert gas environment. Due to the smaller atomic mass and the lower displacement threshold energy for C atoms on the C sublattice than those of Si atoms on the Si sublattice, there is about a factor of 3-4 higher number of C atoms displaced than Si atoms. A thin foil prepared in a commercial Ar-ion-milling unit (FISCHIONE model 1010) using 3-5 keV dual ion beam was examined in a transmission electron microscope (TEM/FEI Technai 20, 200 keV).

Results and discussion

Transmission electron images of the faceted voids created during irradiation are shown in Fig. 1(a)-(c). These images were taken utilizing different beam directions of B~$[0\bar{1}1]$, $[\bar{1}\bar{1}1]$, and [001], respectively (B; electron-beam direction). The {111} planes are indicated by the inset Thompson tetrahedron; four {111} faces named α to δ correspond to the observed crystal {111} planes and six edges correspond to the six <110> directions. The voids were imaged in slightly under-focused conditions, where the contrast arose from a weak absorption component and phase-contrast component due to defocus. Faceted voids are generally observed as polygonal shaped with dark peripheries in the under-focused condition. Through-focus and dark-field image analysis revealed that those polygonal defects were certainly voids without containing any stacking faults and dislocations. Stereo-micrograph analysis revealed that those defects were widely distributed over the specimen foil, distinguishable from surface pits.

In the B~$[0\bar{1}1]$ beam direction (Fig. 1 (a)), the projection view of voids appear as triangular shaped features containing two sides perpendicular to $[\bar{1}11]$ and [111] directions and a slight rounded side parallel to [011] direction. In comparison with a Thompson tetrahedron, the former two sides likely correspond to the edge-on β and δ surfaces, respectively. Meanwhile, the rounded side likely corresponds to α/γ edge, where vast majority of corners at the ends of the sides are rounded or truncated by the β or δ planes. Note that all the “triangular” voids formed in the same grain are oriented in the identical direction as shown in Fig. 1 (a). This feature will be discussed later. In the B~$[\bar{1}\bar{1}1]$ beam direction (Fig. 1 (b)), the projection view of voids appear as rounded triangles. Three bright lines connecting the triangle center with corners are generally seen inside the rounded triangle, each line is parallel to $[\bar{2}1\bar{1}]$, $[\bar{1}\bar{2}1]$, and [112] direction, respectively. The image contrast of inner edge of faceted voids was well simulated by theoretical calculation [14], where the intersecting faces was known to be shown as bright line. Orientation of these bright lines and periphery of the rounded triangle is well accorded with the projection view of the inset Thompson tetrahedron. Therefore, the bright lines most likely correspond to the surface intersecting edges at β/δ, α/δ, and α/β, respectively. In the B~ [001] beam direction (Fig. 1 (c)), the voids appear to be more rounded shape in projection. Two bright lines orthogonally crossed are observed inside some voids, where each line likely correspond to the α/β edge for the line perpendicular to [110] and γ/δ edge for the line perpendicular to $[\bar{1}10]$. The rounded features observed in Fig 1 (c) indicate that most tetrahedral void edges would not be straight but slightly rounded toward the outside of the void. The curvature of the {111} surfaces, which are sufficiently away from edges, is supposed to be insignificant considering the relatively straight projection view of the edge-on surfaces (β, δ) as shown in Fig. 1 (a). By comparing the void images taken from three different directions with each corresponding Thompson tetrahedron, the shape of the voids is confidently determined to be near tetrahedral with {111} facets with vertices slightly truncated by {111} planes. Note that all the “triangular” voids formed in the same grain are identically oriented as clearly seen in Fig. 1 (a).

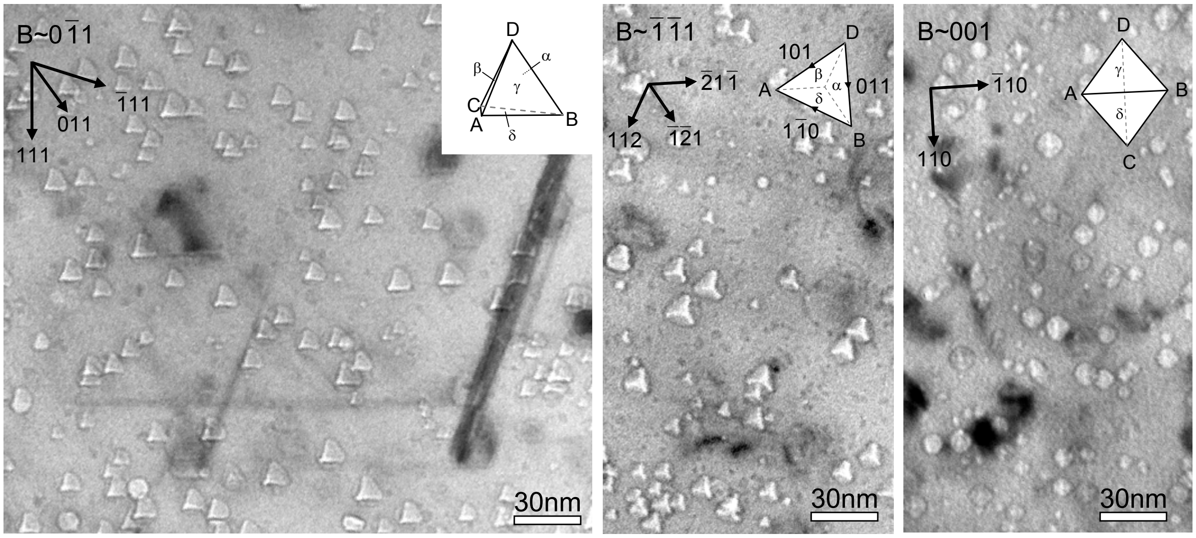

Fig. 1. Microstructure of tetrahedral voids in 3C-SiC after neutron irradiation at 1460˚C to 5.8 × 10^{25} n/m^2. The electron beam direction is close to; (a) $[0\bar{1}1]$, (b) $[\bar{1}\bar{1}1]$, and (c) [001] zone axis. The {111} planes are indicated by the inset Thompson tetrahedron; four {111} faces named *α* to *δ* correspond to the observed crystal {111} planes and six edges correspond to the six <110> directions.

Often in crystals with low stacking fault energy like SiC, stacking fault tetrahedra or Frank faulted loops are energetically preferred over voids when cluster size is relatively small [15, 16]. Presence of gas atoms (either pre-existing or created through nuclear transmutation) might prevent the collapse of a void in the early stage of the vacancy accumulation [17]. Such gas-stabilized voids tend to be in more spherical shapes, generically referred to in the literature as bubbles. However, it can be assumed that the voids examined here are not filled with gas at any significant pressure because of the very limited gas production rates for the highly pure SiC [18]. Therefore, the pressure of these gases is not a likely cause for the observed rounded features.

An important question is the underlying reason for the unidirectional distribution of the voids observed (see Fig. 1 (a)). In the usual case, the void surfaces may be randomly selected by offering equal opportunities to all {111} planes. Then, both types of “triangular” voids, which are symmetric to [011] or $[01\bar{1}]$, should be observed in B~$[0\bar{1}1]$ beam direction. However, that was not the case for 3C-SiC. This phenomenon has not been reported earlier. A possible explanation for such observation is that all the surfaces are either of the Si- or C-terminated {111} surface exclusively, as briefly described below.

The atomic surfaces can be created by bond cleavage at either widely spaced or narrowly spaced {111} interplanar binding; those are single-bond surface and triple-bond surfaces, respectively. For the binary crystal with zinc blende structure, each ideal surface may be terminated at only one element (Si or C atomic layer for SiC). One can expect that the triple-bond surfaces are unfavorable for void surfaces because of its higher surface energy related to the higher dangling bond density [19]. Fig. 2 shows the schematic image of the tetrahedral voids in 3C-SiC, where voids are viewed from the $[0\bar{1}1]$ direction at the atomic level. Edge-on void surfaces are indicated by solid lines for the left-hand void and dashed lines for the right-hand void. Each open circle and closed circle can be either a Si atom or C atom. All four faces (two edge-on and the remaining two faces) of the left-handed void in the figure are made of only open circles. The faces of the right-handed void, which is [011] or $[01\bar{1}]$ symmetrical to the left-side void, are made of atoms indicated by closed circles. The unidirectionally-oriented tetrahedral voids indicate that all the surfaces of observed voids contain only one element of Si or C atoms as is clear from the Fig. 2. That is to say, the results indicate that either Si-single-bond-terminated or C-single-bond-terminated surfaces is favored as the void surface, and the other is unfavored.

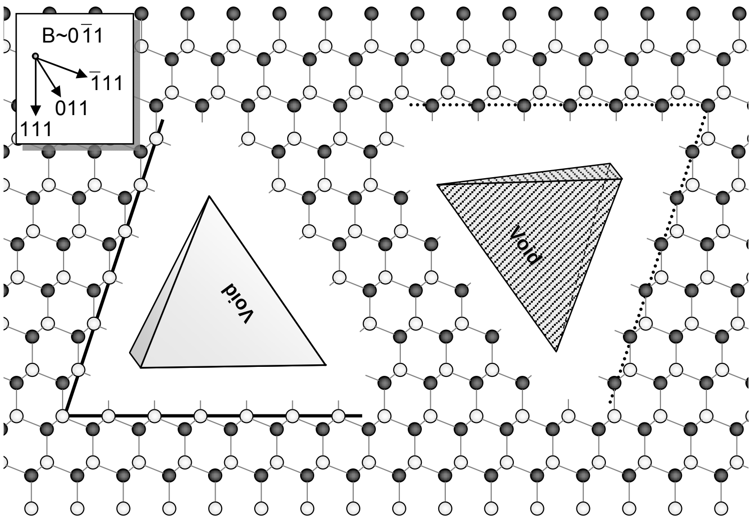

Fig. 2. Possible configurations of {111} tetrahedral voids in 3C-SiC. All four surfaces (two edge-on and the remaining two faces) are made of only open circles for the left-hand void, closed circles for the right-hand void. Each open and closed circle can be either a Si or C atom.

This rule may also affect the three dimensional void shape in this crystal. The void with {111} facets in cubic crystals can have the geometrically alternative shape of octahedron as well as the tetrahedral void shape, where the octahedron is generally preferred due to the lower total surface energy for a given volume in spite of the increase in edge and vertex energy at any TEM visible size. Lack of octahedral voids in 3C-SiC may be because the octahedral void geometrically needs both Si- and C-terminated {111} surfaces for its formation. If the surface energy still controls the equilibrium void shape and distribution in the irradiated SiC, and the energy is sufficiently different between Si- and C-terminated {111} surfaces, the unidirectional formation of tetrahedral voids may occur. The difference of surface energy between the two polar surfaces has not been clarified yet. However, the surface energy of the C-terminated (111) is considered likely to be significantly less than that of Si-terminated surface because of the faster growth rate of C-surfaces of 3C-SiC during the CVD process [20]. The lower surface energy for C-terminated surfaces resulting from stronger surface relaxation comparing to Si-surface has also been theoretically estimated [21-23], though theoretical values are widely scattered and depend strongly on the potential energy functions employed. The absence of octahedral voids indicates that the Si-terminated surface energy is at least 1.5 times greater than the C-terminated surface, by comparing total surface area between pure tetrahedron and octahedron for the same number of contained vacancies. It is comparable to the theoretical simulations showing 1.3-3.4 times higher surface energy for Si-terminated surfaces. It should be pointed out that further study on other possible mechanisms that may be responsible for inducing the unidirectional formation of the tetrahedral voids may help to provide a more complete representation of the finding. Specifically, electronic structure, chemical properties of the void surface, and difference of the displacement damage rates between Si and C under neutron irradiation may be interrelated to the geometric aspects studied here.

In summary, irradiation-induced voids formed in irradiated SiC were tetrahedrally bounded by {111} lattice planes, and the distribution was unidirectionally-oriented in the each grain. Entire surfaces of the unidirectional voids are shown to be the same atomic layer (either Si {111} - or C $\{\bar{1}\bar{1}\bar{1}\}$ - surfaces) due to the crystallographic characteristics of zinc blende structure. This implies that the one of the two atomic surfaces is favored in forming void surfaces and the other is unfavorable. The absence of usual octahedral voids involving both surface types indicates at least 1.5 times higher surface energy for Si{111} than C$\{\bar{1}\bar{1}\bar{1}\}$ assuming the surface energy dominates the void shape.

References

[1] C. Cawthorne and E. Fulton, Nature **216**, 575 (1967).
[2] L.K. Mansur, Nucl. Technol., **40**, 5 (1978).
[3] F. A. Kröger, *The Chemistry of Imperfect Crystals* (North-Holland, Amsterdam, 1964).
[4] V. V. Voronkov and R. Falster, J. Crystal Growth, **194**, 76 (1998).
[5] G. Wulff, Z. Kristallogr., **34**, 449 (1901).
[6] M. C. Desjonquères and D. Spanjaard, *Concepts in Surface Physics* (Springer Verlag, Berlin, 1993).
[7] J.O. Stiegler. in: *Proc. Int. Conf. on Radiation-Induced Voids in Metals*, edited by J.W. Corbett and L.C. Inniello, *CONF-710621* (Alvany, June 9–11, 1971), p. 292.
[8] G.L. Kulcinski, B. Mastel, J.L. Brimhall, Radiation. Eff., **2**, 57 (1969).
[9] R.C. Rau, R.L.Ladd, J. Mottef, J. Nucl. Mater., **33**, 324 (1969).
[10] Y. Katoh, L.L. Snead, Jr., C.H. Henager, A. Hasegawa, A. Kohyama, B. Riccardi, H. Hegeman. J. Nucl. Mater. **367-370**, 659 (2007).
[11] Z. C. Feng, A. J. Mascarenhas, W. J. Choyke, and J. A. Powell, J. Appl. Phys. **64**, 3176 (1988).
[12] S. Kondo, Y. Katoh, L.L. Snead, J. Nucl. Mater. **382**, 170 (2008).
[13] R.J. Price, J. Nucl. Mater. **46**, 268 (1973).
[14] A.J.E. Foreman, H.S. Von Harrach, D.K . Saldin, , Philos. Mag. A **45**, 625 (1982).
[15] J. Silcox and P.B. Hirsch, Philos. Mag. **4**, 72 (1959).
[16] S.J. Zinkle, Philos. Mag. A **55**, 111 (1987).
[17] S.J. Zinkle, Philos. Mag. A **55**, 127 (1987).
[18] H.L. Heinisch, L.R. Greenwood, W.J. Weber, R.E. Williford, J. Nucl. Mater. **327**, 175 (2004).
[19] G. A. Wolff and J. D. Broder, Acta Cryst. **12**, 313 (1959).
[20] H. Nagasawa, K. Yagi, T. Kawahara, N. Hatta, G. Pensl, W. J. Choyke, T. Yamada, K. M. Itoh, and A. Schöner, in: Silicon Carbide, Recent Major Results, edited by W. J. Choyke, H. Matsunami, and G. Pensl (Springer, Berlin, 2004), pp. 207-228.
[21] E. Pearson, T. Takai, T. Halicioglu and W.A. Tiller J. Crystal Growth **70**, 33 (1984).
[22] T. Takai, T. Halicioglu, and W. A. Tiller, Surf. Sci. **164** (1985) 341-352.
[23] X. Luo, G. Qian, W. Fei, E.G. Wang, and C. Chen., Phys. Rev. B **57**, 9234 (1998).

MECHANICAL CHARACTERIZATION OF SILICON CARBIDE COMPOSITES FOR HFIR-18J EXPERIMENT IN UNIRRADIATED CONDITION

— Y. Katoh, K. Ozawa, L.L. Snead (Oak Ridge National Laboratory), Y.B. Choi (Hiroshima University), T. Hinoki (Kyoto University), and A. Hasegawa (Tohoku University)

OBJECTIVE

This work has as an objective of determining the mechanical properties of the silicon carbide composite materials produced for the purpose of evaluating high temperature irradiation performance in the HFIR-18J experiment.

SUMMARY

A suite of silicon carbide ceramics and composite materials were prepared in various specimen types for the purpose of evaluating irradiation performance at high to very high temperatures in the HFIR RB-18J experiment. Detailed information of the materials prepared is provided. Properties including tensile strength, dynamic elastic modulus, interlaminar shear strength, and trans-thickness tensile strength were determined in an unirradiated condition.

PROGRESS AND STATUS

Introduction

Silicon carbide (SiC) ceramics and continuous fiber composites are promising commercial materials for fusion applications due to the exceptional radiation stability, high temperature performance, and low activation properties inherent to SiC. An extensive neutron irradiation campaign HFIR-18J was carried out in US-Department of Energy/Japan-MEXT (Ministry of Education, Culture, Sports, Science and Technology) fusion blanket/materials collaboration program for the purposes of 1) gaining a fundamental understanding of irradiation effects in SiC composites and their constituents in aggressive, fusion-relevant conditions, 2) determining the effects of neutron irradiation on various properties of new generation materials, 3) advancing constitutive modeling of irradiation effects in composites, and 4) determining irradiated engineering properties in support of blanket systems research and development.

In the HFIR-18J experiment, composite materials were fabricated with three different near-stoichiometric SiC fibers and/or high thermal conductivity graphite fibers, thin, ultra-thin, or multilayer interphases, and the SiC matrix made through chemically vapor-infiltration (CVI) or transient eutectic-phase (NITE; nano-infiltration and transient eutectic-phase) processes are being evaluated for mechanical and transport properties following irradiation up to ~7 dpa at temperatures nominally in an 800-1300ºC range. Properties such as axial tensile strength, dynamic elastic modulus, interlaminar shear strength, and trans-thickness tensile strength in an unirradiated condition are given in this report, in addition to the detailed information of materials preparation.

Experimental Procedure

Materials

Materials tested in the HFIR-18J experiment are listed in Table 1. The monolithic SiC ceramics included in the experimental matrix are Rohm & Haas chemically vapor-deposited (CVD) SiC, Coorstek CVD SiC, Hoya single crystal 3C-SiC, and a liquid phase-sintered SiC which represents the matrix material of the NITE composites. Coorstek CVD SiC is of similar chemical purity with the Rohm & Haas but have smaller grain sizes. The high electrical resistivity grade CVD SiC was included to examine the post irradiation electrical properties.

Table 1 – Details of SiC and SiC/SiC materials

Material	Abbreviation	Code	Identifier Prefix	Description (for composites, fiber / interphase / matrix)
CVD SiC R&H	CVD-SiC	CD1	R	Rohm & Haas Co. CVD-SiC, Standard resistivity grade SC-001, Lot# 9130
CVD SiC Coors	CVD-Coors	CD2	C	Coorstek Pure-SiC CVD-SiC, Standard grade, Lot# 549220-1
Single-Crystal 3C-SiC	SC-SiC	SXS	n/a	Hoya single crystal 3C-SiC, Lot# SBB12AH, N-doped 9.53E+18 cm^{-3}
NITE Matrix SiC	LPS-SiC	LPS	L	Liquid phase-sintered SiC for matrix of NITE SiC/SiC, Lot# KS05
HR-Grade CVD SiC R&H	HR-SiC	CD3	D	Rohm & Haas Co, CVD-SiC, High-resistivity grade SC-003, Lot# 9191
TySA CVI Reference	TySA-CVI-Ref	TRF	T	Tyranno-SA3 7.5 micron (SA3-S1I16PX), 2D Plain Weave (PSA-S17I16PX), 17x17 tpi / PyC(150nm) / CVI-SiC
TySA CVI Thin Interphase	TySA-CVI-TI	TTI	X	Tyranno™-SA Grade-3 7.5 micron (SA3-S1I16PX), 2D Plain Weave (PSA-S17I16PX), 17x17 tpi / PyC(50nm) / CVI-SiC
TySA CVI Thick Fiber	TySA-CVI-TF	TTF	F	Tyranno™-SA Grade-3 10 micron (SA3-S1F08PX), 2D Plain Weave (PSA-S17F08PX), 17x17 tpi / PyC(150nm) / CVI-SiC
Nicalon-S CVI Reference	HNLS-CVI-Ref	SRF	A	Hi-Nicalon™ Type-S 900denier (#383213), 2D Plain Weave (HNS9P2424), 24.25x25 tpi / PyC(150nm) / CVI-SiC
Nicalon-S CVI Thin Interphase	HNLS-CVI-TI	STI	E	Hi-Nicalon™ Type-S 900denier (#383213), 2D Plain Weave (HNS9P2424), 24.25x25 tpi / PyC(50nm) / CVI-SiC
Nicalon-S CVI ML Interphase	HNLS-CVI-ML	SML	M	Hi-Nicalon-S 2D-PW(0/90) / (PyC/SiC) multilayer interphase / CVI-SiC
SiC/C Hybrid Fabric CVI	Hybrid-CVI	HFC	H	Tyranno-SA3 7.5 micron (SA3-S1I16PX) / P-120S Graphite Fiber, Orthogonal 3D Weave / PyC(150nm) / CVI-SiC
TySA NITE Composite PG3	TySA-NITE	NTE	N	Tyranno-SA3 UD-XP / PyC / NITE-SiC PG3, Lot# 0408
TySA NITE Composite LG06	TySA-NITE-LG	NTL	K	Tyranno-SA3 UD / PyC / NITE-SiC Lab-Grade #LG06, Lot# LG06
TEM in Graphite Tube	SiC-TEM-Tube	TEM	P	Coated TEM discs for He-injection in SiC tube
Fiber in Graphite Tube	SiC-Fiber-Tube	FBR	P	SiC fiber bundle in SiC tube
Ceramics in TZM Tube	TZM-Tube	TZM	P	Lithium oxide ceramics and diffusion pairs in sealed TZM packet
NITE Joint	SiC-Joint	JNT	J	CVD-SiC joint by NITE, provided by Kyoto University
GE Nicalon-S ICVI	HNLS-CVI-GE	GES	S	GE Power Systems Hi-Nicalon-S 2D-SW / PyC / ICVI-SiC, Provided by PNNL
JAERI 3D Nicalon-S ICVI	HNLS-CVI-3D	JHC	YR	Hi-Nicalon-S 3D / PyC / ICVI-SiC, provided by PNNL
JAERI 3D TySA ICVI	TySA-CVI-3D	JTC	YR	Tyranno-SA 3D / PyC / ICVI-SiC, provided by PNNL
JAERI 3D TySA ICVI-PIP	TySA-CVI-PIP	JTP	YR	Tyranno-SA 3D / PyC / (ICVI+PIP)-SiC, provided by PNNL

The composite materials were prepared by CVI or NITE matrix densification process. For the two dimensional (2D) CVI composites, either Tyranno™-SA3 7.5um fibers, Tyranno™-SA3 10um fibers, or Hi-Nicalon™ Type-S fibers were used as the reinforcement, either in plain-weave or satin-weave architecture with the 0/90º stacking sequence. An orthogonal three-dimensional (3D) CVI composite was also prepared incorporating Tyranno™-SA3 fibers in the in-plane directions and a high thermal conductivity pitch-based graphite fiber P-120S in the through-thickness direction. Limited data of the mechanical and thermophysical properties of these composites were previously determined and published. [5] The NITE composites were prepared using Tyranno™-SA3 fibers in the uni-directional (UD) or UD cross-ply architecture and relatively thick pyrocarbon interphase. [3]

Included in the graphite TEM tubes were transmission electron microscopy disc samples of the standard resistivity grade Rohm & Haas CVD SiC and Hoya single crystal 3C-SiC. Some of the samples were coated with NiAl for the purpose of examining the effect of in-situ helium injection on microstructural development. In the fiber tubes, Tyranno™-SA3 and Hi-Nicalon™ Type-S bare fibers were included.

The CVD SiC joint samples with the NITE joining were provided by Kyoto University. Details of the NITE joint is provided elsewhere.[1] The GE Power Systems (currently GE Energy) isothermal CVI composite was provided by the Pacific Northwest National Laboratory (PNNL). The three isothermal CVI and CVI+polymer impregnation and pyrolysis (PIP) hybrid matrix composites were produced at the Japan Atomic Energy Research Institute (currently Japan Atomic Energy Agency) and provided through PNNL. [7] Limited information of these materials is found elsewhere. [6]

Properties Evaluation

Dynamic elastic modulus was determined at room temperature using the impulse excitation of vibration method per ASTM Standard C1259-01.

Tensile properties of the composite materials were evaluated using specimens machined from flat plates so that the longitudinal direction was parallel to one of the fiber directions. Miniature tensile geometry that had been developed for neutron irradiation studies on ceramic composites was employed.[4] The rectangular geometry with the gauge size (length × width × thickness) of 12 mm × 4 mm × 2 mm is within a range where a systematic gauge size effect is observed. Tensile tests were conducted in accordance with the general guidelines of ASTM C1275-00. The tensile test incorporated several unloading/reloading sequences in order to allow analysis on the hysteretic response. For the testing at room temperature, the specimens were clamped by wedge grips with aluminum end tabs on both faces of the grip sections. The strain was determined by averaging the readings of strain gauges adhered to both faces of the center gauge section. The crosshead displacement rate was 0.5 mm/min for all tests.

Interlaminar shear strength (ILSS) of the composite materials was determined by a double-notched shear (DNS) test per ASTM C1292-00. The specimen dimensions were 20 mm x 4 mm x 2 mm so that two DNS specimens could be accommodated in a space for one tensile bar of 40 mm x 4 mm x 2 mm in the irradiation vehicle. The notch separation was chosen to be 6 mm. Trans-thickness tensile strength (TTS) of the composite materials was determined by a diametral compression test at room temperature. In this test, diametral compressive load applied to a small diameter disc (or truncated disc) specimen is converted to tensile load in the perpendicular orientation leading to the failure in trans-thickness tension. Details of the test procedure are given. [2] Microstructures and tensile fracture surfaces were examined with an optical microscopy and a field emission scanning electron microscopy (FE-SEM).

Results

Microstructures of the composites prepared on the polished cross-sectional surfaces are shown in Figs. 1-7. The micrographs reveal that all the CVI composite materials achieved reasonable intra-fiber-bundle matrix infiltration. However, it is noticed that some of the Hi-Nicalon™ Type-S composites do have substantial interlaminar pores compared to others. In the Hybrid CVI composite, micro-cracking within the CVI SiC matrix perpendicular to the graphite fiber axis direction is extensively observed.

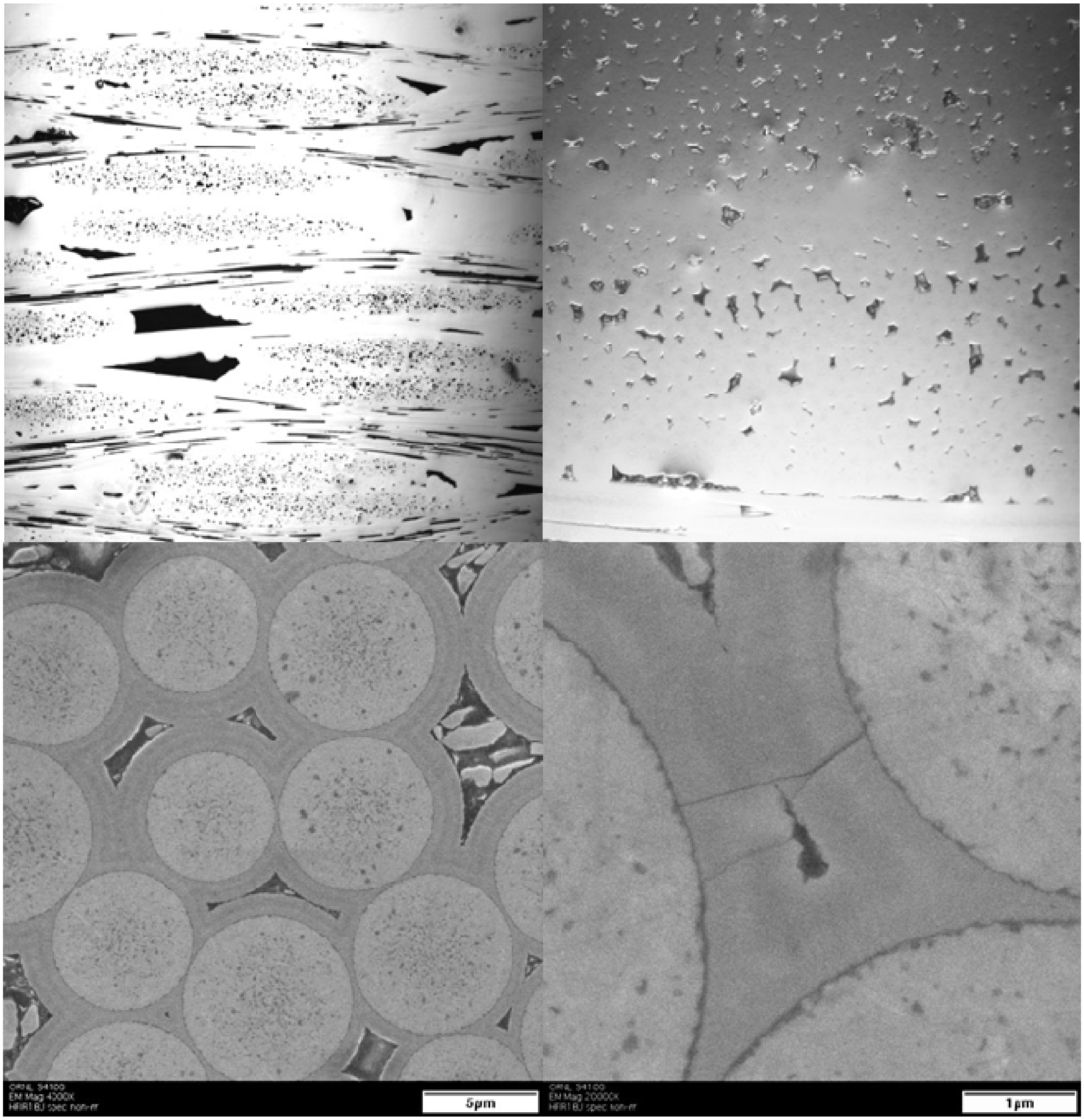

Figure 1. Cross sectional polished surface image of TySA-CVI-Ref composite.

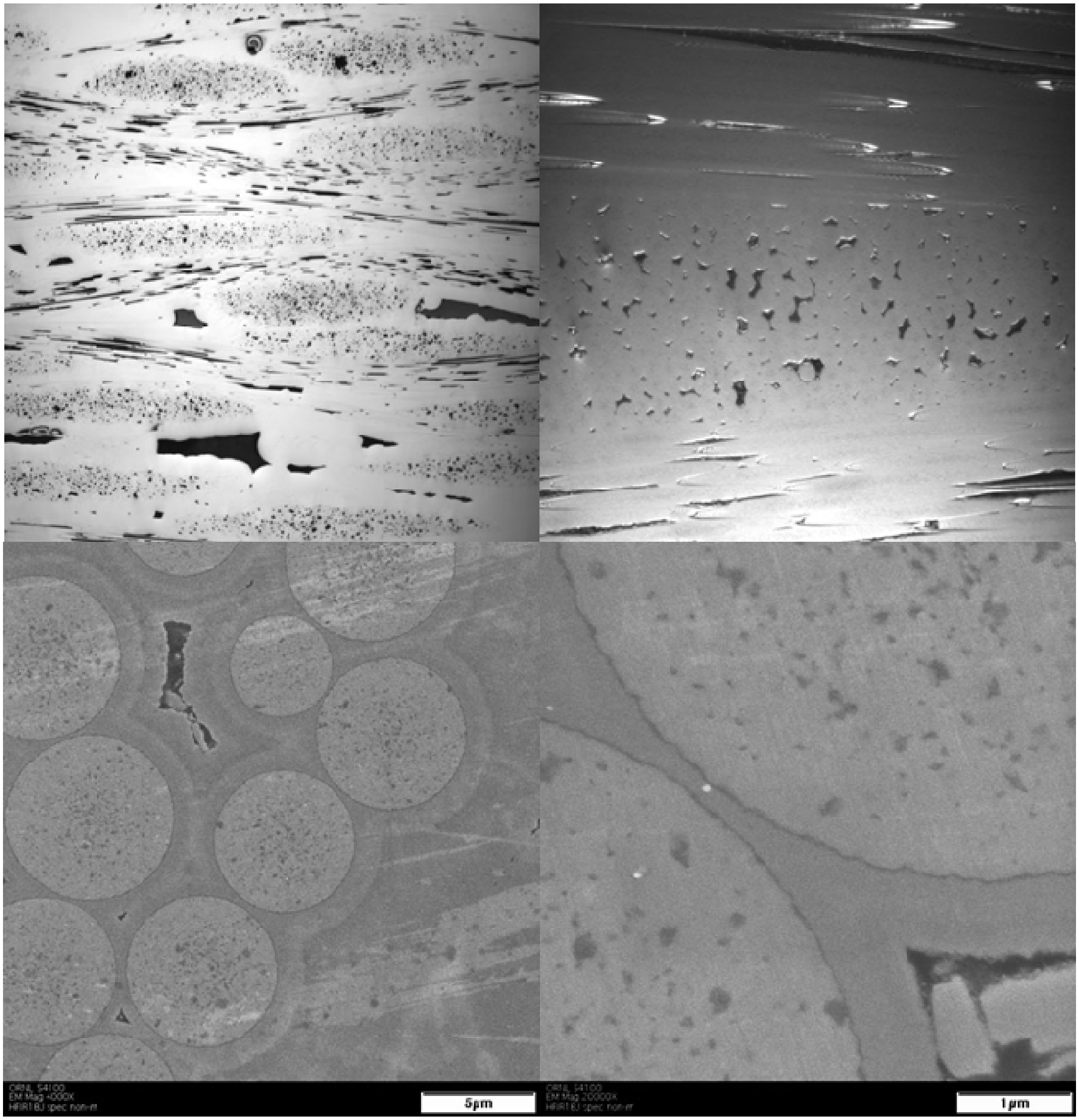

Figure 2. Cross sectional polished surface image of TySA-CVI-TI composite.

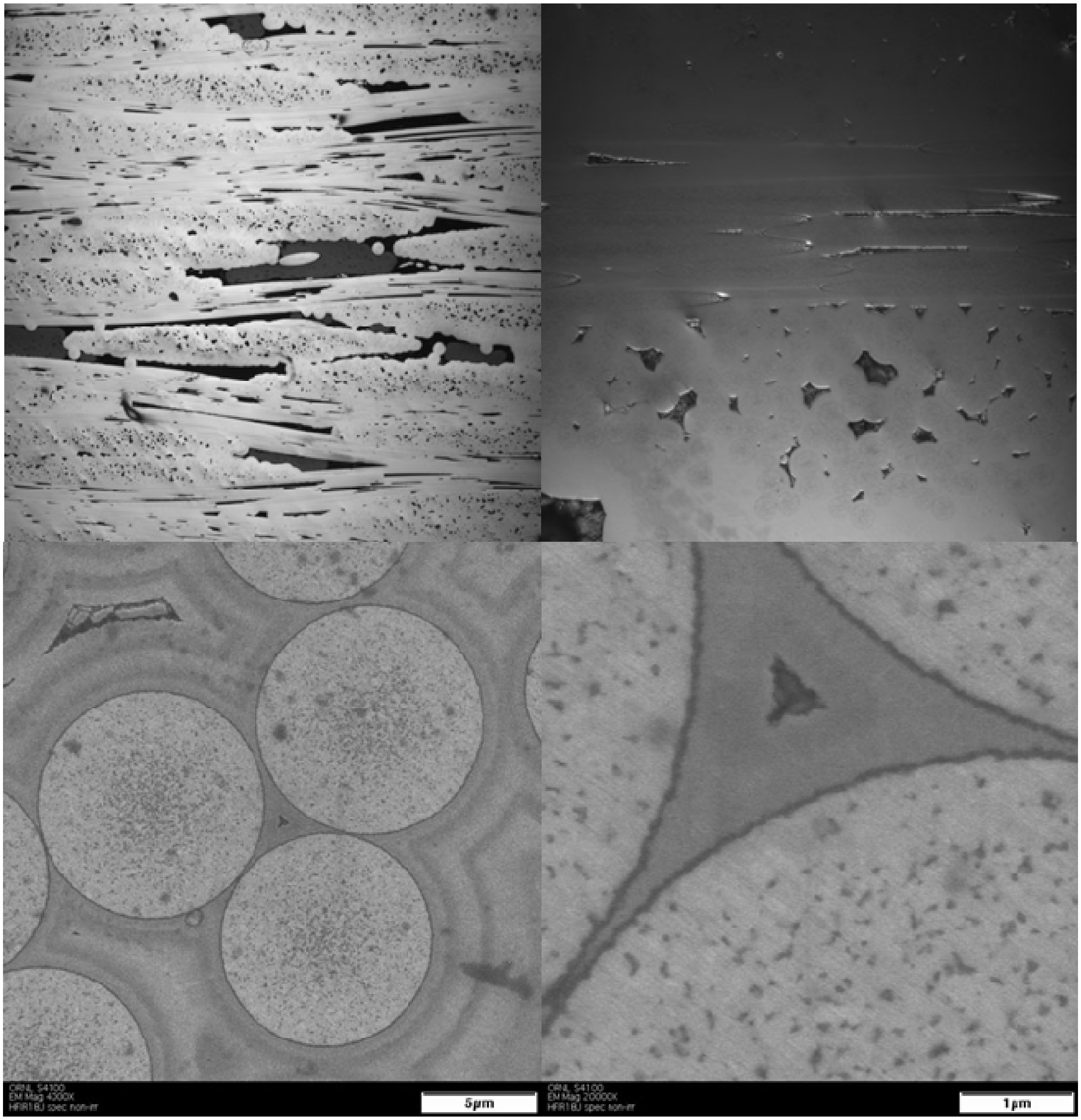

Figure 3. Cross sectional polished surface image of TySA-CVI-TF composite.

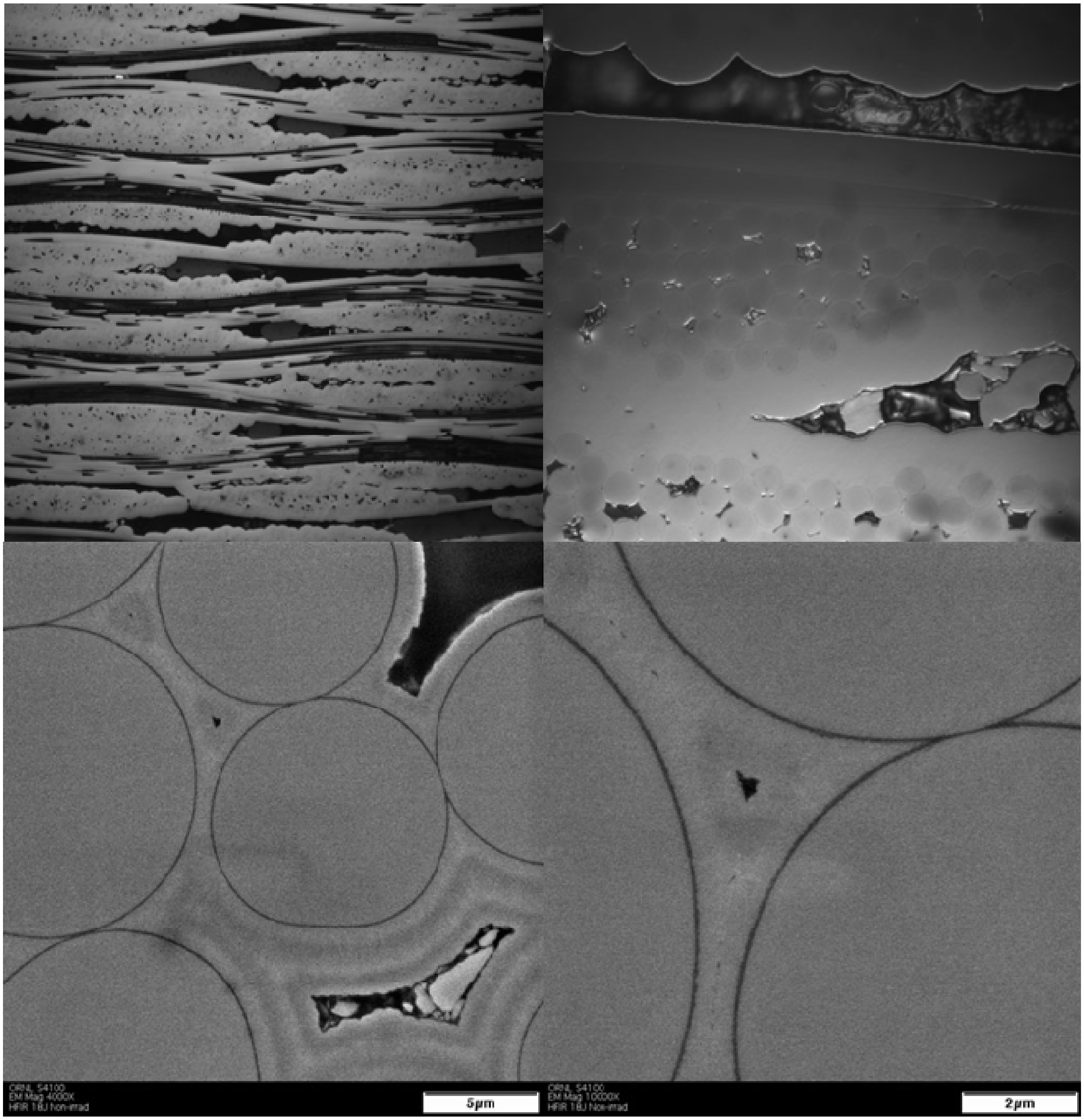

Figure 4. Cross sectional polished surface image of HNLS-CVI-Ref composite.

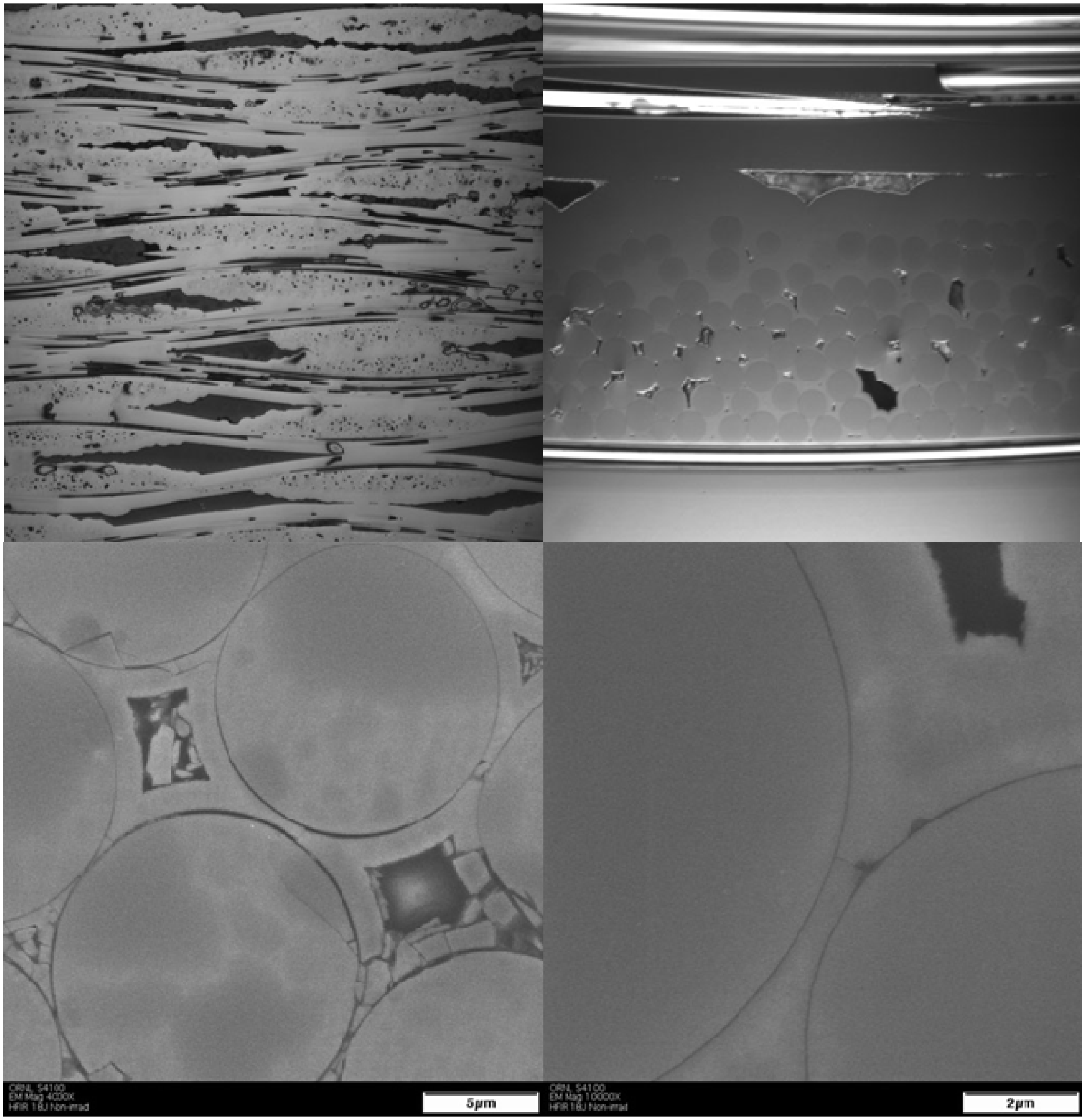

Figure 5. Cross sectional polished surface image of HNLS-CVI-TI composite.

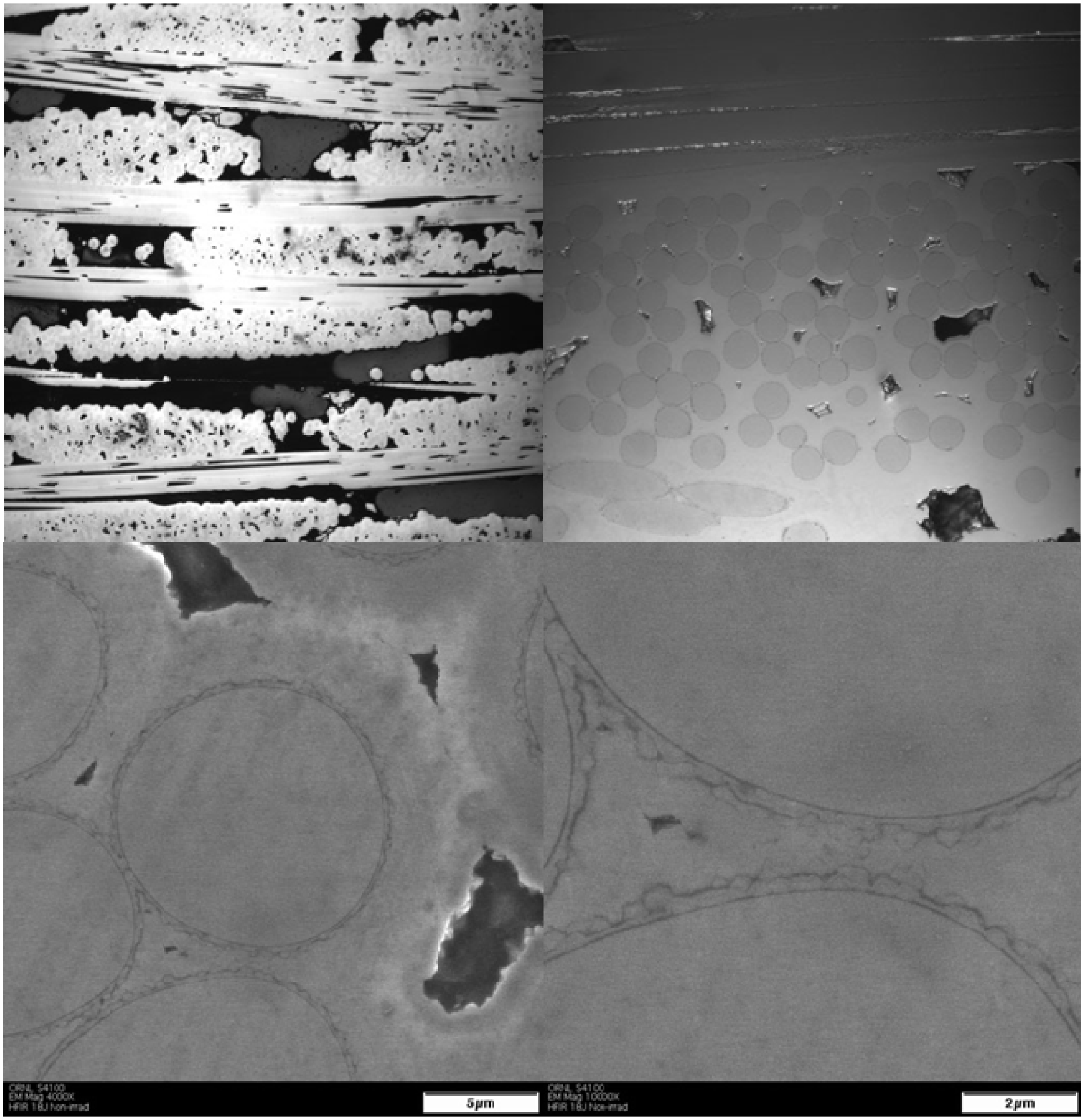

Figure 6. Cross sectional polished surface image of HNLS-CVI-ML composite.

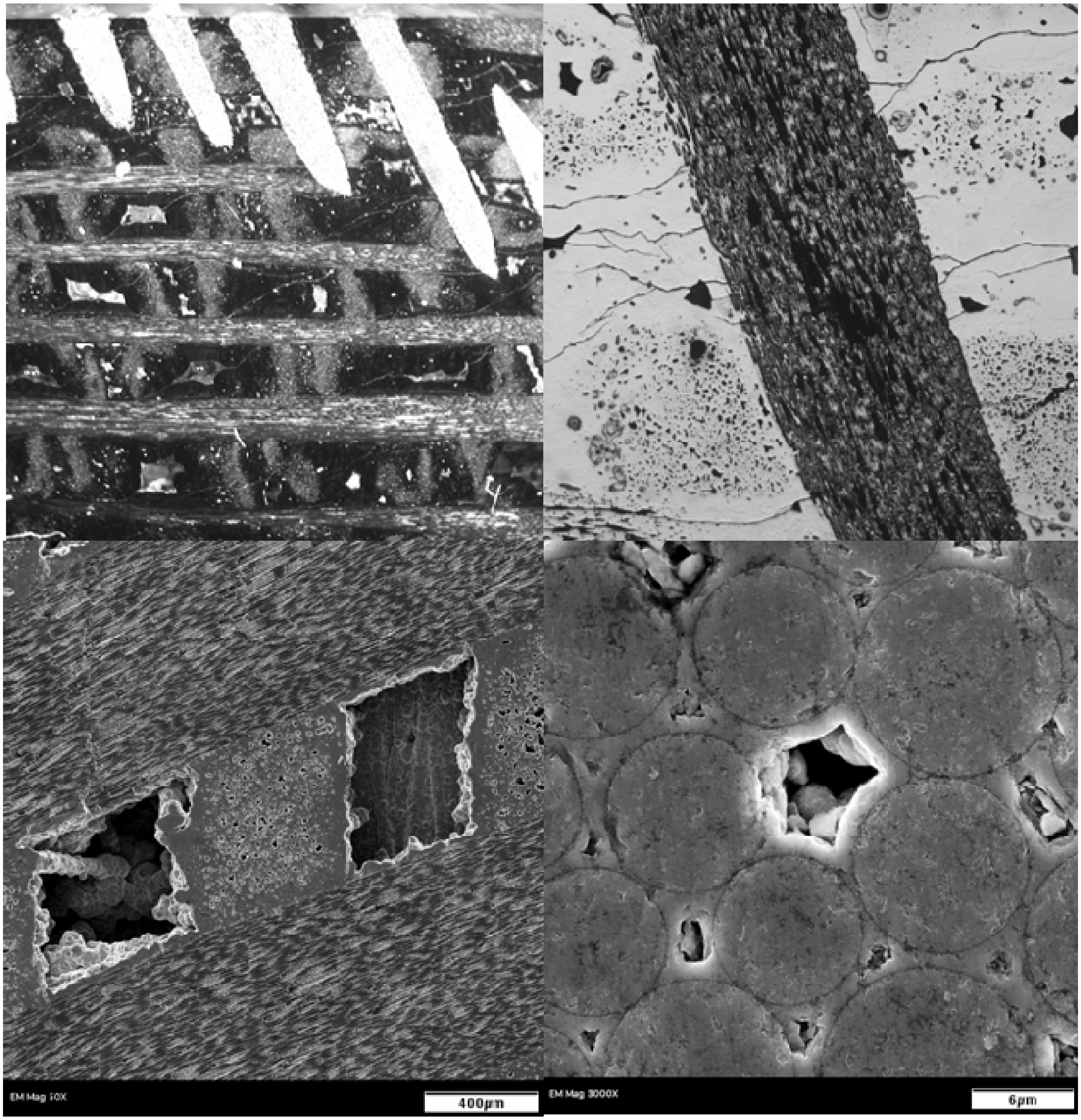

Figure 7. Cross sectional polished surface image of HNLS-CVI-ML composite.

Tensile stress-strain charts are presented in Fig. 8. The intermittent unloading-reloading sequences were incorporated for future evaluation of the interfacial sliding properties. The 2D CVI composites exhibited similar tensile behaviors regardless of fiber type or interphase. The initial tangent modulus, the proportional limit stress (PLS), and the ultimate tensile stress (UTS) for each 2D CVI composites appear to be typical for similar materials. The results from Hi-Nicalon™ Type-S reference and thin interphase 2D composites will be given in a future report. The Hybrid 3D composite exhibited low initial tangent modulus and poor tensile strength due likely to both the matrix pre-cracking and the small volume fraction of the SiC fibers in the loading direction. The NITE composite exhibited the significantly higher initial tangent modulus, PLS, and UTS compared to the CVI composites. The quantitative results are summarized in Table 2.

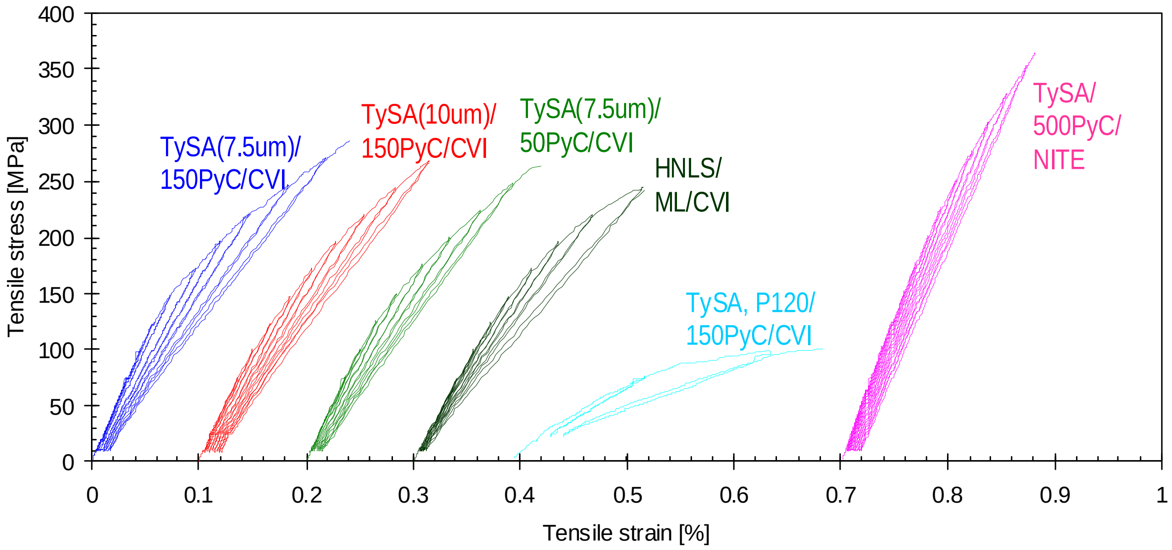

Figure 8. Tensile stress-strain behaviors of the composite materials at room temperature.

Table 2 – Summary of tensile properties of the composite materials. The numbers in parentheses represent one standard deviation.

Material	E [GPa]	PLS [MPa]	UTS [MPa]	Number of test
TySA-CVI-Ref	212 (12)	110 (24)	285 (26)	7
TySA-CVI-TF	201 (13)	104 (20)	304 (34)	3
TySA-CVI-TI	236 (49)	73 (25)	272 (10)	3
HNLS-CVI-TI	182 (8)	104 (16)	232 (27)	4
TySA-NITE	271 (9)	182 (55)	357 (8)	3
Hybrid-CVI	101 (38)	64 (41)	111 (71)	4
Hybrid-CVI tested with specimen dimensions 6 mm x 2.5 mm x 50 mm	95 (10)	82 (14)	98 (3)	n/a

Typical results of the interlaminar shear strength tests are given in Fig. 9. All the Tyranno™-SA3 2D composites exhibited similar values of shear strength at 30 to 35 MPa. The Hi-Nicalon™ Type-S multilayer composite showed slightly lower shear strength as anticipated from the slightly enhanced interlaminar porosity. The interlaminar shear strength of the PyC interphase Hi-Nicalon™ Type-S composites suffered very significantly from the apparently very poor interlaminar matrix densification. The Hybrid 3D composite exhibited the interlaminar shear strength of ~25 MPa, which is slightly lower than those for the Tyranno™-SA3 2D composites, in spite of the presence of the trans-thickness graphite fibers. The lower-than-anticipated shear strength of the Hybrid 3D composite may be attributed to the extensive matrix cracking introduced by the thermal expansion mismatch between the SiC matrix and the graphite fibers. The NITE composite exhibited the highest interlaminar shear strength owing to the dense SiC matrix.

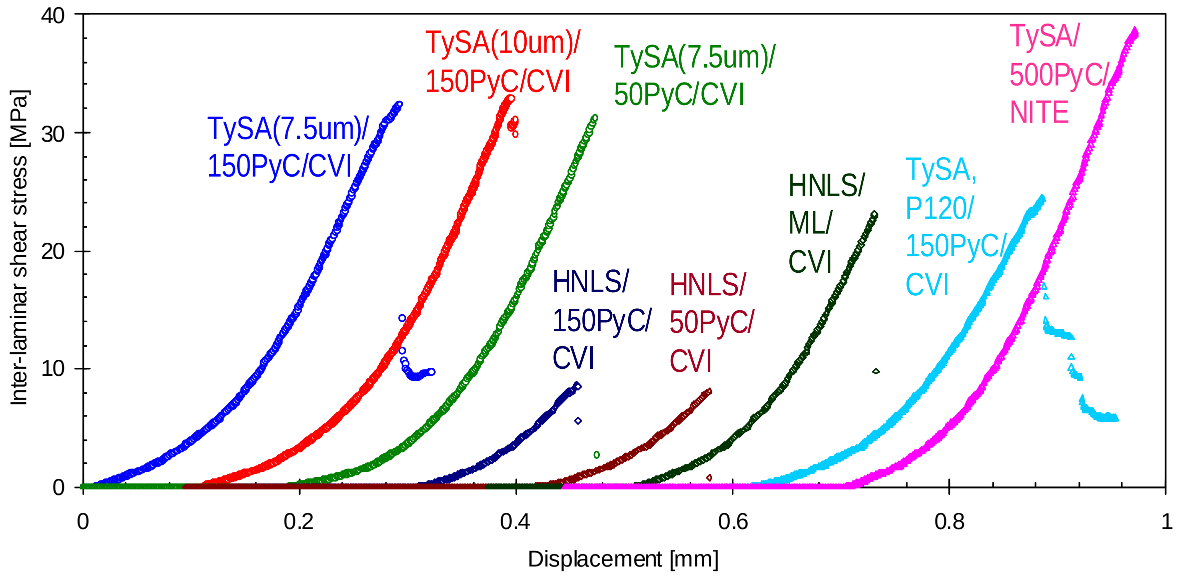

Fig. 9. Interlaminar shear stress vs. crosshead displacement in double notched shear testing of various SiC composites.

Table 3 – Summary of interlaminar shear strength of the composite materials. The numbers in parentheses represent one standard deviation.

Material	ILSS [MPa]	# of test
TySA-CVI-Ref	31.2 (3.7)	8
TySA-CVI-TF	31.9 (13.2)	8
TySA-CVI-TI	29.1 (5.8)	7
HNLS-CVI-Ref	10.8 (5.7)	8
HNLS-CVI-TI	9.6 (2.7)	4
HNLS-CVI-ML	23.3 (5.5)	8
Hybrid-CVI	24.8 (3.5)	6
TySA-NITE-LG	37.0 (3.7)	2

The trans-thickness tensile strength was evaluated for the Tyranno™-SA3 composites with CVI and NITE matrices. The result is given in Fig. 10 and Table 4. The tensile strength values appeared to be ~26 MPa for the CVI composite and ~32 MPa for the NITE composite. The result with CVI composite is consistent with the previous work, in which the trans-thickness tensile strength was measured to be 25 to 30 MPa for 7 different CVI composites with Tyranno™-SA3 or Hi-Nicalon™ Type-S reinforcements.[2] The higher strength for the NITE composite can be attributed to the higher density of the NITE matrix.

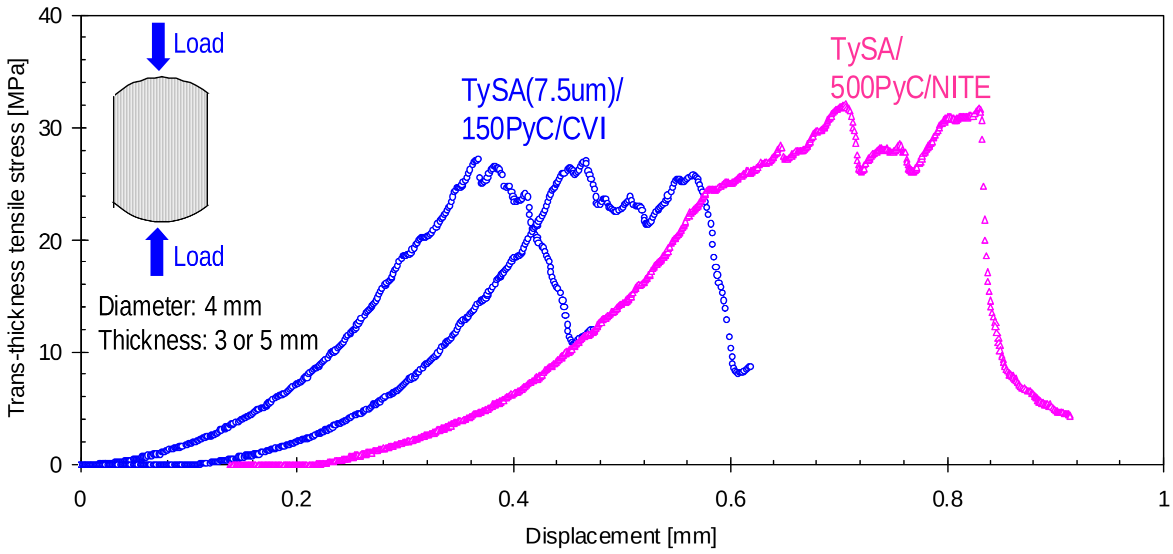

Fig. 9. Trans-thickness tensile stress vs. crosshead displacement in diametral compression testing of Tyranno™-SA3 CVI and NITE composites.

Table 4 – Summary of trans-thickness tensile strength of the composite materials. The numbers in parentheses represent one standard deviation.

Material	TTS [MPa]	Number of test
TySA-CVI-Ref	26.4 (1.4)	5
TySA-NITE-LG	32.0 (-)	1

The dynamic Young’s modulus had been measured before the irradiation capsule was constructed for all the samples which had been supposed to be irradiated and of straight rectangular geometries with reasonable length to thickness ratios. Table 5 summarizes the result of the modulus measurement. The irradiated dynamic modulus will be measured as a part of the post-irradiation examination campaign and will be directly compared with the pre-irradiation values for individual specimens.

Table 5 – Summary of the Young’s modulus of the SiC ceramics and composites. The numbers in parentheses represent one standard deviation.

Material	Dynamic Young’s modulus [GPa]	Number of test
R&H CVD SiC	449 (1.2)	8
NITE Matrix SiC	347 (9.5)	5
TySA-CVI-Ref	254 (11.5)	50
TySA-CVI-TI	273 (11.9)	24
TySA-CVI-TF	250 (16.1)	24
HNLS-CVI-ML	210 (18.3)	24
Hybrid-CVI	129 (21.3)	20
TySA-NITE	335 (10.8)	22
HNLS-CVI-Ref	224 (11.0)	24
HNLS-CVI-TI	211 (36.6)	24
TySA-NITE-LG	370 (28.8)	31

In summary, the SiC-based composite specimens prepared for the irradiation study in the HFIR-18 experiment performed as expected in terms of axial tensile, interlaminar shear, and trans-thickness tensile properties, with the exceptions of interlaminar properties of the PyC-interphase Hi-Nicalon™ Type-S, CVI composites which appeared to have achieved poor interlaminar matrix densification. More detailed evaluation of unirradiated materials including thermal conductivity and fracture resistance is planned.

References

[1] T. Hinoki, N. Eiza, S.J. Son, K. Shimoda, J.K. Lee, and A. Kohyama, Ceramic Engineering and Science Proceedings 26 (2005) 399-405.

[2] T. Hinoki, Y. Maki, A. Kohyama, E. Lara-Curzio, and L.L. Snead, Ceramic Engineering and Science Proceedings 25 (2004) 65-70.

[3] A. Kohyama, 31st International Conference on Advanced Ceramics and Composites, Daytona Beach, 2007.

[4] T. Nozawa, Y. Katoh, A. Kohyama, and E. Lara-Curzio, in: R.H. Jones, A. Kohyama, and B. Riccardi, (Eds.), Fifth International Energy Agency Workshop on SiC/SiC Ceramic Composites for Fusion Energy Application, PNNL-SA-37623, Pacific Northwest National Laboratory, 2002, pp. 74-86.

[5] T. Nozawa, Y. Katoh, L.L. Snead, T. Hinoki, and A. Kohyama, Ceramic Engineering and Science Proceedings 26 (2005) 311-318.

[6] T. Nozawa, K. Ozawa, Y. Katoh, and A. Kohyama, Materials Transactions 45 (2004) 307-310.

[7] R. Yamada, N. Igawa, and T. Taguchi, Journal of Nuclear Materials 329-333 (2004) 554-557.

MODELING THE ELECTRICAL CONDUCTIVITY OF SiC$_F$/SiC FOR FCI-APPLICATION –

G. E. Youngblood and E. Thomsen (Pacific Northwest National Laboratory)*

OBJECTIVE

The primary objectives of this task are: (1) to assess the properties and behavior of SiC$_f$/SiC composites made from SiC fibers (with various SiC-type matrices, fiber coatings and architectures) before and after irradiation, and (2) to develop analytic models that describe these properties as a function of temperature and dose as well as composite architecture. Recent efforts have focused on examining the electrical and thermal conductivity properties of SiC$_f$/SiC composites considered for application in FCI-structures in support of the U.S. dual-coolant, helium lead-lithium fusion reactor blanket concept.

SUMMARY

Using a combination 2/4-probe method to measure the electrical resistance across a disc-shaped CVD-SiC sample with evaporated gold electrodes, the average specific contact resistances at 200ºC and 500ºC were determined to be 12±2 and 7±1 Ωcm^2, respectively. The measured transverse electrical conductivity values for a high quality 2D-SiC/CVI-SiC composite made with Nicalon™ type S fabric were much lower than similar values measured for the same material with its SiC seal coat removed. This observation suggests that the pyrocarbon fiber coatings form an interconnected, highly conductive carbon network within the interior regions of the composite, and are largely responsible for the overall transverse electrical conductivity of the composite. At lower temperatures, the composite SiC seal coat should be an effective electrical insulator in the transverse direction across such 2D-SiC/SiC composites. However, the effectiveness becomes less as the temperature increases due to the rapidly increasing conductivity of SiC with increasing temperature. Nevertheless, the seal coat thickness (and type) can easily be adjusted during the composite fabrication to control the overall transverse electrical conductivity, an important parameter in the design of a FCI-structure. A simple three-layer series electrical conduction model fails to explain the unexpected low electrical conductivity values observed for the 2D-Nic S/CVI-SiC composite with a CVD-SiC seal coat. Importantly, up to 700ºC the transverse EC-values for a Nic S/CVI composite (with or without seal coat) appear to meet the desired criteria for FCI-application of < 20 S/m.

PROGRESS AND STATUS

Introduction

In the dual-coolant helium lead-lithium (DCLL) fusion reactor blanket concept considered for DEMO, an important component called a Flow Channel Insert (FCI) provides electrical and thermal decoupling of the hot (~700°C) lead-lithium from the load-bearing, structural steel channel walls of the blanket. For application as an FCI component, a silicon carbide, fiber-reinforced composite material made by chemical vapor infiltration (SiC/CVI-SiC) is being investigated [1-3]. The SiC/CVI-SiC for this application should have low transverse electrical and thermal conductivity to reduce MHD-induced pressure drop in the flowing lead-lithium and to protect the steel channel walls from excessive temperature, respectively.

For modeling the performance of various DCLL designs, among other things, the thermal and electrical conduction behavior of the materials used in the FCI-structure are important input parameters. This paper examines the electrical conduction (EC) behavior of high purity SiC made by the chemical vapor deposition process (CVD-SiC) and a high quality, two dimensional (2D)-SiC/CVI-SiC composite made with Nicalon™ type S fiber. Initial results on the effects of contact resistance between SiC and various metallic materials also are reported.

---

* Pacific Northwest National Laboratory (PNNL) is operated for the U.S. Department of Energy by Battelle Memorial Institute under contract DE-AC06-76RLO-1830.

A 2D-SiC/CVI-SiC composite is very inhomogeneous. Normally, the SiC fibers are coated with pyrocarbon to provide fiber protection during composite fabrication as well as composite mechanical toughness. Furthermore, a significant amount of porosity (~10-15%) exists within the composite. Small diameter, needle-shaped pores are aligned parallel to the woven fiber tows, which contain 500 individual filaments; and larger, roughly lamellar-shaped pores are aligned with their flat planes parallel and between the woven fabric layers. The geometry of this porosity is a result of the woven fabric stacking and the SiC-matrix fill-in process by vapor infiltration that requires interconnected porosity. Detailed effects of this 2D-SiC/CVI-SiC layered structure on the transverse thermal conductivity have been described in reference [4].

In 2D-composites, the directional anisotropy of the EC is even more dramatic than observed for thermal conduction. Typically, the ratio of the in-plane to the transverse EC in 2D-SiC/CVI-SiC is >1000 near room temperature. It steadily decreases for increasing temperatures, but still is >50 at 600ºC. This condition is primarily due to the preferred in-plane alignment of the continuous and highly electrically conductive pyrocarbon fiber coatings, even though the volume of the carbon phase normally is only 1-2%. Furthermore, the carbon fiber coatings form a conductive interconnected network within the close-packed fiber tows, and to some degree they also interconnect the fiber fabric layers. In fact, the degree of interconnectivity of the carbon network forms the dominant electrical conduction path in both the in-plane and the transverse directions in 2D-SiC composites. However, in the transverse direction, the somewhat continuous SiC fill-in matrix, as well as the large interlaminar-shaped pores, may interrupt the carbon network in many places. Normally, the composite outer surfaces are coated with a dense, relatively thin SiC seal coat applied by CVD during the CVI-fabrication process. The seal coat also shields the carbon-networked interior region of the composite.

Thus, a reasonable electrical conduction model across a 2D-SiC/CVI-SiC plate is an interior, carbon net-worked SiC fabric-layered region in series with two outer layers of the densely adherent, single phase CVD-SiC seal coat. The transverse EC(T) for such a three-layered composite can be expressed by:

$$EC(T) = EC_c[1 - f(1 - R)]^{-1} \qquad [1].$$

In Eq. [1], T is temperature, f is the seal coat fractional volume, and EC_c is the transverse EC across only the net-worked interior region of a 2D-SiC/CVI-SiC. Roughly f = t/L and is a small quantitiy, where t is the average total thickness of the seal coats and L is the overall thickness of the composite. Also, R is the ratio EC_c/EC_{CVD}, where EC_{CVD} is the electrical conductivity of the seal coat.

The EC of carbon (~10^4–10^6 S/m) is much higher than that of SiC, and exhibits only slightly increasing EC-values with increasing temperature. As a result, electrical conduction in the interior region of the composite is controlled by the amount of carbon, and especially the amount or lack of interconnectivity of the carbon network. The EC of SiC, a semi-conductor, increases rapidly with increasing temperature. Because the volume of the SiC matrix phase is much larger than that of the carbon interface material, at higher temperatures EC of SiC becomes increasingly important. At sufficiently high temperatures, $R \approx 1$, and $EC(T) \sim EC_c$ in Eq. [1]. Likewise, at lower temperatures, $R<1$, and $EC(T) < EC_c$, more so for larger values of f. Obviously, f, an easily controllable fabrication design parameter, is especially important at lower temperatures.

Experimental Procedure

Electrical conductivity measurements as a function temperature for monolithic SiC and various SiC/SiC composites have routinely been made in this laboratory over the last four years and have been described in previous reports [5-6]. Briefly, we make dc electrical resistance measurements (assuming ohmic conduction for a uniform, constant applied current) using a 4-probe method for slender bar samples (~15 x 6 x 2 mm^3) and a 2-probe method for relatively thin, disc-shaped samples (~10 mm dia x 2 mm tk). The EC is calculated from the measured potential drop and the appropriate sample geometry factor. The samples are heated in a tube furnace under various flowing inert or reducing gas atmospheres. The temperature control and measurement system is totally automated. In a typical EC-run, the system is programmed to increase or decrease the sample temperature in steps between room temperature and ~800°C at a rate of ±1ºC/min, with a 15 min hold time at every 40°C step. For such a run, the complete 800ºC temperature cycle requires about 12 hours and conveniently can be carried out overnight with little attention.

A combination 2/4-probe method was developed whereby the electrical contact resistance at the interface between an applied metal electrode and a sample surface (a single phase material, usually CVD-SiC) can be estimated [5]. The contact resistance is simply the difference between the simultaneous 2- and 4-probe resistance measurements with a slight correction due to differences in the voltage probe separations for the two types of probe connections. However, only the 2-probe method has been used so far for our composite disc samples, although future measurements will examine various SiC/SiC composite/electrode combinations using the 2/4-probe method.

The EC of a high quality, 8-ply 2D-Nic S/CVI-SiC (made by GE Power Systems Composites using Hi-Nicalon™ type S fabric) was examined. Hereafter, this material will be referred to as simply "Nic S/CVI." Full characterization of this material was reported previously [7]. For this Nic S/CVI material, the thickness of each SiC seal coat surface layer was ~0.05 mm, as estimated from numerous SEM views of sample cross-sections. The electrical resistance was measured on disc samples of this material after the seal coat had been ground off to expose numerous underlying carbon coated fibers now intersecting the sample surface. Three different types of electrodes were applied to samples after removing the seal coat: (1) evaporated gold (our normally used electrode), (2) evaporated carbon and (3) porous nickel. The gold and carbon electrodes were applied in a similar manner using a SEM coater and were expected to make excellent electrical contact with the exposed carbon network at the sample surfaces. The porous nickel electrodes were formed by first applying a NiO paste to the disc surfaces, and then reducing the NiO in an argon + 3% H_2 atmosphere at 800°C (a method developed in our solid oxide fuel cell program). Measurements were made in a dry, hi-purity argon atmosphere on samples with gold or carbon electrodes. Measurements for samples with the Ni electrodes were made in the argon + 3% H_2 atmosphere after the NiO had been reduced in place at 800ºC. The preferred electrode-SiC connection used in the semi-conductor industry is nickel [8].

Results and Discussion

When combination 2/4-probe EC-measurements were made on two different CVD-SiC disc samples with evaporated gold electrodes, average specific contact resistances at 200ºC and 500ºC were estimated to be 12±2 and 7±1 Ωcm^2, respectively. The uncertainties represent just the differences in measurements between the two samples. A value of ~10 Ωcm^2 is in line with values obtained by Morley for CVD-SiC in contact with liquid Pb-Li at T < 400ºC or so, although Morley observed considerable variation between setups [9]. Morley also observed a rapidly continuous decrease in the specific contact resistance as temperatures increased for T > 400ºC, which agrees with the trend that we observed. For our case, the contact resistance at the interface between CVD-SiC and evaporated gold electrodes was a significant portion of the overall CVD-SiC sample resistance, and led to considerable uncertainty in the calculated EC for CVD-SiC disc samples when using a 2-probe method.

The 2/4 probe method of estimating the specific contact resistance has not been carried out on SiC/SiC composites because the two small diameter holes required to seat the potential probes for the 4-probe measurement would penetrate through the single phase SiC seal coat and into the carbon networked interior region. Therefore, the observed difference in resistance values for the two 2/4-probe connection cases would not represent the true contact resistance at the metal electrode-SiC interface. For this reason, only 2-probe measurements were made for the following composite disc sample cases.

In Figure 1, the calculated specific resistance (= resistance x surface area) as a function of temperature for two different disc samples, GE3 and GE4, are compared. Both samples were cut from the same plate of Nic S/CVI material after grinding off the SiC seal coat. Initially, measurements were made on GE3 with gold electrodes, then, after grinding the gold off and applying Ni electrodes, a second set of measurements was made on the same sample. At this time, only measurements with carbon electrodes on the GE4 sample have been made.

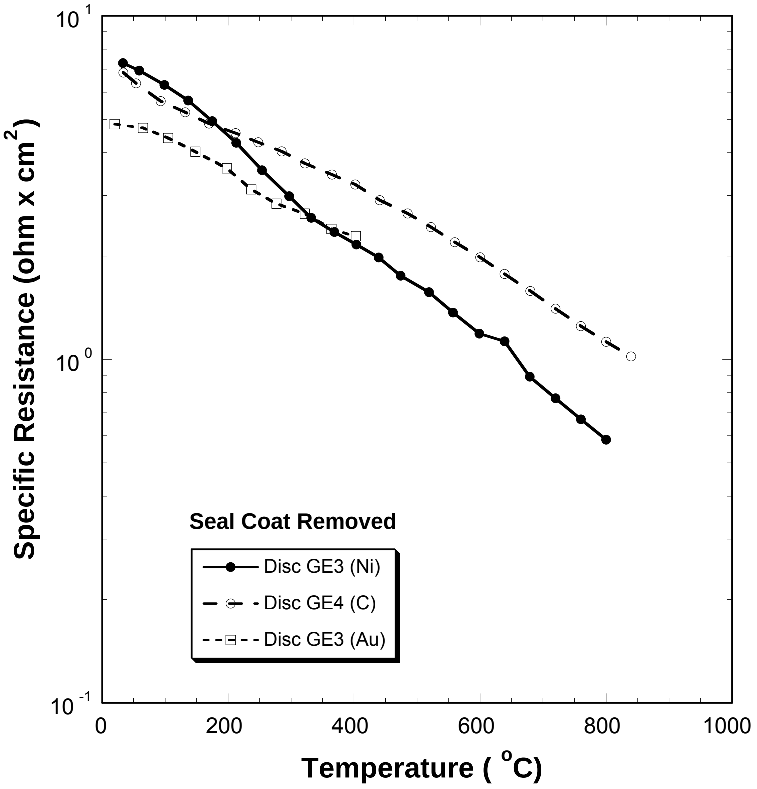

Figure 1. The specific resistance as a function of temperature for disc samples of GE "Nic S/CVI" composite after removing the SiC seal coat. The electrical resistance measurements were made using the 2-probe method on samples with three different electrodes (porous Ni, evaporated C and Au). For clarity, only the data obtained for decreasing temperatures are shown.

The specific resistance of these ~1-cm. diameter disc samples continuously decreased from ~6 to 0.8 Ωcm^2 as the temperature increased from RT to ~800ºC, respectively. As discussed, the contact resistance for these cases is expected to be minimal. Katoh [10] estimated the specific contact resistance for a similar setup to be <0.01 Ωcm^2. The ±10% variation between EC-values for different samples of the same material, and even between different runs on the same sample, appears to reflect the inhomogeneous nature of these composites or perhaps even small differences in sample surface preparation.

In Figure 2, the EC-values as a function of reciprocal temperature for various SiC-based materials are compared. In this figure, new data obtained for disc samples of "Nic S/CVI" (with and without SiC seal coat) and of R&H CVD-SiC are indicated with symbols. Previously reported EC-data for bar samples of CVD-SiC (Weber, Morton, and Hi-Purity) are indicated with bold solid lines. The literature EC-values for very high purity CVD-SiC (R&H Hi-Resistance CVD-SiC) also are indicated with bold solid lines [11]. Previously reported data for a Nicalon™ type S fiber bundle also are shown [5].

As discussed previously [5], the wide variation of EC-values for monolithic CVD-SiC reflects the influence of type and even small differences in the amounts of impurity between nominally the same materials. The negative slopes of the 1000/T dependence increase going from the upper to the lower set of bold-faced curves. The 1000/T slopes generally increase as the expected level of impurity in the tested CVD-SiC materials decreases. The activation energies (Eact), estimated from an Arrhenius best-fit straight line to the higher temperature data for these CVD-SiC materials, decrease from ~0.12 eV to ~0.28 eV from top to bottom, in line with the decrease in the impurity levels, also top to bottom.

The EC(T)-values of our Nic S/CVI composite (no S.C.) very closely match similar values reported by Katoh for a similar composite made with Nicalon™ type S or with Tyranno™ SA fabric, except for Katoh's cases the carbon existed as multilayer coatings [10]. From the relatively high values of EC(T) for T<400ºC, Katoh, et al., concluded that transverse conduction was primarily through the carbon interphase network in the low temperature regime. In the high temperature regime, the steeper 1000/T temperature dependence suggested ever-increasing contributions from the SiC fibers and matrix. In fact, in this temperature regime, the 1000/T slopes for the composite SiC/SiC materials without seal coats approach that of the R&H and "Hi-Purity" CVD-SiC materials.

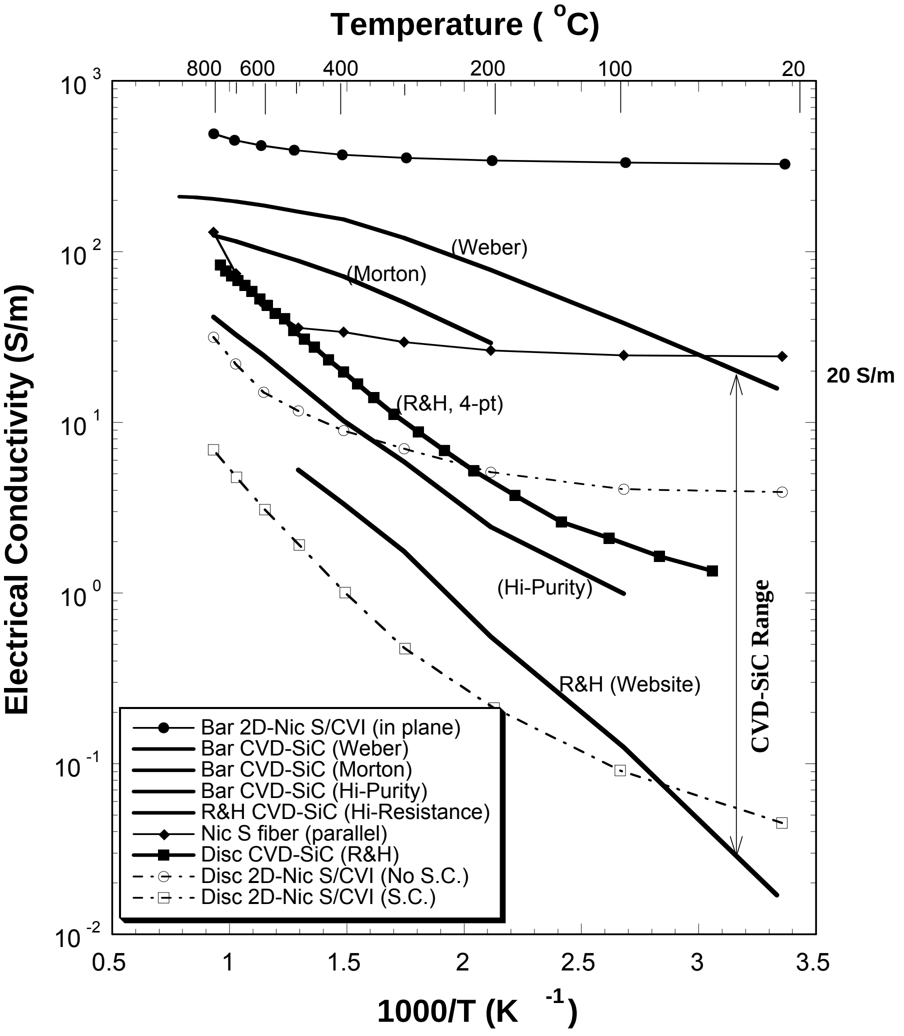

Figure 2. Electrical Conductivity as a function of reciprocal temperature for SiC-based materials. The EC measurements were performed using a 4-probe method for the bar samples and the Nic S fiber bundle, and a 2-probe method for the disc samples. The conduction was normal to the plane for the 2D-Nic S/CVI disc samples, where the SiC seal coat was either removed (no S.C.) or left intact (S.C.).

Interestingly, in Fig. 2 the shape of the curve representing the EC-values measured along the length of a bare Nicalon™ type S tow segment is very similar to the curve shape for Nic S/CVI (no S.C.), except that the Nic S EC-values are about x10 higher. Tanaka, et al. [12], reported a room temperature EC-value of 34 S/m for an early version of Hi-Nicalon™ type S fiber, which is in approximate agreement with our measurement at room temperature. However, Tanaka observed that when a thin (~56 nm), carbon rich surface layer (the carbon-rich layer naturally occurs during type S fiber fabrication) was removed by oxidation, the EC-value decreased to 0.5 S/m, which is in line with the room temperature EC-value of "Hi-Purity" CVD-SiC shown in Fig. 2. Here again the dominant influence of electrical conduction through very thin, carbon-rich layers in the type S fibers or through thin, fiber-coating carbon networks in SiC/CVI-SiC composites, especially in the lower temperature regime, is evident.

Somewhat surprisingly, the observed magnitudes of the transverse EC-values for the Nic S/CVI composite were even lower than the EC-values for the extremely high resistance CVD-SiC material fabricated by Rohm and Haas. Furthermore, the EC temperature dependence of this CVI-SiC composite with its seal coat intact more closely matches that of the high purity CVD-SiC than of Nic S/CVI (no S.C.).

Importantly, up to 700ºC the transverse EC-values for Nic S/CVI composite (with or without seal coat) appear to meet the desired criteria for FCI-application of < 20 S/m.

To examine these unexpected results further, it is instructive to use our series model (Eq. [1]) to predict the overall EC-values for transverse conduction to see if different thicknesses of SiC seal coat play a role. The seal coat thickness (or even type of material) is easily controlled during fabrication, so such a model would be a valuable tool for FCI-structural design. For instance, Henager, et al., have described different types of thermal barrier coatings potentially attractive for use in a nuclear environment, and which potentially could have application in forming FCI-structures [13].

Predictions of the EC-values for two cases were modeled, each for a seal coat of total thickness 0.001, 0.005 and 0.01 mm (f = 0.005, 0.025 and 0.05, respectively). The 0.01-mm thickness conforms to the actual seal coat thickness measured for our Nic S/CVI material. For the two cases, to calculate the input R-value we used the measured EC(T)-values for the Nic S/CVI material together with either the measured values of EC(T) for Hi-Purity CVD-SiC or a set of EC(T)-values derived for a hypothetical CVD-SiC with extremely low EC-values (i.e., a highly insulating seal coat case). To generate the EC(Hypo) values, the formula:

$$EC(Hypo) = (1.80 \times 10^6/K)\exp(-4094/K) \qquad [2]$$

was used. In Eq. [2], K is the temperature in Kelvin and the exponential numerical term is equivalent to a thermal activation energy Eact = 0.35 eV. Some representative predictions are shown in Fig. 3.

In Figure 3, only the predicted EC(T)-values for a single f-value of 0.05 are shown. The predicted curve barely deviates from the ECc curve, and then only for T<100ºC. Obviously, according to our simple series model, a seal coat of nominal high purity SiC and of a typical 0.05-mm thickness makes little difference in the overall EC compared to that of the interior region.

The lower set of dashed lines shown in Fig. 3 was calculated for a range of f-values (0.05, 0.025 and 0.005) to emphasize the relative effects of a thinner and thinner seal coat. As expected, for all f-values, the predicted EC(T) values approximate the ECc-values for T > 400ºC, and start to dramatically deviate below ECc-values for T < 400ºC or so, with the thickest seal coat deviating the most. Again, the model predicted EC-values are much greater than the measured values. Furthermore, the 1000/T temperature dependence of the model predictions is entirely different than observed, especially at lower temperatures where the contributions of the ever-decreasing EC-values of the seal coat SiC should become more important.

At this time a logical explanation for the discrepancy of the measured from the modeling results is not apparent. Perhaps the lack of continuous interconnectivity through the carbon network becomes more important, or is more complex at lower temperatures. Or perhaps the contact resistance between composite surfaces and applied electrodes plays a more important role than considered. Further work must be done before deciding on a preferred electrode material for different experimental setups.

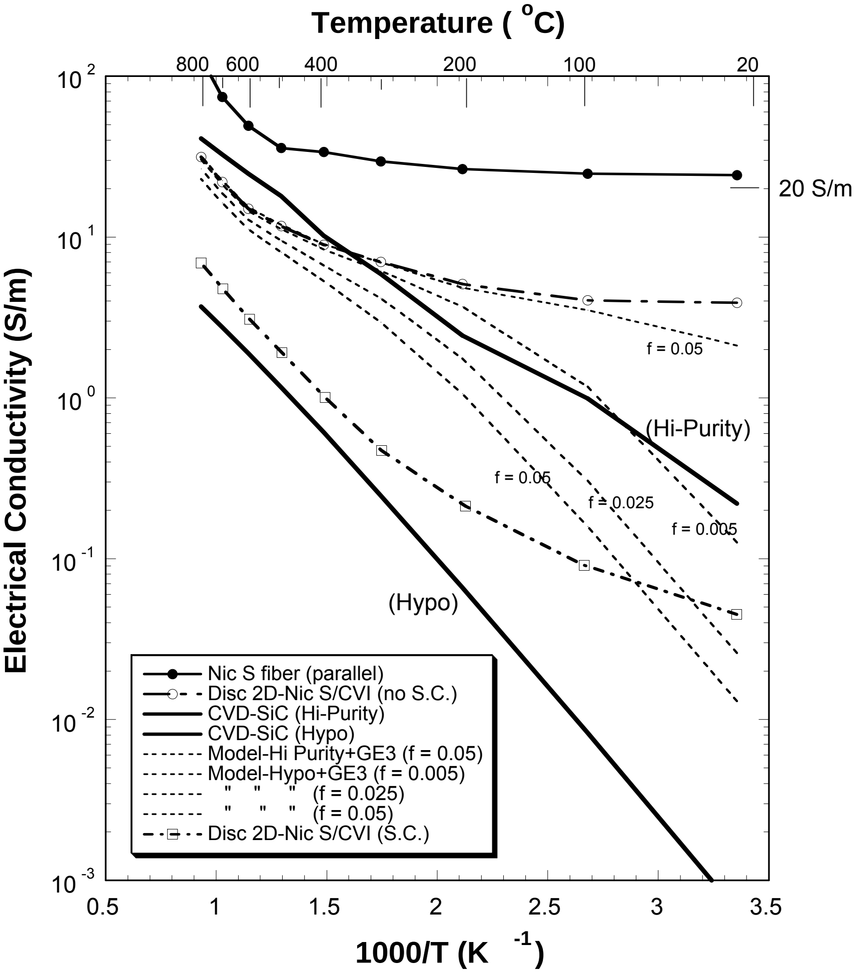

Figure 3. Model predictions of EC(T) for a Nic S/CVI composite with different thicknesses (or f-values) of SiC seal coat. The various EC prediction curves (shown as short dashed lines) are compared to measured EC-values for this Nic S/CVI material and the input EC-values for the interior Nic S/CVI (no S.C.) and either Hi-Purity or the hypothetical CVD-SiC.

CONCLUSIONS

1. Using a combination 2/4-probe method to measure the electrical resistance across a disc-shaped CVD-SiC sample with evaporated gold electrodes, the average specific contact resistances at 200ºC and 500ºC were determined to be 12±2 and 7±1 Ωcm^2, respectively.
2. The measured transverse electrical conductivity values for a high quality 2D-SiC/CVI-SiC composite made with Nicalon™ type S fabric were much lower than similar values measured for the same material with its SiC seal coat removed. This observation suggests that the pyrocarbon fiber coatings form an interconnected, highly conductive carbon network within the interior regions of the composite, and are largely responsible for the overall transverse as well as the in-plane electrical conductivity.

3. At lower temperatures, the SiC seal coat should be an effective electrical insulator in the transverse direction across such 2D-SiC/SiC composites. However, the effectiveness becomes less as the temperature increases due to the rapidly increasing conductivity of SiC with increasing temperature. Nevertheless, the seal coat thickness (and type) can easily be adjusted during the composite fabrication to control the overall transverse electrical conductivity, an important parameter in the design of a FCI-structure.
4. A simple three-layer, series electrical conduction model fails to explain the unexpected low electrical conductivity values observed for the 2D-Nic S/CVI-SiC composite with a CVD-SiC seal coat.
5. Importantly, up to 700ºC the transverse EC-values for a Nic S/CVI composite (with or without seal coat) appear to meet the desired criteria for FCI-application of < 20 S/m.

REFERENCES

[1] N.B. Morley, et al., “Current understanding of feasibility of SiC/SiC composites for flow channel inserts in Dual Coolant Pb-17Li blankets,” presented at TBM meeting, June 4, 2004, UCLA.

[2] G.E. Youngblood, R.J. Kurtz and R.H. Jones, “Development of SiC/SiC for application as a flow channel insert,” pp 3-8 in Fusion Materials Semiannual Progress Report (FMSPR) for period ending Dec. 31, 2004 (DOE/ER-0313/37).

[3] N.B. Morley, et al., “Recent research and development for the dual-coolant blanket concept in the US,” Fus. Eng. And Design, 83(7-9), (2008) 920-927.

[4] Gerald E. Youngblood, David J. Senor and Russell H. Jones, “Modeling the transverse thermal conductivity of 2D-SiC/SiC composites made with woven fabric,” Fusion Sci. and Tech 45(4), (2004) 583-591.

[5] G.E. Youngblood, E. Thomsen and G. Coffey, “Electrical conductivity of SiC/SiC,” pp 46-51 in FMSPR for period ending Dec. 31, 2005 (DOE/ER-0313/39).

[6] G.E. Youngblood, , E. Thomsen and G. Coffey, “Electrical conductivity measurements of SiC-based materials,” pp. 17-23 in FMSPR for period ending December 31, 2006 (DOE/ER-0313/41).

[7] G.E. Youngblood and R.H. Jones, “Characterization of a 2D-SiC/SiC composite made by ICVI with Hi-Nicalon type S fabric, ” pp 34-40 in FMSPR for period ending June 30, 2003 (DOE/ER-0313/34).

[8] J. Crofton, L.M. Porter and J.R. Williams, « The physics of ohmic contacts to SiC, » Physica Status Solidi (B), Applied Research 202 (1997) 581.

[9] N.B. Morley, private communication.

[10] Y. Katoh, S. Kondo, L.L. Snead, Effect of neutron irradiation on dc electrical conductivity of SiC ceramics and composites for fusion FCI-applications,” pp. 18-25 in FMSPR for period ending December 31, 2007 (DOE/ER-0313/43).

[11] CVD Silicon Carbide™ technical data sheet, 2008, Rohm and Haas website.

[12] Tanaka, et al., “Recent progress of Hi-Nicalon type S development,” presentation at Cocoa Beach, FL Jan. 30, 2003 and published later in Ceram. Eng. And Sci. Proc.

[13] C.H. Henager, Jr, et al., “Coatings and joining for SiC and SiC-composites for nuclear energy systems,” J. Nucl. Mater. 367-370 (2007) 1139-1143.

MECHANICAL PROPERTIES OF TRI-AXIALLY BRAIDED CARBON FIBER COMPOSITE

—K. Ozawa, Y. Katoh, L.L. Snead, J.W. Klett (Oak Ridge National Laboratory), and W.E. Windes (Idaho National Laboratory)

OBJECTIVE

The main objective of this study is to investigate the axial and inter-laminar mechanical properties of the tri-axially braided carbon fiber composite.

SUMMARY

Tensile, inter-laminar shear and trans-thickness tensile properties of tri-axially braided carbon fiber-reinforced carbon matrix (C/C) composites were evaluated. The C/C composites exhibited the quasi-ductile behaviors with initial elastic behavior, second linear portion and non-linear region. Tensile properties of the C/C composites such as ultimate tensile strength, elastic tensile modulus, and proportional limit stress depended on the axial fiber volume fraction. Relatively low inter-laminar shear (2.2 MPa) and quite low trans-thickness tensile (0.7 MPa) strength obtained, which indicates the very weak strength of carbon matrix itself.

PROGRESS AND STATUS

Introduction

Carbon-based composites are promising materials for high heat flux applications in fusion plasma devices because of their high temperature mechanical properties, high thermal conductivity, superior thermal shock resistance, low activation properties, and maturity as industrial materials [1, 2]. Particularly, pitch-based continuous carbon fiber reinforced carbon matrix (C/C) composites are considered suitable for fusion applications due to their superior thermal conductivity and irradiation resistance compared with C/C composites using carbon fibers from other production routes [3]. Although properties of C/C composites have been most extensively studied among various ceramic matrix composites, they are in fact highly dependent on the fiber type, reinforcement architecture, and the matrix forming process. The primary purpose of this study is to investigate the axial and inter-laminar mechanical properties of pitch fiber, pitch matrix C/C composite in a tri-axially braided architecture.

Experimental Procedure

The C/C composite samples were fabricated in Oak Ridge National Laboratory. The reinforcement fiber was P-25 mesophase pitch carbon fiber manufactured by Amoco BP Chemical Co. Ltd. The fiber bundles were tri-axially braided with 0^o and $\pm 55^o$ braiding angles. These fiber bundles were impregnated with A-240 petroleum pitch (Ashland Petroleum Company). The densification cycles of impregnation, carbonization, and graphitization were conducted four or five times. The density of the composites was 1.3-1.5 g/cm^3, and the longitudinal fiber volume fraction was ~30%.

Tensile specimens were machined from the composite plates so that the longitudinal direction was parallel to 0^o direction. Edge-loaded contoured specimens were used (Fig. 1 (b)). Tensile tests were conducted following the general guidelines of ASTM standard C1275-00. For the testing at ambient temperature, specimens were clamped by wedge grips with aluminum end tabs on both faces of the gripping sections in order to prevent compression buckling at the edges of the specimens. The strain was determined by averaging the readings of strain gauges bonded to both faces of the center gauge section. The crosshead displacement rate was 0.5 mm/min for all tests. The tensile Young's modulus of the composites, E, was defined as a tangential modulus of the initial linear segment at 5-25 MPa. The proportional limit tensile stress (PLS) was defined as the maximum stress to satisfy $(E\varepsilon_{meas.}-\sigma_{meas.}) / \sigma_{meas.} \leq 0.05$, where $\sigma_{meas.}$ is the applied stress at strain $\varepsilon_{meas.}$ [4]. The ultimate tensile strength (UTS) was defined as failure load divided by the original gauge cross-section.

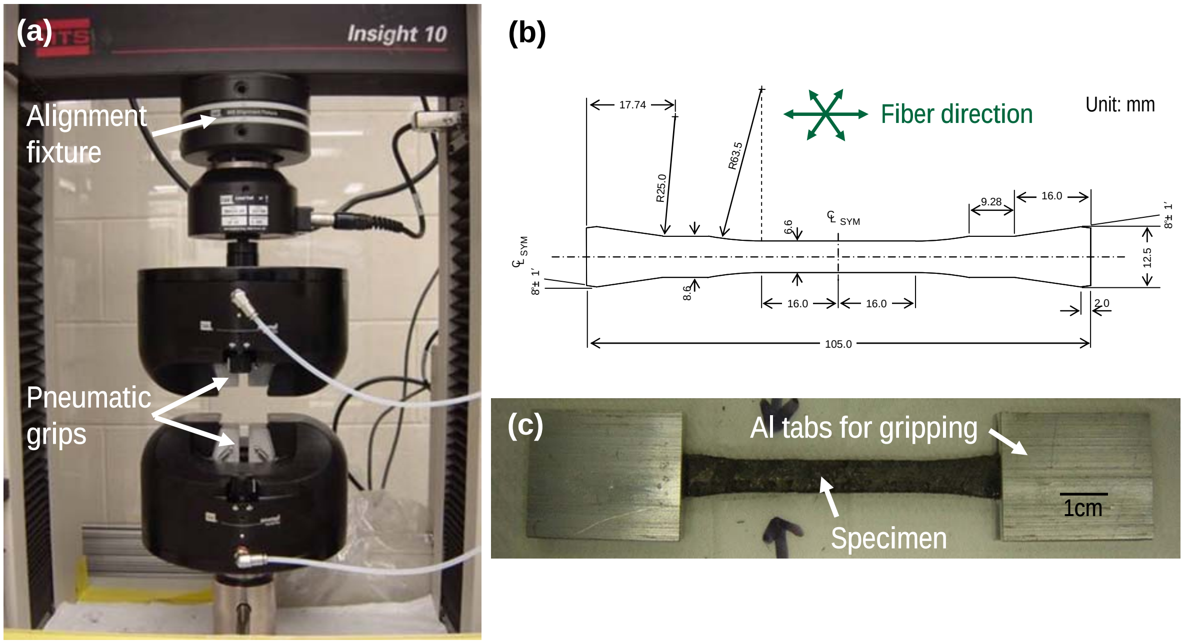

Fig. 1: (a) Tensile test apparatus with the alignment fixture, (b) schematic design of tensile test specimen used in this study, and (c) tensile test specimen with aluminum tabs.

Double notched shear test method was selected to evaluate inter-laminar shear strength, in accordance with ASTM standard C1292-00. Notched specimens (20.0^L x 4.0^W x 3.0^T mm with 6.5 mm notch separation) were loaded in compression parallel to the fiber longitudinal direction at a constant crosshead rate of 0.5 mm/min (Fig. 2). All tests were conducted at room temperature in air. Teflon sheets were used for providing lateral support to prevent the specimen buckling. Inter-laminar shear strength was defined as the maximum load divided by the fracture surface area. In this study, the fracture surface area was estimated by the notch separation multiplied specimen width because of the difficulty to measure the original fracture surface area after each test. Details on the test procedure and other related issues (such as notch effect and size effect) are described elsewhere [5, 6].

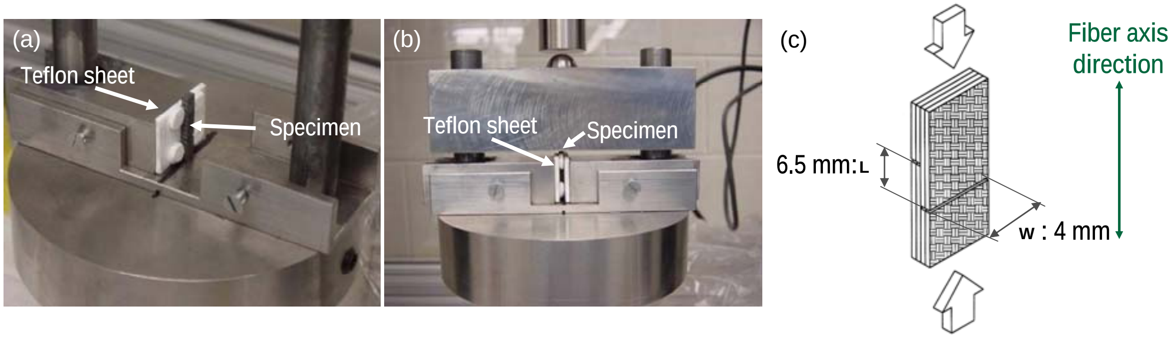

Fig. 2: (a), (b) Apparatus for the double notched shear test, and (c) schematic image of double notched shear test specimen.

Trans-thickness tensile test was conducted following the guidelines of ASTM standard C1468-06. 5.0^L x 5.0^W x 3.0^T specimen was adhered by epoxy glue to a pair of holders, with 5 mm square faces (Fig. 3). The holders were connected to the load train using a pair of universal joints to promote self-alignment of the load train during the movement of crosshead to minimize sample bending. All tests were conducted with the crosshead speed of 0.5 mm/min at ambient temperature. Trans-thickness tensile strength was defined as the maximum load divided by specimen length multiplied specimen width.

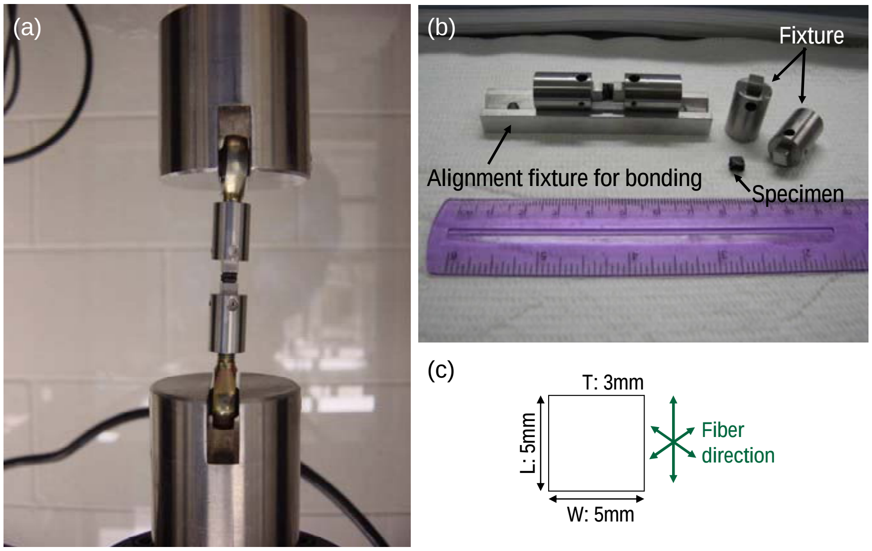

Fig. 3: (a), (b) Apparatus for the trans-thickness tensile test, and (c) schematic design of trans-thickness tensile test specimen

Results and Discussion

Tensile properties

Fig. 2 exhibits the typical tensile stress-strain curves of tri-axially braided C/C composites. The tensile properties are also summarized in Table 1. All specimens were fractured by delamination. Each of the curves for the composites exhibits quasi-ductile behavior consisting of an initial proportional region that corresponds to the elastic deformation, a second linear portion during which matrix cracks in transverse fiber bundles progressively develop, and a further non-linear portion due to domination of the matrix cracks in the longitudinal fiber bundles and the fiber failures. Tensile strength of 100~200 MPa, elastic tensile modulus of 90~130 GPa, and proportional limit stress of 50~130 MPa were obtained.

These significant differences of tensile properties (UTS, E, PLS) in each composite are primary attributed to the effective fiber volume content in the loading axis. It is well known that the ultimate tensile strength is proportional to the axial fiber volume fraction, according to the global load shearing theory by Curtin [7], indicating below:

$$\sigma_{\mathrm{u}} = V_f \sigma_{\mathrm{c}} \left(\frac{2}{m+2} \right)^{\frac{1}{m+1}} \left(\frac{m+1}{m+2} \right) \tag{1}$$

$$\sigma_{\mathrm{c}} = \left(\frac{\sigma_0^m \tau L_0}{r} \right) \tag{2}$$

with σ_u being the ultimate tensile strength, σ_c the characteristic strength, σ_0 the Weibull mean strength, m the Weibull modulus, τ the frictional sliding resistance, V_f the fiber volume fraction, L_0 the gauge length, and r the fiber radius, respectively. In order to examine the relationship between the tensile strength and the axial fiber volume fraction, each specimen was cut possibly near at the fractured position, and the cross-sectional optical images were carried out to determine the axial fiber volume fraction. As plotted in Fig. 5 (a), it was confirmed that the large differences in axial fiber content provided the differed tensile strength in each composite and that the tensile strength is almost proportional to the axial volume fraction.

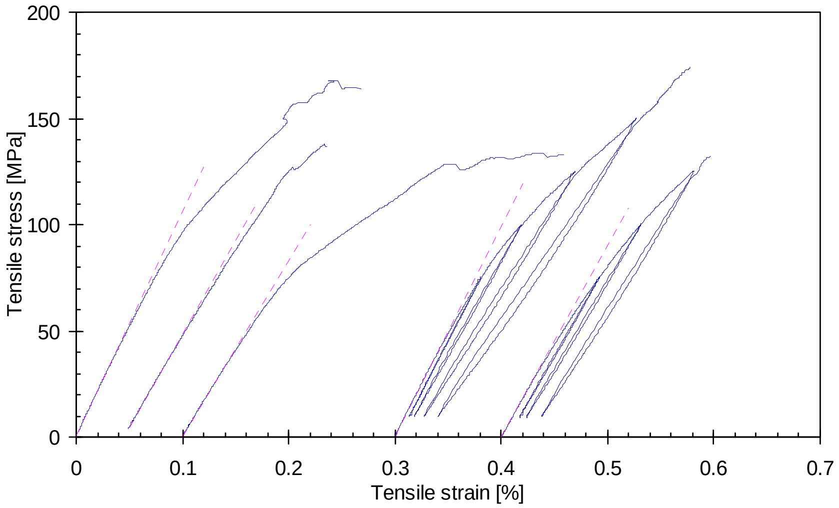

Fig. 4: Typical tensile stress-strain monotonic/unloading-reloading curves of tri-axially braided C/C composites. The curves have been sifted for clarity.

Table 1: Tensile properties of tri-axially braided C/C composites.

Tensile Modulus (E)	**Proportional limit stress (PLS)**	**Ultimate tensile strength (UTS)**	**Fracture strain**	**# of valid tests**
93 ± 15 GPa	**72 ± 22 MPa**	**143 ± 28 MPa**	**0.261 ± 0.107 %**	**14**

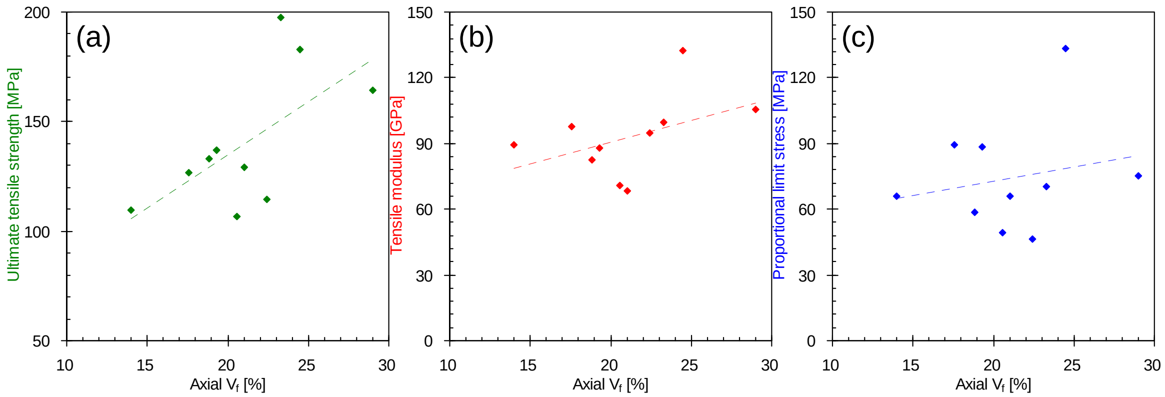

Fig. 5: Dependence of axial volume fraction on (a) UTS, (b) E, and (c) PLS.

As with the tensile strength, the difference of the tensile Young's modulus and proportional limit stress in the composites may be also attributed primarily to the axial fiber volume content (Fig. 5 (b), (c)). Compared with the 0^{o} axial loading fiber bundles, the influence of the $\pm 55^{o}$ fiber bundles on tensile modulus might be much smaller, so tensile modulus can be roughly described as the following using the role of mixture:

$$E = E_f V_f + E_m (1 - V_f) \tag{3}$$

where E_f, E_m denotes the Young's modulus of fiber and matrix, respectively. Additionally, the Young's modulus of the matrix presumed to be smaller than that of the fiber (159 GPa). Therefore, the tensile modulus of the composites can be dependent on the axial fiber volume fraction.

The analytical model of the PLS in 3-D composite systems is currently unavailable. But in 2-D composite systems, it is well known that both of the PLS and the matrix cracking stress rely on the axial fiber volume fraction [8, 9]. In addition, it is confirmed that the stresses were dependent on the axial fiber volume content and they were strongly related in three directional SiC/SiC composites [10]. Therefore, in the case of the tri-axially braided C/C composites, the similar behavior seems to be occurred.

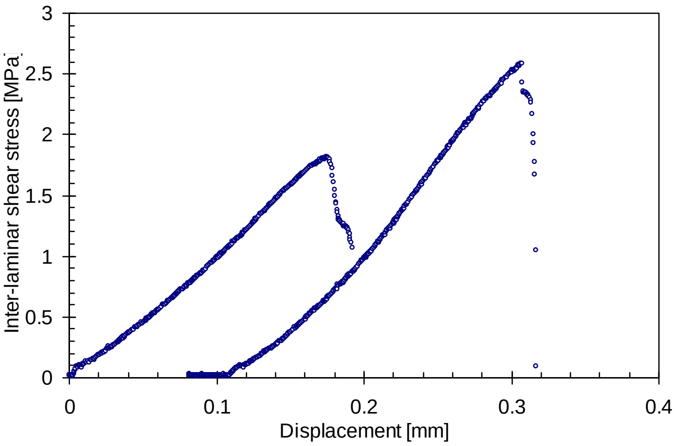

Fig. 6: Loading curves of the double notched shear test. The curves have been sifted for clarity.

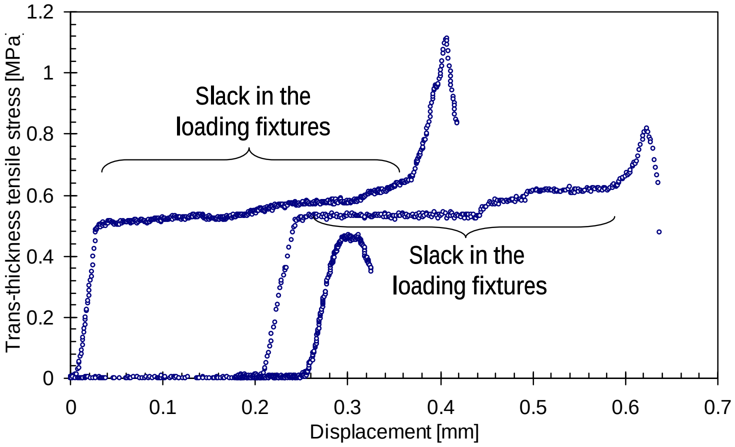

Fig. 7: Stress-displacement curves of trans-thickness tensile tests. The curves have been sifted for clarity.

Inter-laminar shear and trans-thickness tensile property

The loading curves of the double notched shear test were shown in Fig. 6. The curves showed almost linear responses and then shear fractures were occurred. The average inter-laminar shear strength of 2.2±0.6 MPa were measured. Fig. 7 also exhibits the stress-displacement curves of the trans-thickness tensile test. In the curves linear behaviors except the slack in the loading fixtures were measured. Eight tests were conducted and average trans-thickness tensile strength of 0.7±0.4 MPa were obtained. Those relatively weak strengths can be primary due to the low carbon matrix strength itself in addition to the inner porosity.

References

[1] L.L. Snead, in Carbon Materials for Advanced Technologies, Ed., T.D. Burchell (Pergamon, 1999) 389.

[2] V. Barabash, M. Akiba, J.P. Bonal, G. Federici, R. Matera, K. Nakamura, H.D. Pacher, M. Rodig, G. Vieider and C.H. Wu, J. Nucl. Mater. 258-263 (1998) 149.

[3] T.D. Burchell, W.P. Eatherly, J M Robbins and J.P. Strizak, J. Nucl. Mater. 191-194 (1992) 295.

[4] J.P. Piccola, Jr., M.G. Jenkins and E. Lara-Curzio, ASTM STP 1309 (1997) 3.

[5] E. Lara-Curzio, and M.K. Ferber, ASTM STP 1309 (1997) 31.

[6] E. Lara-Curzio, D. Bowers and M.K. Ferber 230, (1996) 226.

[7] W.A. Curtin, J. Am. Ceram. Soc. 74 (1991) 2837.

[8] Z.C. Xia, R.R. Carr and J.W. Hutchinson, Acta metall. Mater. 41 (1993) 2365.

[9] A.G. Evans and F.W. Zok, J. Mater. Sci., 29 (1994) 3857.

[10] T. Nozawa, Y. Katoh, L.L. Snead, T. Hinoki, and A. Kohyama, Ceram. Eng. and Sci. Proc. 26 (2005) 311.

RESULTS OF FRACTURE TOUGHNESS TESTS OF SEVERAL RAFM STEELS IRRADIATED IN JP-27 CAPSULE IN HFIR — M. A. Sokolov (Oak Ridge National Laboratory)

OBJECTIVE

The objective of this present work is to perform fracture toughness evaluation of several heats of F82H RAFM steel irradiated in JP-27 capsule in the High-Flux Isotope Reactor (HFIR).

SUMMARY

Large number of 3-point bend multi-notch specimens of several RAFM steels was irradiated at 300°C and 400°C in capsule JP-27 up to ~22 dpa. These specimens were tested in the hot cell and results are reported here.

TEST RESULTS

Three-notch bend bar specimen was used in this irradiation experiment for fracture toughness studies. The specimens were 1.65-mm thick and 3.3-mm wide. Specimens were tested in general accordance with ASTM E1921 standard. Test temperatures were coordinated between JAEA, UCSB and ORNL based on available tensile data and direct hardness measurements on bend bars prior to the fracture toughness tests. Table 1 provides fracture toughness test results of all specimens tested. The main goal of this study was to measure the reference fracture toughness transition temperature, T_o. Thus, the test temperatures were selected such that tests would be performed in the transition region where specimens would break by cleavage. Despite these efforts several specimens did not cleave. This highlights one more time the very narrow temperature window that is available to generate meaningful results from very small specimens like those used in this experiment. Some of these specimens developed J-R curve from which J-integral at the onset of stable crack growth, J_Q, was determined and reported in Table 1. The other specimens run out of measuring capacity without stable growth or cleavage. For those specimens, the final J-integral value at the end of the test, J_{final}, is reported in the Table 1.

Several heats of F82H steel were irradiated in this experiment. The IEA and Mod. 3 heats are designated as F82H-IEA and F82H-MOD3, respectfully. Mod.1 heat was studied with various heat treatments that had additional designations F82H-MOD1E, F82H-MOD1F, F82H-MOD1G, and F82H-MOD1H. Also, two heats of F82H steel alloyed with 1.4% of Ni^{58} and Ni^{60} are designated as F82H-58Ni and F82H-60Ni, respectfully. In addition to fracture toughness data, target irradiation temperature, dose, and average hardness are also reported in Table 1.

Table1. Fracture toughness results

Material	Irr. T °C	Dose dpa	ID	Test T °C	J_c kJ/m^2	K_{Jc} MPam$^{1/2}$	H_v	Remarks
F82H-IEA	300	18	034M	26	16.08	61.21	N/A	
			037D	50	84.24	139.51	364	J_{final}
			037M	50	37.88	93.55		
			037U	50	39.41	95.42		
			035D	75	50.41	107.43	360	J_Q
			035M	50	12.24	53.18		
			035U	65	21.82	70.81		
			036D	26	5.77	36.67	353	
			036M	50	11.31	51.12		
			036U	75	39.44	95.03		
	400	22	044D	-80	92.89	149.91	338	J_{final}
			044M	-100	14.09	58.59		
			045D	-100	17.32	64.96	298	
			045U	-100	94.62	151.83		
			046D	-40	84.17	141.71	310	J_{final}

			046M	-60	81.55	139.98		J_{final}
			046U	-100	13.4	57.14		
			047D	-80	124.68	173.68	315	
			047U	-80	19.95	69.48		
F82H-58Ni	300	16	534D	65	47.15	104.09	436	
			534M	75	68.52	125.25		
			534U	75	16.56	61.57		
			535D	75	31.59	85.04	437	
			535M	75	28.61	80.93		
			535U	75	67.62	124.43		
			536D	75	26.46	77.79	433	
			536M	75	29.77	82.56		
			536U	75	65.03	122.02		
	400	21	544D	-80	110.31	163.37	346	
			544M	-90	97.45	153.82		
			544U	-90	353.18	292.82		
			545D	-60	98.27	153.66	N/A	
			545M	-80	81.05	140.04		
			545U	-110	120.6	171.70		
			546D	-90	94.84	151.74	365	
			546M	-100	79.97	139.58		
			546U	-100	98.44	154.86		
			547D	23	106.79	157.85	392	
			547M	-20	90.76	146.64		
			547U	-60	69.12	128.87		
F82H-60Ni	300	16	634D	75	39.33	94.89	436	
			634M	75	44.8	101.28		
			634U	75	32.12	85.76		
			635D	65	39.12	94.81	429	
			635M	65	30.67	83.95		
			635U	65	36.28	91.31		
			636D	65	29.9	82.89	430	
			636M	65	58.64	116.08		
			636U	65	40.64	96.64		
	400	21	644D	26	77.85	134.70	N/A	
			644M	26	10.69	49.91		
			644U	26	364.12	291.31		J_{final}
			645D	-40	109.12	161.35	345	J_{final}
			645M	-80	117.58	168.67		J_{final}
			645U	-122	87.95	146.93		
			646D	-120	115.56	168.37	N/A	
			646M	-136	30.75	87.09		
			646U	-147	144.21	188.95		
			647D	-120	86.12	145.35	324	
			647M	-120	109.18	163.65		
			647U	-120	108.99	163.51		
F82H-MOD3	300	18	H34D	50	73.08	129.94	354	J_{final}
			H34M	29	51.72	109.74		J_Q
			H34U	-20	35.08	91.16		
			H35D	0	36.21	92.29	364	
			H35M	0	34.16	89.64		J_Q
			H35U	-20	72.79	131.32		J_{final}
			H36D	-20	52.92	111.97	364	J_Q

			H36D	-40	33.99	90.05		
	400	22	H44D	-140	23.86	76.77	292	
			H44M	-140	33.62	91.12		
			H44U	-140	58.34	120.03		
			H45D	-140	33.15	90.48	290	
			H45M	-140	6.63	40.47		
			H45U	-140	69.54	131.05		
			H46D	-140	56.63	118.26	301	
			H46M	-140	68.94	130.49		
			H46U	-140	68.73	130.29		
			H47D	-140	49.74	110.83	310	
			H47M	-140	56.07	117.68		
			H47U	-140	42.72	102.71		
F82H-MOD1E	300	13	XE34D	-40	14.42	58.66	325	
			XE34M	-20	78.33	136.23		J_{final}
			XE34U	-40	9.31	47.13		
			XE35D	26	89.79	144.66	325	J_{final}
			XE35M	-20	9.64	47.79		
			XE35U	0	21.67	71.40		
			XE36D	26	35.19	90.56	323	
			XE36M	26	61.70	133.15		
			XE36U	26	85.41	141.09		
F82H-MOD1F	300	14	XF34D	26	89.57	144.48	312	J_Q
			XF34M	26	31.68	85.93		
			XF34U	26	89.21	144.19		J_{final}
			XF35D	26	95.98	149.56	332	J_{final}
			XF36D	-20	24.79	76.63	337	
			XF36M	-10	25.22	77.16		
			XF36U	-10	18.13	65.42		
F82H-MOD1G	300	13	XG34D	-40	5.35	35.72	298	
			XG34M	-20	34.74	90.72		
			XG34U	-20	52.67	111.71		
			XG35D	-20	13.15	55.82	329	
			XG35M	-20	14.52	58.65		
			XG35U	0	7	40.58		
			XG36D	-10	100.57	154.09	315	J_{final}
			XG36M	-40	6.38	39.02		
			XG36U	-20	30.13	84.49		
F82H-MOD1H	300	17	XH34D	-20	9.44	47.29	347	
			XH34M	0	8.66	45.13		
			XH34U	0	92.87	147.9		J_Q
			XH35D	23	89.49	144.50	354	J_{final}
			XH35M	-20	21.24	70.94		
			XH35U	-20	22.27	72.64		

PRECIPITATE EVOLUTION IN LOW-NICKEL AUSTENITIC STAINLESS STEELS DURING NEUTRON IRRADIATION AT VERY LOW DOSE RATES -
Y. Isobe, M. Sagisaka (Nuclear Fuels Limited), F. A. Garner (Pacific Northwest National Laboratory) and T. Okita (University of Tokyo)

OBJECTIVE

The objective of this effort is to explore the microstructural development of austenitic steels when irradiated at very low displacement rates.

SUMMARY

Neutron-induced microstructural evolution in response to long term irradiation at very low dose rates was studied for a Russian low-nickel austenitic stainless steel designated X18H9 that is analogous to AISI 304. The irradiated samples were obtained from an out-of-core support column for the pressure vessel of the BN-600 fast reactor with doses ranging from 1.7 to 20.5 dpa generated at 3.8×10^{-9} to 4.3×10^{-8} dpa/s. The irradiation temperatures were in a very narrow range of 370-375°C. Microstructural observation showed that in addition to voids and dislocations, an unexpectedly high density of small G-phase precipitates was formed that are not usually observed at higher dpa rates in this temperature range.

A similar behavior was observed in a Western stainless steel, namely AISI 304 stainless steel, irradiated at similar temperatures and somewhat higher dpa rates in the EBR-II fast reactor, indicating that irradiation at low dpa rates for many years can lead to a different precipitate microstructure and therefore different associated changes in matrix composition than are generated at higher dpa rates. The contribution of such radiation-induced precipitation to changes in electrical resistivity was measured in the X18H9 specimens and was shown to cause significant deviation from predictions based only on void swelling.

PROGRESS AND STATUS

Introduction

Not all components of a fusion reactor will be subjected to high atomic displacement rates. Some components outside the plasma containment may experience relatively low displacement rates but data generated under long-term irradiation at low dpa rates are more difficult to obtain.

In the present study the neutron-induced microstructural evolution in response to long term irradiation at very low dose rates was studied for a Russian low-nickel austenitic stainless steel that is analogous to AISI 304. The irradiated samples were obtained from an out-of-core anti-crush support column for the pressure vessel of the BN-600 fast reactor. Specimens chosen for examination had doses ranging from 1.7 to 20.5 dpa generated at 3.8×10^{-9} to 4.3×10^{-8} dpa/s. The irradiation temperatures were in a very narrow range of 370-375°C.

Experimental details

The pipe being examined served for almost three decades in the BN-600 fast reactor located in Zarechney, Russia. It was removed for examination in support of plant life extension efforts. This power plant reached its 30 year lifetime in 2008. The pipe was originally produced by extrusion but due to the age of this pipe no record has survived concerning its initial post-production thermal-mechanical condition

The pipes measured composition after production was specified in its certificate and was found to be Fe-8.75Ni-17.66Cr-1.36Mn-0.38Si-0.21Cu-0.09C-0.025P-0.020S in wt% as shown in **Table 1**. The Russian designation for this steel is X18H9 and is analogous to AISI 304 stainless steel. The pipe was originally 9.5 cm in diameter with 2.0 cm thick walls. Some small changes in dimension are expected due to swelling, phase instability and possibly light corrosion. Sodium was flowing on both the inside and outside of the pipe. There was very little change in temperature axially and radially in the pipe because the pipe lay far outside the core. The primary cause of temperature increase is gamma heating at rather low levels. Across the wall thickness the temperature increase due to gamma heating was calculated to be <1ºC. Such small variations ensure that the primary operational variable in this examination is that of dpa rate.

Using a diamond milling machine remotely in a hot cell, five annular sections were cut at various elevations on the pipe and their microstructure and changes in resistivity were evaluated. The irradiation conditions of each section are shown in **Table 2**. Note that all differences in dose arise only from differences in dpa rate as all specimens were derived from a single component in this constant time experiment.

Specimens were prepared from each section to study the microstructure by transmission electron microscopy. In particular, characteristics of porosity and second phase precipitates were determined. Radiation–induced changes of electrical resistivity were measured using the electrical potential technique. The measurement uncertainty was within ±0.5 %.

Table 1 – Chemical Composition of Fe-18Cr-9Ni Steels

Composition, weight %.								
Pipe measurements prior to irradiation (certificate data)								
C	Mn	Si	P	S	Ni	Cr	Cu	Fe
0.09	1.36	0.38	0.025	0.020	8.75	17.66	0.21	balance
Specification of Fe-18Cr-9Ni (X18H9, Russia)								
0.13-0.21	<2.0	<0.8	<0.03	<0.02	8.0-10.0	17.0-19.0	<0.2	balance
AISI 304L (Japan, USA)								
<0.03	<2.0	<1.0	<0.04	<0.03	8.0-13.0	18.0-20.0	-	balance

Table 2 – Irradiation Characteristics of Examined Specimens

Specimen section #	Damage, dpa	Temperature, ºC	Displacement rate, dpa/s
1	1.7±0.2	372±1	$(3.8\pm0.4)\cdot10^{-9}$
2	9.9±0.3	373±1	$(2.10\pm0.04)\cdot10^{-8}$
3	12.4±0.3	375±1	$(2.60\pm0.06)\cdot10^{-8}$
4	16.2±0.3	373±1	$(3.40\pm0.06)\cdot10^{-8}$
5	20.5±0.4	376±1	$(4.30\pm0.08)\cdot10^{-8}$

Results

Microscopy revealed voids in all irradiated specimens. In **Table 3** the average sizes and concentrations of the voids as well as the swelling values estimated from histograms of the void size distribution are presented. It is seen that the concentration of voids in specimens irradiated to different dpa levels have relatively similar values with the void mean radius increasing monotonically with dpa. The voids in specimens irradiated to 1.7 dpa are small, and in general they are free-standing and not associated with precipitates which exist at rather low density, but are often associated with dislocations (**Fig. 1b**). As the damage dose increases the fraction of voids associated with second phase precipitates increases and the precipitate density also increases. Void-precipitate associations at 20.5 dpa are shown in **Fig. 1h**. Micro diffraction data identified the precipitates as G–phase although its lattice parameter is slightly smaller than that of classical G-phase. This phase is not normally observed at this temperature in irradiations conducted at higher dpa rate.

Other phases formed primarily along grain boundaries were identified as the M_6C and $M_{23}C_6$ carbides .In addition, extended areas of α-phase were sometimes observed to form in the γ matrix as seen at 20.5 dpa in **Fig. 1g**.

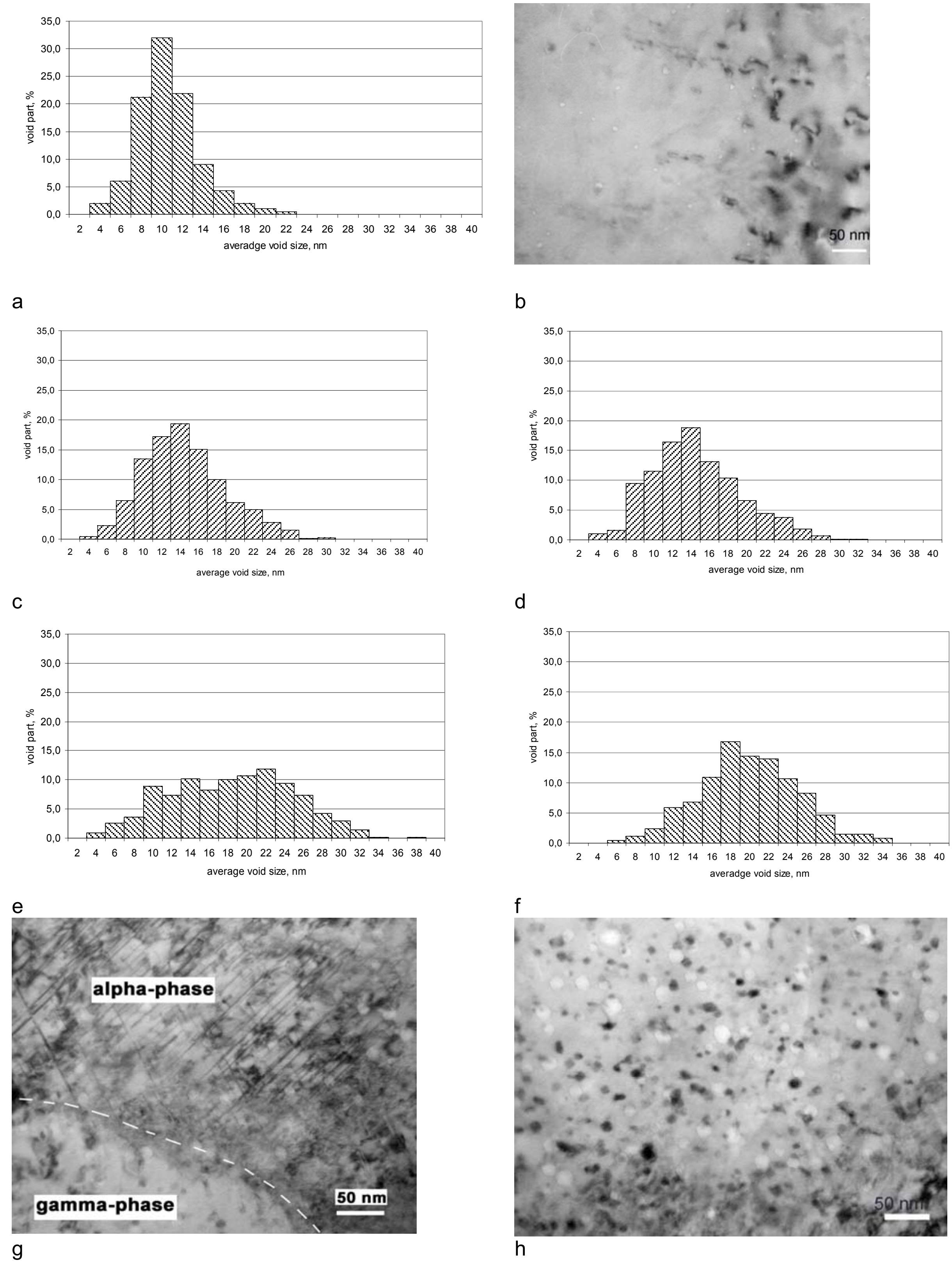

Figure 1 Microstructures of Fe-18Cr-9Ni specimens. Panels a, c, d, e, f show histograms of void size distribution at doses of 1.7, 9.9, 12.4, 16.2 and 20.5 dpa. Voids at 1.7 and 20.5 dpa are shown in panels b and h. Occasional α-phase formation in the γ matrix is shown in panel g. Micrographs were provided in advance of publication by E. N. Shcherbakov of the Institute of Nuclear Materials.

Table 3 Average characteristics of voids in specimens irradiated to different dpa levels

Section #	Damage, dpa	Average size of voids, nm	Concentration of voids, $10^{21}m^{-3}$	Swelling, %
1	1.7	10	4.1	0.25
2	9.9	13	5.2	1.00
3	12.4	14	5.0	0.95
4	16.2	17	4.1	1.60
5	20.5	19	5.8	2.30

The electrical resistivity data of these specimens are listed in **Table 4** along with the local values of swelling determined by microscopy. Since no archive pipe was available the value of 72.9 10^{-8} ohm.m at 0 dpa was determined by measuring specimens from a plate produced by the same composition and melting method. This introduces the largest potential source of error in the experiment.

Table 4 – Average values of electrical resistivity (ρ).

section #	Damage , dpa	Swelling, %	ρ, 10^{-8} ohm·m
1	1.7	0.25	74.1
2	9.9	1.00	72.3
3	12.4	0.95	72.9
4	16.2	1.60	72.2
5	20.5	2.30	73.8

Discussion

With swelling there arise concurrent changes in electrical and elastic properties. It was shown in [1, 2] that if there are no other structural changes or especially when swelling dominates the microstructure, swelling-induced changes in electrical resistance can be successfully calculated from the formula below;

$$\frac{\Delta R}{R_0} = \frac{5 \cdot S}{4 \cdot S + 6} \tag{1}$$

Where ΔR is the absolute change in electrical resistivity; R_0 is the value of the initial condition of the material, and S is the swelling represented as a volume fraction. A comparison of the measured relative change in resistivity (plotted points) to change predicted using swelling (dashed line) is shown in **Figure 2**.

It is obvious that the experimental values do not follow the predicted curve, with the resistivity initially rising above the predicted curve and then falling under the curve before returning to the swelling-dominated prediction at the highest swelling level. This result shows that precipitate evolution and its concurrent effect on matrix composition is initially overwhelming the void contribution. First, if the 0 dpa values are accepted even though it is not explicitly an archive value, there appears that there may be two phase states in the evolution, one which initially increases the resistivity and a later one that decreases it even if the 0 dpa value is not completely representative.

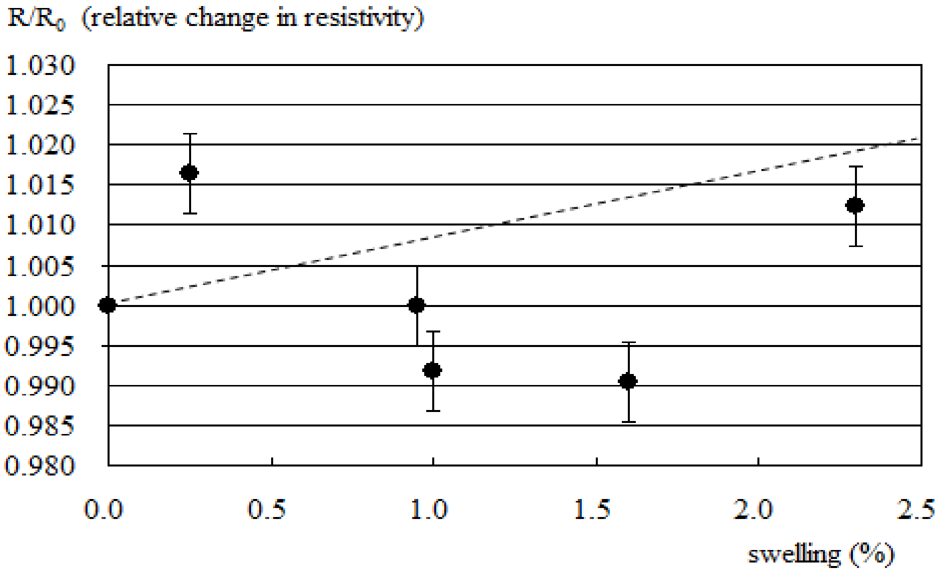

Figure 2 Comparison of experimentally obtained relative change in resistivity (plotted points) to change predicted using swelling (dashed line).

It is often assumed that significant precipitation is not a feature of the radiation-induced microstructure of AISI 304 at temperatures and dose rates relevant to light water reactors or fast reactors in far-from-core locations. However, as shown in Figure 3 high densities of small precipitates have been observed in AISI 304 stainless steel in EBR-II fast reactor at a near-identical temperature of 379°C compared to the BN-600 pipe when irradiated for several decades in the lower-flux reflector regions of EBR-II [3, 4]. In this case, however, the precipitates were identified as being $M_{23}C_6$ [3]. Such prolific precipitation has not been reported in this steel when irradiated at higher dpa rates in the EBR-II core. Ferrite was specifically sought but not found in 304 specimens.

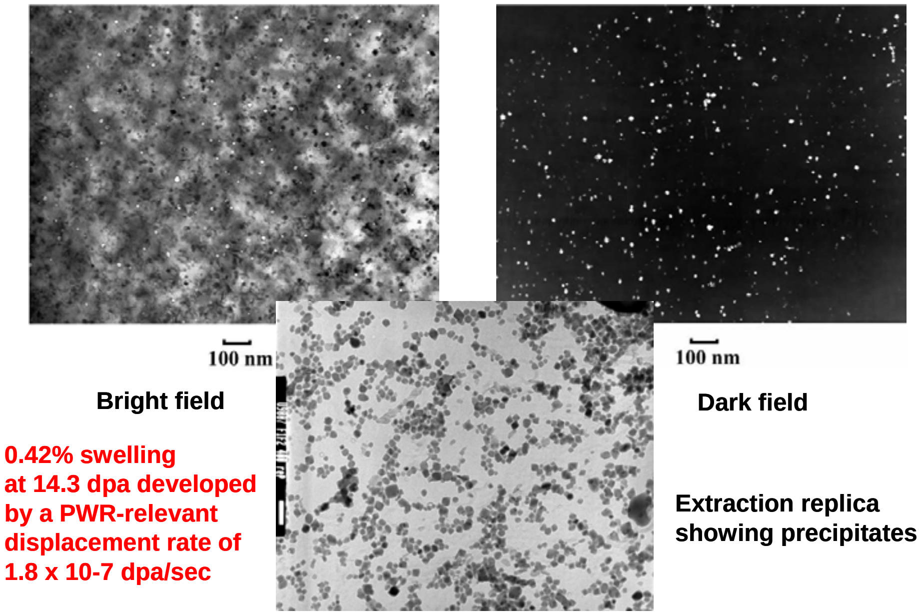

Bright field

Dark field

0.42% swelling at 14.3 dpa developed by a PWR-relevant displacement rate of 1.8 x 10-7 dpa/sec

Extraction replica showing precipitates

Figure 3. Concurrent void formation and $M_{23}C_6$ precipitation after irradiation at a PWR-relevant dpa rate of 1.8 x 10^{-7} dpa/sec in EBR-II at 379ºC, as observed in bright field, dark field and via extraction. [3, 4]

The microstructural evolution observed in the present study as well as in the EBR-II case indicates that irradiation at low dpa rates for many years leads to a different precipitate microstructure and therefore different associated changes in matrix composition than are generated at higher dpa rates. Rather than invoking only the longer times required for diffusion at lower temperatures, one possibility is that the small precipitate sizes characteristic of lower temperature irradiation are more stable at lower dpa rates, since the thermodynamic driving forces favoring precipitation must compete with the radiation-induced recoil dissolution, the latter strongest at smaller precipitate sizes and higher dpa rates.

The difference between formation of $M_{23}C_6$ and G-phase in these two examples may reflect not only small differences in steel composition, but also the somewhat higher dpa rate in the EBR-II case (1.8 x 10^{-7} dpa/sec) vs. that of the current study (≤4.3 x 10^{-8} dpa/sec). Borodin and coworkers have shown that radiation-induced segregation of nickel to previously formed precipitates can induce MX or carbide precipitates to change both composition and crystal structure to form G-phase [5]. Normally, G-phase formation is favored by higher nickel level or by the presence of titanium, neither of which applies to the BN-600 pipe. However, G-phase formation has been observed in Ti-free AISI 316 steel which has higher nickel content than AISI 304. [6].

Regardless of the phase formed, however, there will be consequences on the electrical and thermal resistivity as well as the elastic properties of the alloy matrix. Removal of carbon especially into precipitates is known to increase the density of the steel [7, 8] and to change the resistivity and elasticity parameters [1, 2], with the net effect depending on what other elements are removed to form the precipitate. The time-dependent phase evolution of stainless steels during irradiation is known to be exceptionally sensitive to dpa, dpa rate, temperature, irradiation history, starting thermal-mechanical treatment and both minor and major elemental compositional differences [8-11]. In some cases the austenite matrix can be transformed into ferrite by removal of nickel and other elements into precipitates [12-14].

In addition to changes arising from the compositional alteration of the alloy matrix, there may be contributions to resistivity changes arising from the crystalline state of the precipitates. Noting that α-phase was observed in the BN-600 pipe, lets consider the potential influence of forming this phase which has less electrical resistance than γ-phase and therefore should contribute to a decrease in resistance. The specific electrical resistivity of a two-phase system (a system of a single-phase matrix with unconnected second phase particle) is determined by an equation described in [15].

$$\gamma = \gamma_0 \cdot \left(1 + \frac{c}{(1-c)/3 + \gamma_0/(\gamma_1 - \gamma_0)}\right), \qquad (2)$$

Where γ is the specific conductivity of the alloy; γ_0 is the specific conductivity of the matrix, γ_1- is the specific conductivity of second phase particles and *c* their concentration. This equation can be manipulated to yield

$$\frac{\Delta r}{r_0} = -\frac{c}{(1+2c)/3 + r_1/(r_0 - r_1)}, \qquad (3)$$

Where r_0, r_1 are the specific resistance of matrix and α-phase; Δr is the difference between steel containing α-phase, and without it. If $r_1 = \beta \cdot r_0$ then

$$\frac{\Delta r}{r_0} = -\frac{c}{(1+2c)/3 + \beta/(1-\beta)}. \qquad (4)$$

Since X18H9 (Fe-18Cr-9Ni) has r_0 =72.7x10^{-8} ohm.m in its initial state and ferrite has r_1 =56.6 x10^{-8}

ohm.m, then $\beta = 0{,}779$ and (4) transforms to

$$\frac{\Delta r}{r_0} = -\frac{c}{(1+2c)/3+3{,}52}. \tag{5}$$

When *c* is small a first approximation yields

$$\frac{\Delta r}{r_0} = -\frac{c}{3{,}85}. \tag{6}$$

Combining (1) and (6) yields

$$\frac{\Delta R}{R_0} = \frac{5S}{4S+6} - \frac{c}{3{,}85}, \tag{7}$$

and predicts that negative resistivity changes on the order of the swelling can occur for swelling levels in the 1-2% range. This suggests that it may be possible to identify the content of precipitates nondestructively using information known about the resistivity of various precipitates.

While the irradiation temperatures of the BN-600 and EBR-II cases presented in this paper are not very low compared to that in other published studies, it is significant to note that voids were observed at only 1.7 dpa at the lowest dpa rate in BN-600. This observation is consistent with a growing body of evidence that the incubation regime of void formation in austenitic stainless steels decreases progressively as the dpa rate declines, leading not only to more swelling at lower dpa rates but also to an extension of the swelling regime to lower temperatures [16-23]. Voids have been observed in several steels at very low doses at temperatures down to ~280ºC which is the inlet temperatures of the BOR-60 and BN-350 fast reactors.

Conclusions

The neutron-induced microstructural evolution in response to long term irradiation at 372-376ºC at very low dose rates in BN-600 was studied for a Russian low-nickel austenitic stainless steel that is analogous to AISI 304. Microstructural observation showed that in addition to voids and dislocations, an unexpectedly high density of small G-phase precipitates was formed that are not usually observed at higher dpa rates in this temperature range. A similar behavior was observed in a Western stainless steel, namely AISI 304 stainless steel, irradiated at similar temperatures and somewhat higher dpa rates in the EBR-II fast reactor, indicating that irradiation at low dpa rates for many years can lead to a different precipitate microstructure and therefore different associated changes in matrix composition than are generated at higher dpa rates. At relatively low swelling levels precipitation can cause significant deviations in resistivity compared to that predicted on the basis of void swelling alone.

Acknowledgements

This report presents a small fraction of the results of a joint study conducted at the Institute of Nuclear Materials in Zarechney, Russian Federation under Project # RUP2-1670-SK-06 funded by the Japanese Ministry of Education, Culture, Sports, Science and Technology. The contributions of Drs. A. Kozlov and E. Shcherbakov to this paper are especially appreciated.

REFERENCES

1. A. V. Kozlov, E. N. Shcherbakov, S. A. Averin, and F. A Garner, "The Effect of Void Swelling on Electrical Resistance and Elastic Moduli in Austenitic Steels", Effects of Radiation on Materials: 21st International Symposium. ASTM STP 1447, 2003, pp. 66-77.
2. I. I. Balachov, E. N. Shcherbakov, A. V. Kozlov, I. A. Portnykh and F. A. Garner, "Influence of Irradiation-Induced Voids and Bubbles on Physical Properties of Austenitic Structural alloys, "J. Nucl. Mater. 329-333 (2004) 617-620.
3. G. M. Bond, B. H. Sencer, F. A. Garner, M. L. Hamilton, T. R. Allen and D. L. Porter, "Void Swelling of Annealed 304 Stainless Steel at ~370-385ºC and PWR-Relevant Displacement Rates", Ninth International Symposium on Environmental Degradation in Nuclear Power Systems – Water Reactors, F. P. Ford, S. M. Bruemmer and G. S. Was, Eds., The Minerals, Metals and Materials Society (TMS), 1999, pp. 1045-1050.
4. F. A. Garner and L. R. Greenwood, "Survey of Recent Developments Concerning the Understanding of Radiation Effects on Stainless Steels Used in the LWR Power Industry"11th Intern. Conf. On Environmental Degradation of Materials in Nuclear Power Systems - Water Reactors, 2003, pp. 887-909.
5. O. V. Borodin, V. N. Bryk, V. N. Voyevodin, I. M. Neklyudov, V. K. Shamardin V. S. Neustroev, "Microstructural Evolution of Austenitic Stainless Steels Irradiated in a Fast Reactor", Effects of Radiation on Materials: 17th International Symposium, ASTM STP 1270, 1996, pp. 817-830.
6. P. J. Maziasz, "Formation and Stability of Radiation-Induced Phases in Neutron-Irradiated Austenitic and Ferritic Steels", J. Nuclear Materials 169 (1989) 95-115.
7. F. A. Garner, W. V. Cummings, J. F. Bates and E. R. Gilbert, "Densification-Induced Strains in 20% Cold-Worked 316 Stainless Steel During Neutron Irradiation," Hanford Engineering Development Laboratory, HEDL-TME-78-9, June 1978.
8. F. A. Garner, Chapter 6: "Irradiation Performance of Cladding and Structural Steels in Liquid Metal Reactors," Vol. 10A of Materials Science and Technology: A Comprehensive Treatment, VCH Publishers, 1994, pp. 419-543.
9. T. M. Williams, "Precipitation in Irradiated and Unirradiated Austenitic Steels", Effects of Radiation on Materials, 11th Conference, ASTM STP 782, 1982, pp. 166-185.
10. W. J. S. Yang, "Precipitate Evolution in Type 316 Stainless Steels Irradiated in EBR-II", Radiation-Induced Changes in Microstructure: 13th International Symposium, ASTM STP 955, 1987, pp. 628-646.
11. P. J. Maziasz, "Overview of Microstructural Evolution in Neutron-Irradiated Austenitic Stainless Steels", J. Nuclear Materials 205 (1993) 118-145.
12. D. L. Porter, F. A. Garner and G. M. Bond, "Interaction of Void-Induced Phase Instability and Subsequent Void Growth in AISI 404 Stainless Steel", Effects of Radiation on Materials:19th International Symposium, ASTM STP 1366, 2000, pp.884-893.
13. H. R. Brager and F. A. Garner, "Radiation-Induced Evolution of the Austenite Matrix in Silicon-Modified AISI 316 Alloys," in Proceedings of AIME Symposium on Irradiation Phase Stability," Pittsburgh, PA, October 5-9, 1980, pp. 219-235.
14. T. M. Williams, R. M. Boothby and J. M. Titchmarsh, "Solute Segregation and Microstructural Instability in Neutron Irradiated 12Cr-15Ni-Si Austenitic Alloys", proceedings of Materials for Nuclear Core Applications, vol. 1, Bristol, England, 27-29 October 1987, pp. 293-299.
15. B. G. Lifshits, V. C. Karposhin and Ya. L. Linetsky, Physical Properties of Metals and Alloys, Metallurgy 1980.
16. T. Okita, N. Sekimura, T. Sato, F. A. Garner and L. R. Greenwood, "The Primary Origin of Dose Rate Effects on Microstructural Evolution of Austenitic Alloys during Neutron Irradiation", Journal of Nuclear Materials 307-311 (2002) 322-326.

17. T. Okita, N. Sekimura, F. A. Garner, L. R. Greenwood, W. G. Wolfer and Y. Isobe, "Neutron-Induced Microstructural Evolution of Fe-15Cr-16Ni Alloys at ~ 400°C During Neutron Irradiation in the FFTF Fast Reactor", 10th International Conference on Environmental Degradation of Materials in Nuclear Power Systems – Water Reactors, 2001, issued on CD format, no page numbers.

18. F. A. Garner, S. I. Porollo, A. N. Vorobjev, Yu. V. Konobeev and A. M. Dvoriashin, "Void Swelling at Low Displacement Rates in Annealed X18H10T Stainless Steel at 30-56 dpa and 280-332°C", 9th International Conference on Environmental Degradation of Materials in Nuclear Power Systems – Water Reactors, 1999, pp. 1051-1059.

19. S. I. Porollo, Yu. V. Konobeev, A. M. Dvoraishin, V. M. Krigan and F. A. Garner, "Determination of the Lower Temperature Limit of Void Swelling of Stainless Steels at PWR-relevant Displacement Rates", 10th International Conference on Environmental Degradation of Materials in Nuclear Power Systems – Water Reactors, 2001, issued on CD format, no page numbers.

20. S. I. Porollo, Yu. V. Konobeev, A. M. Dvoriashin, A. N. Vorobjev, V. M. Krigan and F. A. Garner, "Void Swelling at Low Displacement Rates in Annealed X18H10T Stainless Steel at 4 to 56 dpa and 280-332°C", Journal of Nuclear Materials 307-311 (2002) 339-342.

21. F. A. Garner, N. I. Budylkin, Yu. V. Konobeev, S. I. Porollo, V. S. Neustroev, V. K. Shamardin, A. V. Kozlov, "The Influence of DPA rate on Void Swelling of Russian Austenitic Stainless Steels," 11th International Conference on Environmental Degradation of Materials in Nuclear Power Systems – Water Reactors, 2003, pp. 647-656.

22. O. P. Maksimkin, K. V. Tsai, L. G. Turubarova, T. Doronina and F. A. Garner, "Characterization of 08Cr16Ni11Mo3 Stainless Steel Irradiated in the BN-350 Reactor," J. Nuclear Materials 329-333 (2004) 625-629.

23. O. P. Maksimkin , K. V. Tsai , L. G. Turubarova , T. A. Doronina and F. A. Garner, "Characterization of Microstructural Conditions of AISI 321 Analog Stainless Steel Irradiated at Low Dpa Rates in the BN-350 Reactor", J. Nuclear Materials 367-370 (2007) 990-994.

COMPATIBILITY OF MATERIALS EXPOSED TO ISOTHERMAL Pb-Li – B. A. Pint (Oak Ridge National Laboratory, USA)

OBJECTIVE

One proposed U.S. test blanket module (TBM) for ITER uses ferritic-martensitic alloys with both eutectic Pb-Li and He coolants at ~475°C. In order for this blanket concept to operate at higher temperatures (~700°C) for a DEMO-type reactor, several Pb-Li compatibility issues need to be addressed. Some of the issues being currently investigated are the use of corrosion resistant alloys and coatings, the transformation of alumina exposed to PbLi and the effect of impurities on dissolution of these materials.

SUMMARY

Specimens from six Pb-Li capsule experiments exposed for 1000h at 700° or 800°C were further characterized to determine the extent of attack. The $LiAlO_2$ reaction product appeared to spall in some cases, although this may be due to the Pb-Li cleaning process after exposure. The most unusual result was the large Al loss from the coating on Fe-9Cr-2W after 1000h at 700°C in Pb-Li. If this result indicates the rate of Al loss, it has strong implications for the coating lifetime at this temperature. Also, the mass loss from type 316 stainless steel and resulting microstructure were compared for commercial Pb-Li and high purity Pb-Li. The experimental plan is outlined for the next series of 1000h capsule experiments beginning in January 2009.

PROGRESS AND STATUS

Introduction

A recent focus of the U.S. fusion energy program has been on developing a proposal for a test blanket module (TBM) for ITER. The dual coolant Pb-Li (DCLL) TBM concept has both He and eutectic Pb-Li coolants and uses ferritic steel as the structural material with a SiC/SiC composite flow channel insert (FCI).[1] The interest in this concept has focused compatibility-related research on Pb-Li. Many materials have poor compatibility with liquid Li,[2] but the activity of Li is very low in Pb-17Li,[3] and this allows a wider range of materials to be considered. However, Pb-Li readily dissolves many conventional alloys above 500°C. While the TBM maximum operating temperature will be <500°C to limit compatibility issues, this blanket concept would be more attractive for a commercial reactor with a higher maximum operating temperature, perhaps >700°C if oxide dispersion strengthened (ODS) ferritic steels[4] were used. However, at these higher temperatures, compatibility is even more of a concern. Therefore, static capsule exposures have been conducted on materials at 700° and 800°C.[5-7] The goal of this series of six capsules was to (1) use Al-containing alloys and coatings to study the transformation of α-Al_2O_3 to $LiAlO_2$.[8] and (2) determine the effect of switching from high-purity Pb and Li to commercial purity Pb-17Li in the capsule. The previous report[7] included the initial results from these capsules and this report includes additional characterization. The next series of capsule experiments is now being prepared to follow up on these results.

Experimental Procedure

Static capsule tests were performed using Mo inner capsules and type 304 stainless steel outer capsules to protect the inner capsule from oxidation. Specimens were held inside the Mo capsule by a Mo wire. The specimens were ~1.5 mm thick and 4-5 cm^2 in surface area with a 0.3 μm surface finish. The capsules were loaded with 125g of commercial purity Pb-14.3at.%Li in an argon-filled glove box. The Pb-Li and specimen chemistry along with details of how the specimens were prepared was reported previously.[7] A summary of conditions and mass change after exposure is given in Table I. To remove residual Pb-Li on the surface after exposure, specimens were soaked in a 1:1:1 mixture of acetic acid, hydrogen peroxide and ethanol for up to 72 h. Post-test surfaces were initially examined using x-ray diffraction (XRD) and secondary electron microscopy (SEM). The specimens that formed a surface oxide were then coated with copper to protect that layer, sectioned and metallographically polished for analysis by electron microprobe analysis (EPMA).

Results and Discussion

Table I summarizes the mass change data along with two previous exposures where high purity Pb and Li were used instead of commercial Pb-Li.[5-7] The mass change for 316SS at 700°C was slightly higher in this exposure than in the previous exposure in high purity Pb-Li indicating that the higher O content in commercial Pb-Li did not have a beneficial effect on dissolution. Figure 1 shows polished cross-section of both 316SS specimens exposed at 700°C. A similar Ni-depletion zone was observed in both specimens.

Figure 2 shows a polished cross-section of uncoated T92 after exposure at 700°C. In general, the W and Mo were not depleted near the surface. In areas that showed obvious metal loss, such as in Figure 2a, there was Cr depletion. However, Cr depletion was not observed in all locations as shown in the second Cr profile in Figure 2b.

Figure 3 shows the surface of the aluminized T92 specimen that showed only minimal mass loss, Table I, presumably due to the formation of a protective oxide layer, that was identified by XRD as $LiAlO_2$.[7] Figure 4 shows a polished cross-section of the same specimen. The rougher areas in Figure 3 are typical of the as-deposited coating where the outer layer is not completely uniform, see Figure 4b. However, there are some smoother areas (arrow in Figure 3), which appear to be where the oxide has spalled. Figure 4a shows a region with a relatively thick oxide layer including some oxide protrusions or pits. The region analyzed in Figure 4b showed very little oxide on the surface, Figure 4c. The arrow in Figure 4b indicates a pit where an oxide protrusion may have been located, such as those seen in Figure 4a. As is typical of these coatings,[9] N from the substrate reacts with the Al to form acicular AlN particles at the coating-substrate interface, Figure 4d. Figure 4e shows Cr-rich precipitates in the substrate and lower half of the coating that are likely carbides.

Aluminum profiles from two locations on the exposed coating are shown in Figure 5. For comparison, the Al profile from a typical coating made by this process on alloy T91 (Fe-9Cr-1Mo) also is shown.[10] As expected, little interdiffusion occurred during the exposure.[11] However, a large fraction of the coating Al reservoir appears to have been depleted during the exposure. It is not clear if the depletion is due to

Table 1. Mass change of specimens after 1000h exposures in Pb-17Li with a Mo capsule.

Specimen	Pre-oxidation	Temperature	Mass Change (mg/cm^2)
316SS	none	700°C	- 5.06
316SS	none	700°C	- 3.79 (high purity Pb and Li)
T92	none	700°C	- 3.47
T92 + CVD Al	none	700°C	- 0.09
PM FeCrAl	none	800°C	- 1.93
ODS FeCrAl	2h at 1000°C	700°C	- 0.06
ODS FeCrAl	none	700°C	- 0.20 (high purity Pb and Li)
Ni-42.5Al+Hf	2h at 1200°C	800°C	- 0.51

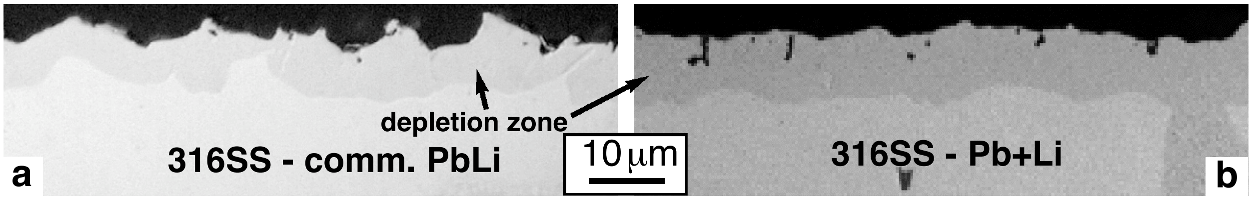

Figure 1. Light microscopy of polished cross-section of type 316 stainless steel after 1000h at 700°C (a) commercial purity Pb-Li and (b) high purity Pb-Li.

dissolution or oxide formation. Except for selected areas where the oxide was extremely thick, no significant metal loss appears to have occurred, otherwise the tail of the Al profile would not match the as-deposited profile. Further analysis is required to determine if this depletion could be due to only oxide formation or also include some oxide dissolution. Prior work on aluminized Fe-Cr steel showed similar penetration attack of a 100*μ*m thick coating on EUROFER 97 with a peak Al content of ~60 at.% after exposure for 6292 h at 480°C in flowing Pb-Li.[12] In that case, the oxide was assumed to be Al_2O_3 and the starting coating was not characterized to determine the amount of Al lost from the coating during exposure. If Al depletion is a concern, one solution is to increase the Al content in the coating. An example is shown in Figure 5 where the Al activity was increased during the deposition process to increase the amount of Al in a T91 substrate. However, minimizing the amount of Al in the first wall may be desired.

Figure 6 shows the surface of PM FeCrAl (Kanthal alloy APMT [13]) after exposure at 800°C. This material is a candidate tubing alloy for construction of a high-temperature loop. This specimen was not pre-oxidized before exposure which may explain the mass loss and the non-uniform attack, similar to the pits observed for aluminized T92. Some of the mass loss could be due to oxide spallation which was evident in some areas with bare metal exposed, Figure 6b. The morphology of the $LiAlO_2$ layer (identified by XRD [7]), Figure 6c, was very similar to that observed on NiAl+Hf and ODS FeCrAl after exposure at 800°C, although both of those specimens were pre-oxidized before exposure. The pits were evident in the

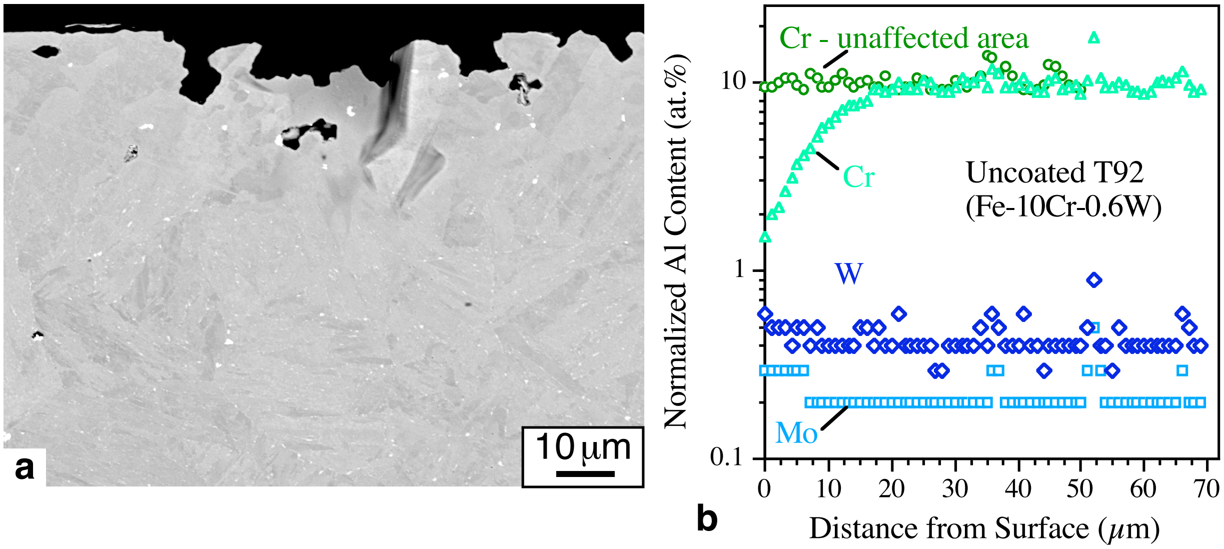

Figure 2. (a) SEM image of T92 polished cross-section after 1,000h at 700°C in commercial Pb-Li. (b) EPMA composition profiles showing no W or Mo depletion and only Cr depletion in regions where there was clear metal loss such as (a). In unaffected areas where there was no obvious metal loss, no Cr loss was detected.

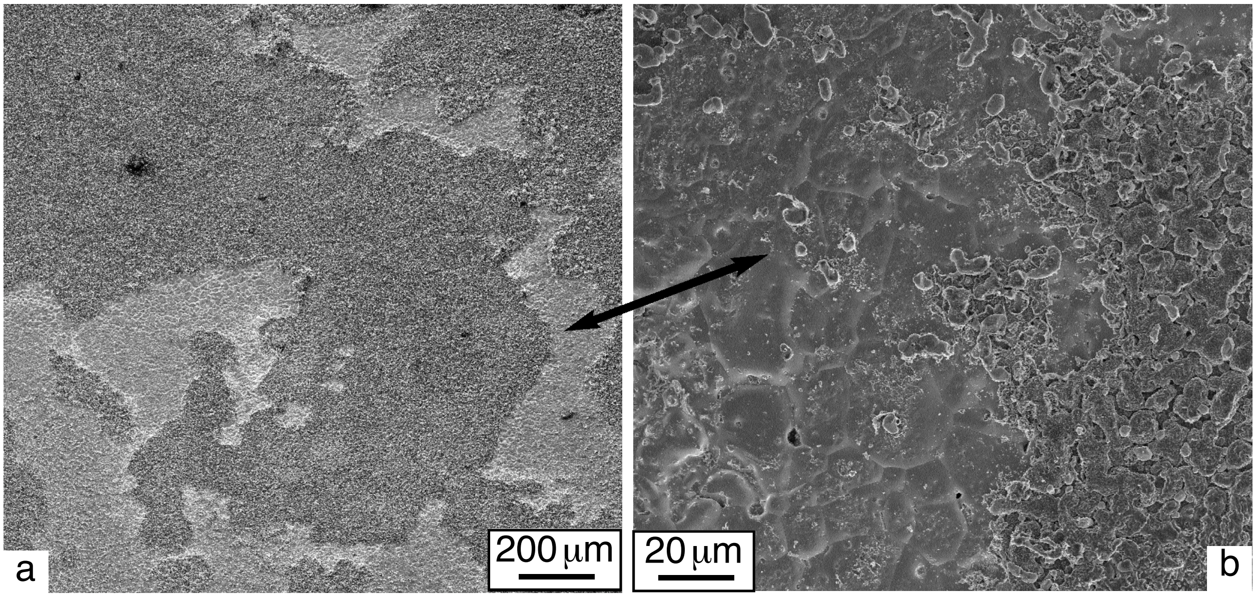

Figure 3. SEM plan view images of the reaction product on aluminized T92 after exposure to Pb-17Li at 700°C for 1,000h. Higher magnification in (b) shows smoother areas

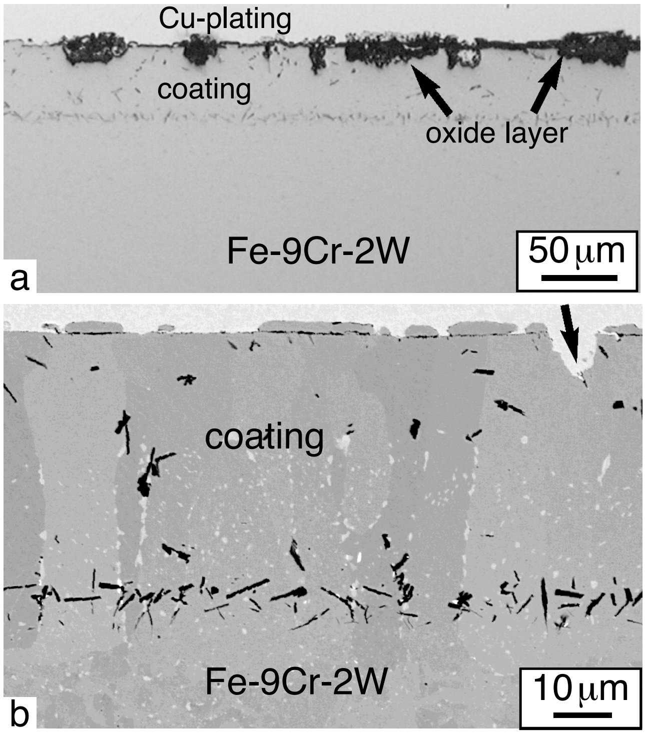

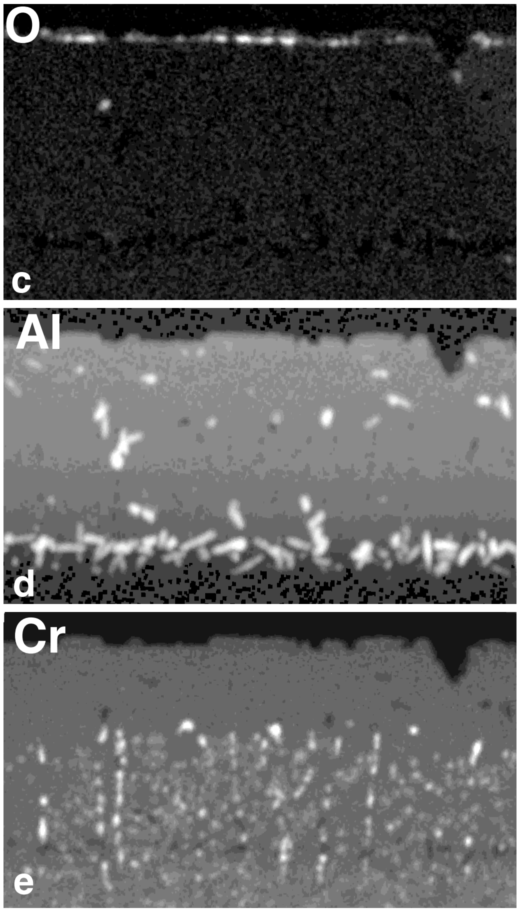

Figure 4. Polished cross-section of aluminized T92 after exposure to PbLi for 1kh at 700°C. (a) light microscopy, (b) secondary electron image, and EPMA maps of the same region in (b) are shown in (c) O, (d) Al and (e) Cr.

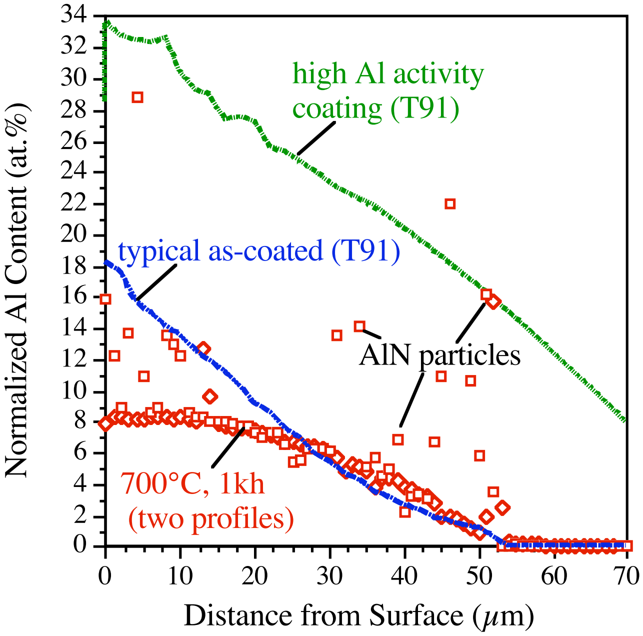

Figure 5. Normalized Al content by microprobe analysis as a function of depth for a typical as-deposited coating on Fe-9Cr-1Mo substrate and coating on Fe-9Cr-2W after exposure for 1kh at 700°C in PbLi. Profile for a coating with a higher Al activity also is shown for comparison.

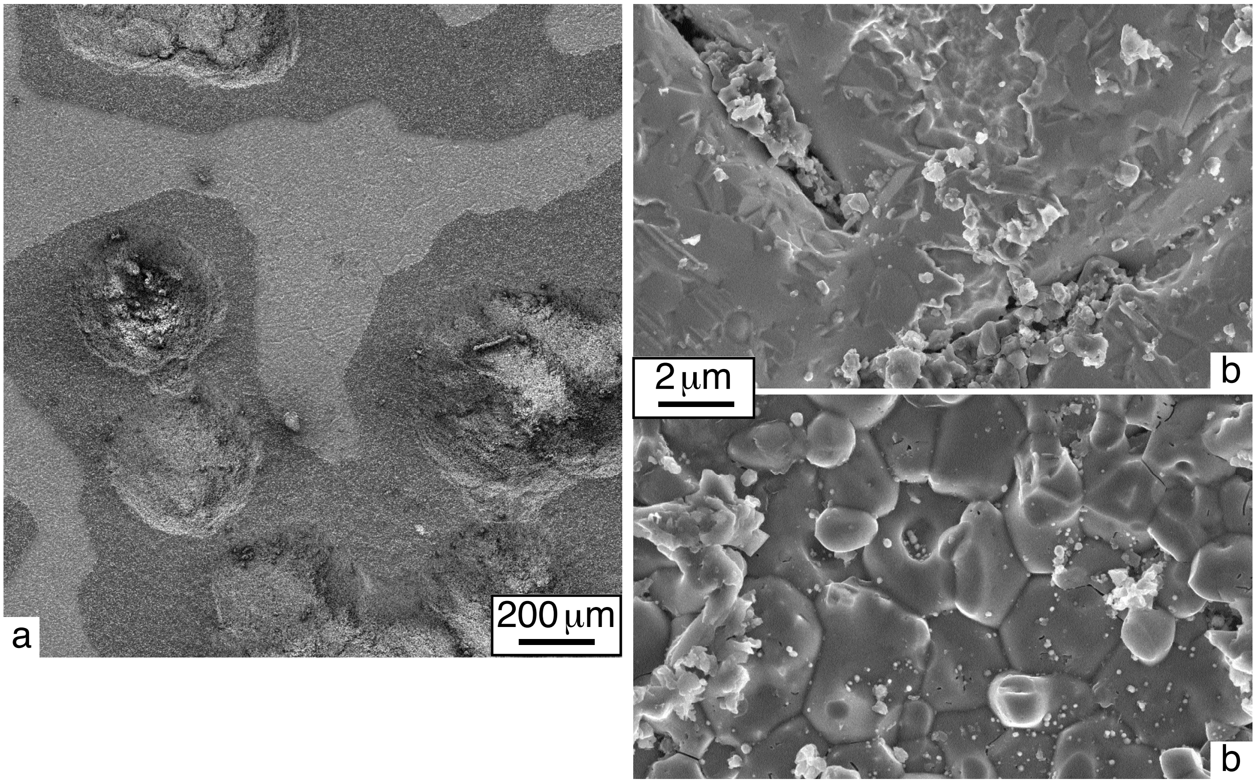

Figure 6. SEM plan view images of the reaction product on PM FeCrAl after exposure to Pb-17Li at 800°C for 1,000h, higher magnification in (b) shows bare metal revealed by spallation and in (c) the morphology of the $LiAlO_2$ surface layer.

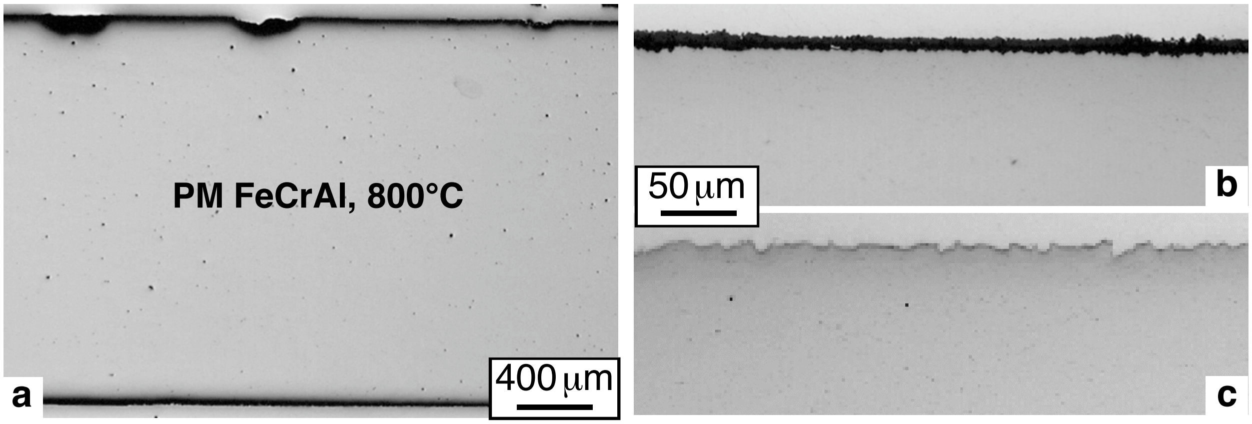

Figure 7. Light microscopy of polished cross-section of PM FeCrAl exposed for 1,000h at 800°C to commercial purity Pb-Li, (b,c) are higher magnification showing areas with and without surface oxide.

polished cross-section, Figure 7a. At higher magnification, some areas showed a uniform surface oxide, Figure 7b, whereas in other areas the $LiAlO_2$ layer had spalled. The cross-section was examined by EPMA but no composition gradients were observed beneath the surface, including Al.

Finally, Figure 8 shows the oxide layer remaining on the pre-oxidized specimens, NiAl+Hf and ODS FeCrAl (Plansee alloy PM2000) exposed at 800° and 700°C, respectively. Both specimens initially had a layer of α-Al_2O_3 on surface before exposure. After exposure, both oxide layers had transformed to $LiAlO_2$.[7] As this has already been studied by TEM for ODS FeCrAl exposed at 800°C,[8] further characterization of these specimens does not appear to be necessary. For ODS FeCrAl, a prior Pb-Li exposure at 700°C showed a slightly higher mass loss when the specimen was not pre-oxidized, Table I. This result suggests that pre-oxidation reduces dissolution. However, the previous exposure also used high purity Pb and Li which may have altered the result.

To follow up on these results, a new series of capsule experiments is being assembled for exposure beginning in January 2009, Table 2. The performance of uncoated and aluminized T92 will be examined at 600°C to determine the protective behavior of the coating and measure the Al loss from the coating after exposure. Additional aluminized T92 specimens will be exposed at 700°C in order to examine (1) the effect of pre-oxidation on coating behavior and (2) the effect of O content in the Pb-Li on oxide formation. In order to reduce the O content of the Pb-Li, ~1g of Zr chips will be added to the capsule. A lower O content may inhibit the surface oxide layer from forming. The effect of Li on the surface product will be studied in the last two capsule experiments. Aluminized T92 will be exposed to unalloyed Pb with no Li addition in order to study the phase of the reaction product. Pre-oxidized ODS FeCrAl will be exposed at 500°C to see if the transformation of α-Al_2O_3 to $LiAlO_2$ occurs at 500°C.

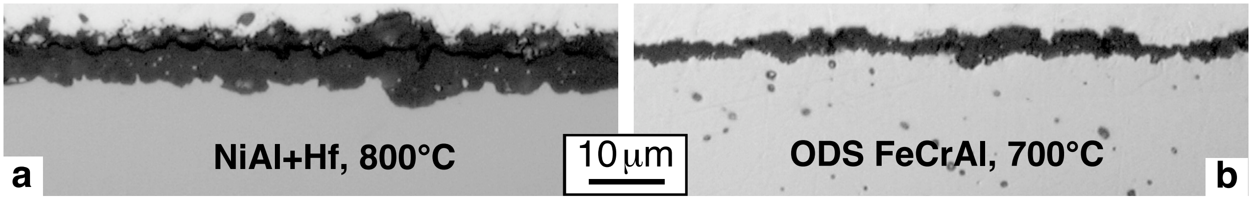

Figure 8. Light microscopy of polished cross-section of pre-oxidized specimens exposed for 1,000h to commercial purity Pb-Li, (a) Ni-42Al+Hf at 800°C and (b) ODS FeCrAl at 700°C.

Table 2. Experiment plan for next series of 1000 h Mo capsules begun in January 2009

Specimen	Pre-oxidation	Temperature	Purpose
T92	none	600°C	Baseline data
Aluminized T92	none	600°C	Effect of coating at 600°C
Aluminized T92	none	700°C	Add Zr, create low O PbLi
Aluminized T92	2h at 800°C	700°C	Determine effect of pre-oxidation
Aluminized T92	none	700°C	Expose to unalloyed Pb
ODS FeCrAl	2h at 1000°C	500°C	Check oxide transformation at 500°C

References

[1] M. Abdou, D. Sze, C. Wong, M. Sawan, A. Ying, N. B. Morley and S. Malang, Fus. Sci. Tech., 47 (2005) 475.

[2] J. E. Battles, Intern. Mater. Rev. 34 (1989) 1.

[3] P. Hubberstey, J. Nucl. Mater. 247 (1997) 208.

[4] S. Ukai and M. Fujiwara, J. Nucl. Mater. 307 (2002) 749.

[5] B. A. Pint, J. L. Moser and P. F. Tortorelli, J. Nucl. Mater. 367-370 (2007) 1150.

[6] B. A. Pint, Fus. Sci. Tech. 52 (2007) 829.

[7] B. A. Pint, DOE/ER-0313/44 (2008) 67.

[8] B. A. Pint and K. L. More, J. Nucl. Mater. 376 (2008) 108.

[9] Y. Zhang, B. A. Pint, K. M. Cooley and J. A. Haynes, Surf. Coat. Tech. 200 (2005) 1231

[10] Y. Zhang, B. A. Pint, K. M. Cooley and J. A. Haynes, Surf. Coat. Tech. 202 (2008) 3839.

[11] Y. Zhang, A. P. Liu and B. A. Pint, Mater. Corr. 58 (2007) 751.

[12] J. Konys, W. Krauss, Z. Voss and O. Wedemeyer, J. Nucl. Mater., 367-370 (2007) 1144.

[13] B. Jönsson, R. Berglund, J. Magnusson, P. Henning and M. Hättestrand, Mater. Sci. Forum, 461-464 (2004) 455.

IRRADIATION EFFECTS ON DIELECTRIC MIRRORS IN INERTIAL FUSION POWER REACTOR APPLICATION

L. L Snead, K. Leonard, and G. E. Jellison Jr.[1]
Mohamed Sawan[2]
Tom Lehecka[3]

[1]*Materials Science and Technology Division, Oak Ridge National Laboratory.*
Oak Ridge Tennessee, SneadLL@ORNL.gov
[2]*Fusion Technology Institute. University of Wisconsin. Madison. Wisconsin. Sawan@engr.wisc.edu.*
[3]*Penn State E-O Center. Penn State University. Freeport, PA 16229. TLehecka@eoc.psu.edu.*

OBJECTIVE

The objective of this work is to experimentally screen the irradiation stability of dielectric mirrors against an inertial fusion application, specifically the High Average Power Laser Program.

SUMMARY

This paper discusses the neutron exposure expected in the HAPL dielectric mirrors and an experimental program comprised of fabrication of advanced dielectric mirrors and testing of these mirrors exposed to prototypical irradiation environment. Specifically, three dielectric mirror types were fabricated to reflect in the KrF laser wavelength of 248 nm and these mirrors irradiated at ~ 175°C in the dose range of 0.001 to 0.1 x 10^{25} n/m^2 (E>0.1 MeV.) This dose range spans the range calculated with a recently developed 3-D Monte Carlo code. Mirrors were visually inspected following irradiation and reflectivity and laser induced damage threshold measured. All mirrors were intact following irradiation and did not appear to degrade significantly either in reflectivity or damage threshold. This finding is somewhat in contradiction to earlier work on dielectric mirrors, which suggested poor performance of dielectric mirrors at an order of magnitude lower neutron dose. Moreover, the current finding suggests the possibility for using dielectric mirrors to much high dose levels.

PROGRESS AND STATUS

`

I. APPLICATION OF DIELECTRIC MIRRORS IN THE HAPL PROGRAM

The High Average Power Laser (HAPL) program aims at developing laser inertial fusion energy based on direct drive targets and a dry wall chamber. [1] Power plant designs are assessed with 350 MJ yield targets driven by forty KrF gas (or Diode Pumped Solid State) laser beams at 5 Hz repetition rate. The final optics system that focuses the laser onto the target includes grazing incidence metallic mirrors (GIMM) located at 24 m from the target with 85° angle of incidence. A focusing dielectric mirror (M2) and a plane dielectric turning mirror (M3) to direct and focus the incoming laser beam. The turning mirror is inclined at a 45° angle relative to the laser beam. The optical beam cross section is rectangular, with a high aspect ratio of 6. The dielectric mirrors are placed out of the direct line-of-sight of the target. However, secondary neutrons resulting from interactions of the streaming source neutrons with the GIMM and the containment building can result in significant flux at the dielectric mirrors. The GIMM is embedded within the biological shield and neutron traps are utilized directly behind the GIMM and M2 in the concrete shield, as shown in Figure 1, to reduce neutron streaming through the beam line.

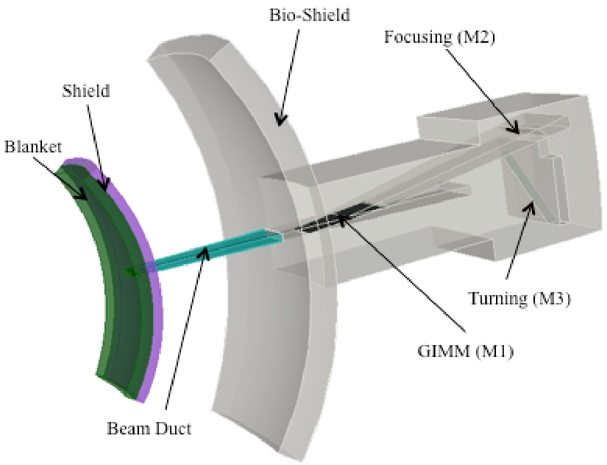

Figure 1. Schematic 3-D image for HAPL final optics.

As part of the HAPL program a robust program has been underway to develop GIMM options, which are currently focused on the alloyed aluminum system[2]. These efforts have included selection of optimized materials systems, determination of the laser induced damage threshold (a function of the deposited heat), and the effect of surface dust and debris on long-term performance of the mirrors. More recently, multilayered dielectric mirrors have been explored as a possible lower fluence, higher reflectivity option. The remainder of this paper discusses issues related an irradiation performance study of dielectric mirrors for the HAPL program.

II. NUCLEAR ENVIRONMENT FOR HAPL OPTICS

Three-dimensional (3-D) neutronic calculations were carried out using the recently developed DAG-MCNP Monte Carlo code [3] that allows calculations to be performed directly within the CAD model. The impact of the GIMM design options on neutron streaming and nuclear environment at the dielectric final optics was thereby assessed. [4] Three substrate materials, SiC and the Al alloys AlBeMet162 and Al-6061 for the GIMM were considered. The SiC GIMM with foam density factor of 0.125 was found to yield the lowest flux values at the dielectric mirrors with the AlBeMet GIMM yielding a factor of 1.6 higher values. The fast neutron flux decreases by about two orders of magnitude as one moves from the GIMM to the focusing mirror with an additional two orders of magnitude attenuation at the turning mirror accompanied with significant spectrum softening. The fraction of the neutrons above 0.1 MeV changes from 97% at the GIMM to 86% at M2, and 41% at M3.

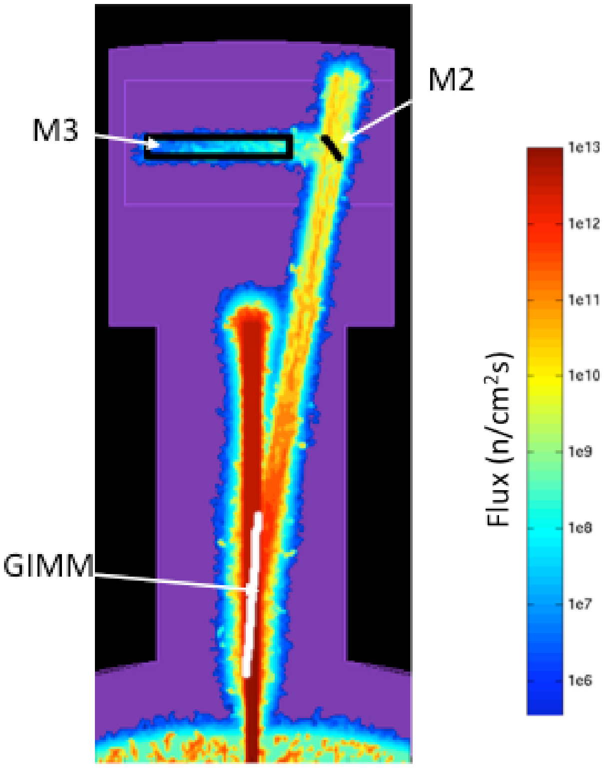

Figure 2. Fast neutron flux distribution in the final optics system.

Figure 2 gives a high-resolution map of the fast neutron flux (E>0.1 MeV) along the beam line for the SiC GIMM design option with 0.125 foam density factor. The fast neutron flux is reduced significantly at the turning mirror M3 due to the sharp bend in the penetration at M2 and utilizing a neutron trap behind M2. Table I gives the highest fast neutron fluence per full power year (FPY) in the GIMM and dielectric mirrors. For a plant lifetime of 30 FPY, the values for fast neutron fluence at the dielectric mirrors M2 and M3 are $2.2x10^{23}$ n/m^2 (~0.022 dpa) and $4.1x10^{21}$ n/m^2 (~0.00041 dpa). The GIMM is expected to be replaced every 2 FPY with fluence level of $9x10^{24}$ n/m^2 (~0.9 dpa).

Table I. Fast neutron fluence per FPY at final optics

	Fast Neutron Fluence per FPY (m^{-2} per FPY)
GIMM (M1)	$4.54x10^{24}$
Focusing Mirror (M2)	$7.18\ x10^{21}$
Turning Mirror (M3)	$1.37x10^{20}$

III. EXPERIMENTAL

III.A Materials and Irradiation

Dielectric mirrors consisting of alternating layers of Al_2O_3/HfO_2, HfO_2/SiO_2, and SiO_2/Al_2O_3 were deposited on sapphire substrates through electron-beam vapor deposition with ion assist by Spectrum Thin Films, Inc. In addition to the mirrors, single layer coatings were deposited onto sapphire substrates for later evaluation of the substrate/film interfaces. The dielectric mirrors were designed for maximum reflectance at a wavelength of 248 nm and consisted of ¼ l thick films of 36, 27 and 40 nm for the Al_2O_3, HfO_2 and SiO_2 layers respectively. The mirrors consisted of 14 bi-layers for the Al_2O_3/HfO_2 mirrors, 11 for the HfO_2/SiO_2 and 26 bi-layers SiO_2/Al_2O_3 mirrors. Sapphire substrates of 6 mm diameter by 2 mm thick were used having a surface roughness less than 1.0 nm with 10/5 scratch dig value over sample and a surface figure of l/10.

Samples were irradiated in the hydraulic tube facility of the High Flux Isotope Reactor (HFIR) at ORNL. The neutron flux for the position utilized was $1.7x10^{19}$ n/m^2-s (thermal) and $5.8x10^{18}$ n/m^2-s (E>0.1 MeV). The mirrors, single layer coating samples and substrate-only samples were encapsulated in specially designed 1100 grade aluminum holders that secure the samples in position by their edges to prevent damage to the optical surfaces. At each irradiation condition three of each mirror type and a single bar (0.3 x 0.3 x 2 cm) of GE-124 fused silica was irradiated. An illustration of the holder containing the mirror samples only is shown in Figure 3. The samples were sealed under ultra high purity Helium gas. Each capsule contained a SiC bar forced in contact with the backside of the sample used to determine the irradiation temperature, post-irradiation. The technique used to determine irradiation temperature from these monitors was the change in electrical resistivity upon isochronal annealing.[5] Samples were irradiated to doses of 10^{22}, 10^{23} and 10^{24} n/m^2 (E>0.1 MeV) corresponding to approximate displacement doses of 0.001, 0.01 and 0.1 dpa. This conversion is typical for ceramic materials and assumes sublattice-average displacement energy of 40 eV. [6] From analysis of the temperature monitors the mirror temperature during irradiation was determined to be in the approximately 175°C.

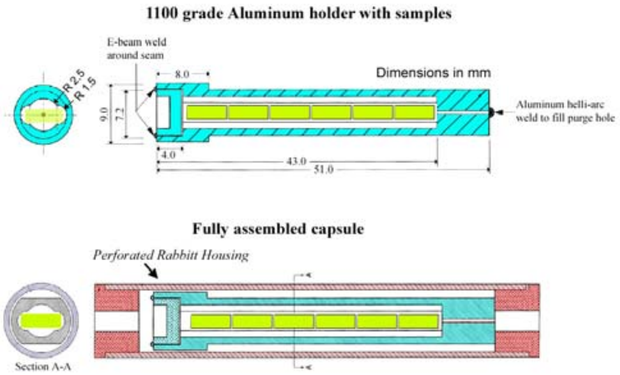

Figure 3. Schematic of HFIR irradiation capsule containing six mirror samples. Capsule design containing GE-124 bar not shown.

Vacuum annealing treatments at 300 and 400°C were conducted on the irradiated mirrors following initial optical testing. Samples were heated at 3º/minute to temperature and held for 1.5 hours under $< 1x10^{-6}$ torr followed by furnace cooling.

Laser induced damage threshold was measured was measured using the system transported from the Penn State EOC and installed into the LAMDA facility at ORNL and depicted in Figure 4. It was comprised of a GAM Laser operated at the KrF frequency of 248 nm with an ~ 130 mJ/puls output, ~ 18 ns pulse length and d125 Hz maximum rep rate. The position of the lens, along with the laser energy, is use to determine the ultimate energy to the dielectric mirror sample as shown in Figure 5. Due to beam non-uniformities at the 0, 10 and 20 mm focal position only focal distances greater than 30 mm were considered for this work.

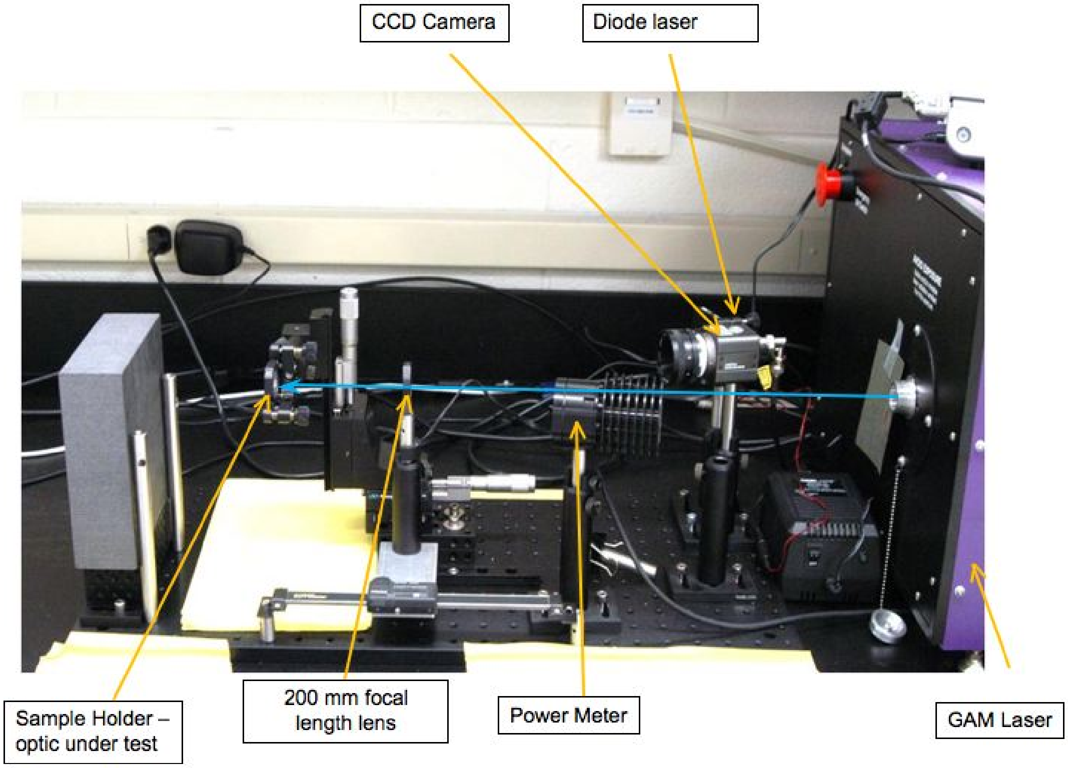

Figure 4. Bench-top set-up of LIDT measurement equipment temporarily installed by Tom Lahecka in the LAMDA facility at ORNL.

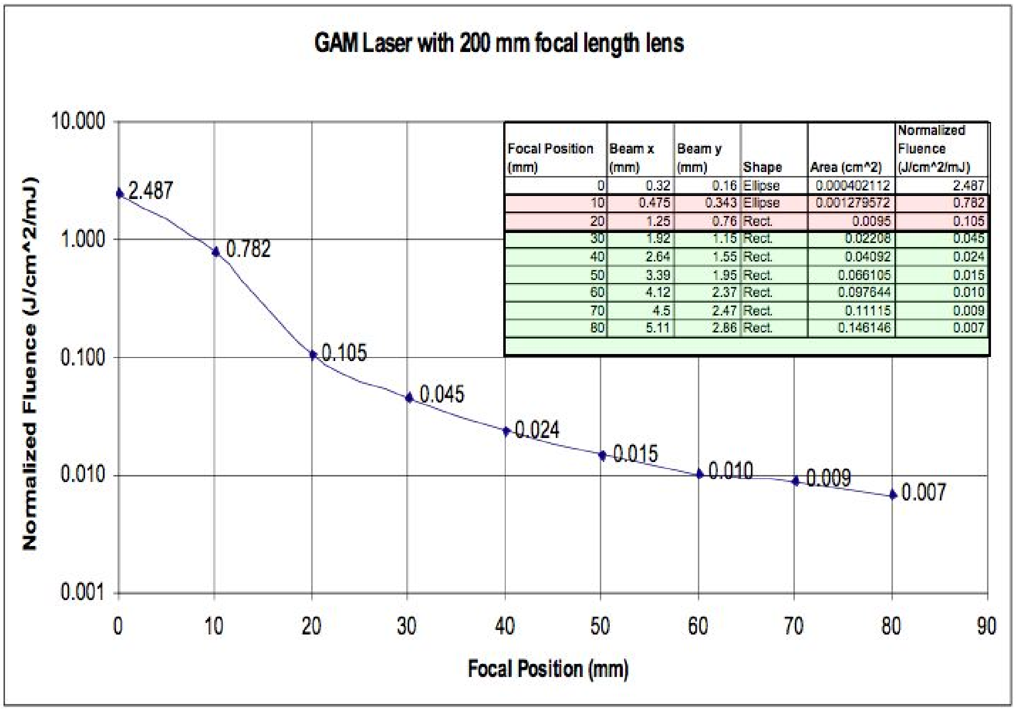

Focal Position (mm)	Beam x (mm)	Beam y (mm)	Shape	Area (cm^2)	Normalized Fluence (J/cm^2/mJ)
0	0.32	0.16	Ellipse	0.000402112	2.487
10	0.475	0.343	Ellipse	0.001279572	0.782
20	1.25	0.76	Rect.	0.0095	0.105
30	1.92	1.15	Rect.	0.02208	0.045
40	2.64	1.55	Rect.	0.04092	0.024
50	3.39	1.95	Rect.	0.066105	0.015
60	4.12	2.37	Rect.	0.097644	0.010
70	4.5	2.47	Rect.	0.11115	0.009
80	5.11	2.86	Rect.	0.146146	0.007

Figure 5. Normalized laser fluence as a function of focal position.

III.B Results

The irradiated capsules were disassembled and dielectric mirrors, SiC thermometry, and fused silica bars removed for inspection and analysis. Samples were cleaned in isopropyl alcohol to remove any debris resulting from the capsule disassembly process. Dielectric mirrors showed no visible signs of surface abrasion, film delamination, cracking, or pitting following irradiation and handling. Figure 6 gives an example of the condition of the mirrors in the control and irradiation condition as a function of the vacuum anneal. The mirrors on the left are tilted so the smooth surfaces reflect the overhead (visible spectrum) lighting to reveal the integrity of the films. Upon irradiation the samples as visualized in the “flat” condition have an apparent darkening which increases with increasing neutron dose. Annealing of the irradiated materials at 300 and 400ºC for 1.5 hrs resulted in a reduction in the irradiation-induced darkening. These observations were consistent for all mirrors studied and reproducible for the triplicate-irradiated mirrors. A slight speckling was observed in some of the mirror surfaces following annealing, however, this appeared randomly in the visual observation and showed no specific trend with regards to mirror type, dose or thermal treatment.

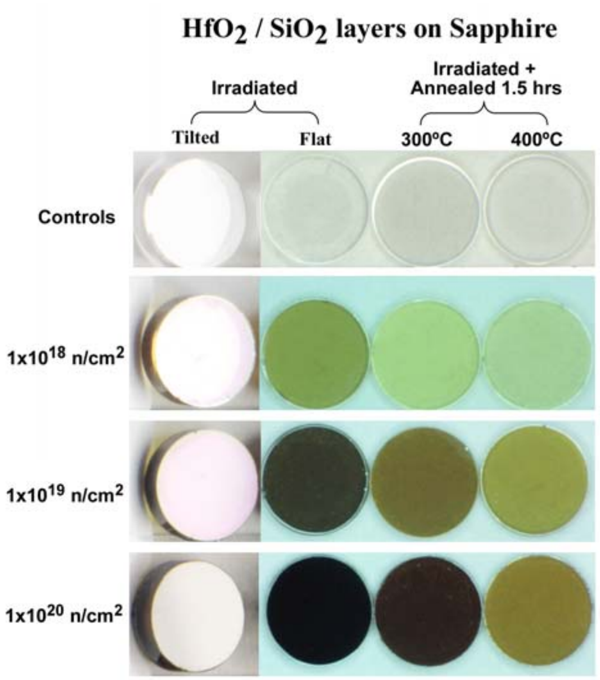

Figure 6. Optical inspection of HfO_2/SiO_2 mirrors in the non-irradiated and neutron irradiated condition as a function of post-irradiation annealing temperature.

The GE-124 fused silica bar samples also underwent a slight discoloration with irradiation, though the darkening was not as pronounced as in the mirror samples of figure 6. Results on the densification of the fused silica irradiated in this experiment is shown in Figure 7 for each irradiation dose. For the upper dose of this study (1e25 n/m2) the material underwent a 2.26% compaction. While this data set data is limited, the rate of compaction has dramatically slowed and perhaps reached a saturation level at the uppermost dose level. As will be discussed later, saturation in compaction for amorphous silica at this dose is expected.

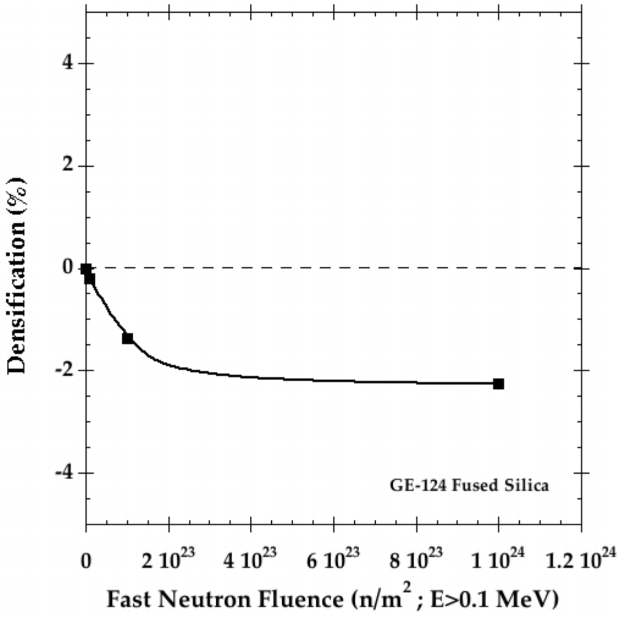

Figure 7. Densification of GE-124 fused silica irradiated with dielectric mirrors.

Results on the relative dielectric mirror reflectance are given in Figures 8, 9, and 10, for the Al_2O_3/SiO_2, HfO_2/SiO_2, HfO_2/Al_2O_3 mirrors respectively. It is stressed that this is relative reflectance. Due to the size of the sample and the preliminary nature of the study the absolute reflectance of the mirrors is not known at the time of this publication. Measurement of absolute reflectance of these mirrors is ongoing. As will be seen later, it is likely that these mirrors are well short of the ideal >99% reflectance. Figures 8-10 are normalized to each other specifically to demonstrate the frequency response. By inspection of these figures, a real shift in the working range (flat top) occurred. The direction of this shift was towards lower wavelengths with increasing irradiation dose. It is noted that the HfO_2/Al_2O_3 mirrors were fabricated out of specification, with its working range below the 248 nm specified. However, this is not thought to impact the general findings of this paper.

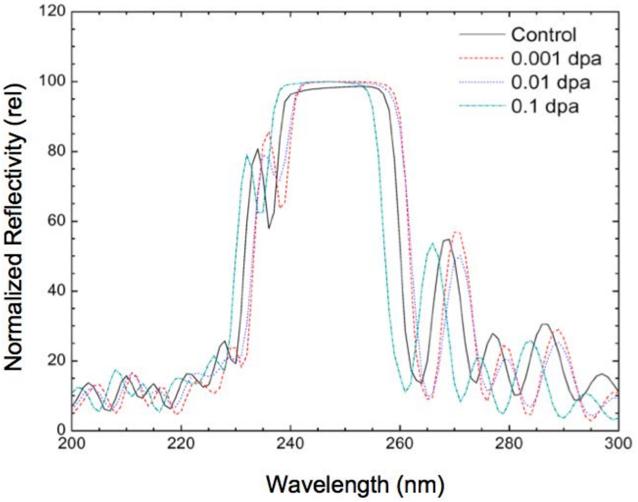

Figure 8. Effect of neutron irradiation on the relative reflectance of Al_2O_3/SiO_2

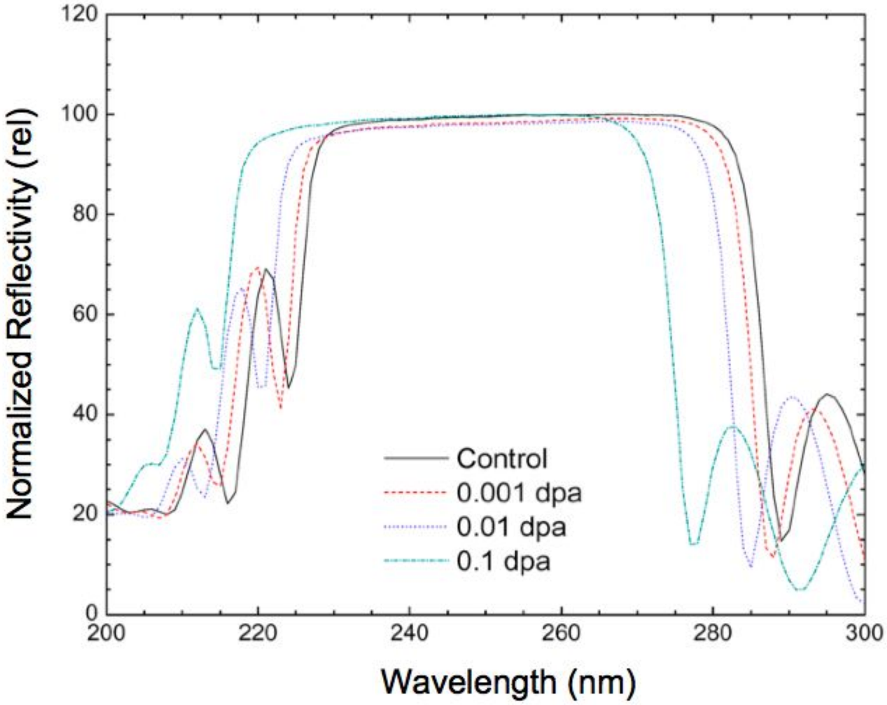

Figure 9. Effect of neutron irradiation on the relative reflectance of HfO_2/SiO_2.

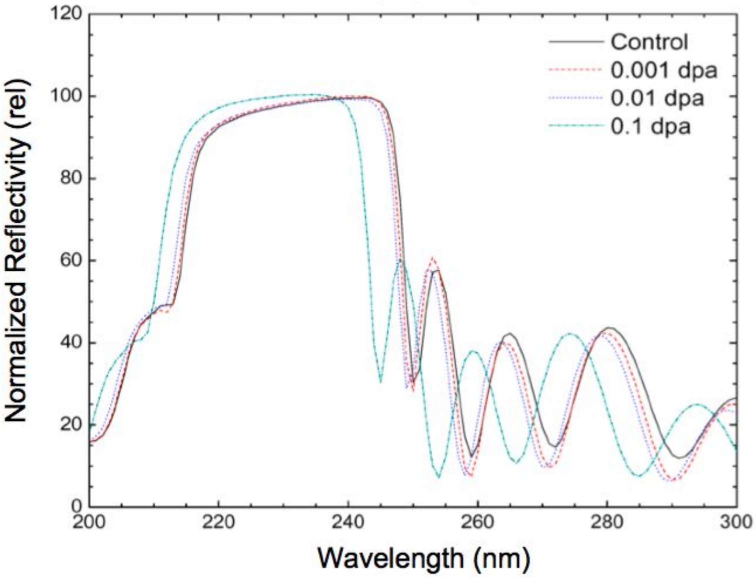

Figure 10. Effect of neutron irradiation on the relative reflectance of HfO_2/Al_2O_3.

Each of the mirror types were annealed in vacuum and visually inspected. Following annealing, no apparent change occurred, though a minor frequency shift in the working range did occur.

Testing of laser induced damage threshold was carried out on all non-irradiated mirrors and a complete series of as-irradiated alumina/silica mirrors. With this set-up an estimate of the reflectivity was also possible. It was found that both the hafnia/silica and hafnia/alumina mirror has very low laser induced damage thresholds in the virgin condition and therefore not tested in the irradiated condition. Moreover, the *approximate* reflectance of these mirrors was also unacceptably low. However, the alumina/silica mirror did have fairly good approximate reflectance (see Table II) and the reflectivity did not apparently degrade as a function of irradiation. As seen in Table III the laser induced damage threshold (LIDT) for the hafnia/silca and hafnia/alumina mirrors was less than 1 J/cm^2 , which is considered a target value for the HAPL program. However, the alumina silica mirrors behaved in both the non-irradiated state (LIDT>1 J/cm^2) and did not appear to degrade upon irradiation. It is important to note that these tests were carried out on a single sample and therefore any conclusions are statistically limited.

Table II. Results of reflectivity using the LIDT set-up.

Mirror	**Reflectance**				**Note**
	Virgin	**0.001 dpa**	**0.01 dpa**	**0.1 dpa**	
Control Mirror	93%	NA	NA	NA	Spectrophotometer measured R form company was 99.7%
HfO_2/SiO_2	41%	NT	NT	NT	Possible damage before reflectivity measurement completed
HfO_2/Al_2O_3	52%	NT	NT	NT	Possible damage before reflectivity measurement completed
Al_2O_3/SiO_2	86-87%	84-86%	78-83%	80-84%	

NA: not applicable; NT: not tested

Table III. Results of laser induced damage threshold

Mirror	**Laser Induced Damage Threshold**				**Note**
	Virgin (J/cm^2)	**0.001 dpa**	**0.01 dpa**	**0.1 dpa**	
Control Mirror	0.9<d<1.2	NA	NA	NA	Agrees with standard
HfO_2/SiO_2	d<0.43	NT	NT	NT	Clearly damaged before alignment completed at lowest fluence available (80 nm, 11kV)
HfO_2/Al_2O_3	d<0.9	NT	NT	NT	Appeared to survive alignment, but damaged at 80 nm, 16 kV
Al_2O_3/SiO_2	1.3<d<1.95	1.3<d<1.95	1.2<d<1.3	1.2<d<1.3	Both non-irradiated and 0.001 dpa damaged after ~ 10 second at fluence listed (50 nm). 0.01 and 0.1 damaged after ~ 60 seconds at the high fluence.

NA: not applicable; NT: not tested

IV. DISCUSSION

By alternating thin transparent dielectric materials of differing refractive index this class of mirror can be capable of reflecting greater than 99% of incident laser light. This is in contrast to GIMM's, which typically range from <40% reflectivity in the UV range (for silver or gold) to as high as 80-90% for the HAPL candidate aluminum alloy system.

Unfortunately, the early work on the neutron irradiation of dielectric mirrors by Farnum et al. [7] was not encouraging. For the long-wavelength mirrors of his work, DC magnetron sputtered bi-layers of hafnia/silica, zirconia/silica, and titania/silica were deposited onto silica substrates. In each case the thickness of the layers ranged from 332-642 nm, or about and order of magnitude thicker than those of this study. The spallation neutron producing LASREF facility was used to produce uniform displacement damage through the mirrors for a reported irradiation temperature of 270-300°C as inferred from a similar capsule design. The reported total integrated neutron fluence was 1.1×10^{23} n/m^2. In addition to the neutron dose, Farnum reports an associated gamma dose of 1.1×10^9 Gy. While Farnum did not report on reflectivity of his long-wavelength mirrors he did report that three of the five mirrors suffered either film crazing or total film flaking, with the fourth possibly suffering film damage as well. One mirror, a TiO_2/SiO_2 plate polarizer did not show visible degradation.

The neutron dose of the Farnum work was of similar magnitude to the HAPL M3 mirror (2.2×10^{23} n/m^2, see Section II,) and for this reason the seemingly negative results of his work were of concern. However, more recent work in support of the ITER diagnostic program[8,9] for similar dose appeared more promising. Specifically, Orlovskiy[9] reports on multilayer dielectric mirrors deposited by evaporation on the high-purity KS-4V silica glass. The bi-layers chosen were titania/silica and zirconia/silica. At the lower irradiation dose of that study (1×10^{21} n/m^2, E>0.1 MeV) neither mirror type exhibited visible damage. For the higher irradiation dose (1×10^{23} n/m^2 , E>0.1 MeV) only the titania/silica mirror was irradiated. The reported irradiation temperature was "near ambient water temperature 50°C." This higher dose irradiated mirror showed no visible signs of irradiation damage and no reduction in spectral reflection, though did show a movement in the working range to lower wavelengths similar to that seen in the current study.

Given that the mirrors of the present study have not indicated any visible degradation (film decohesion) or spectral reflectivity degradation, there is a clear trajectory of improvement in these materials from the work of Farnum (0.01 dpa, visible film degradation), to Orlovskiy (0.01 dpa, no visible or spectral reflectance degradation for titania/silica), to this work (0.1 dpa, no decohesion or spectral reflectance degradation for a range of materials.)

When considering the irradiation effects in high quality dielectric mirrors, the three most likely effects of irradiation are:

- altered refractive index of material.
- altered thickness of layers.
- interfacial stress due to differential swelling in layers or between layers and substrate.

The first and second points will primarily impact the reflection but will also influence the working range of the mirror. Unfortunately, there is not a large body of work on the effect of irradiation on the optical properties of many of the materials comprising these dielectric mirrors. For instance there is essentially no information on the effects of neutrons on swelling or optical properties of hafnia. However, there is information on silica and alumina to draw on. For the case of silica (amorphous SiO_2, like the SiO_2 bilayers of all materials discussed here and the KS-4V glass of the Orlovskiy work and the substrate of the Farnum work) irradiation causes pronounced densification.[10,11] In the current work this is demonstrated in the densification of the GE-124 fused silica (see Figure 7.) Previously, Primak[10] demonstrated that the refractive index is proportional to silica densification following a general Lorentz law. Primak showed that a nominal change in 2% density of silica resulted in about a 0.75% change in refractive index. Unfortunately, the irradiation-induced refractive index of the other mirror materials used in the present study is not known. However, there is a body of work on alumina swelling. It is clearly understood that polycrystalline Al_2O_3 (one of the bilayers for this study), and single crystal Al_2O_3 (the substrate for this study) will both undergo volumetric expansion under neutron irradiation. At the irradiation temperature for which dielectric mirrors are to be used this swelling is caused by point defect strain within the crystal and is a function of both irradiation temperature and dose. A comparison of the expected swelling of polycrystalline (which closely matches single crystal) alumina[12] is given in Figure 11 along with the GE-124 fused silica. It is noted that the microstructure of the Al_2O_3 bilayer of this study has not been characterized though is assumed to be microcrystalline, low-density Al_2O_3 typical of other optical grade alumina.

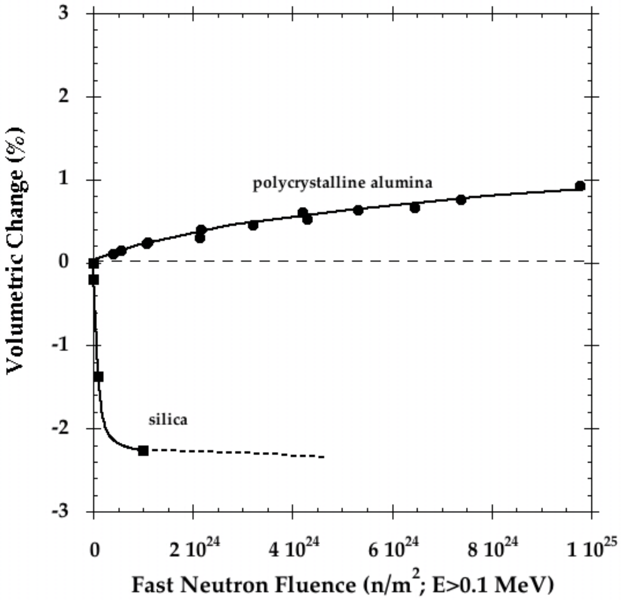

Figure 11. A comparison of literature data on swelling in polycrystalline alumina with compaction in GE-124 fused silica.

The behavior shown in Figure 11 underlines a potential issue facing the dielectric mirrors. In both of the previous studies discussed the substrates used were amorphous silica, and both combined ceramic and amorphous silica as the bi-layers. As these mirrors are irradiated, differential dimensional change (as example, Figure 11) of constituents can result in an stress buildup within the multilayers whose magnitude is a competition between the rate of irradiation-induced differential swelling and the rate at which irradiation-induced creep can mitigate the developing stresses. Reduced viscosity (essentially irradiation-creep) due to displacive irradiation is known to occur in glassy materials, with the first discussion of this phenomenon reported as early as 1960 (Mayer, 1960.) A clear indication of the significant effect irradiation can have on the viscosity of glass is given by Zhu (Zhu, 1994), who irradiated Herasil 1 with 10 MeV protons in the temperature range of 220°C to 600°C. The dose rate for these experiments was 2.3×10^{-7} dpa/s, which compares well with the displacement rate of this study (5.8×10^{-7} dpa/s.) The Herasil 1 silica was tested in tension during irradiation in the applied load range of 5-100 MPa with the sample initially undergoing a rapid reduction in length due to the irradiation-induced silica compaction. Following this, sample elongation due to irradiation-reduced viscosity was clearly observed. While the experiment was carried out at a few hundred degrees, the irradiation-reduced viscosity was equivalent to thermally-induced viscosity of ~ 1200°C. In other words, the displacive irradiation reduced the silica viscosity by several orders of magnitude to a value of ~ 10^{13} Pa-s. This level of viscosity is associated with the annealing point (point at which internal stress is relieved in ~ 15 minutes.) Irradiation-creep has been seen in crystalline ceramics such as SiC[13]though the report by Zhu which documented enhanced viscosity in silica did not find evidence for irradiation creep in Al_2O_3 or SiC. At least for those experimental conditions vitreous silica was more capable of deformation under applied strain during irradiation.

While there is only limited information on irradiation-reduced viscosity in silica and irradiation-creep in ceramics, from those findings it is a reasonable conclusion that closely matching the irradiation-induced dimensional change of the mirror substrate with the non-silica constituent of the multilayer mirror is prudent. While silica appears to be more capable of response to applied stress than the ceramic materials, the fact that the substrate is so much thicker than the coatings, if the substrate was silica its densification would dominate, possibly resulting is large stresses in combination with the ceramic bilayers. Therefore, a matched substrate and ceramic layer with a more compliant silica layer (or a paired ceramic layer) may prove more resistant to irradiation.

For the case of the Farnum[7] mirrors, which consisted of much thicker bi-layers and a larger cool-down temperature from irradiation as compared to the current work or that of Orlovskiy, a larger induced stress would be expected, possibly explaining the resulting mirror failures. Upon annealing the irradiation-densified silica, or irradiation-swollen ceramics, the material is restored to near original density. For glass the relative recovery is proportional to annealing temperature, with glass exhibiting near complete restoration by ~ 1100°C,[10] while for alumina requires a somewhat higher annealing temperature (~1400°C.) [14] For the case of the silica/alumina mirror of this study, the 400°C vacuum anneal would have resulted in an *expansion* of silica of about 0.1% and an alumina *contraction* of about 0.02%.[10,14] (This assumes the behavior of the mirror bi-layers is similar to that of the fully dense materials.) For these post-irradiation annealing experiments the annealing temperatures are such that no thermal creep should have taken place, and with the absence of irradiation the result would be an increases stress similar to the stress which would occur due to the mismatch in coefficients of thermal expansion.

V. CONCLUSIONS

A series of neutron irradiations have been carried out on multilayer dielectric mirrors deposited by electron beam vapor deposition on sapphire substrates designed to operate in the KrF wavelength range of 248 nm. Multilayer combinations included the glass/ceramic combinations of silica/alumina and silica/hafnia as well as the ceramic/ceramic combination alumina/hafnia. Irradiations were carried out to a maximum dose of 0.1 dpa, corresponding to dielectric mirror fluence greater than currently considered for the High Average Power Laser inertial fusion power application.

All three mirror combinations survived the neutron irradiation without visible degradation. A shift in working range towards lower wavelength occurred upon irradiation becoming more pronounced with higher fluence. However, at the maximum dose of this study, 0.1 dpa, the shift was relatively minor, on the order of 10 nm.

The mirrors were vacuum annealed in the non-irradiated and irradiated condition to determine the integrity of the inter-layer strength and to determine whether significant irradiation-induced residual stress was present. Visual inspection of mirrors following annealing indicated no apparent film degradation. All mirrors were screened for laser induced damage threshold. The alumina/hafnia and silica/hafnia mirror had very poor LIDT as well as apparent reflectivity. However, the alumina/silica mirror had both good reflectivity and LIDT in the virgin condition, but retained these acceptable properties upon irradiation. The results of this study offer a clear improvement in mirror performance over previous dielectric mirrors studied under neutron irradiation. The superior performance is tentatively attributed to the selection of a more irradiation stable substrate (sapphire,) and the selection of very thin and very high purity dielectric layers. Moreover, it is speculated that the choice of a mirror substrate whose irradiation-induced changes are closely matched to the behavior of the ceramic components of the mirror leads to a more radiation tolerant system. Further work to better understand the behavior of the microstructures of these materials under irradiation and the study of the developing interlayer stress is anticipated and could lead even greater tolerance of this class of mirrors to neutron irradiation.

ACKNOWLEDGMENTS

The authors would like to thank Joel McDuffee, Bob Sitterson, and Marie Williams for help with construction of the irradiation capsules and Patricia Tedder for assistance with radiological aspects of this work. Irradiations were carried utilizing the High Flux Isotope Reactor, a Department of Energy user facility. This work was funded by the Department of Energy High Average Power Laser Program under a contract to the Oak Ridge National Laboratory. The Oak Ridge National Laboratory is managed by UT-Battelle under contract DE-AC05-00OR22725.

REFERENCES

1. J. D. Sethian, A. R. Raffray, J. Latkowski et al., J. Nuclear Materials **347** (3), 217 (2005).
2. M. S. Tillack and J. E. Pulsifer, Fusion Engineering and Design (submitted 2008).
3. M. Wang, D. L. Henderson, T. Tautges et al., Fusion Science and Technology **47** (4), 1079 (2005).
4. M. Sawan, A. Ibrahim, T. D. Bohm et al., Fusion Engineering and Design **Submitted**.
5. L. L. Snead, A. M. Williams, and A. L. Qualls, presented at the The Effects of Radiation on Materials: 21st International Symposium, 2003 (unpublished).
6. F. W. Clinard, Jr., G. F. Hurley, and L. W. Hobbs, Journal of Nuclear Materials **108&109**, 655 (1982); S. J. Zinkle and C. Kinoshita, Journal of Nuclear Materials **251**, 200 (1997).
7. E. H. Farnum, F. W. Clinard, Jr, S. P. Regan et al., Journal of Nuclear Materials **219**, 224 (1995).
8. K. Vukolov, presented at the 8th Meeting of the ITPO Topical Group on Diagnostics, Culham, 14-18 March 2005, Culham, UK., 2005 (unpublished).
9. I. I. Orlovskiy and K. Y. Vukolov, Fusion Engineering and Design **74**, 865 (2005).
10. W. Primak, Phys Rev **110**, 1240 (1958).
11. T. Yano, K. Fukuda, M. Imai et al., Journal of Nuclear Materials **367-370**, 730 (2007).
12. G.P. Pells, Journal of the American Ceramic Society **77** (2), 368 (1994).
13. Y. Katoh, L. L. Snead, T. Hinoki et al., J. Nuclear Materials **367-370**, 758 (2007).
14. B. S. Hickman and D. G. Walker, Journal of Nuclear Materials **18**, 197 (1966).

MODELLING THERMODYNAMICS OF ALLOYS FOR FUSION APPLICATION -

A. Caro, P. Erhart, M. Serrano de Caro, B. Sadigh (Lawrence Livermore National Laboratory), S.G. Srinivasan, and C. Jiang (LANL). L. Malerba (Belgium), J. Wallenius (Sweden), A. Stukowski (Germany)

OBJECTIVE

This research has two main objectives:

- The development of computational tools to evaluate alloy properties, using the information contained in thermodynamic functions. We aim at improving the ability of classical potentials to account for complex alloy behavior; and,
- The application of these tools to predict properties of alloys under irradiation, in particular the FeCr system.

SUMMARY

We develop a strategy to model radiation damage in FeCr alloys, system in which magnetism introduces an anomaly in the heat of formation of the solid solution that is at the basis of its unique behavior. Magnetism has implications for the precipitation of excess Cr in the *a*' phase in the presence of heterogeneities. These complexities pose many challenges for atomistic (empirical) methods. To address such issues we develop a modified, many-body potential by rigorously fitting thermodynamic properties, including free-energy. Multi-million atom displacement Monte Carlo simulations in the transmutation ensemble, using both our new potential and our new MC code, are able to predict properties of non equilibrium processes like heterogeneous precipitation, and dislocation – precipitate interactions, enabling the study of hardening and embrittlement under irradiation.

Our work aims at developing theoretical and numerical methodologies that are directly applicable to multi-scale modeling addressing the specific issues related to multi-component, multi-phase systems in non-equilibrium states, such as solid-solution hardening, point defect-solute interactions, stoichiometry effects, static and dynamic strain aging, dislocation-solute interactions, and in general the aspects of microstructure evolution that are affected by irradiation. At its present stage of development, we have been able to predict numerous thermodynamic properties of FeCr mainly related to ordering and precipitation; we have found new intermetallic phases and suggested the existence of a dependence of the solubility limit on the degree of order of the alloy. At present, we are studying dislocation mobility in the solid solution and the heterogeneous phase, and we are developing a new algorithm to perform Monte Carlo simulations inside the miscibility gap, a technique that will allow us to study interfacial energies and nucleation sizes.

In collaboration with LANL, we have also studied the structural and elastic properties of cementite (Fe3C) from first principles calculations as a first step in the development of a classical potential for the Fe-C system able to describe the martensitic phase of steels. The paper is published.

In collaboration with European groups (Belgium, Sweden) we have performed a careful comparison between the two existing approaches to model FeCr at the level of interatomic

potentials, namely the European 2 band model and our composition dependent model. The paper is published.

In the algorithm development side, the work of B. Sadigh and P. Erhart on the mathematical formulation of a ‘fluctuation constrained Metropolis Monte Carlo’ has been finished, and with the visit of A. Stukowski from Germany it has just been implemented in Lammps, a free MD code from Sandia. He has also implemented our composition dependent model for molecular dynamics of FeCr into Lammps what makes it available for the community.

PROGRESS AND STATUS

In this report we will describe the work done to determine the influence of short range order (SRO) in the solubility of Cr in Fe, leaving a detailed description of the other subjects reported in the Summary in the corresponding publications.

SRO is an anomaly originated in the negative heat of formation (hof) of this alloy for Cr content below about 5 at%. In this region of composition, and because the negative hof, the mixture is expected to have ordered phases. In the period covered in the last report, we described our search for ordered intermetallic phases. Now we report on our findings regarding how short range order affects the location of the *solvus*, i. e. the solubility limit in FeCr.

By comparing the thermodynamics of the random alloy with the short-range ordered alloy, we extracted the contributions of SRO to the free energy coming from the enthalpy of mixing and from the vibrational and configurational entropies. We conclude that the effects of SRO are significant, doubling the solubility limit of Cr at low temperatures (≈300 K), and that this effect is mainly due to the contribution of SRO to the enthalpy.

We reassessed the previously published phase diagram [1, 2] by explicitly taking into account the effects of SRO on the three functions entering the expression for the free energy, namely, the mixing enthalpy and the vibrational and configurational entropies. We found significant effects of SRO on the location of the *solvus*. We also corrected an error in previous publications [1, 2] regarding the position of the miscibility gap according to the same cohesive model used here.

General methodology

Choice of cohesive model

The evaluation of thermodynamic functions requires information about the dynamical properties of the system, which usually are beyond the capabilities of *ab initio* techniques. Within the latter approach this difficulty is usually addressed by making use of approximations such as the harmonic assumption for vibrational entropies. Here, however, we follow a different strategy which first approximates the energy of the system in terms of a classical interatomic potential for the alloy, and from there the thermodynamic functions are obtained via computational thermodynamics. The interatomic potential for Fe–Cr used in this work, the so-called concentration dependent model (CDM), and the approach to computational thermodynamics are described in detail in [3–8]. There are other cohesive energy models in the literature that, as this one, do not explicitly include magnetism but also reproduce well the Fe–Cr complex behavior. These are a cluster expansion (CE) developed by Lavrentiev *et al* [9] and a two-band model (2BM) interatomic potential developed by Olsson *et al* [10]. The CE involves a cohesive model that is only applicable on a rigid lattice, and thus inherently neglects the effects of relaxations and vibrations, so it is less suitable for the current study. The two interatomic potentials, 2BM and CDM, are ad hoc extensions of the embedded atom method (EAM) [11] where additional parameters describing the local concentration are introduced. Though both models are suitable for the current study, here we opted for the CDM whose predictions of ordering have recently been analyzed by Erhart *et al* [12] as part of the work funded by this program.

Free energy computation

In this work the free energy per particle $F(T)$ at a given temperature T is obtained through a thermodynamic integration between the state of interest and a reference state at temperature $T0$ of known free energy $F(T0)$ [13]. This methodology applied to solids is described by Frenkel and Ladd [31]. Its application to binary disordered solid solutions is explained and used in [4–8]. As a part of this work, modifications to the latter methodology are applied to account for SRO in binary solid solutions.

The configurational entropy per particle, $S\mathrm{conf}(x)$, is usually taken to be that of a perfectly random mixture, as we did in all our previous studies. However, the presence of SRO decreases the configurational entropy becoming one of the factors affecting the free energy that we address in this work.

To take into account the effects of order on the configurational entropy of the alloy, we worked out the connection between SRO and pair-probabilities and the relation between the latter and the entropy.

The methodology presented above has been implemented in a numerical package [4–8], the so-called thermodynamic package (TDP) that calculates the free energy for a certain atomic arrangement of atoms with a given degree of SRO, as a function of temperature.

Pair-probabilities and SRO

To quantify the SRO in the alloy, the Warren–Cowley parameter [14] was introduced as a tool to evaluate the pair-probabilities in an alloy. The SRO parameter, $\eta v\ \alpha$, in the vth nearest neighbor shell for a representative atom of type A in a binary AB alloy is defined. Combining the definition of the SRO parameter with the standard Ising theory for a binary alloy [15, 16], all the pair-probabilities are uniquely defined as a function of concentration and SRO parameter

This result is used below to estimate the configurational entropy For details see [G. Bonny, P. Erhart, A. Caro, R. C. Passianot, L. Malerba, and M. Caro. "The influence of short range order on the thermodynamics of Fe-Cr alloys. In press in Modelling and Simulations in Mat Sci and Eng. (2009)].

Implementation of SRO

Configurational entropy and SRO

The configurational entropy is a measure of the degree of disorder in an alloy. For a binary perfectly random alloy the configurational entropy assumes that all the lattice positions are equivalent and uncorrelated [19]. However, in an alloy with a certain degree of order not all lattice sites are equivalent and a certain degree of correlation exists between lattice positions. In the case of SRO, all lattice positions can be assumed to be equivalent and the correlation between lattice sites decreases fast with increasing distance. The cluster variation method (CVM) provides expressions for the entropy [15, 16, 17], which can take into account non-equivalent lattice sites and correlations up to a certain predefined basic cluster size. Each basic cluster is considered as an uncorrelated independent species, which means that all correlations are described within the basic cluster.

Since we aimed at describing states with a certain degree of SRO, we choose the basic clusters to be pairs. The CVM entropy including pairs up to the *n*th nearest neighbor distance in a bcc lattice is a known analytic function that reduces to the random entropy in the case of the randomly disordered alloy. Note that, for an alloy exhibiting SRO, lattice sites separated by long distances are uncorrelated. For the case under study, we verified that the inclusion of third nearest neighbour pairs modifies the entropy only by 0.005%, confirming the short range of the correlations.

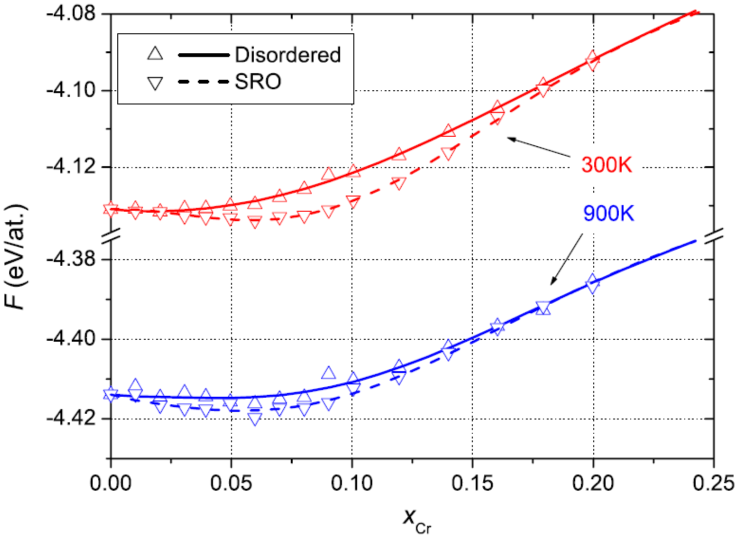

Figure 1: Isotherms of the free energy surface for the SRO and random alloy.

Post-processing

Following the procedure described in the previous section, a free energy surface for the disordered alloy and four free energy surfaces for the runs at 600–900K including a degree of order were obtained. To conveniently post-process the raw data, two Redlich–Kister (RK)-expansions [18] per data set were fitted, valid in the ranges 0–30%Cr and 30–100%, respectively.

The phase boundaries for the phase diagram are easily obtained from the parameterized free energy surfaces using the common tangent method [19]. Application of this method generated four sets of phase boundary curves, valid in the range around 300, 500, 700 and 900 K, for the SRO alloy. These four sets of boundaries are merged into one set of phase boundaries by means of a linear interpolation between two exact isotherms at *T*low and *T*high. Using this interpolation scheme, a phase diagram taking into account SRO is obtained that can be compared with the phase diagram corresponding to the randomly disordered alloy.

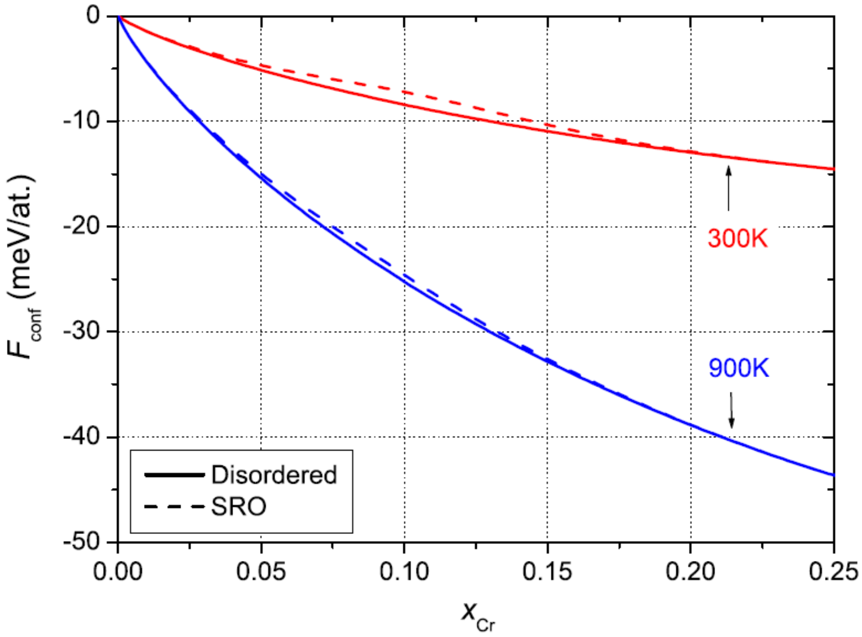

Figure 2: Isotherms of the configurational free energy for the SRO and random alloy.

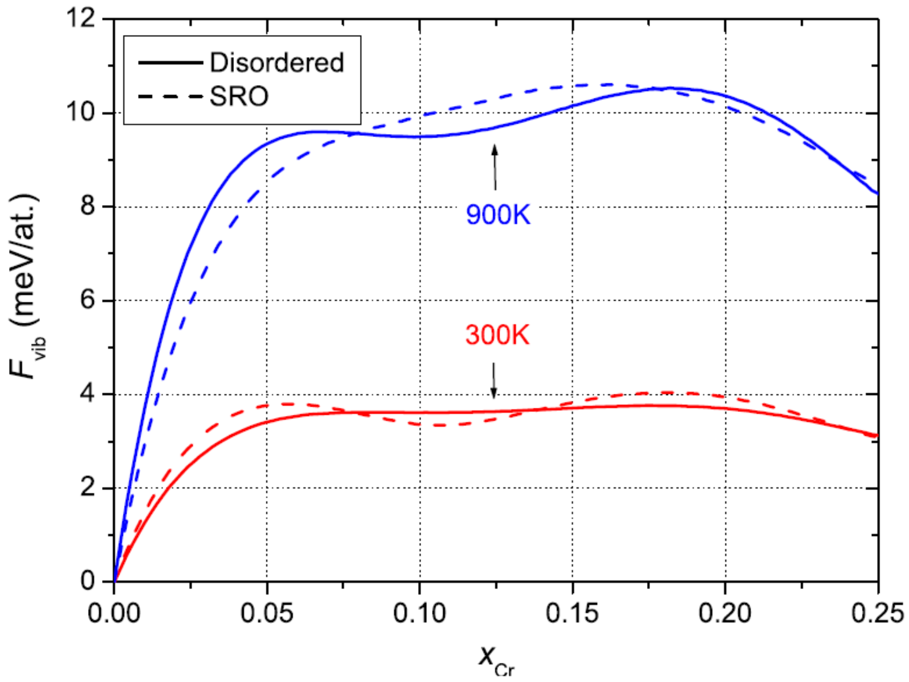

Figure 3: Isotherms of the excess vibrational free energy for the SRO and random alloy.

Thermodynamic functions

Two isotherms at 300 and 900K are shown in figure 1. In this plot the free energy from the random and SRO alloys are compared. To illustrate the quality of the RK-expansion fit, the raw data are superposed on the fits, represented by the full lines. From the plot it is clear that the isotherms for the SRO alloy are lower than the isotherms of the random alloy. The difference is about 7 meV atom−1 at 300K and 4 meV atom−1 at 900 K. To investigate the origin of this difference, the free energy is further separated in the enthalpy and entropy contributions, as described in appendix A and discussed below.

The contribution of the configurational entropy to the free energy, *F*conf = −*T S*conf, is presented in figure 2 where the configurational free energy for the random and SRO alloy are compared at 300 and 900 K. As expected, SRO pushes the configurational free energy up. The magnitude by which the free energy is shifted, however, is less than 1.3 meV atom−1 at 300K and 0.7 meV atom−1 at 900 K, which is of the order of magnitude of the numerical errors. We conclude then that the effect of SRO on the configurational entropy is of minor importance; therefore the past/future use of the disordered configurational entropy is justified, a statement that represents a first conclusion of this work.

The effect of the SRO on the excess vibrational free energy, *F*vib = −*T S*vib, is illustrated in figure 3 for the temperatures 300 and 900 K. Here too the difference between the SRO and random solutions is less than 1 meV, which makes us conclude that the effect of SRO on the vibrational entropy is negligible. It should be noted, however, that in this concentration range the excess vibrational free energy is positive and acts opposite to the configurational free energy, but is about four times smaller in absolute value, i.e. has a negligible contribution to the stability of the phase. This result is in agreement with direct vibrational entropy calculations using the same potential performed in [20, 21]. It is however contrary to experimental observations, where the excess vibrational free energy is found to be negative and not negligible by −0.18 and −0.20*k*B atom−1 for a random Fe53Cr47 alloy at 300K and the high temperature limit [22], respectively. However, this shortcoming of the potential is not expected to affect the outcome of this study at a low temperature, even compared with experiments.

The effect of the SRO on the excess enthalpy is illustrated in figure 4 at the temperatures 300 and 900 K. It is clear that the difference between the SRO and random solutions is significant, about 8 meV at 300K and 4 meV at 900 K. Note that the excess enthalpy is independent of temperature for the random case, while it is strongly temperature dependent in the SRO case. This is due to the changes in SRO of the alloy with temperature, as shown.

Thus the combined effect of the SRO on the configurational entropy, the excess vibrational entropy and the excess enthalpy gives a significant shift in the free energy. From this discussion it is clear that this effect is dominated by the enthalpy, thereby stressing the importance of having the latter quantity properly described by the cohesive model.

The phase diagram

The shift in free energy introduced by SRO is translated into a shift of the Fe-rich phase boundary presented in figure 5. The phase boundary is shifted towards the Cr-rich side by approximately 4% Cr at a low temperature, an amount that implies doubling the solubility limit of Cr in the *α* phase. This shift, however, decreases fast with increasing temperature and disappears at about 900 K, even though SRO is still present. This observation suggests that the sudden disappearance of SRO due to the magnetic transition from ferro to para-magnetism (at Curie temperature, *T*Curie ≈ 1050 K) will not have a drastic impact on the phase diagram. Therefore the phase boundary is expected to show a smooth transition at the Curie temperature. At the Cr-rich side the phase boundary remains unchanged, as expected, since the Cr-rich alloy does not exhibit SRO.

In figure 6 our prediction for the Fe-rich phase boundary is compared with the standard CALPHAD phase diagram (in the range of the ferro-magnetic phase outside the range of formation of the *σ*-phase) [23, 24] and with some experimental low temperature data points from the works of Filippova *et al* [25] and Kuwano [26], which include data from both irradiation and thermal ageing experiments, respectively. In both works Moessbauer spectroscopy was used to identify SRO or *α*' precipitation. In the plot, the square (green) points denote the observed SRO, the bold (black) points denote precipitates observed and the italic (red) points denote estimated phase boundary points by the respective authors. The low temperature data come from irradiated samples. Taking this into account, the experimental data points are used to describe the low temperature phase diagram, other than CALPHAD, which does not take low temperature data into account. Furthermore, the low temperature CALPHAD phase boundary is not consistent with the experimentally observed SRO at low Cr content.

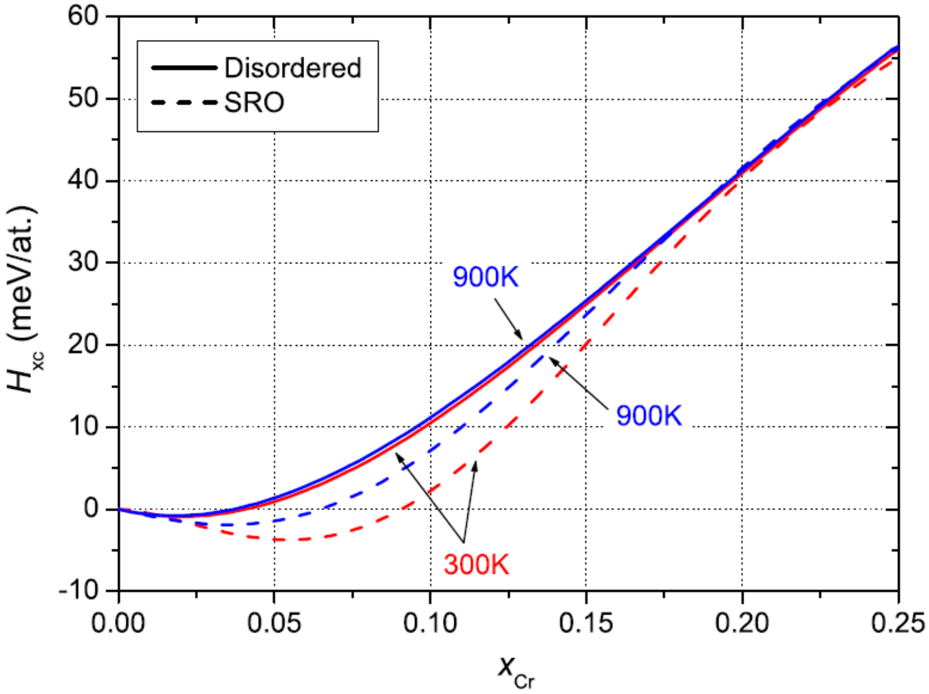

Figure 4: Isotherms of the excess enthalpy for the SRO and random alloy.

Figure 6 shows that the phase boundary obtained from our simulations matches the experimental data quite closely at temperatures below 700 K, with the salient feature that the *solvus* is very steep, and the Cr solubility at low *T* is very large, in contrast to the commonly accepted phase diagram of Fe–Cr. At higher *T'*s the discrepancy is significant as the miscibility gap does not close under melting temperature ≈2000 K, whereas the ferromagnetic metastable (neglecting the slow σ formation) miscibility gap closes around 900K [16]. This only reflects that the cohesive model and its predictions are valid at T's low compared with the FM/PM transition. [20, 21].

Conclusions

We have then investigated the effect of SRO on the thermodynamic properties of the Fe–Cr alloys by means of atomistic simulations. The free energy of the SRO alloy is significantly lower than the random alloy at low temperature and still noticeably lower at high temperature: the decrease in free energy due to SRO is attributed mainly to the decrease in enthalpy. The difference in the configurational and vibrational entropy between the SRO and random alloy is significantly smaller than in the case of the enthalpy. In fact, the effect of the configurational and vibrational entropy falls within the numerical precision of the calculations and is therefore of minor importance. Improvements in the description of the excess vibrational entropy may slightly affect these results but not invalidate the general conclusion that indicates that the *solvus* is quite steep and that the solubility of Cr is further enhanced by the development of order in the alloy.

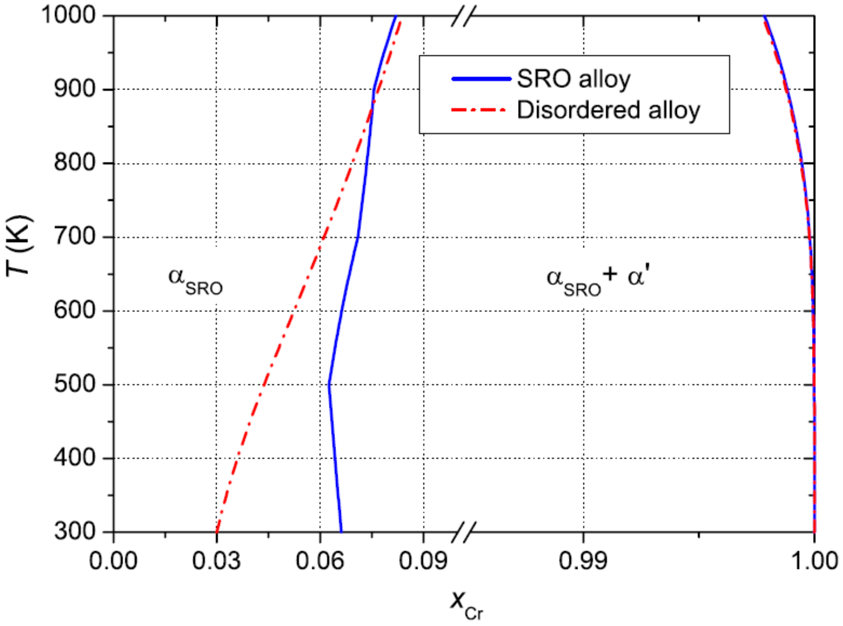

Figure 5: The phase boundaries for the SRO and random alloy.

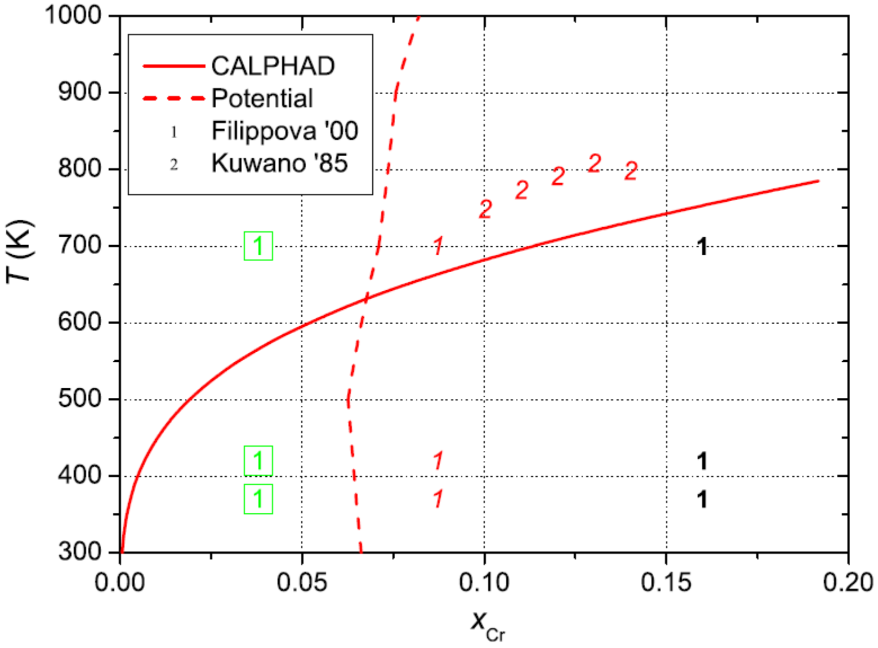

Figure 6: The phase diagram obtained from our simulations compared with experimental data. The points outlined in boxes (green in the online version) denote the observation of SRO, the points in bold font (black in the online version) denote precipitation observed, and the points in italic font (red in the online version) denote estimated phase boundary points by the respective authors.

The effect of SRO on the Fe-rich phase boundary is significant at a low temperature, where the boundary is shifted towards the Cr-rich region by almost doubling the solubility limit compared with the phase boundary for the random alloy. At about 900K the phase boundaries obtained from the SRO alloy and the random alloy coincide, while SRO is still observed in agreement with experiments where SRO is expected up to the Curie temperature [27]. This suggests only a minor impact of disordering due to the magnetic transition at the Curie temperature on the phase boundaries.

In summary, the main contributions of this work are as follows.

- The implications of the change in sign in the heat of mixing of Fe–Cr at a low Cr composition imply dramatic changes in the phase diagram, showing large solubility at low *T* and a steep phase boundary.
- A consequence of the complex heat of mixing and tendency to order is that the calculation of the thermodynamic functions must include the presence of SRO, whose influence on the location of the *solvus* is significant.
- The results presented in this work, based on *ab initio* energetics and interatomic potentials thermodynamics, seem to match well the experimental phase diagram below 700K and is in striking contrast to the phase diagram of Fe–Cr as appears in the CALPHAD database.

References

[1] Caro A, Caro M, Lopasso E M and Crowson D A 2006 *Appl. Phys. Lett.* **89** 121902

[2] Caro A, Caro M, Klaver P, Sadigh B, Lopasso E M and Srinivasan S G 2007 *TMS JOM* **59** 50

[3] Caro A, Crowson D A and Caro M 2005 *Phys. Rev. Lett.* **95** 75702

[4] Ogando Arregui E, Caro M and Caro A 2002 *Phys. Rev.* B **66** 054201

[5] Ogando E, Caro M and Caro A 2002 *Comput. Mater. Sci.* **25** 297

[6] Lopasso E M, Caro M, Caro A and Turchi P E A 2003 *Phys. Rev.* B **68** 214205

[7] Caro A, Turchi P E A, Caro M and Lopasso E M 2005 *J. Nucl. Mater.* **336** 233

[8] Caro A, Caro M, Lopasso E M, Turchi P E A and Farkas D 2006 *J. Nucl. Mater.* **349** 317

[9] Lavrentiev M Y, Drautz R, Nguyen-Manh D, Klaver T P C and Dudarev S L 2007 *Phys. Rev.* B **75** 14208

[10] Olsson P, Wallenius J, Domain C, Nordlund K and Malerba L 2005 *Phys. Rev.* B **72** 214119

[11] Daw M S and Baskes M I 1984 *Phys. Rev.* B **29** 6443

[12] Erhart P, Caro A, Serrano de Caro M and Sadigh B 2008 *Phys. Rev.* B **77** 134206

[13] Frenkel D and Smit B 1996 *Understanding Molecular Simulation—From Algorithms to Applications* [14] Cowley J M 1950 *Phys. Rev.* **77** 669

[15] Inden G and Pitsch W 1991 *Materials Science and Technology* (*Phase Transformations in Materials* vol 5). Ed R W Cahn *et al* (Weinheim: Wiley) p 497

[16] Ducastelle F 1991 *Cohesion and structure* (*Order and phase stability in alloys* vol 3) (Amsterdam: North-Holland)

[17] Kikuchi R 1951 *Phys. Rev.* **81** 988

[18] Redlich O and Kister A T 1948 *Indust. Eng. Chem.* **40** 345

[19] DeHoff R T 2006 *Thermodynamics in Materials Science* (London: CRC Press)

[20] Pasianot R C, Bonny G and Malerba L 2007 *Proc. Congreso SAM/CONAMET (San Nicolas)*

[21] Bonny G, Pasianot R C, Malerba L, Caro A, Olsson P and Lavrentiev M Yu 2008 Numerical prediction of thermodynamic properties of Fe–Cr alloys using semi-empirical cohesive models: where do westand? *J. Nucl.Mater.* submitted

[22] Fultz B, Anthony L, Robertson J L, Nicklow R M, Spooner S and Mostoller M 1995 *Phys. Rev.* B **52** 3280

[23] Andersson J-O and Sundman B 1987 *CALPHAD* **11** 83

[24] Saunders N and Miodownik A P 1998 *CALPHAD (Calculation of Phase Diagrams): A Comprehensive Guide* (*Pergamon Materials Series* vol 1) ed R W Cahn (Oxford: Pergamon)

[25] Filippova N P, Shabashov V A and Nikolaev A L 2000 *Phys. Met. Metallogr.* **90** 145 AQ6

[26] Kuwano H 1985 *Trans. Japan Inst. Met.* **26** 473

[27] Mirebeau I, Hennion M and Parette G 1984 *Phys. Rev. Lett.* **53** 687
(London: Academic Press)

ATOMISTIC STUDIES OF PROPERTIES OF HELIUM IN BCC IRON: COMPARISON OF FE–HE AND FE MATRIX POTENTIALS

—David M. Stewart, Stanislav Golubov (Oak Ridge National Laboratory and the University of Tennessee), Yuri Ostesky, Roger E. Stoller, Tatiana Seletskaia, and Paul Kamenski (Oak Ridge National Laboratory)

SUMMARY

In fusion applications, helium caused by transmutation plays an important role in the response of RAFM steels to neutron radiation damage. We have performed atomistic simulations using a new 3-body Fe–He inter-atomic potential combined with the Ackland iron potential. The results are compared with older (Wilson) and more recent (Juslin-Nordund) Fe-He pair potentials, and with alternate iron matrices. With the ORNL potential, interstitial helium is very mobile and coalesces together to form interstitial clusters. We have investigated the mobility of these clusters. If the He cluster is sufficiently large the cluster can push out an Fe interstitial, creating a Frenkel pair. The resulting helium-vacancy cluster is not mobile. The ejected SIA is mobile, but is weakly trapped by the He–V cluster. If more helium atoms join the He–V cluster, more Fe interstitials can be pushed out, and they combine to form an interstitial dislocation loop. The reverse process is also studied. Multiple helium atoms can be trapped in a single vacancy, and if there are few enough, the vacancy can recombine with an Fe interstitial to create a helium interstitial cluster. These mechanisms are investigated together in larger simulations that examine the nucleation of He defects. Results are compared based on temperature, interatomic potentials used and helium concentration.

PROGRESS AND STATUS

Introduction

Helium produced in neutron irradiated iron plays an important part in its mechanical properties. The growth, migration and coalescence behavior of helium bubbles is very sensitive to the properties of individual He interstitials and helium-vacancy clusters [1]. A new He–Fe inter-atomic potential has been developed at ORNL, based on extensive fitting to first-principles calculations of point defects and clusters [2–5]. This potential has been used to investigate the properties of helium and helium-vacancy clusters in MD and MS simulations.

Helium diffuses very fast in the matrix, but is easily trapped in vacancies [6]. It is possible for a self-interstitial to recombine with the vacancy, kicking the helium back into an interstitial position. Previous calculations [5] showed that recombination is possible not only for a single substitutional He, but even when the vacancy contains multiple Helium atoms. If the vacancy contains 5 or less atoms, it is found to be energetically favorable for it to recombine with the SIA to form a helium interstitial cluster. For 6–8 atoms there is no clear winner, and for more than 8 it is more favorable for the SIA to be trapped close to a He–V cluster without recombining with it.

A dynamic simulation of a He_8 interstitial cluster at 600K showed that the reverse process (i.e. Frenkel pair formation) can happen—an iron atom is pushed out of its lattice site, creating a He_8V cluster and an SIA. The SIA was trapped beside the cluster.

Simulation Method

The general procedure followed is: Generate perfect BCC lattice. Introduce the defect(s) to be studied. Relax at constant volume using a mixture of conjugate gradient and simulated annealing, and save the atom positions in units of the lattice constant. Start the MD simulation.

The MD simulations used NVE dynamics. The lattice constant and initial velocities were chosen to give close to zero pressure and the desired initial temperature. The boundary conditions are periodic in *X*, *Y* and *Z*, which are ⟨100⟩ directions. The velocity Verlet algorithm with a timestep of 0.3fs is used. As volume and temperature correction are not used, when processes that release energy are simulated the temperature and pressure both rise during the simulation.

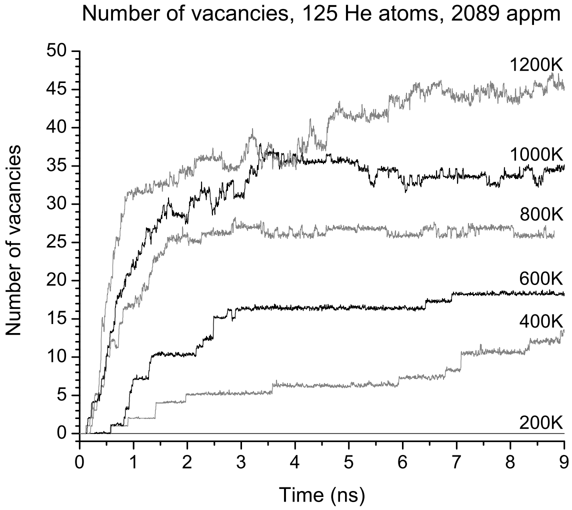

Figure 1. Vacancy production

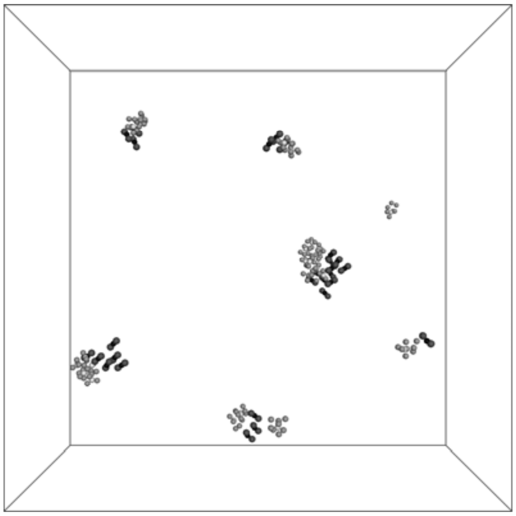

Figure 2. Clusters at 800K at t = 3.2ns

Coalescence

In order to study the process of Frenkel pair formation by helium interstitial clusters, dynamic simulations were run with 125 helium atoms in a 31×31×31 BCC iron matrix (60,000 iron atoms). At 200K, there was insufficient kinetic energy to break up even a pair of He atoms, so the helium slowly and inexorably coalesced until it formed interstitial clusters too big to be mobile, He_4 or bigger. The largest observed cluster was He_8. No vacancies or SIAs were observed. At 400K, He_2 and He_3 were still mostly stable but more clusters were mobile so coalescence happened faster. When clusters reached 8 or 9 helium atoms, a single SIA was ejected. None of the ejected SIAs escaped their HeV cluster. At higher temperatures, smaller clusters like He_2 and He_3 were short lived, reducing the number of surviving clusters. The clusters that did form were bigger since the number of available He atoms was fixed at 125. The higher the temperature, the less He atoms were needed to eject an SIA. Higher temperatures also led to more SIAs escaping the HeV cluster where they were created. These SIAs were usually captured by larger clusters that had SIAs. The SIAs were observed to form small dislocation loops.

The number of vacancies (equal to the number of SIAs ejected) is plotted as a function of time in Fig. 1. A snapshot of the 800K simulation after 3.2 nanoseconds is shown in Fig. 2. All the helium has coalesced into 9 clusters, all of which have pushed out from 1 to 6 SIAs. The SIAs have formed interstitial loops beside some of the clusters.

Similar simulations were run with different potential combinations. Results for Ackland [7] + ORNL [2–5], Mendelev [8] + ORNL [2–5] and Ackland [7] + Wilson [9] are shown in Fig. 3. With Ackland + Wilson, Frenkel pairs formed much faster than they did with the ORNL potential, and nearly twice as many were formed. This is because an SIA can be ejected from an interstitial cluster of only 2 or 3 Heliums. The Mendelev + ORNL combination formed bubbles at a rate and quantity that was between the other two combinations. For Ackland + Juslin–Nordlund [10] (not shown on the graph), the helium remained separated as interstitial atoms and Frenkel pairs were not created.

In order to see the effect of the helium concentration, additional simulations were run with the same number of helium atoms (125) in larger box of 40×40×40. This gives 128,000 iron atoms and thus a concentration of 976 appm He. The number of vacancies created for the 600K run is shown in Fig. 4. The bubbles took longer to form when the concentration was lower, but the number and size distribution was similar.

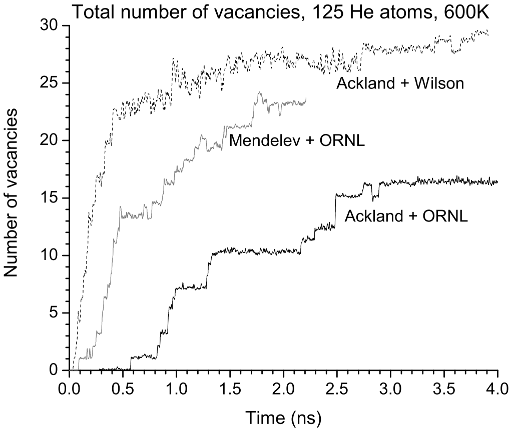

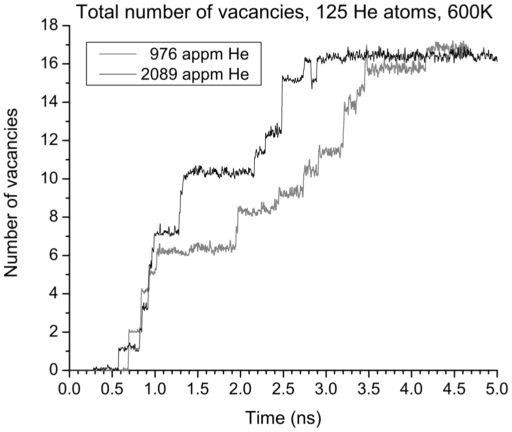

Figure 3. Coalescence for different potentials.   Figure 4. Coalescence for different box sizes.

Cluster Diffusion

The rate of diffusion of helium interstitial clusters was also measured. Simulations of clusters consisting of up to 6 He atoms were run for 15ns in a 10×10×10 box at a range of different temperatures. In all cases, the clusters do one of three things:

- remain as a cluster;
- dissociate into smaller clusters and/or atoms; or
- eject one or more SIAs.

The cluster diffusion rate is considered to be the diffusion rate of the centre of mass of the He atoms. An Arrhenius plot of the rates is shown in Fig. 5. When a cluster remains intact, the diffusion rate is calculated using the whole simulation, and shown as a solid symbol in Fig. 5. In many cases, a cluster dissociates or ejects an SIA only after a considerable amount of time. In these cases, the diffusion rate is calculated from the simulation up to that point, and shown as empty symbols in Fig. 5.

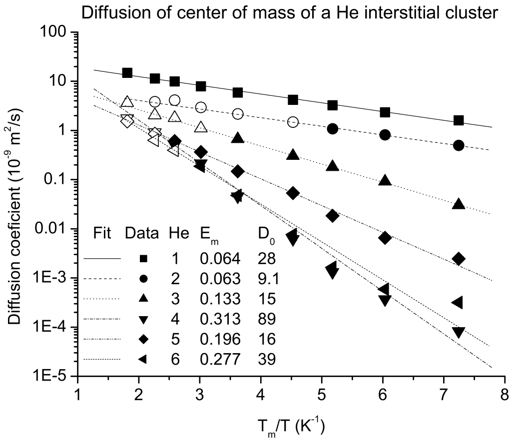

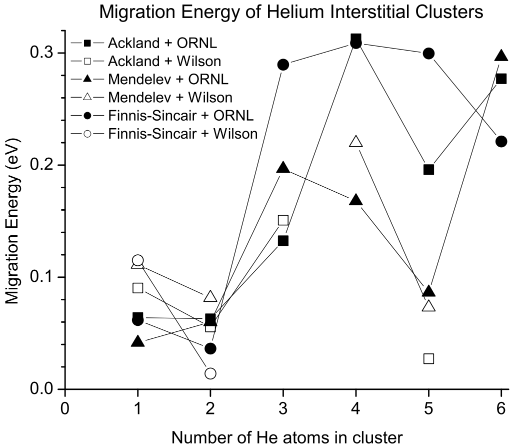

Figure 5. Arrhenius plot for Ackland + ORNL.   Figure 6. Migration energy results.

Arrhenius fits are done for several different combinations of matrix and He–Fe potentials, and the resulting energy barriers are plotted in Fig. 6. The test matrix for this measurement was 2 He–Fe potentials times 3 Fe matrix potentials times 6 He interstitial cluster sizes times 9 different temperatures.

The Juslin–Nordlund He–Fe potential predicts that all clusters will dissociate into individual interstitial Helium atoms, so there are no cluster diffusion rates for this potential with any matrix.

The Ackland matrix potential with the ORNL He–Fe potential showed almost identical barriers of about 0.06eV for a single He and the He_2 pair. He_3 had the next lowest barrier and then He_5. He_4 and He_6 both had the highest barriers of about 0.3eV.

The Mendelev matrix with the ORNL He–Fe potential showed different behavior. The barrier for a single He was only 0.04eV while for He_2 remained at 0.06eV. But the next lowest was He_5 with a barrier of only 0.09eV. He_3 and He_4 showed very close diffusion rates and barriers of about 0.18eV. The highest barrier was He_6 with 0.3eV.

With the Finnis–Sinclair matrix [11] and the ORNL He–Fe potential, the He_2 cluster had a lower barrier than a single He. Clusters of size 3, 4 and 5 showed very close diffusion rates and barriers of about 0.3eV, while He_6 had a barrier closer to 0.2eV.

The Ackland matrix potential with the Wilson He–Fe potential also showed the He_2 cluster with a lower barrier than a single He. Surprisingly, the He_5 cluster had an even lower barrier of only 0.03eV, based on simulations below 400K. At 400K and higher, it ejects an SIA too quickly to calculate a diffusion rate. The He_3 cluster shows very strange behavior, repeatedly ejecting an SIA and recombining with it. This suggests that the two states have similar energy. That the SIA was always available to recombine is an artifact of the simulation, as it has periodic boundary conditions and a small size. The He_4 cluster remained intact for a long time, especially at low temperatures, but would eject an SIA rather than move. At all temperatures, the He_6 cluster ejected an SIA too quickly to calculate a diffusion rate.

The Mendelev matrix potential with the Wilson He–Fe potential again shows decreasing barriers from the single He to the He_2 cluster to the He_5 cluster. The He_4 cluster showed very slow diffusion—the barrier was 0.2eV, but it had an extremely low pre-exponential factor. Above about 400K He_4 and He_5 ejected an SIA too quickly the gather diffusion data. At all temperatures, the He_3 and He_6 clusters immediately ejected an SIA.

References

[1] S.I. Golubov, R.E. Stoller, S.J. Zinkle, and A.M. Ovcharenko, Kinetics of coarsening of helium bubbles during implantation and post-implantation annealing, Journal of Nuclear Materials 361 (2007), pp. 149–159.

[2] T. Seletskaia, Y.N. Osetsky, R.E. Stoller, and G.M. Stocks, Magnetic Interactions Influence the Properties of Helium Defects in Iron, Physical Review Letters 94 (2005), pp. 046403.

[3] T. Seletskaia, Y.N. Osetsky, R.E. Stoller, and G.M. Stocks, Calculation of helium defect clustering properties in iron using a multi-scale approach, Journal of Nuclear Materials 351 (2006), pp. 109–118.

[4] T. Seletskaia, Y.N. Osetsky, R.E. Stoller, and G.M. Stocks, Development of a Fe He interatomic potential based on electronic structure calculations, Journal of Nuclear Materials 367 (2007), pp. 355–360.

[5] D.M. Stewart, last semiannual report

[6] H. Trinkaus and B. Singh, Helium accumulation in metals during irradiation–where do we stand? Journal of Nuclear Materials 323 (2003), pp. 229–242.

[7] G.J. Ackland, D.J. Bacon, A.F. Calder, and T. Harry, Computer simulation of point defect properties in dilute Fe-Cu alloy using a many-body interatomic potential, Philosophical Magazine A-Physics of Condensed Matter Structure Defects and Mechanical Properties 75 (1997), pp. 713–732.

[8] M.I. Mendelev, S. Han, D.J. Srolovitz, G.J. Ackland, D.Y. Sun, and M. Asta, Development of new interatomic potentials appropriate for crystalline and liquid iron, Philosophical Magazine 83 (2003), pp. 3977–3994.

[9] W. Wilson and R. Johnson, Rare Gases in Metals, Interatomic Potentials and Simulation of Lattice Defects, Battelle Institute Materials Science Colloquia, 1972, 375-390 (1972).

[10] N. Juslin and K. Nordlund, Pair potential for Fe–He, Journal of Nuclear Materials 382 (2008) 143–146.

[11] M.W. Finnis and J.E. Sinclair, A simple empirical N-body potential for transition metals, Phil. Mag. A 50 (1984), pp. 45–55.

Implementation of a Fe-He 3-body Interatomic Potential

R. E. Stoller[1], S. I. Golubov[1,2], P. J. Kamenski[3], T. Seletskaia[1], and Yu. N. Osetsky[1]

[1]*Materials Science and Technology Division*
Oak Ridge National Laboratory, Oak Ridge, TN 37831-6138
[2]*Department of Materials Science and Engineering,*
University of Tennessee, Knoxville, TN
[3]*Department of Materials Science and Engineering*
University of Wisconsin, Madison, WI (now University of Oxford, UK)

Abstract

The implementation of a recently-developed interatomic potential describing the interactions of helium in bcc iron is described. This He-Fe potential was based on an empirical fit to the results of *ab initio* calculations of both the formation and relaxation energies of small helium defect structures in iron. The fitting database included substitutional and interstitial helium, as well as small helium and helium-vacancy clusters. In contrast to previous He-Fe pair potentials, fitting the *ab initio* forces and energies required the use of a three-body interaction term. The implementation of this potential for atomistic simulations using molecular dynamics presented certain challenges which are discussed here to facilitate its further use in materials research, particularly to investigate the behavior of iron-based alloys that may be employed in fusion energy systems.

Introduction

Helium produced by nuclear transmutation has a substantial impact on radiation-induced microstructural evolution [1-4] and is therefore a concern for DT fusion reactor environments. Since no materials irradiation facility exists that can produce prototypical levels of helium and atomic displacements, computational modeling and simulation plays a primary role in understanding the impact of helium. Although computational tools have advanced appreciably in recent years, most relevant atomistic work on the effects of helium in iron have employed a relatively old pair potential to describe the He-Fe interactions [5]. The underlying assumption of the adequacy of a pair potential to describe these interactions was challenged by recent *ab initio* calculations [6,7], leading to the development of a three-body Fe-He interatomic potential [8,9].

The purpose of this report is to provide details on how the three-body potential was implemented in a molecular dynamics (MD) simulation code, and to correct typographical errors in some of the coefficients that were published previously [9]. Results of a large number of MD simulations investigating the behavior of the potential and a comparison with the Wilson [5] and a more recent pair potential [10] are included in this volume in a report by Stewart, et al. [11].

Description of Fe-He Three-body Potential

(i) Total Potential Energy

The total potential energy of a Fe crystal doped with He is given by

$$\begin{aligned} U_{total} &= \sum_{i=1}^{I_{Fe}} U_{Fe}(\rho_i) + \sum_{i=1}^{I_{Fe}-1} \sum_{j=i+1}^{I_{Fe}} U_{FeFe}\left(r_{ij}\right) + \sum_{i=1}^{I_{He}-1} \sum_{j=i+1}^{I_{He}} U_{HeHe}\left(r_{ij}\right) \\ &+ \sum_{i=1}^{I_{He}} \sum_{j=1}^{I_{Fe}} U_{HeFe}\left(r_{ij}\right) + \sum_{i=1}^{I_{He}} \sum_{j=1}^{I_{Fe}-1} \sum_{k=j+1}^{I_{Fe}} U_{HeFeFe}\left(r_{ij}, r_{ik}, \theta_{jik}\right). \end{aligned} \tag{1.1}$$

The first and second summation terms in Eq. (1.1) correspond to a pure iron, embedded atom potential. Three different iron matrix potentials have been studied, including the Finnis and Sinclair potential [12], the 1997 Ackland et al. potential [13], and the 2004 Ackland et at. potential [14]. The third term on the right hand side of equation (1.1) describes helium-helium interactions through the pair potential developed by Aziz et al. [15]. The last two terms on the right hand side of Eq. (1.1) correspond to two-body helium-iron interactions and three-body helium-iron-iron interactions Ref. [9]. This summary shall clarify only those last two terms in Eq. (1.1).

Note that all the function names in Eq. (1.1), e.g. Φ, φ etc., have been changed in order to present the equation in more conventional form. The summation index description on the right hand side of Eq. (1.1) has also been changed compared to that is written in Ref. [9] in order to correct some errors. Indeed the second term in Eq. (1) in Ref. [9] is given in such a way that leads to double-count each pair contributions; the third term leads to double-count each pair also (and does not omit when $j = i$), the fourth term incorrectly omits the pair when $j = i$ (considering they are from different subsets), and the fifth term double-counts all Fe-He-Fe triplets. The summation indexes in the first term on the right hand side of Eq. (1.1) are also written in a different way compared to that in Ref. [9] in order to be consistent with summation index description used in that other terms.

(ii) Two-body He-Fe Interaction

The helium-iron two-body potential energy is given by

$$U_{HeFe} = \begin{cases} \exp\left(b_1 + b_2 r_{ij} + b_3 r_{ij}^{\ 2} + b_4 r_{ij}^{\ 3} + b_5 r_{ij}^{\ 4}\right), & r_{ij} < 1.6, \\ a_1 + a_2 r_{ij} + a_3 r_{ij}^{\ 2} + a_4 r_{ij}^{\ 3} + a_5 r_{ij}^{\ 4} + a_6 r_{ij}^{\ 5}, & 1.6 \le r_{ij} < 2.2, \\ p_1 \exp\left(-p_4\left(\dfrac{r_{ij}}{p_3} - 1\right)\right), & 2.2 \le r_{ij} < 4.1, \\ p_1 \exp\left(-p_4\left(\dfrac{r_{ij}}{p_3} - 1\right)\right)\left(1-\lambda\right)^3\left(1 + 3\lambda + 6\lambda^2\right), & 4.1 \le r_{ij} < 4.4, \end{cases} \tag{2.1}$$

where r_{ij} is the distance between He, (i), and Fe atom, (j), given by

$$r_{ij} = \sqrt{\left(x_j - x_i\right)^2 + \left(y_j - y_i\right)^2 + \left(z_j - z_i\right)^2} \tag{2.2}$$

The variable λ in Eq. (2.1) is related to r_{ij} as follows

$$\lambda = \frac{r_{ij} - r_b}{r_c - r_b}, \tag{2.3}$$

where the parameters r_b and r_c are cutoff parameters given in Table 1. The parameters a, b, and p in Eq. (2.1) are also presented Table 1. The distances and energies in Eq. (2.1) are given in Angstroms and eV, respectively. Note that by mistake Eq. 4 in Ref. [9] was presented as a function of x instead of r_{ij}. To be clear, in this summary, lowercase x variables correspond to the x positions of atoms. The use of x in Eq. (3) of Ref. [9] has been changed to λ. Note also, that the parameter p_2 in Eq. (2) in Ref. [9] was omitted here since it was fit to be zero.

The forces on He and Fe atoms arising from the two-body potential (2.1) can be calculated using

$$\vec{F} = -\nabla U. \tag{2.4}$$

Taking into account the third Newtonian law

$$\vec{F}_i = -\vec{F}_j. \tag{2.5}$$

Based on Eqn. (2.5), it is sufficient to calculate the force acting on only one of the Fe (or the He) atoms. Taking into account Eq. (2.4) the x-component of the force on the j-th atom is given by:

$$\left(F_j\right)_x = \begin{cases} -U_{HeFe}\left(b_2 + 2b_3 r_{ij} + 3b_4 r_{ij}^2 + 4b_5 r_{ij}^3\right)\left(\dfrac{x_j - x_i}{r_{ij}}\right), r_{ij} < 1.6, \\ -\left(a_2 + 2a_3 r_{ij} + 3a_4 r_{ij}^2 + 4a_5 r_{ij}^3 + 5a_6 r_{ij}^4\right)\left(\dfrac{x_j - x_i}{r_{ij}}\right), 1.6 \le r_{ij} < 2.2, \\ p_1 \exp\left(-p_4\left(\dfrac{r_{ij}}{p_3} - 1\right)\right)\dfrac{\left(x_j - x_i\right)}{r_{ij}}\left[\dfrac{p_4}{p_3}\right], 2.2 \le r_{ij} < 4.1, \\ p_1 \exp\left(-p_4\left(\dfrac{r_{ij}}{p_3} - 1\right)\right)\dfrac{\left(x_j - x_i\right)}{r_{ij}}\left[\dfrac{30}{r_c - r_b}\lambda^2\left(1-\lambda\right)^2 + \dfrac{p_4}{p_3}\left[\left(1-\lambda\right)^3\left(1 + 3\lambda + 6\lambda^2\right)\right]\right], 4.1 \le r_{ij} < 4.4. \end{cases} \tag{2.6}$$

Forces in the y and z directions can be calculated by replacing the x_j and x_i terms with the corresponding y_j and y_i or z_j and z_i values, respectively. The force on the i atom, F_i , is is given by Eq. (2.5).

(iii) Three-body He-Fe-Fe Interaction

The potential energy function for the helium-iron-iron three-body interaction is given by

$$U_{HeFeFe}\left(r_{ij},r_{ik},\theta_{jik}\right)=f\left(r_{ij}\right)f\left(r_{ik}\right)\cos^2\left(\theta_{jik}-\chi\right), \tag{3.1}$$

where r_{ij} and r_{ik} are the distances between the helium atom located at a position (i) and two Fe atoms located at positions (j) and (k), respectively, and θ_{jik} is the angle between the corresponding vectors $\overrightarrow{r_{ij}}$ and $\overrightarrow{r_{ik}}$. The function $f(r)$ is given by

$$f(r)=\begin{cases}\alpha, & r\le r_{b3},\\ \alpha(1-\Lambda)^3\left(1+3\Lambda+6\Lambda^2\right), & r_{b3}<r\le r_{c3},\end{cases}$$
$$\Lambda=\frac{r-r_{b3}}{r_{c3}-r_{b3}}, \tag{3.2}$$

where the parameters α, r_{b3} and r_{c3} are given in Table 2 together with the parameter χ. Note that the angle θ_{jik} varies from zero to π. Instead of using the variable a^Y for the scaling factor, as is used in Ref. [9], the parameter α is used since the use of "a" may be confusing since it is normally used for the lattice parameter.

Taking into account that the distances r_{ij} and r_{ik} are determined by the coordinates of atoms as follows:

$$r_{ij}=\sqrt{\left(x_j-x_i\right)^2+\left(y_j-y_i\right)^2+\left(z_j-z_i\right)^2},$$
$$r_{ik}=\sqrt{\left(x_k-x_i\right)^2+\left(y_k-y_i\right)^2+\left(z_k-z_i\right)^2}, \tag{3.3}$$

the angle θ_{jik} is given by:

$$\theta_{jik}=\arccos\left(\frac{\left(x_j-x_i\right)\left(x_k-x_i\right)+\left(y_j-y_i\right)\left(y_k-y_i\right)+\left(z_j-z_i\right)\left(z_k-z_i\right)}{r_{ij}r_{ik}}\right). \tag{3.4}$$

It can be also shown that the third Newtonian law in the case takes the following form

$$\vec{F}_i=-\left(\vec{F}_j+\vec{F}_k\right). \tag{3.5}$$

Thus it is enough to calculate forces on two atoms only, e.g. on two Fe atoms. By using Eq. (2.4) the x-component of the force acting on j-Fe atom can be presented as follows:

$$\left(F_j\right)_x=-\left(\frac{df\left(r_{ij}\right)}{dx_j}\right)f\left(r_{ik}\right)\cos^2\left(\theta_{jik}-\chi\right)$$
$$-f\left(r_{ij}\right)f\left(r_{ik}\right)\frac{\sin\left(2\left(\theta_{jik}-\chi\right)\right)}{\sin\left(\theta_{jik}\right)}\frac{d\cos\left(\theta_{jik}\right)}{dx_j}, \tag{3.6}$$

where:

$$\frac{df\left(r_{ij}\right)}{dx_j}=\begin{cases}0, & r_{ij}\le r_{b3},\\ -30\alpha\Lambda^2\left(1-\Lambda\right)^2\dfrac{\left(x_j-x_i\right)}{r_{ij}\left(r_{c3}-r_{b3}\right)}, & r_{b3}<r_{ij}\le r_{c3},\\ 0, & r_{ij}\ge r_{c3},\end{cases}$$

$$\frac{d\cos\left(\theta_{jik}\right)}{dx_j}=\frac{\left(x_k-x_i\right)}{r_{ij}r_{ik}}-\cos\left(\theta_{jik}\right)\frac{\left(x_j-x_i\right)}{r_{ij}^2}. \tag{3.7}$$

The y and z components of the force can be obtained from equations (3.6) and (3.7) by replacing x coordinates with y and z coordinates, respectively. The force acting on the k-Fe atom can be obtained from the same equations by replacing j-coordinates with k-coordinates and vice versa. Finally, the force acting on the He atom is given by Eq. (3.5).

Table 1. Parameters for pair potential given by Eq. (2.1).

$b_1=-2.142600207811$	$a_1=-285.7450302953$	$p_1=0.167753$
$b_2=32.965470333178$	$a_2=794.5913355517$	$p_2=0.00$
$b_3=-52.893449935488$	$a_3=-856.9376372455$	$p_3=2.432258$
$b_4=30.970079966695$	$a_4=452.5323035795$	$p_4=3.727249$
$b_5=-6.398785336260$	$a_5=-117.6519447529$	$r_b=4.1$
	$a_6=12.0878858024$	$r_c=4.4$

Table 2. Parameters for three-body potential given by Eqs. (3.1) , (3.2).

α	0.7
r_{b3}	1.75
r_{c3}	2.2
χ	0.44

Thus the set of equations (1.1)-(3.7) along with the iron matrix parameters in Refs. [12-15] represents a full and comprehensive description of the potential energy and forces acting on He and Fe atoms in an Fe crystal doped with He.

Energy and Force Acting On the He Atom In a Given Triplet Configuration

The complex nature of the forces and the energy landscape for a given Fe-He-Fe triplet are illustrated in Figs. 1 to 3 which are presented to provide a visualization of the three-body potential. The results are from calculations for a single Fe-He-Fe triplet. The most significant observation that can be drawn from these figures is the strong angular dependence of the three-

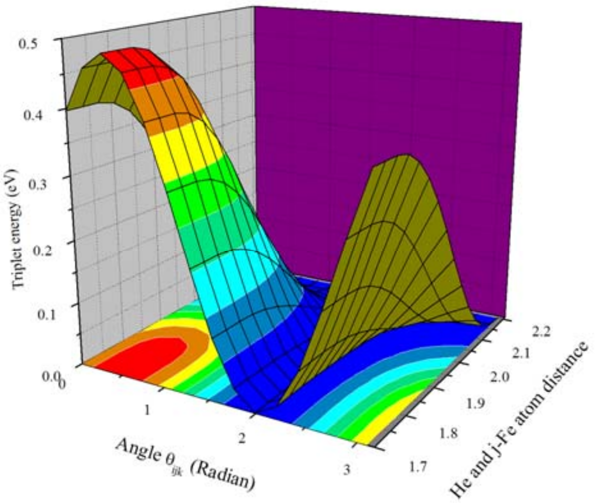

Figure 1. Energy of Fe-He-Fe triplet as a function of θ and r_{ik} where r_{ij} is equal to 1.8 Angstrom.

body term. As discussed in Ref. [9], the angular dependence and value of χ were chosen to guarantee the tetrahedral site provided the lowest interstitial formation energy. This leads to a relatively weak dependence on the distance between helium and either iron atom in the triplet when the angle is near that associated with the tetrahedral location, θ_{jik}~1.92 rad. For example, energy minimum of the He-Fe-He triplet at this angle shown in Fig. 1 only weakly depends on the He-Fe separation but varies strongly with the angle. The absolute force on the helium atom is similarly minimized as shown in Fig. 2. The decision to use the triplet angle to stabilize the tetrahedral interstitial is in contrast to the recent pair potential by Juslin and Nordlund [10] in which a steep radial (He-Fe spacing) was used to accomplish this purpose. A comparison of the two approaches as yielded significant differences [11].

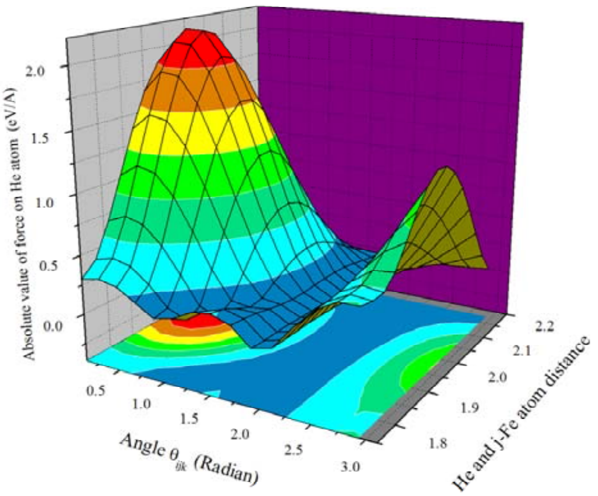

Figure 2. Absolute value of the force acting on the He atom as a function of θ and r_{ik} where r_{ij} is equal to 1.8 Angstrom.

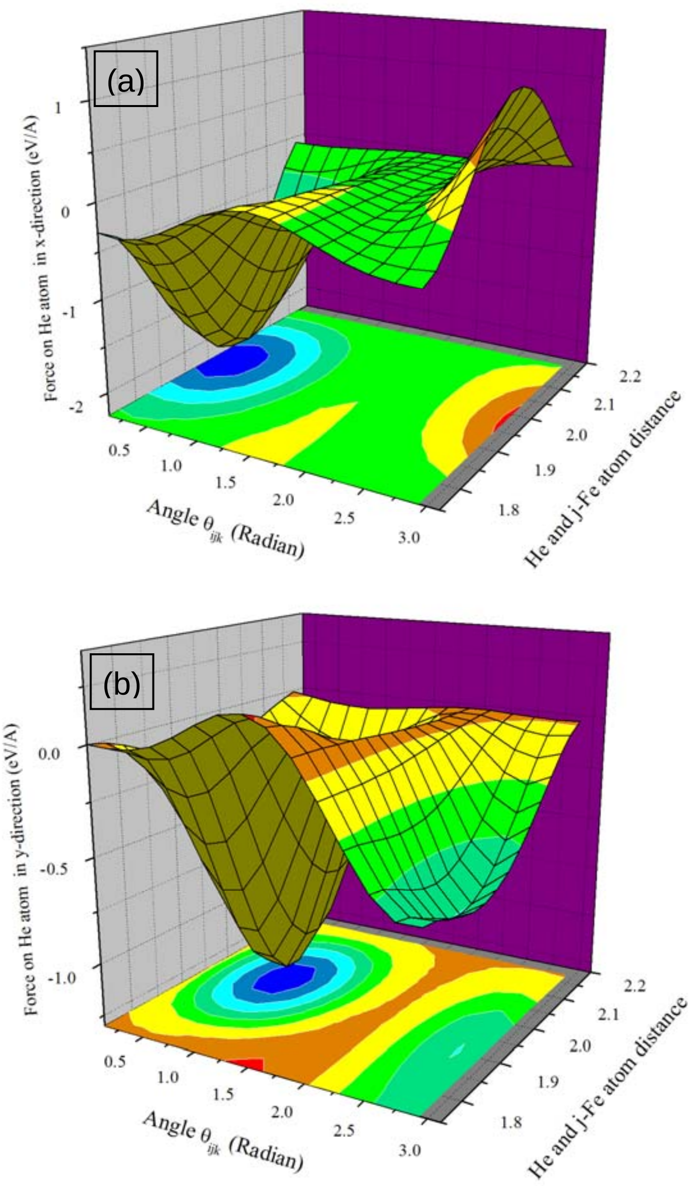

Figure 3. Force acting on the He atom in the (a) x-direction and (b) y-direction in the x-y plane as a function of θ and r_{ik} where r_{ij} is equal to 1.8 Angstrom.

Additional information on the forces on a helium atom near the tetrahedral position is given in Fig. 3 which shows the forces in two principle directions for a helium atom located in a {100} plane. In both cases the force is near zero and relatively insensitive to He-Fe distance near the specified angle.

Influence of Three-body Term on He Atom Migration

The influence of the three-body term on the He migration path is shown in Figs. 4 to 8, for which the calculations were done for one He atom in an unrelaxed Fe lattice. Fig. 4 shows the energy change for a He atom passing from one tetrahedral site to another along a <110> direction (illustrated in Fig. 5), which is the energetically favored migration path as mentioned in Ref. [9]. It is clear that the addition of the 3-body term changes both the magnitude and the shape of the energy barrier. The local energy minimum produced in the intermediate region in the case of three-body potential relates to the types of Fe-He-Fe triplets that arise in this intermediate configuration. The five nearest neighbors in this region are shown in Fig. 5.

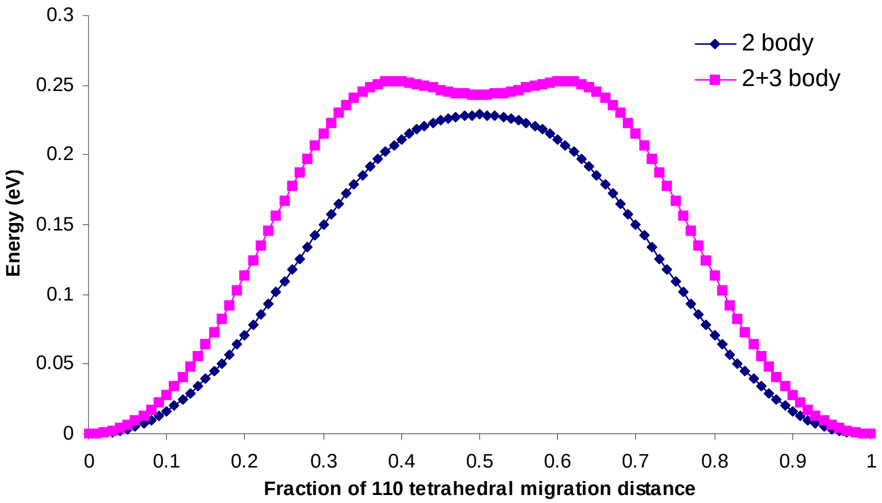

Figure 4. Migration energy barrier for a He atom passing from one tetrahedral site to another along a <110> direction. Note that both energy curves have been shifted such that the He atom in the tetrahedral sites has an energy equal to zero. This data are obtained for an unrelaxed lattice.

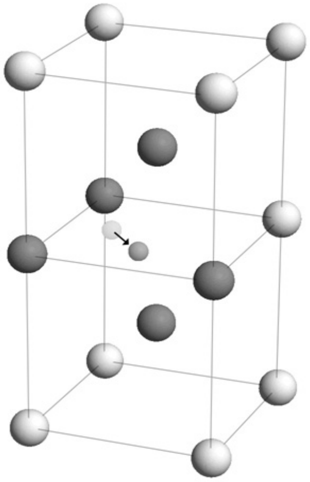

Figure 5. <110> He migration in bcc Fe. The five nearest neighbors during this migration are darkened. *Provided by Dr. Y. Matsukawa, ORNL (now University of IL)*

The Fe-He-Fe triplets formed in the intermediate region either (a) form an angle close to the preferential angle, *and/or* (b) have at least one long distance vector. Both (a) and (b) lead to smaller energy contributions for the given triplet. So, instead of a smooth energy barrier for migration given by the purely repulsive two-body potential shown in the figure, the 3-body contribution produces a meta-stable triangular site found half way through the migration shown Figure 5.

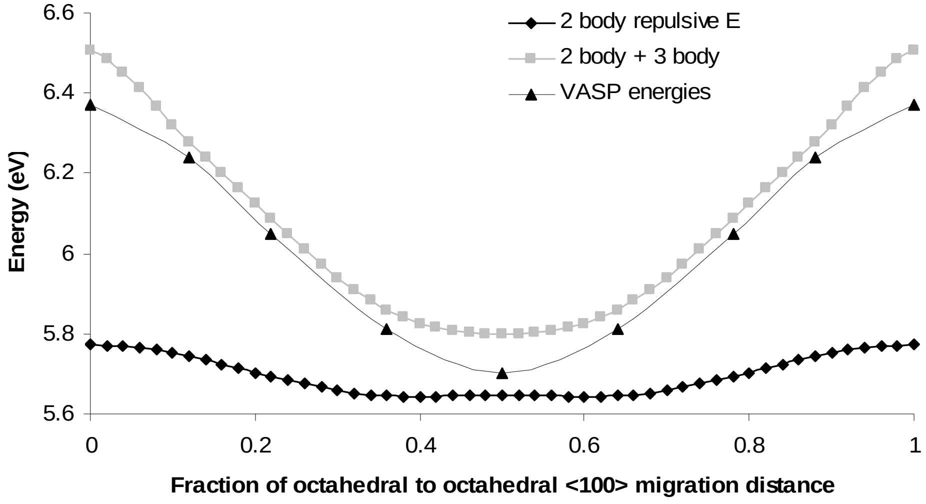

Figure 6. Energy of a He atom moving along a <100> direction from one octahedral site to another. Note that the He atom goes through a tetrahedral site mid-way. This data is for an unrelaxed lattice.

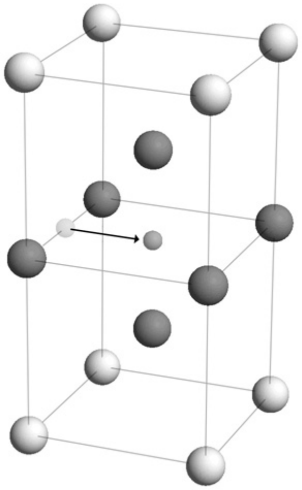

Figure 7. <100> Octahedral interstitial He migration in bcc Fe. The six nearest neighbors for the final octahedral configuration are darkened. *Provided by Dr. Y. Matsukawa, ORNL (now University of IL).*

The migration path described energetically in Figure 6 can be seen in Figure 7. The 2-body repulsive energy shown in Figure 7 produces an octahedral to tetrahedral site energy difference of 124 meV. When the 3-body term is added, the energy difference is 711 meV, which is much closer to the VASP energy difference of 670 meV. Also, the 2-body repulsive potential makes the tetrahedral site a local energy maximum (by a small amount), whereas with the 3-body term added, the tetrahedral site is a local energy minimum. This migration path from one octahedral site directly to another passes through a tetrahedral site which is mid-way through the motion. The energy minimum along this path is clearly the tetrahedral site. The energy landscape for He migration along the <010> and <001> orthogonal (relative to Figures 6 and 7) principle directions is shown in Figure 8, illustrating that the tetrahedral site is a local energy minimum in each principle direction.

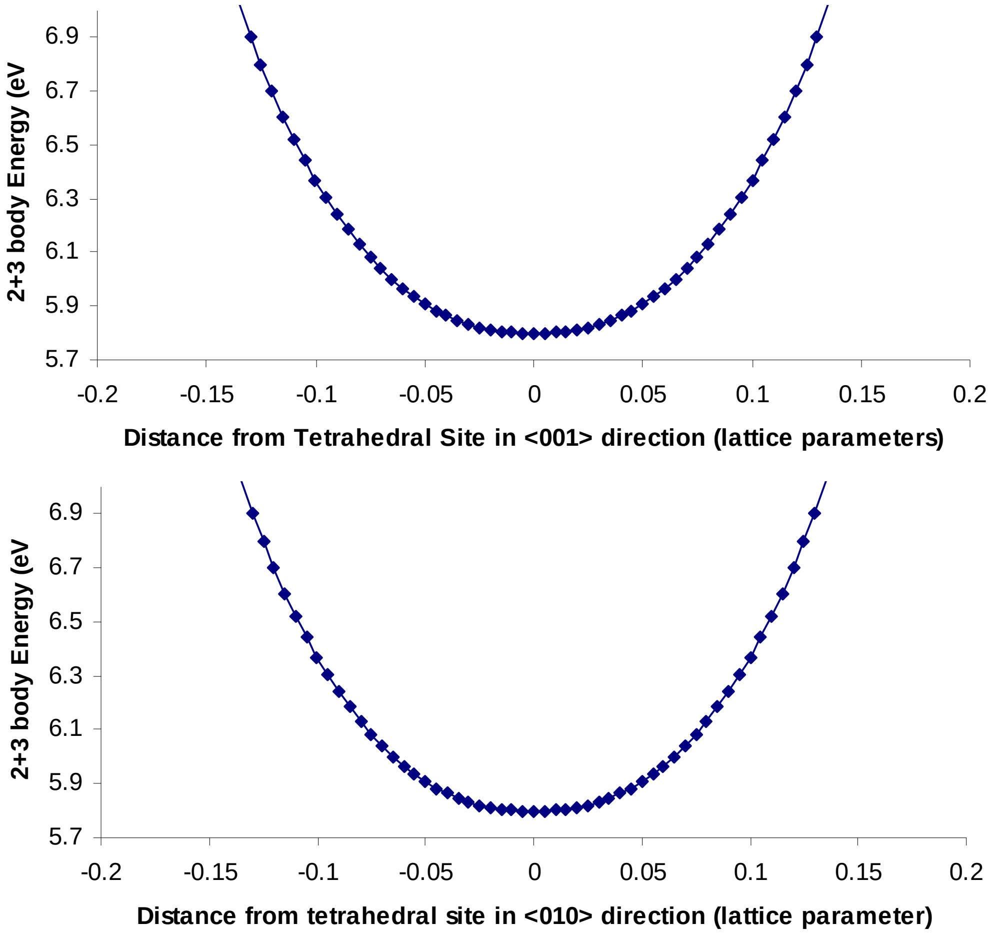

Figure 8. Energy of a He atom moving along the other two principle directions relative to Figures 6 and 7, showing the tetrahedral site as a local energy minimum in each principle direction.

Summary

The procedure, equations, and coefficients necessary to implement the new ORNL Fe-He three-body potential have been described. The energy landscape provided by this new potential is substantially more complex than that of a simple pair potential, but provides results in good agreement with *ab initio* calculations. Significant differences in the behavior of He and He-vacancy clusters have been observed when comparing results obtained with the three-body potential with that obtained with pair potentials [11], and the use of the new potential is recommended.

Acknowledgements

Research sponsored by the Division of Materials Sciences and Engineering and the Office of Fusion Energy Sciences, U.S. Department of Energy, under contract DE-AC05-00OR22725 with UT-Battelle, LLC.

References

1. R. E. Stoller, Journal of Nuclear Materials 174 (1990) 289-310.
2. R. E. Stoller and G. R. Odette, Journal of Nuclear Materials 154 (1988) 286-304.
3. R. E. Stoller, P. J. Maziasz, A. F. Rowcliffe and M. P. Tanaka, Journal of Nuclear Materials 155-157 (1988) 1328-1334.
4. R. E. Stoller and G. R. Odette, "A Comparison of the Relative Importance of Helium and Vacancy Accumulation in Void Nucleation," Radiation-Induced Changes in Microstructure, 13th International Symposium, ASTM STP 955, F. A. Garner, N. H. Packan and A. S. Kumar, Editors, American Society of Testing and Materials, Philadelphia, 1987, pp. 358-370.
5. W. Wilson and R. Johnson, Rare Gases in Metals, Interatomic Potentials and Simulation of Lattice Defects, Battelle Institute Materials Science Colloquia, 1972, 375-390 (1972).
6. T. Seletskaia, Y.N. Osetsky, R.E. Stoller, and G.M. Stocks, Physical Review Letters 94 (2005), pp. 046403.
7. Chu-Chun Fu, F. Willaime, and P. Ordejon, Phys. Rev. Lett. 92, 175503, (2004).
8. T. Seletskaia, Y.N. Osetsky, R.E. Stoller, and G.M. Stocks, Journal of Nuclear Materials 351 (2006), pp. 109–118.
9. T. Seletskaia, Y.N. Osetsky, R.E. Stoller, and G.M. Stocks, Journal of Nuclear Materials 367-370 (2007), pp. 355–360.
10. N. Juslin and K. Nordlund, Journal of Nuclear Materials 382 (2008) 143–146.
11. D. M. Stewart, S. I. Golubov, Yu. N. Ostesky, R. E. Stoller, T. Seletskaia, and P. J Kamenski, "Atomistic Studies Of Properties Of Helium In Bcc Iron: Comparison of Fe–He And Fe Matrix Potentials," this volume.
12. M.W. Finnis and J.E. Sinclair, Philos. Mag. A **50** (1984) 45.
13. G.J. Ackland, D.J. Bacon, A.F. Calder, and T. Harry, Philos. Mag. A **75** (1997) 713.
14. G.J. Ackland, M.I. Mendelev, D.J. Srolovitz, S. Han, and A.V. Barashev, J. Phys.: Condens. Matter **16** (2004) S2629.
15. R.A. Aziz, A.R. Janzen, and M.R. Moldovan, Phys. Rev. Let. **74** (1995) 1586.

STEADY-STATE SIZE DISTRIBUTION OF VOIDS IN METALS UNDER CASCADE IRRADIATION.-

A.V. Barashev (The University of Liverpool), S.I. Golubov (Oak Ridge National Laboratory, *University of Tennessee*)

OBJECTIVE

The theory of radiation damage in metallic materials predicts that under cascade-irradiation conditions the voids should approach a steady state, which is characterised by a maximum mean void size. It is shown in this Letter that the steady-state concentrations of voids of different size are described by the Gaussian distribution with the maximum size mentioned above to be the most probable value. The evolution of voids towards the steady state is analysed.

SUMMARY

The steady state of the void population predicted by the theory under cascade-irradiation conditions has been analyzed. The following conclusions have been drawn.

1) The theoretical steady-state SDF of voids is described by a Gaussian distribution, which is quite narrow, in contrast to much bigger spread of void sizes observed.
2) At high void density, when $\alpha >> 1$, the irradiation dose required to reach the steady state is higher than those at which void lattices are observed. Hence, the void size saturation of randomly distributed voids and in the lattice are not related to each other.
3) At low void density, when $\alpha \leq 1$, the irradiation dose required to reach the steady state is relatively small and might be a reason for the incubation period of swelling frequently observed.

PROGRESS AND STATUS

I. Introduction

Since the prediction [1] and discovery [2] of swelling in metals in nuclear reactors, much effort has been made to formulate a theory of the phenomenon. The 'Production Bias Model' (PBM) in its modern form succeeds in explaining several striking observations, for example, enhanced swelling rates near grain boundaries and in materials with small grain size and under neutron compared to electron irradiation [3-6]. The model owns its success to the recognition of two distinguishing features of defect production by high-energy recoils. First, that clusters of self-interstitial atoms (SIAs) are formed directly in displacement cascades, the fact revealed both experimentally [7] and in molecular dynamics (MD) simulations [8,9], and, second, that these clusters execute one-dimensional diffusion [9-13], a phenomenon proposed in [9,14] for the explanation of the void-lattice formation [15,16].

The model predicts that, if a random distribution of voids is maintained, a steady state should establish at high irradiation doses, which is characterised by a maximum void size, r_m, above which the net vacancy flux to voids is negative. This is because the cross-section of the interaction of three-dimensionally (3-D) diffusing vacancies with voids is proportional to the void radius r, while that of the 1-D migrating SIA clusters to r^2. As a result, above some critical radius, the latter becomes higher than the former. It has been shown that $r_\mathrm{m} \approx 2\pi r_\mathrm{d} / Z_\mathrm{v}$, where r_d is the dislocation capture radius for the SIA clusters and Z_v is the capture efficiency of dislocations for vacancies [3]. Note that this expression does not include the dependence on the dislocation bias for point defects: $B = Z_\mathrm{i} / Z_\mathrm{v} - 1$, where Z_i is the capture efficiency of dislocations for single SIAs, which accounts for one of the main driving forces for the void growth [1].

In this Letter we derive the dependence of the critical void radius on the dislocation bias factor and an equation for the steady-state size distribution function (SDF) of voids and analyse how voids approach the steady state.

II. Steady-state size-distribution function

Let us assume that the primary damage produced in cascades consists of 3-D mobile single vacancies and SIAs and 1-D mobile SIA clusters. In addition, let us assume that the void nucleation stage is over and the mobile defects interact only with existing voids of the number density N and dislocations of the density ρ. Then, according to the PBM (see, *e.g.* [6]), the rate of swelling is equal to the difference in arrival rates of vacancies, j_{v}, single SIAs, j_{i}, and SIAs in clusters, j_{cl}, to voids

$$\frac{dS}{d\phi} = j_{\mathrm{v}} - j_{\mathrm{i}} - j_{\mathrm{cl}} = \frac{4\pi rN}{4\pi rN + Z_{\mathrm{v}}\rho} - (1-\varepsilon_{\mathrm{i}}^{\mathrm{g}})\frac{4\pi rN}{4\pi rN + Z_{\mathrm{i}}\rho} - \varepsilon_{\mathrm{i}}^{\mathrm{g}}\frac{\pi r^2 N}{\pi r^2 N + \pi\rho r_{\mathrm{d}}/2}, \qquad (1)$$

where $S = 4\pi r^3 N/3$, r is the mean radius of voids, $\varepsilon_{\mathrm{i}}^{\mathrm{g}}$ is the fraction of the SIAs produced in the clustered form and ϕ is the irradiation dose. The irradiation dose is in displacements per atom (dpa) and accounts for the fraction of defects that survived intra-cascade recombination, ε_S; hence it corresponds to the dpa calculated using the NRT standard procedure [17] and multiplied by ε_S.

Eq. (1) cannot be used below some temperature, when the vacancy or SIA diffusivity is so low that recombination reactions between mobile species are important. At higher temperature, the defect nobilities do not enter the analysis and the swelling is determined by partitioning of defects between sinks, as in Eq. (1). Since the recombination between cascade-produced mobile vacancies and SIAs in clusters have not been studied so far, any estimates are not available. Another limitation is due to neglecting vacancy emission from voids, which requires high vacancy super-saturation and thus restricts the analysis to temperatures below ~(0.5÷0.6) T_{m}, where T_{m} is the melting temperature, depending on the dose rate. Also, it is assumed that the void nucleation stage is separated from the growth stage due to reduced thermal stability of void nuclei. The validity of this assumption and the nucleation itself is in fact one of the fundamental unresolved problems, which is closely connected with the validity of conventional assumption of homogeneous spatial distribution of defects in the system and is analysed in [18,19].

It can readily be obtained from Eq. (1) that the maximum mean void radius, which corresponds to zero swelling rate, is

$$r_{\mathrm{m}} \approx \frac{2\pi r_{\mathrm{d}}}{Z_{\mathrm{v}}}\left(1 + \frac{1-\varepsilon_{\mathrm{i}}^{\mathrm{g}}}{\varepsilon_{\mathrm{i}}^{\mathrm{g}}}B\right), \qquad (2)$$

where we omitted higher order terms in B. (For a comprehensive analysis see in a separate paper [18].) According to Eq. (2), r_{m} increases with decreasing $\varepsilon_{\mathrm{i}}^{\mathrm{g}}$, so that there is no saturation of swelling in the limit of $\varepsilon_{\mathrm{i}}^{\mathrm{g}} = 0$, *i.e.* for electron irradiation, as expected. It worth mentioning that a more rigorous analysis predicts an unlimited swelling even at finite $\varepsilon_{\mathrm{i}}^{\mathrm{g}}$ somewhat smaller than *B* [18].

In order to derive the steady-state SDF of voids, $f(x) = f(x,\phi = \infty)$, where the number of vacancies in a void of radius r_x is $x = 4\pi r_x^3/3\Omega$, Ω is the atomic volume, we consider the Smoluchowski (continuity) equation for the diffusion of voids in the size space:

$$\lim_{\varphi\to\infty}\frac{\partial f(x,\phi)}{\partial\phi} = \frac{d}{dx}\left\{-V(x)f(x) + \frac{d}{dx}\left[D(x)f(x)\right]\right\} = 0. \qquad (3)$$

Here $V(x) = j_{\mathrm{vx}} - j_{\mathrm{ix}} - j_{\mathrm{clx}}$ is the velocity and $D(x) = (j_{\mathrm{vx}} + j_{\mathrm{ix}} + j_{\mathrm{clx}})/2$ is the diffusion coefficient, where $j_{kx} = j_k r_x / rN$ $(k = \mathrm{v,i})$ and $j_{\mathrm{cl}x} = j_{\mathrm{cl}} r_x^2 / r^2 N$. Eq. (3) represents the familiar master equation for the evolution of the SDF of voids *via* absorption and emission of different defects in the diffusion limit of large void size (see, *e.g*. [20,21]). Its solution that provides zero flux of voids (the term in curly brackets) is

$$f(x) = A\exp\left[\int dxV(x)/D(x)\right]/D(x), \tag{4}$$

where A is a normalising constant. We expect that, in most cases, the SDF will be a narrow function around $x_\mathrm{m} = 4\pi r_\mathrm{m}^3/3\Omega$, such that $|x/x_\mathrm{m} - 1| << 1$. With this condition, it is readily obtained that, to a first approximation, $D(x)$ is a constant and

$$\frac{V(x)}{D(x)} \approx \lambda\varepsilon_\mathrm{i}^\mathrm{g}\left(1 - \frac{r_x}{r_\mathrm{m}}\right) \approx \frac{\lambda\varepsilon_\mathrm{i}^\mathrm{g}}{3}\left(1 - \frac{x}{x_\mathrm{m}}\right), \tag{5}$$

where

$$\lambda = 1 + \frac{1-\varepsilon_\mathrm{i}^\mathrm{g}}{\varepsilon_\mathrm{i}^\mathrm{g}}\frac{B}{1+\alpha}, \tag{6}$$

$\alpha = 4\pi r_\mathrm{m} N/Z_\mathrm{v}\rho$ and only the first order term in B is retained. By substituting Eq. (5) into Eq. (4), one obtains the SDF as Gaussian distribution centred on the most probable size, x_m:

$$f(x) \approx C_0\sqrt{\frac{\lambda\varepsilon_\mathrm{i}^\mathrm{g}}{6\pi x_\mathrm{m}}}\exp\left[-\frac{(x - x_\mathrm{m})^2}{6x_\mathrm{m}/\lambda\varepsilon_\mathrm{i}^\mathrm{g}}\right], \tag{7}$$

where $C_0 \approx \int dxf(x)$ is the total void concentration. The SDF has a half-width at half-maximum of $\sigma = \sqrt{x_\mathrm{m}6\ln 2/\lambda\varepsilon_\mathrm{i}^\mathrm{g}}$ and is thus narrow: $\sigma << x_\mathrm{m}$ for reasonable values of $\varepsilon_\mathrm{i}^\mathrm{g}$ (~0.5 according to MD studies of displacement cascades in Fe and Cu for the primary knock-on atom energy $E_\mathrm{PKA} \approx$ 10keV [22]). We note that the experimentally observed spreads of void sizes are obviously much bigger and reasons for this are discussed below.

Figure 1 shows the SDF calculated using Eq. (7) for B=0.04, α=1, $\varepsilon_\mathrm{i}^\mathrm{g}$=0.25, 0.5 and 1 (open symbols and connecting lines). In this figure, $x_\mathrm{m}^1 \approx 10^4$ corresponds to $r_\mathrm{m}^1 \approx \pi$ nm and is the most probable void size for $\varepsilon_\mathrm{i}^\mathrm{g}$=1. As can be seen, with decreasing $\varepsilon_\mathrm{i}^\mathrm{g}$, the SDF becomes wider and shifts towards bigger void size due to increase of x_m according to Eq. (2). Additional data shown on the same graph by full symbols are the result of a full-scale calculations of the temporal evolution of SDF, performed using a computer code described in ref. [4,21], and compare perfectly well with the analytical results. We note that the case of electron irradiation is obtained in the limit $\varepsilon_\mathrm{i}^\mathrm{g} \to 0$. Eqs. (2) and (7) are not supposed to be valid in this case, but, show qualitatively correct behaviour, namely, that there is no saturation of swelling.

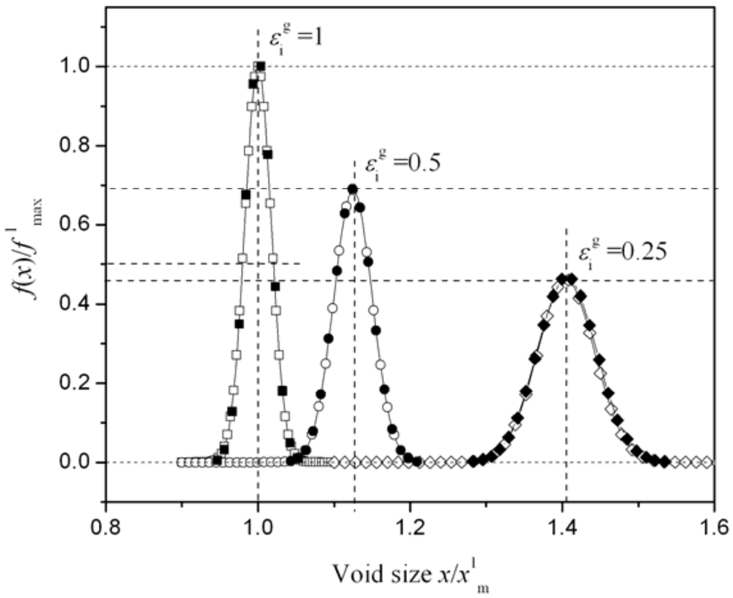

Figure 1. The SDF of voids calculated for B=0.04, α=1 and ε_i^g=0.25, 0.5 and 1. x_m^1=10^4 is the most probable void size for ε_i^g=1. The SDFs are normalised by the maximum value, $f_{\max}^1$, calculated for ε_i^g=1, assuming C_0 to be the same.

The analysis presented is limited to random distribution of voids and any correlation in void positions, *e.g.* due to formation of ordered structures [15,16], would unavoidably change the kinetics [23]. The most significant result is the contradiction of a very narrow width of the theoretical SDF with much bigger spreads of the void sizes observed. This discrepancy seems important for uncovering fundamental mechanisms of damage accumulation, and is discussed further below.

III. Approach of the steady state

To analyse how the steady state is established, we simplify Eq. (1) by taking $Z_i = Z_v$:

$$\frac{dS}{d\phi} \approx \frac{\varepsilon_i^g \alpha r r_m (r_m - r)}{(r_m + \alpha r)(r_m^2 + \alpha r^2)}. \tag{8}$$

In the limiting case, when $r << r_m$ and voids are dominant sinks, the dose dependence of the mean void radius from its initial value r_0, formed during nucleation stage not considered here, is readily obtained

$$r = \left[r_0^5 + \frac{5\varepsilon_i^g Z_v \rho r_m}{(4\pi N)^2}\phi \right]^{1/5}, \quad \alpha\left(\frac{r}{r_m}\right)^2 >> 1, \tag{9}$$

which is similar to that obtained in [4,24].

Eq. (8) predicts a big difference in doses required to reach the equilibrium at low and high void density. This effect is demonstrated by the full-scale calculations of the dose dependence of the mean void radius on the irradiation dose performed using a computer code described in ref. [4,21]. The results are shown in Fig. 2. The value of ε_S is assumed to be equal to 0.1 (*i.e.* ~ half that given by MD simulation of cascades for E_{PKA} > 5keV [22]; the factor of ½ is an assumed fraction of defects that recombine during the cascade annealing). The value of π corresponds to the void saturation radius at $\varepsilon_i^g = 1$ or B=0. As can be seen, when the void size is small enough, the curve calculated for α =100 is described satisfactorily by Eq. (9). Also, the doses required for reaching the steady state in this case is higher compared to that for α =0.01 by more than three orders of magnitude (a precise value is unknown since the calculations for α =100 were terminated at 100dpa). There are two important consequences of this effect.

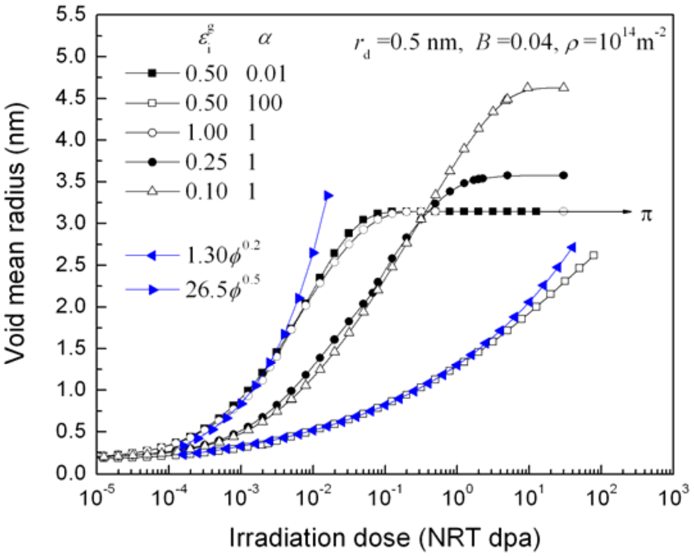

Figure 2. The dependence of the mean void radius on the irradiation dose, ϕ, calculated for different values of ε_i^g and α.

First, the steady state of void population distributed randomly is likely to be unrelated to the void lattices formation and possible saturation of swelling in void lattices. Indeed, the formation of void lattices in metals and alloys under cascade irradiation is observed at high void densities and in the dose range from several to several tens of dpa [16]. As can be seen from Fig. 2, at a high void density, α =100 (for $\varepsilon_i^g = 0.5$), the irradiation dose required to reach the steady state is much higher than 100 dpa, hence much higher than in experiments. In addition, it has been shown previously [23] that the formation of free channels between voids in void lattices provides escape roots for the SIA clusters to dislocations and leads to a significant increase of the void saturation radius. Thus, there must be some other reasons behind the saturation observed.

Second, it is usually observed that, at relatively low void densities, when $\alpha \le 1$, voids start to grow after some incubation period and the growth is unlimited [25]. Our calculations presented on Fig. 2 show that the dose required to reach the steady state in these conditions is small, ~1 dpa for α =1 and ε_i^g =0.25, and generally in the range from 10^{-2} to 10 dpa depending on ε_i^g and α. It is tempting to think that the incubation period of swelling could be because voids reached their critical radius. It is worth mentioning that, despite many successes of the PBM in explaining features of microstructure evolution of metallic materials under neutron irradiation at low irradiation doses (<1dpa), an unlimited void growth observed at higher doses after the incubation period of swelling cannot be explained in the framework of the model as formulated. Possible ways of resolving this contradiction are proposed in a separate paper [18].

The c-type voids were the smallest and made the smallest contribution to swelling, while the a-type voids were the largest.

ACKNOWLEDGEMENTS

The research was sponsored by a research grant from the UK Engineering and the Physical Sciences Research Council (A.V.B.) and by the Office of Fusion Energy Sciences U.S. Department of Energy, under contract DE-AC05-00OR22725 with UT-Battelle, LLC (S.I.G.).

REFERENCES

[1] G.W. Greenwood, A.J.E. Foreman, D.E. Rimmer, J. Nucl. Mater. 4 (1959) 305.
[2] C. Cawthorne, E.J. Fulton, Nature 216 (1967) 575.
[3] H. Trinkaus, B.N. Singh, A.J.E. Foreman, J. Nucl. Mater. 199 (1992) 1.
[4] B.N. Singh, S.I. Golubov, H. Trinkaus, A. Serra, Yu.N. Osetsky, A.V. Barashev, J. Nucl. Mater. 251 (1997) 107.
[5] S.I. Golubov, B.N. Singh, H. Trinkaus, Philos. Mag. A 81 (2001) 2533.
[6] B.N. Singh, M. Eldrup, S.J. Zinkle, S.I. Golubov, Philos. Mag. A 82 (2002) 1137.
[7] B.V. Guerard, D. Grasse, J. Peisl, Phys. Rev. Lett. 44 (1980) 262.
[8] T. Diaz de la Rubia, M.W. Guinan, Phys. Rev. Lett. 66 (1991) 2766.
[9] A.J.E. Foreman, W.J. Phythian, C.A. English, Philos. Mag. A 66 (1992) 671.
[10] M. Kiritani, J. Nucl. Mater. 251 (1997) 237.
[11] T. Hayashi, K. Fukmuto, H. Matsui, J. Nucl. Mater. 307-311 (2002) 993.
[12] K. Arakawa, K. Ono, M. Isshiki, K. Mimura, M. Uchikoshi, H. Mori, Science 318 (2007) 956.
[13] Yu.N. Osetsky, D.J. Bacon, A. Serra, B.N. Singh, S.I. Golubov, Philos. Mag. A 83 (2003) 61.
[14] A.J.E. Foreman, UKAE Authority Harwell Report No. AERE-R-7135 (1972).
[15] J.H. Evans, Nature 229 (1971) 403.
[16] W. Jäger, H. Trinkaus, J. Nucl. Mater. 205 (1993) 394.
[17] M.J. Norgett, M.T. Robinson, I.M. Torrens, Nucl. Eng. and Design 33 (1975) 50.
[18] A.V. Barashev and S.I. Golubov, ORNL Report ORNL/TM-2008/141 (2008), available online via the US DOE information bridge http://www.osti.gov/bridge.
[19] A.V. Barashev, S.I. Golubov, submitted to Philos. Mag. (2008).
[20] F.C. Goodrich, Proc. R. Soc. London A 277 (1964) 167.
[21] S.I. Golubov, A.M. Ovcharenko, A.V. Barashev, B.N. Singh, Philos. Mag. A 81 (2001) 643.
[22] D.J. Bacon, Yu.N. Osetsky, R. Stoller, R.E. Voskoboinikov, J. Nucl. Mater. 323 (2003) 152.
[23] A.V. Barashev, S.I. Golubov, H. Trinkaus, Philos. Mag. A 81 (2001) 2515.
[24] B.N. Singh, A.J.E. Foreman, Philos. Mag. A 66 (1992) 975.
[25] F.A. Garner, M.B. Toloczko, B.H. Sencer, J. Nucl. Mater. 276 (2000) 123.
[26] A.V. Kozlov, I.A. Portnykh, L.A. Skryabin, E. A. Kinev, J. Nucl. Mater. 307–311 (2002) 956.
[27] I.A. Portnykh, A.V. Kozlov, V.L. Panchenko, V.M. Chernov, F.A. Garner, J. Nucl. Mater. 367–370 (2007) 925.

Kinetics of Self-Interstitial Cluster Aggregation Near Dislocations and their Influence on Hardening

Ming Wencor[a] , Akiyuki Takahashi[b] , Nasr M. Ghoniem[a]

[a]*Department of Mechanical and Aerospace Engineering*
University of California, Los Angeles
Los Angeles, CA 90095

[b]*Department of Mechanical Engineering,*
Tokyo University of Science, Chiba, Japan

Abstract

Kinetic Monte Carlo (KMC) computer simulations are performed to determine the kinetics of SIA cluster "clouds" in the vicinity of edge dislocations. The simulations include elastic interactions amongst SIA clusters, and between clusters and dislocations. Results of KMC simulations that describe the formation of "SIA clouds" during neutron irradiation of bcc Fe and the corresponding evolution kinetics are presented, and the size and spatial distribution of SIA clusters in the cloud region are studied for a variety of neutron displacement damage dose levels. We then investigate the collective spatio-temporal dynamics of SIA clusters in the presence of internal elastic fields generated by static and mobile dislocations. The main features of the investigations are: (1) determination of the kinetics and spatial extent of defect clouds near static dislocations; (2) assessment of the influence of localized patches of SIA clouds on the pinning-depinning motion of dislocations in irradiated materials; and (3) estimation of the radiation hardening effects of SIA clusters. The critical stress to unlock dislocations from self-interstitial atom (SIA) cluster atmospheres and the reduced dislocation mobility associated with cluster drag by gliding dislocations are determined.

1 Introduction and Background

Self Interstitial Atom (SIA) clusters that readily form in a variety of irradiated bcc, fcc and hcp metals are usually treated as nano-scale prismatic dislocation loops. These clusters nucleate on the periphery of collision cascades and subsequently perform fast thermally-activated one-dimensional (1-D) motion [1]. The motion and interaction of SIA clusters have drastic effects on the physical and mechanical properties of irradiated materials, most notably their influence on void swelling [2] and radiation hardening [3, 4]. The interaction between a single SIA cluster and other clusters, stacking fault tetrahedra, or single dislocations have been extensively studied by atomistic simulations [5, 6, 7]. Nevertheless, some of the most important phenomena associated with SIA clusters, such as their spatial segregation into heterogeneous aggregates and their agglomeration around dislocations in "clouds" similar to Cottrell atmospheres [3, 8], have not yet been investigated because of the size limitations of atomistic simulations. These phenomena are the result of the collective behavior of a large number of SIA clusters, and as such one must rely on statistical mechanics or equivalent computer simulation techniques to resolve the spatio-temporal dynamics of SIA cluster ensembles. Analytical calculations [4] as well as Kinetic Monte Carlo (KMC) simulations [8] have shown that the motion and interactions of SIA clusters lead to the formation of dislocation loop rafts and the decoration of dislocations by SIA clusters. However, the kinetics of SIA cluster cloud evolution, the collective interaction between SIA clusters and dislocations, and the spatial heterogeneity of SIA aggregates have not yet been explored.

The formation of SIA cluster rafts and clouds around dislocations have significant impact on the onset of plastic yield and subsequent hardening as a result of dislocation interaction with spatially segregated SIA clusters. When the applied stress is increased above a critical value, grown-in dislocations that are trapped by SIA cluster clouds may drag some of these clusters along, and thus freed dislocations would have reduced mobility. Drag on dislocations by SIA clusters, and dislocation interaction with immobile vacancy clusters or with other dislocations determine the rate of work-hardening in the post-yield deformation regime. In irradiated materials, the presence of irradiation-induced defects alters the plastic deformation behavior significantly, and it is therefore important to investigate the role played by SIA cluster ensembles.

Radiation hardening has been described by the change in the critical resolved shear stress (CRSS) due to an array of defects in the two limiting cases of "strong" or "weak" obstacles. If the obstacles are strong, the change in CRSS is expressed as $\Delta\tau = \alpha\mu b/l$, where α is a parameter representing the obstacle strength, μ is the shear modulus, b is the magnitude of the Burgers vector and l is the average inter-obstacle distance. On the basis of Orowan's work for strong obstacles [9], Seeger [10] developed a hardening model in which vacancy clusters are referred to as "depleted zones". An alternative obstacle-controlled hardening model was developed for weak obstacles by Friedel-Kroupa-Hirsch (FKH) [11, 12]. In this limiting case, the increase of the critical shear stress by a random array of obstacles of diameter d and volume density N is given by $\Delta\tau = \frac{1}{8}\mu bdN^{2/3}$. Correlation with experiments in both these limiting cases is qualitative at best, and has only been examined for the onset of plastic flow, i.e. at the yield point. Although these analytical models have been used to explain experimental observations, they suffer from uncertainties associated with describing the obstacle strength. In addition, they do not provide any information on post-yield deformation, including the observed yield drop during tensile testing of irradiated materials. In analogy with the Cottrell hardening model due to an atmosphere of impurities [13] around dislocations, Singh, Trinkaus and Foreman proposed the mechanism of cascade induced source hardening (CISH) [3, 4]. Their approach provides a rational explanation for the observed occurrence of yield drop in irradiated fcc metals. Singh et al. [3] proposed that the irradiation-induced increase in the yield stress is a consequence of trapping the majority of F-R sources by "defect clouds", and their subsequent release when the applied stress exceeds a critical value. The issue of dislocation pinning by radiation-induced SIA clusters and the subsequent depinning of dislocations upon application of an external stress field is central to the understanding of radiation hardening. The physics of SIA cluster cloud formation and the interaction between dislocations and such clouds require more detailed computer simulations.

The objective of the present study is to investigate the kinetics of SIA cluster cloud evolution in the presence of internal elastic fields generated by dislocations, and the subsequent influence of the formation of such clouds on dislocation motion under applied stress. The effects of dislocation pinning by SIA clouds on radaition hardening will also be assessed. The present investigation is based on the model developed in reference [8], with the following new features: (1) the kinetics and spatial extent of defect clouds near static dislocations; (2) the interaction between mobile dislocations and *glissile* SIA clusters; and (3) the hardening effects due to SIA clusters. First, we present results of KMC simulations that describe the formation of SIA clouds during neutron irradiation of bcc Fe and the corresponding evolution kinetics in section § 2.2. We report on the size and spatial distribution of SIA clusters in the cloud region as function of the neutron displacement damage dose. The results are then used in section § 3 as input to Parametric Dislocation Dynamics (PDD) simulations aimed at determination of the influence of SIA clouds on dislocation motion and on the critical stress for dislocation unlocking from SIA defect atmospheres. Conclusions are finally presented in section § 4.

2 Kinetics of SIA Cluster Cloud Evolution

2.1 Computer Simulation Method

To study the spatial distribution of SIA clouds around dislocations and the evolution kinetics of such clouds in bcc Fe, we utilize KMC simulation methodology of Wen, Ghoniem and Singh [8]. Elastic interactions between irradiation-induced SIA clusters and dislocations are incorporated in the present KMC simulations of SIA defect cloud evolution. The interaction between SIA clusters is calculated by linear elasticity theory, where the cluster is treated as a circular infinitesimal prismatic dislocation loop with its Burgers vector in a closed-packed $\langle 111 \rangle$-direction normal to its habit plane. The relationship between the loop radius, R, and the number of self-interstitial atoms in the cluster, N, is $N = \sqrt{3}\pi R^2/a^2$, where $a =$ 0.2867 nm is the lattice constant of iron. Although small irradiation-induced interstitial clusters made of parallel $\langle 110 \rangle$ dumbbells are found to be stable in bcc iron [15], larger clusters adopt either the $\langle 111 \rangle$ or the $\langle 100 \rangle$ orientation [16], as observed in experiments [17]. Interstitial loops of the $\langle 100 \rangle$-type are regarded as nearly immobile, based on experimental evidence and the fact that migration energies larger than 2.5 eV have been reported [16]. Therefore, the present investigation will focus on $\langle 111 \rangle$ interstitial clusters as the dominant type in clouds and rafts in bcc Fe. The numerical method developed by Ghoniem and Sun [18] is employed to evaluate the interaction between small defect clusters and dislocations. Since SIA clusters are glissile, they perform 1-D random motion in the slip direction parallel to the Burgers vector of the loop. An SIA cluster may change its moving direction by a thermally activated Burgers vector change. However, as the cluster size increases, thermally-activated reorientation from one Burgers vector to another becomes increasingly more difficult. Reorientation of the Burgers vector can still take place when one accounts for the elastic interaction energy between clusters, or between clusters and dislocations [8].

To analyze the spatial distribution of SIA clusters in the vicinity of dislocations and the kinetics of cloud buildup, we first consider a KMC model that involves the interaction between an edge dislocation and SIA clusters. A computational box of $300a \times 300a \times 300a$ is used and the simulation box edges are oriented parallel to the cubic axes. An edge dislocation with $\mathbf{b} = a/2[\bar{1}11]$ lying on a (101) plane is inserted in the simulation box. The simulation box represents an isolated region around a straight edge dislocation in an infinite medium, where the stress field is due to the dislocation and the surrounding SIA clusters. A periodic boundary condition is imposed on the motion of SIA clusters in and out of the simulation box to preserve a net zero flux for existing SIA clusters.

2.2 Formation of SIA Clouds Near Edge Dislocations

KMC simulations require detailed information on defect production due to displacement cascades. Only a very small fraction of defects produced in collision cascades can escape recombination reactions within the cascade volume and migrate freely through the lattice [19]. We therefore used the initial defect configurations produced by 100 keV displacement cascades, obtained from MD simulations of Stoller [19] as input, and performed separate KMC simulations to obtain the number and configuration of SIA clusters that escape the immediate cascade region and migrate long distances in the matrix. The conversion of the number of Frenkel pairs N_F produced by a single displacement cascade to damage dose P (in units of dpa) is given by $P = N_F/N_t$, where N_t is the total number of atoms in the simulation volume. KMC simulation results of a single 100 keV displacement cascade results in 36 SIA clusters with size ranging from 1 to 35 SIAs. The fraction of SIAs in large clusters (containing more than 14 SIAs) is 54%. The size distribution of large clusters resulting from KMC simulations of single cascades are then used as input in the present study. Specifically, in the present KMC simulations, 60% of all interstitial clusters initially introduced into the simulation box contain 14-SIAs, 20% contain 21-SIAs, and the rest contain 35-SIAs. We introduce this size distribution of SIA clusters because TEM observations of are not capable of differentiating smaller clusters [4].

In post-irradiation experiments, the material is first irradiated in an unstressed condition to a particular damage dose level that corresponds to a specific density of SIA clusters. To simulate irradiation conditions, we assume here that the dislocation is rigid and fixed in the simulation volume, and a sequence of 100 keV displacement cascades are continuously introduced into the simulation box at a fixed dose rate of 5×10^{-6} dpa/s. For every single cascade, the number and size distribution of clusters are assumed to be identical, while they are randomly placed in the simulation box.

Diffusion of interstitial clusters is governed by a generalized size-dependent Arrhenius law, developed by Osetsky et al. [5] to describe the 1-D diffusional transport behavior of SIA clusters

$$\omega = \omega_0 n^{-S} \exp\left(-\frac{E_m}{k_B T} \right) \tag{1}$$

where E_m is the average effective activation energy, n the number of SIAs in the cluster, and ω_0 is a pre-exponential factor. The value of E_m was found to be close to that of an individual crowdion. For clusters containing up to 91 SIAs in iron, it is estimated that $E_m = 0.023 \pm 0.003$ eV for $\langle 111 \rangle$ clusters [5]. By fitting to the results of numerous simulations, the following parameter values for Fe were found to describe the MD data very well, and are used in our KMC simulations: $\omega_0 = 6.1 \times 10^{12}$ s^{-1}, and $S = 0.66$. Rotation to other close-packed glide directions is also governed by an Arrhenius law, with an assumed attempt frequency the is the same as ω_0, and an assumed activation energy of 0.05 eV per crowdion. This linear dependence of the energy barrier for rotation on cluster size is adopted on the basis of MD simulations confirming that the motion of SIA clusters is the result of the motion of individual $\langle 111 \rangle$ crowdions [5], and that the reorientation may occur in a one-by-one fashion [20]. For small interstitial clusters, such as 2- or 3-SIAs clusters, the activation energy for rotation predicted by atomistic simulations [21] is higher than the value given by the simple 0.05 eV per crowdion relationship used in the present study. However, actual values for the rotation energy barriers are as yet unknown for the large clusters used in our simulations because the time-scale involved is prohibitive for MD simulations. For large clusters involved in the present study, the current estimated value of 0.05 eV per crowdion will result in the energies for rotation bigger than 0.7 eV, and is sufficient to preserve the preferential 1-D motion of large interstitial clusters [8]. It is noted that the elastic interaction energy between SIA clusters and dislocations at a close range, or between SIA clusters themselves when they are within a few atomic distances from one another is sufficiently strong that clusters reorient regardless of the exact value of the activation barrier.

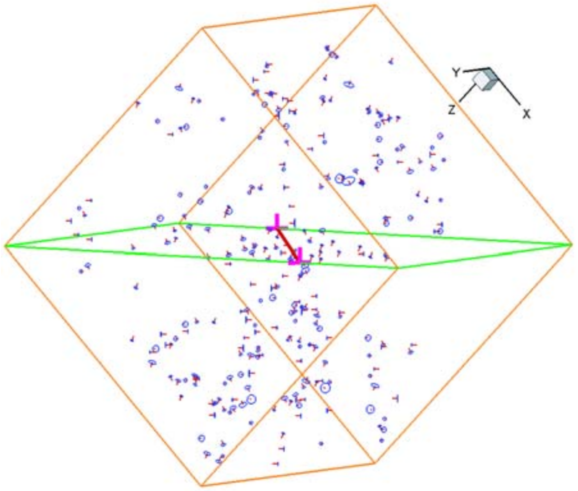

(a)

Figure 1: KMC simulation result of microstructure in bcc Fe irradiated at 300 K with an initial number of 400 SIA clusters and a rotation energy barrier of 0.2 eV/crowdion.

The presence of internal stress fields, for example, dislocations and SIA clusters, would further enhance the 3D nature of SIA cluster transport. The possibility of the Burgers vector rotation may increase in the presence of the elastic interaction between clusters, and/or between clusters and dislocations. We performed additional simulations to demonstrate that cluster rotation is a prerequisite to the formation of dislocation decorations. Fig. 1 shows KMC simulation results of the microstructures in bcc Fe with an initial number of 400 SIA clusters distributed in the simulation box at 300 K with an energy barrier for rotation of 0.2 eV/crowdion. The simulation results indicate that dislocation decoration is negligible for a relatively small amount of irradiation-induced damages if interstitial clusters perform pure 1-D motion. Simulations with an energy barrier of 1 eV/ crowdion produced similar results to those of Fig. 1. However, experimental results [22] show that even at a very low damage dose, 0.0001 dpa, a clear increase in the yield stress is observed, from an unirradiated value of 138 MPa to 160 MPa after irradiation. This suggests that dislocation decoration has already started building up at very low damage doses. In order to achieve a certain amount of decoration, SIA clusters must be able to change their orientation with lower energy barriers than energetics would suggest for thermally-activated spontaneous processes.

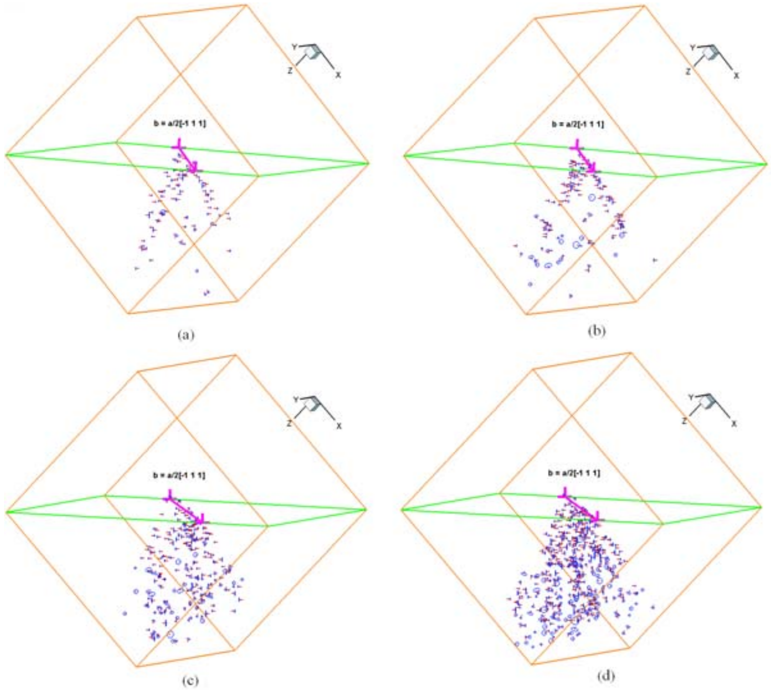

(a)
(b)
(c)
(d)

Figure 2: SIA cluster cloud evolution on the tensile side of an edge dislocation in bcc Fe irradiated at 300 K to a displacement dose level of (a) 2×10^{-4} dpa, (b) 4×10^{-4} dpa, (c) 0.001 dpa, and (d) 0.0026 dpa, respectively. The edge dislocation has a Burgers vector $\mathbf{b} = a/2[\bar{1}11]$. Each SIA cluster is represented by a small circle corresponding to its size with a line segments pointing along its Burgers vector direction. SIA clusters that are trapped in the cloud region are highlighted.

We performed KMC simulations for the evolution of an SIA cloud around an edge dislocation in pure iron irradiated at 300 K up to a displacement dose of 2.6×10^{-3} dpa. A sequence of 100 keV displacement cascades with the previously described size distribution were introduced randomly into the simulation box at a constant rate of 5×10^{-6} dpa. When an extremely mobile 1-D migrating interstitial cluster passes through the neighborhood of a pre-existing dislocation, it feels the influence of the dislocations's strain field. The overall mobility and spatial distribution of SIA clusters are significantly changed as a result of dislocation-cluster interactions. With irradiation damage building up, a significant fraction of initially glissile clusters were found to be attracted to the dislocation forming a `Λ'–shaped cloud. In effect, these clusters re-orient themselves by rotation of their Burgers vectors to respond to the elastic field of the dislocation. Fig. 2(a)-(d) show the time evolution of the cloud build-up process on the tensile side of an edge dislocation in bcc Fe irradiated to 2.6×10^{-3} dpa at 300 K. The stress field of the dislocation,, aided by cluster mutual elastic interactions, render most of the clusters virtually immobile in the vicinity of the edge dislocation. At higher displacement damage doses, the percentage of SIA clusters trapped in the region of attractive elastic interaction is not as high as that at low doses, as the screening effects of existing defects increases, and SIA accumulation in the trapping region approaches saturation.

To give a clear view of the structure of the cloud, we use lighter color for SIA clusters outside the SIA cloud and highlight those that were trapped in the cloud region in Fig. 2. Even at low damage doses, for example at 0.0002 dpa as shown in Fig. 2(a), SIA clusters are already trapped in the region of positive dilatational strain in the vicinity of the edge dislocation, where the elastic interaction between the dislocation and the SIAs is attractive. The clusters form two wings that are 30° with respect to the normal direction of the slip plane. It is observed that most of the trapped defect clusters have Burgers vectors that are parallel to that of the edge dislocation. In view of the initial random distribution of SIA clusters' Burgers vectors, the present results confirm that SIA clusters near dislocations rotate their Burgers vectors in response to the influence of the strain field of the edge dislocation. As the displacement damage dose increases, the two wings consisting of SIA clusters continue to grow, and become more packed and prominent because of additional cluster trapping. With further agglomeration of SIA clusters in extended cluster wings, trapped clusters start to precipitate in between the two wings and lead to the eventual disappearance of the distinct and separate wings, as shown in Fig. 2(c). Fig. 2(d) shows that at 0.0026 dpa, a wedge-shaped SIA cluster "cloud" has been fully developed along the dislocation line. The formation of a Cottrell-like atmosphere in the vicinity of dislocations has been investigated experimentally, theoretically and numerically [3, 4, 8]. However, the characteristic arrangement and morphology of SIA clouds (which are important for studying microstructure evolution and the corresponding effects plastic deformation) have never been examined. The present simulations indicate that at low damage dose, a `Λ'–shaped wing structure made up of SIA clusters is formed first, and wedge-shaped clouds are finally developed when SIA clusters are immobilized in the space between the wings.

In the trapping region close to the slip plane of the edge dislocation, the Burgers vectors of most clusters are parallel to the edge dislocation's Burgers vector. In the outer region, however, the orientational distribution of the Burgers vectors is almost random. This implies that as the cloud evolves, the attractive stress field of the edge dislocation is gradually shielded by the defect clusters in the cloud. New cluster trapping takes place now ahead of the existing configuration resulting from the elastic interaction between clusters themselves and their mutual immobilization. Because the dominant mechanism for cluster trapping is cluster-cluster interaction instead of dislocation-cluster interaction, metastable immobile complexes consisting of SIA clusters with non-parallel Burgers vectors may form. Furthermore, we can expect that at a certain stage, SIA cluster trapping will stop, and that the defect cluster concentration in the trapping region will reach saturation. This saturation behavior is a consequence of two effects: (1) the buildup of the cloud near the edge dislocation, thus neutralizing its stress field, and (2) the evolution of damage in the matrix in between dislocations. In this work, damage is represented by sessile SIA clusters that are self-trapped in the matrix, but if one takes into account vacancy clusters as well, the saturation may be reached even at smaller dose. SIA loop coarsening may become significant and would eventually lead to the formation of dislocation walls, as pointed out by Trinkaus, Singh and Forman [23].

3 The Influence of SIA Clouds on Dislocation Motion

The interaction between a dislocation and SIA clouds is investigated by the Parametric Dislocation Dynamics (PDD) method, described elsewhere [24]. The stress field of dislocations is calculated by the fast sum method [18], while an analytical form due to Kroupa is utilized to calculate the stress of SIA clusters as infinitesimal dislocation loops [25]. In the following, we present results of dislocation dynamics simulations for the un-pinning process of dislocations from their surrounding SIA cluster clouds. We first consider an isolated patch of SIA clusters, and then present estimates for the hardening effect due to SIA clouds trapping dislocations. We also present results for the interaction between SIA clusters and dislocations under applied stress in an effort to study the influence of SIA clusters on the effective mobility of dislocations in irradiated materials.

3.1 Pinning of Dislocations by SIA Clouds

The interaction between a glissile dislocation and a cloud of SIA clusters is important in two respects. First, one needs to estimate the degree of SIA source hardening at a given displacement damage dose by determining the critical stress necessary to pull a dislocation away from its cloud. Then, once the pinned dislocation pulls away from its cloud, it is interesting to determine the resistance to its glide motion by pockets of cloud remnants that increase the effective back stress on the dislocation. We will investigate here the resistance of localized SIA clouds to dislocation glide motion, where we assess the influence of SIA cluster motion (i.e. sessile versus glissile clusters) on the effective mobility of dislocations. The magnitude of source hardening will also be estimated by PDD simulations.

Fig. 3 shows a typical volume used in the present simulations, of size: 1 μm × 1 μm × 200 nm. The x, y and z axes are along the $[\bar{1}\bar{2}1]$, $[\bar{1}11]$ and $[\bar{1}0\bar{1}]$ directions, respectively. A straight edge dislocation with $[\bar{1}11]$ Burgers vector is placed on the $(\bar{1}0\bar{1})$ slip plane. In order to remove any effects of boundary conditions, the two end points of the dislocation line are restricted to move only along the intersection lines of the slip plane and the two $(\bar{1}\bar{2}1)$ planes at the boundaries. Also, the directions of the tangent vectors of the end points are fixed to the $[\bar{1}\bar{2}1]$ direction, which is parallel to the tangent vector of the initial straight edge dislocation. It should be noted that only glide motion of dislocations is involved in the current study. SIA clouds obtained from previous KMC simulations are directly used as input into the simulation volume. For the sake of simplicity and in view of the formation of immobile complexes consisting of SIA clusters with non-parallel Burgers vectors in SIA clouds, all SIA clusters are assumed to be immobile in these simulations. We will later examine the effects of the simultaneous dynamic motion of the dislocation and SIA clusters in the cloud. The external shear stress is gradually increased by 1MPa, then a time-relaxation is performed for 2000 time steps to obtain an equilibrium shape of the dislocation. This process is repeated until the dislocation breaks away from the SIA cloud, and thus a critical value of the break-away shear stress is determined.

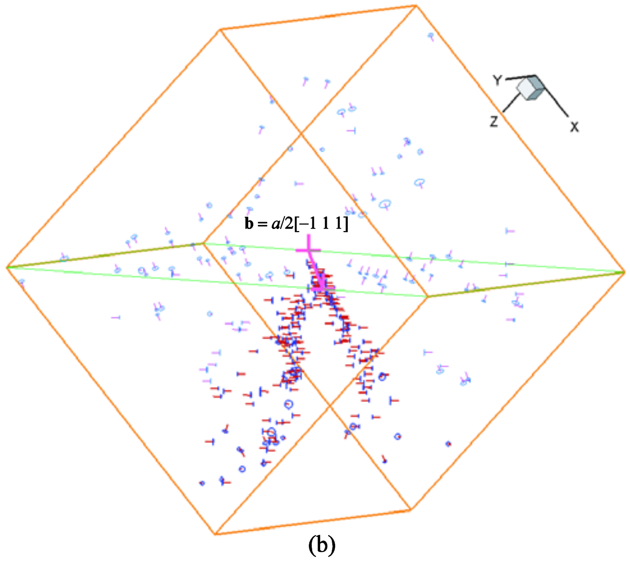

(b)

Figure 3: Schematic of the volume used in PDD simulations of the interaction between a dislocation and an SIA cluster cloud. The dislocation is initially straight, and the SIA cloud is obtained from the results of separate KMC simulations.

We first investigate the motion of a dislocation, locally decorated by an SIA cloud that is 110 nm along the dislocation line. The relative positions of the dislocation and the SIA cloud are directly obtained from previous KMC simulations. The simulations indicate that at low applied stress, the middle of the dislocation, which is decorated by the SIA cloud, cannot move while the rest of the dislocation glides on the slip plane. This behavior suggests that the SIA cloud has a pinning effect on the dislocation. Bowing out of the dislocation is extended by increasing the externally applied shear stress. The dislocation eventually breaks away from the SIA cloud when the applied shear stress reaches a critical value. The interaction between a dislocation and a pre-existing SIA cloud is also of interest, because the cloud may result of pinning of other mobile dislocations on nearby glide planes. Fig. 4 illustrates the relative positions of the dislocation and the SIA cloud as initial simulation conditions. The slip plane of the dislocation is selected at 20 nm and at 40 nm from the top of the SIA cloud. The slip plane at 40 nm from the top is very close to the bottom of the SIA cloud. The moving dislocation is initially free from any decorations, and the distance between the initial dislocation position and the SIA cloud on the slip plane is taken to be 150 nm.

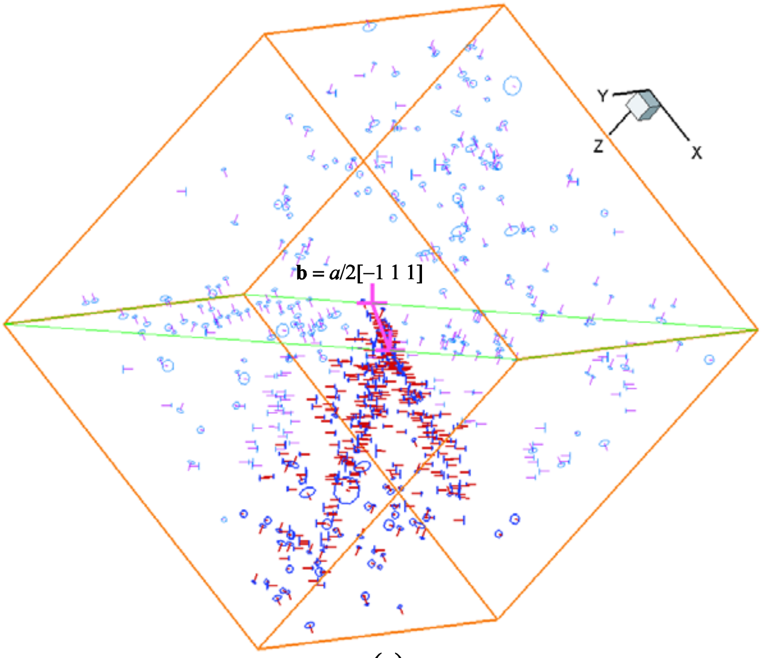

(c)

Figure 4: Dislocation positions in PDD simulations of interactions between a dislocation and a pre-existing SIA cloud.

Fig. 5 shows the dependence of the critical shear stress on the irradiation dose for an SIA cloud formed at 2×10^{-4}, 4×10^{-4}, 10^{-3}, 2×10^{-3} and 2.6×10^{-3} dpa. In the figure, the critical shear stress for the decorated dislocation (i.e. $d=0$) increases from 3 to 19 MPa as the irradiation damage dose increases from 2×10^{-4} to 2×10^{-3} dpa. The critical shear stress at 2×10^{-3} dpa is about 6 times larger than that at 2×10^{-4} dpa. Beyond that range, the critical shear stress begins to saturate because of the shielding effects of the cloud contents. The figure also illustrates the dependence of the critical shear stress on the displacement damage dose (i.e. the cloud content). The dependence of the critical shear stress on irradiation damage dose is similar in the three cases, but the position of the slip plane clearly changes the magnitude of the critical shear stress.

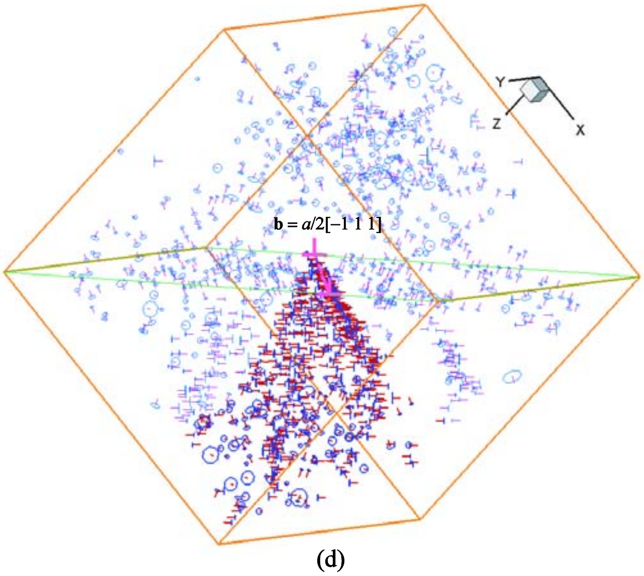

Figure 5: Critical shear stress for cutting through a localized SIA cluster cloud. The critical shear stress of a dislocation decorated with an SIA cloud is also shown ($d = 0$).

When the dislocation glides on the middle slip plane, the critical shear stress becomes smaller than that for the initially decorated dislocation. On the other hand, when the dislocation glides on the bottom slip plane, the critical shear stress again becomes larger. To gain a better understanding of the role of the SIA cloud on resisting the motion of dislocations gliding on various slip planes, we show in Fig. 6 a top view of dislocation configurations as it interacts with the cloud. When dislocations glide on slip planes at the bottom of clouds, they feel long-range repulsive forces, and the dislocation starts to be bend before it physically meets the SIA cloud. Generally, SIA clusters prefer to be on the tension side of the dislocation, and are not likely to be on the compression side. A dislocation feels an attractive force from clusters on the tension side, and a repulsive force from clusters on the compression side. In the case of the middle slip plane, almost half of the SIA clusters are on the compression side, and the rest are on the tension side. Therefore, half of the clusters results in an attractive force, while the other half induces a repulsive force on the dislocation. These two types of forces partially cancel one another, and consequently, the pinning effect of the SIA cloud becomes weaker than that of the case of a cloud directly decorating the dislocation. On the other hand, in the case of the bottom slip plane, the majority of the clusters are on the compression side. The dislocation thus feels mainly a repulsive force, and thus the critical shear stress becomes larger than that in the case of the middle slip plane.

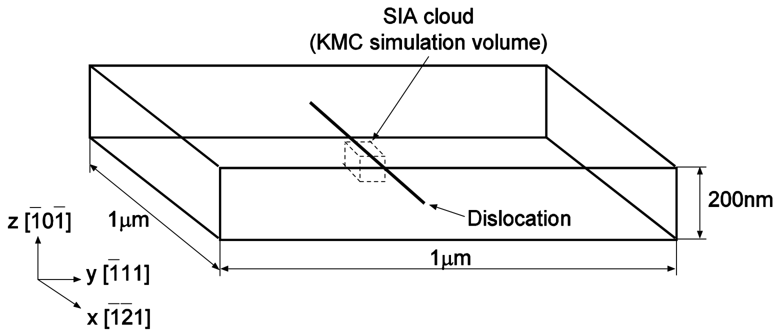

Figure 6: Top view of dislocation configurations as it interacts with a pre-existing SIA cluster cloud on a slip plane 40 nm below the top of the cloud. (a)2 MPa, (b)4 MPa, (c)10 MPa, and (d)11 MPa.

We consider now the process of full dynamic interaction between a moving dislocation and glissile SIA clusters in the cloud. Here, the equations of motion for the dislocation nodes and clusters have to be solved simultaneously. The results of this simulation are shown in Fig. 7 for the clouds at 10^{-3} dpa. The figure clearly shows that the SIA cloud works as a localized obstacle, which results in a pinning effect on the dislocation. As the dislocation approaches the cloud, SIA clusters are swept into various configurations, most of which are self-trapping. However, the dislocation succeeds in dragging a few SIA clusters along, as shown in the figure, which results in reduced dislocation mobility. It is thus reasonable to conclude that SIA clouds act as localized pinning obstacles, and that they also result in increasing the drag on further dislocation motion, and thus reduce dislocation mobility. It is noted that only a very small fraction of SIA clusters that are close to the slip plane of the dislocation in the cloud are dragged by the dislocation. It suggests that the development of the extensive SIA cloud is due to immobile complexes consisting of SIA clusters with non-parallel Burgers vectors that are formed in the cloud. The majority of the SIA clusters in the cloud is held together by mutual cluster-cluster interactions.

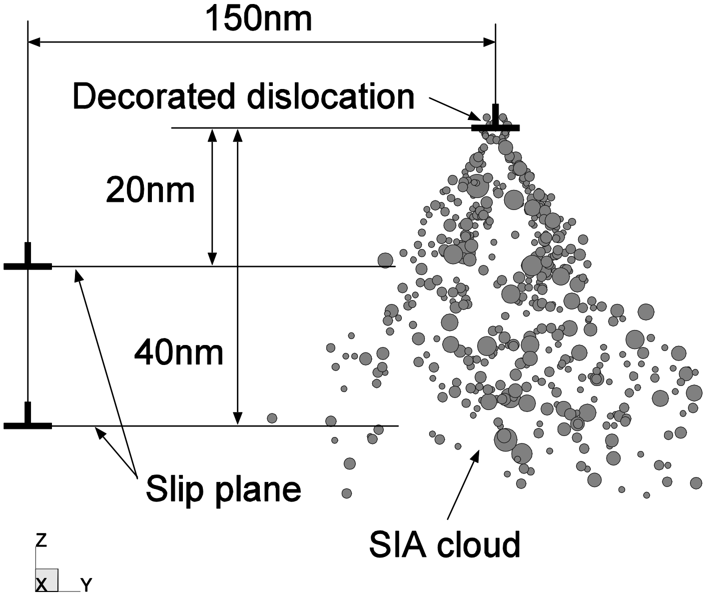

Figure 7: Configurations of a moving dislocation and a dynamic SIA cloud during the interaction between the dislocation and cloud. The applied stress (in MPa) at each snapshot is: (a) 4; (b) 10;(c) 14; (d) 18; (e) 20; and (f) 26.

3.2 Dislocation Depinning and the Influence of SIA Clouds on Hardening

The critical shear stress for dislocation unlocking from extensive decorations by SIA clouds is evaluated here, and this corresponds to the initiation of plastic yield under irradiation. To represent extensive decoration by SIA clouds, we constructed an array of localized SIA cluster clouds from separate KMC simulations along the dislocation line in order to decorate the entire dislocation. Fig. 8 shows the dislocation configurations during the break-away process from the SIA cluster clouds (i.e. source hardening) at 2.6×10^{-3} dpa. In this case, dislocation stops gliding on the slip plane due to the strong pinning by the SIA cloud. A small dislocation segment suddenly gets released from the cloud atmosphere (corresponding to a weak point in the cloud), and the entire dislocation then succeeds to unzip from the cloud. During the unzipping process of the dislocation line from the SIA cloud, all SIA clusters are assumed to be sessile. Fig. 9 shows the critical shear stress as a function of the neutron displacement dose for source hardening by SIA clusters. The critical shear stress (CSS) at 2×10^{-4} dpa is 32 MPa, and the stress increases gradually to 48 MPa at 4×10^{-4} dpa and about 72 MPa at 10^{-3} dpa. The CSS then increases slowly beyond 1×10^{-3} dpa with increasing dose, as seen in Fig. 9.

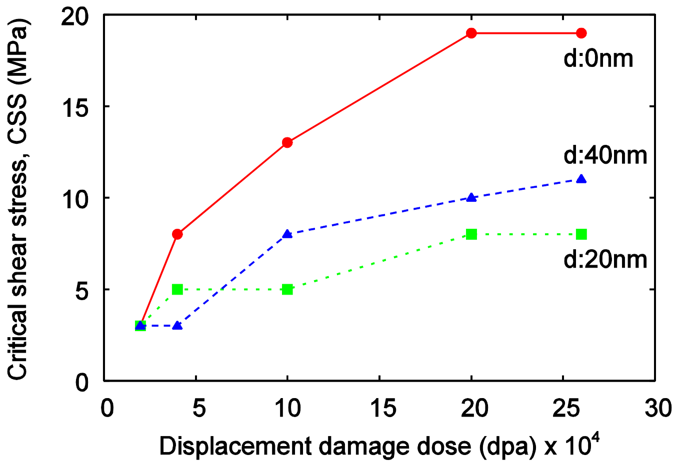

Figure 8: Dislocation configurations as it breaks away from source hardening SIA clouds. (a) 76 MPa, (b) 80 MPa, (c) 84 MPa, and (d) 86 MPa.

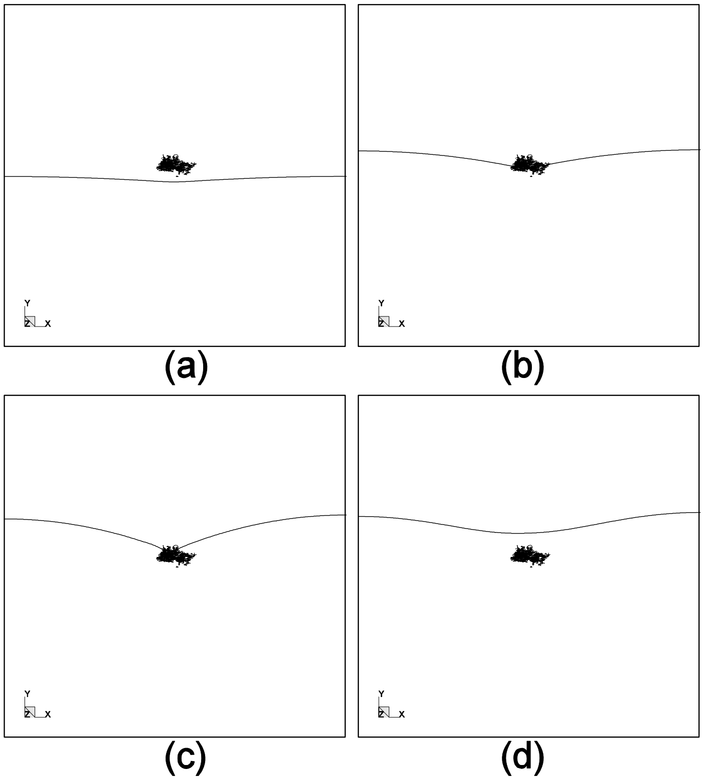

Figure 9: Critical shear stress (CSS) as a function of neutron displacement damage dose due to dislocation source hardening by SIA clouds.

Eldrup *et al.* performed irradiation experiments on Fe in the High Flux Isotope Reactor (HFIR) [22], and determined the stress-strain relationships in tension at a strain rate of 1.2×10^{-3} s^{-1}. Using a Taylor factor of 3.06 [26], we show in Fig. 10 a comparison between their experiments and results of the present simulations. In the model used here, SIA clusters corresponding to a particular dose are introduced in the simulation volume and are allowed to diffuse one-dimensionally till they self-trap or aggregate around the dislocation in a cloud. Thus, one expects that the gradual build-up of SIA clouds in the experimental situation should result in weaker interactions because of recombination events that take place over time. Notwithstanding these limitations, the comparison between experiments and the current model should be taken as qualitative at best, and with these limitations borne in mind. At the low dose of 2×10^{-4} dpa, the measured value of radiation hardening (i.e. increase in yield stress) is lower than the experimental value indicating that the major contribution to the yield strength in the experiments may be due to dislocation-dislocation interactions and dislocation interaction with small vacancy clusters. On the other hand, the calculated values for the increase in the equivalent uniaxial tensile stress at 10^{-3}, 2×10^{-3} and 2.6×10^{-3} dpa are in qualitative agreement with experimental results, and thus it may be possible that SIA cluster hardening becomes dominant.

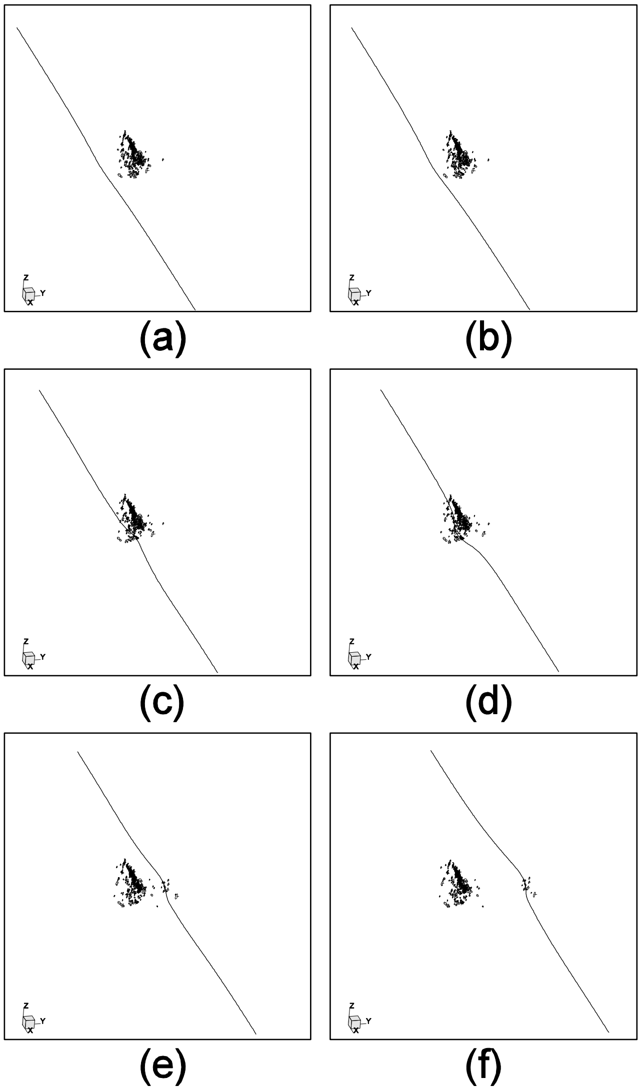

Figure 10: Yield strength as a function of displacement damage dose. PDD simulation results are plotted with solid circles, and experimental results obtained by Eldrup *et al*. [24] are plotted as circles with connecting line.

3.3 Motion of Decorated Dislocations

In this section, we consider the simultaneous motion of dislocations and SIA clusters. All SAI clusters are taken here to be mobile and interactive with the dislocation and amongst themselves. When a dislocation is released from the clouds that decorate it, the long-range elastic interaction between the dislocation and SIA clusters may tend to make some of the clusters that are close to the dislocation line glide along with the line. This may also reduce dislocation mobility [27]. MD simulations have demonstrated that interstitial loops can be dragged at extremely high speed by a gliding dislocation, and a model has been developed to describe the phenomenon of cluster drag [28]. The simulation setup is similar to that used in Section 3.2, and the localized SIA cluster clouds obtained from KMC simulations for bcc Fe irradiated to 0.001 dpa are utilized.

For simplicity, all SIA clusters are assumed to be rigid circular platelets and the analytical solution of the stress field of infinitesimal loops given by Kroupa [25] is utilized to calculate the force exerted on the dislocation line. The equation of motion for the center of a rigid SIA clusters can be written as

$$\frac{dx_i^{SIA}}{dt} = -\frac{M}{L}\int_A \frac{\partial \sigma_{jk}}{\partial x_i} b_j n_k dA \tag{2}$$

where, x_i^{SIA} is the center of the i-th rigid SIA cluster, M is the mobility, L is the circumference of the SIA cluster, A is its area, b_j and n_k are, respectively, the Burgers vector and unit vector normal to the plane of the SIA cluster, and σ_{jk} is the stress tensor due to the dislocation and other SIA clusters. Here, the equations of motion for the dislocation nodes as well as the SIA clusters have to be solved simultaneously. The external shear stress is gradually increased by 1 MPa.

We first investigate the dynamics of an edge dislocation that is decorated by SIA clouds along the dislocation line in bcc iron irradiated to 0.001 dpa at 300 K. The initial relative positions of the dislocation and SIA clouds, as well as the nature of the SIA clusters (glissile or sessile) in the clouds are obtained from separate KMC simulations described in Section 2.2. We show in Fig. 11 a series of snapshots of dislocation configurations as it interacts with the SIA cloud. Since some SIA clusters in the clouds are glissile and trapped in the cloud region only due to mutual cluster-cluster interaction, when the dislocation approaches the cloud, the long-range elastic interaction between the dislocation and SIA clusters may push some of the clusters out of the cloud region, as shown in Fig. 11(a) and (b). As a result of the elastic interaction between SIA clusters and the moving dislocation, some of the glissile clusters in the cloud region lying close to the glide plane of the dislocation are swept along the dislocation line, as the dislocation unzips from the cloud.

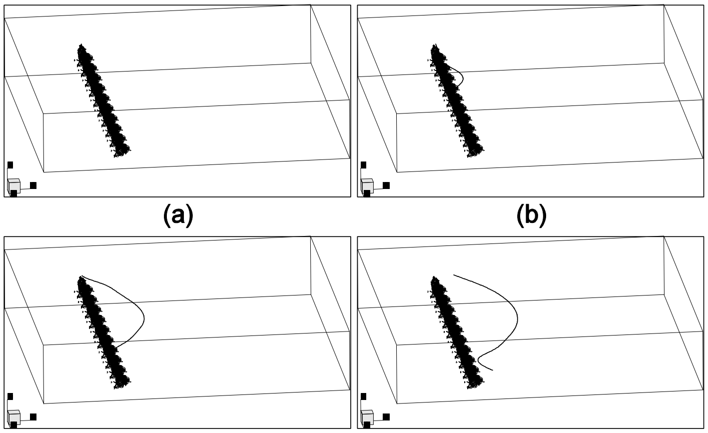
(a) (b)
(c) (d)

Figure 11: Snap-shots of a moving edge dislocation and a decorating SIA cloud, namely a partially mobile cloud, during the release process of the dislocation from the SIA cloud in bcc iron irradiated to 0.001 dpa at 300 K. The applied resolved shear stress at each snapshot is: (a) 40 MPa, (b) 56 MPa, (c) 66 MPa, and (d) 80 MPa, respectively.

We consider now the dynamic interaction process between a moving edge dislocation and a fully mobile SIA cloud, i.e., all the SIA clusters in the cloud are assumed to be glissile. The results of this simulation are shown in Fig. 12. As soon as the dislocation moves, a small number of SIA clusters are pushed out of the cloud and stay at quasi-equilibrium positions at the perimeter of the cloud, as shown in Fig. 12(a) and (b), and the majority of the clusters in the cloud also adjust themselves by moving to new nearby equilibrium positions. As the applied stress increases, the edge dislocation is pulled out of the cloud with a number of SIA clusters dragged along. This process is similar to that of the previous case of an edge dislocation interacting with a decoration cloud containing some immobile SIA clusters.. The two main differences are the critical unlocking stress for the dislocation detrapping from the cloud and the number of SIA clusters dragged by the released dislocation. The dislocation trapped in a fully mobile could is released from the atmosphere at a lower applied shear stress as compared to the previous case, as can be seen in the comparison between 11(b) and 12(b). The number of SIA clusters that is dragged by the moving edge dislocation in Fig. 12 is greater than that in Fig. 11, because the sessile complexes in the decoration cloud have a much stronger restraining force. As the applied shear stress increases, the unlocked dislocation moves faster. When the dislocation velocity reaches to a critical value, the forces exerted on SIA clusters are no longer strong enough to drag them along with the dislocation. As a result, these interstitial clusters are discarded by the moving dislocation. This scenario is indicated by the clusters distributed in the wake of the moving dislocation in both Fig. 11(d) and 12(d).

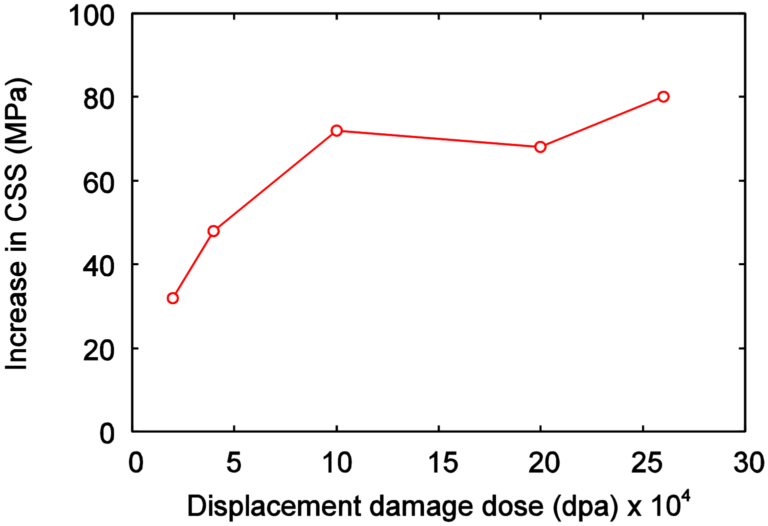

Figure 12: Snap-shots of a moving edge dislocation and a fully mobile SIA cloud during the release process of the dislocation from the SIA cloud in bcc iron irradiated to 0.001 dpa at 300 K. The applied resolved shear stress at each snapshot is: (a) 30 MPa, (b) 48 MPa, (c) 64 MPa, and (d) 80 MPa, respectively.

The effective or average dislocation mobility M is calculated by $v_{ave}/b\tau_{app}$, where v_{ave} is the average velocity of dislocation, b is the magnitude of Burgers vector and τ_{app} is the applied resolved shear stress. Fig. 13 shows the stress dependence of M/M_0, where the mobility is normalized to that of an unirradiated material (M_0). It is observed that the value of M has a rapid increase between 46 MPa and 60 MPa for the interaction of the dislocation with a cloud containing some sessile clusters. On the other hand, the effective dislocation mobility increases gradually as a function of the applied stress for a cloud in which all SIA clusters are glissile. For the dislocation in both Fig. 11 and 12 the dislocation mobility is considerably reduced, compared with that of a dislocation in an unirradiated material, and eventually reaches to a saturation value that depends on the fraction of sessile clusters in the cloud.

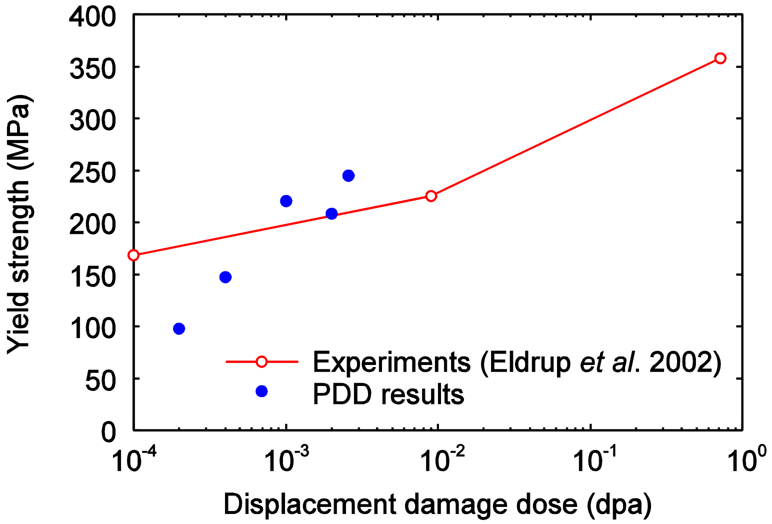

Figure 13: Dislocation mobility M, normalized to the mobility M_0 in unirradiated crystal, versus applied resolved shear stress. Dashed line is for a cloud with a fraction of sessile clusters, and solid line is for a cloud with all mobile clusters.

4 Discussion and Conclusions

The 1-D motion of SIA clusters and the fact that they are associated with a polarized strain field engender unique characteristics to them, and result in several interesting phenomena [3, 4, 8]. The present study, which is based on two different simulation techniques: the KMC and the PDD methods, reveal more detailed aspects of SIA clusters in irradiated iron. Since these simulation methods are both based on the elastic theory of dislocations, they are limited primarily in their spatial resolution to dimensions greater than several interatomic distances. Nevertheless, these simulation methods provide good opportunities for studies of phenomena that involve ensembles of SIA clusters that truly represent bulk behavior, since they provide statistical samples of bulk populations. Thus, the current study is aimed at revealing phenomena that result directly from the *collective* dynamics of SIA cluster ensembles.

It is shown here that when a fixed number of SIA clusters is introduced in the simulation box, and then the clusters are allowed to move both by random and drift motion under the influence of the force field of an edge dislocation, a substantial fraction of them ends up in a defect cloud that decorates the dislocation. A significant portion of SIA clusters are found to be trapped on the tensile side of the edge dislocation (between planes with normals of $\pm 20^{\circ}$ and $\pm 40^{\circ}$ with respect to the slip plane normal). The remaining fraction of SIA clusters is self-trapped in the matrix. Although SIA clusters can change their Burgers vector thermally with an activation energy that we assumed to be 0.05 eV per crowdion [8], the influence of the elastic field of existing dislocations is much more important in re-orienting clusters as they approach the dislocation [4]. Thus, SIA clusters drift towards the dislocation core trying to reach its tensile side, but in the process get self-trapped by their own mutual stress field. As a consequence, random events away from the dislocation core lead to the formation of self-trapped rafts, while those clusters that manage to come close to the dislocation participate in the formation of a decoration cloud, in line with earlier predictions by Trinkaus, Singh and Foreman [4]. The details of the SIA cloud build-up revealed here indicate that the majority of clusters, especially those close to the top of the cloud near the dislocation, are forced to re-orient their Burgers vector and align themselves in the direction of the dislocation's Burgers vector. Thus, the dislocation can be viewed as a strong source of polarization imposed on SIA clusters in the cloud. However, as the cloud builds up in the pyramidical shape consistent with the geometric expansion of the dislocation's stress field, new arrivals to the bottom of the cloud pyramid are shielded from the dislocation's field, and are self-trapped by clusters in adjacent layers.

Our simulations indicate that the buildup speed of SIA clouds is very fast, reaching quasi-equilibrium configurations within 5-20 ns. Thus, simulation of continuous irradiation is essentially equivalent to introduction of SIA cluster increments in the simulation volume that correspond to displacement damage dose increments, and then allowing them to reach their quasi-equilibrium before the next dose increment is added. Simulation results can thus be considered to approximate continuous irradiation if one accounts for the effect of recombination between SIA clusters and nano-size voids that also form in irradiated Fe. One poignant consequence of the saturation behavior in the kinetics of SIA cluster attachment to dislocation clouds is pointing out the need to modify the concept of dislocation bias that is a cornerstone of the rate theory of void swelling [29, 30]. In the rate theory formalism, it is assumed that all dislocations have the same bias factor for absorption of interstitials, regardless of the irradiation dose. The present simulations demonstrate that the rate of absorption of SIAs into the dislocation core is limited by the build-up of its surrounding cloud, and that once the cloud forms, it partially neutralizes the dislocation field. Therefore, one is led to conclude that the dislocation bias towards interstitials is only transient if the dislocation does not move away from its surrounding cloud. The process of shielding of dislocations by SIA clouds parallels the concept of Debye shielding in electromagnetics, where in a plasma environment, electrons flow preferentially to positively charged poles to neutralize their influence on the bulk of the plasma. The spatial extent of the cloud may be regarded to be similar to the Debye shielding length in a plasma.

The details of dislocation interaction with SIA ensembles reveal a few interesting features that are not captured by MD simulations of dislocation interaction with single SIA clusters. When the dislocation is pinned by a continuous cloud along the length of its core, it first develops small perturbations near weak points in the cloud, and then unzips away from the cloud at the critical shear stress. Since the attractive force of the cloud increases slowly with the irradiation dose (or cloud SIA content), it is expected that the CSS increases rapidly with dose early on during irradiation, then more slowly as irradiation proceeds. Once the dislocation is freed from its own cloud, it may encounter other cloud pockets that represent localized resistance to its further motion. Simulations of dislocation interaction with both static and dynamic clouds reveal that the general behavior is essentially the same, and that it resembles the interaction of a dislocation with a penetrable obstacle, such as a precipitate, void or bubble. As the dislocation approaches the cloud, some SIA clusters may re-arrange their configuration, but the majority are locked into their self-trapped positions. The dislocation must therefore bend around the cloud obstacle, and in the process, will drag a few SIA clusters along their glide cylinders. Such dragged clusters slow down dislocation motion once it achieves a critical curved configuration that allows it to be freed from the collective SIA cluster field. If the applied stress is high enough, the dislocation may shed SIA clusters behind and achieve a higher speed as it is no longer resisted by the clusters.

In un-irradiated materials, the yield point in a tensile test is reached when the applied stress is high enough to activate a significant population of F-R sources. However, further increase in plastic strain is governed by work hardening, due to collective dislocation-dislocation interaction mechanisms. The situation is more complex in irradiated materials. The onset of plastic yield is a combination of F-R source activation and dislocation unlocking from SIA cluster atmospheres (source hardening). At low irradiation dose, F-R source activation is expected to dominate, but as the dose increases, source hardening will control the onset of plastic yield. The agreement between the present model of hardening by SIA clusters and experiments is qualitative because it ignores contributions to yield from activated F-R sources. Nevertheless, the magnitude of radiation hardening due to SIA clusters is more in agreement with experiments at high dose, indicating that the majority of dislocations are locked by their SIA clouds, and that yield is controlled by their release from clouds. The development of post-yield plastic flow is more complex, because it entails dislocation interaction with SIA clouds, nano-voids, precipitates in addition to normal work-hardening. Thus, although the present model of hardening captures the major contributions to the onset of plastic yield, it is not sufficient for post-yield behavior. Large-scale dislocation dynamics and crystal plasticity Finite Element Methods may provide future opportunities to model post-yield plasticity of irradiated materials.

Acknowledgments

The present work was supported by the US Department of Energy (DOE), Office of Fusion Energy Sciences (OFES) through grant DE-FG02-03ER54708, and the Office of Nuclear Energy through grant DE-FC07-06ID14748 with UCLA. The authors would like to acknowledge discussions with Dr. B. Singh during the course of this work.

References

[1] T.D. de la Rubia, M.W. Guinan, Phys. Rev. Lett. 66 (1991) 2766.
[2] H. Trinkaus, B. Singh, S. Golubov, J. Nucl. Mater. 283-287 (2000) 89.
[3] B.N. Singh, A.J.E. Foreman, H. Trinkaus, J. Nucl. Mater. 249 (1997) 103.
[4] H. Trinkaus, B.N. Singh, A.J.E. Foreman, J. Nucl. Mater. 249 (1997) 91.
[5] Y.N. Osetsky, D.J. Bacon, A. Serra, B. N. Singh, S. I. Golubov, J. Nucl. Mater. 276 (2000) 65.
[6] Y.N. Osetsky, A. Serra, V. Priego, J. Nucl. Mater. 276 (2000) 202.
[7] D. Rodney, G. Martin, Phys. Rev. B 61 (2000) 8714.
[8] M. Wen, N.M. Ghoniem, B.N. Singh, Phil. Mag. 85 (2005) 2561.
[9] E. Orowan, in: Symposium on Internal Stresses in Metals and Alloys (Institute of Metals, London 1948), p. 451.
[10] A.K. Seeger, in: Proc. of The 2nd United Nations International Conference on The Peaceful Uses of Atomic Energy, Vol. 6 (Geneva, 1958), p. 250.
[11] J. Friedel, Dislocations, Addison-Wesley, Cambridge, MA, 1964.
[12] F. Kroupa, P.B. Hirsch, Discuss. Faraday Soc. 38 (1964) 49.
[13] A.H. Cottrell, Dislocations and Plastic Flow in Crystals, Oxford University Press, London, 1953.
[14] J. Huang, N.M. Ghoniem, J. Comp. Mater. Sci. 23 (2002) 225.
[15] C.C. Fu, J.D. Torre, F. Willaime, J.-L. Bocquet, A. Barbu, Nature Mater. 4 (2005) 68.
[16] J. Marian, B.D. Wirth, J.M. Perlado, Phys. Rev. Lett. 88 (2002) 255507.
[17] T.M. Robinson, Phys. Status Solidi A 75 (1983) 243.
[18] N.M. Ghoniem, L.Z. Sun, Phys. Rev. B 60 (1999) 128.
[19] D.J. Bacon, Y.N. Osetsky, R. Stoller, R.E. Voskoboinikov, J. Nucl. Mater. 323 (2003) 152.
[20] F. Gao, H. Heinisch, R.J. Kurtz, Y.N. Osetsky, R.G. Hoagland, Phil. Mag. 85 (2005) 619.
[21] F. Gao, G. Henkelman, W.L. Weber, L.R. Corrales, H. Jonsson, Nucl. Instr. and Meth. B 202 (2003) 1.
[22] M. Eldrup, B.N. Singh, S.J. Zinkle, T.S. Byun, K. Farrell, J. Nucl. Mater. 307-311 (2002) 912.
[23] H. Trinkaus, B.N. Singh, A.J.E. Foreman, J. Nucl. Mater. 251 (1997) 172.
[24] N.M. Ghoniem, S.-H. Tong, L.Z. Sun, Phys. Rev. B 61 (2000) 913.
[25] F. Kroupa, Dislocation loops, in: B. Gruber (Ed.), Theory of Crystal Defects, Academic Press, New York, 1966, p. 275.
[26] R.E. Stoller, Z.J. Zinkle, J. Nucl. Mater. 349-352 (2000) 283.
[27] M. Makin, Phil. Mag. 10 (1964) 695.
[28] Z. Rong, Y.N. Osetsky, D.J. Bacon, Phil. Mag. 85 (2005) 1473.
[29] R. Bullough, B. Eyre, K. Krishan, Proc. R. Soc. London A 346 (1975) 81.
[30] N.M. Ghoniem, G.L. Kulcinski, Radiat. Eff. 41 (1979) 81.

Length-scale Effects in Cascade Damage Production in Iron

R. E. Stoller[1], P. J. Kamenski[2], and Yu. N. Osetsky[1]

[1]Materials Science and Technology Division
Oak Ridge National Laboratory, Oak Ridge, TN 37831-6138
[2]Department of Materials Science and Engineering
University of Wisconsin, Madison, WI
(now University of Oxford, UK)

Abstract

Molecular dynamics simulations provide an atomistic description of the processes that control primary radiation damage formation in atomic displacement cascades. An extensive database of simulations describing cascade damage production in single crystal iron has been compiled using a modified version of the interatomic potential developed by Finnis and Sinclair. This same potential has been used to investigate primary damage formation in nanocrystalline iron in order to have a direct comparison with the single crystal results. A statistically significant number of simulations were carried out at cascade energies of 10 keV and 20 keV and temperatures of 100 and 600K to make this comparison. The results demonstrate a significant influence of nearby grain boundaries as a sink for mobile defects during the cascade cooling phase. This alters the residual primary damage that survives the cascade event. Compared to single crystal, substantially fewer interstitials survive in the nanograined iron, while the number of surviving vacancies is similar or slightly greater than the single crystal result. The fraction of the surviving interstitials contained in clusters is also reduced. The asymmetry in the survival of the two types of point defects is likely to alter damage accumulation at longer times.

Introduction

Primary damage formation in irradiated metals due to atomic displacement cascades has been extensively investigated using the method of molecular dynamics (MD) [1-11]. These MD simulations have led to a well-accepted understanding of the underlying processes that lead to the formation of stable (on MD time scales) distributions of point defects, i.e. vacancies and interstitials. Both types of point defects are found in the form of isolated mono-defects as well as small defect clusters. The influence of variables such as cascade (or primary knock-on atom, PKA) energy and irradiation temperature have been determined [8] and differences due to the choice of interatomic potential have been explored [10]. A particularly large database of simulations has been accumulated for iron [9] using a modified version of the interatomic potential developed by Finnis and Sinclair [3,12]. Like most MD studies of displacement cascades, the simulations in this database were carried out using perfect crystals with periodic boundary conditions. To the extent that the simulations are representative of radiation damage in iron, they represent only the behavior of single crystal materials.

There has been a limited amount of research carried out to investigate the potential influence of grain size on primary damage formation [11, 13-16]. Computational limitations dictate that such work would focus on nanometer grain sizes, and quite strong effects have been observed [11]. However, there has been no systematic study that statistically demonstrated how a nanograin structure would alter primary damage formation. The same Finnis-Sinclair potential mentioned above has been used in such an investigation of nanocrystalline iron in order to have a direct comparison with the corresponding single crystal database. A sufficient number of simulations were carried out at cascade energies of 10 keV and 20 keV and temperatures of 100 and 600K to obtain a statistically significant comparison. The results demonstrate that the creation of primary radiation damage can be substantially different in nanograined material due to the influence of nearby grain boundaries.

Simulation Method

The simulations were carried out using both serial and parallel versions of the MOLDY [17] MD code and the interatomic potential for iron developed by Finnis and Sinclair [12]. The potential was modified for use in high-energy simulations by Calder and Bacon [3]. This code and potential have been widely used, and the results of the single crystal iron simulations are discussed elsewhere [3,6-9]. All simulations were carried out at constant pressure with periodic boundary conditions. Since the boundary atoms were not damped to remove heat, the kinetic energy of the PKA leads to some lattice heating. This heating has little or no impact on the ballistic phase of the cascade, and the extent to which it may influence the number and configuration of final, stable displacements is not yet clear [8, 18, 19]. Typical MD simulation times are about 15 ps for 10 and 20 keV simulations, which is the time required to dissipate the initial recoil energy and re-thermalize atomic motion. At this point, the number of stable point defects is counted and their configuration determined. The number of isolated point defects (single interstitials and vacancies) and the number of point defects in clusters are determined as well as the size distributions of vacancy and interstitial clusters.

Nanocrystalline construction

To create the nanocrystalline structure, nucleation sites were chosen, the grains were filled using a Voronoi technique [20], overlapping atoms at the grain boundaries were removed, and finally the structure was equilibrated using MD. The nucleation sites were obtained by melting a face centered cubic (fcc) material through Monte Carlo simulation using a simple Lennard-Jones interatomic potential and then scaling the distance between the sites to achieve the desired grain size. This methodology was used over simple random number generation in order to better reproduce a grain size distribution consistent with experiments. A 2x2x2 unit cell system was used resulting in 32 nucleation sites, and hence 32 grains in the final sample.

Each Voronoi polyhedron was filled with atoms placed on a regular bcc iron crystalline lattice, with the lattice orientation randomly selected. Grain boundaries occur naturally when the atomic plains in adjacent polyhedra impinge on one another. Within the boundary region, one atom from any pair of atoms closer than 80% of the nearest neighbor bond distance was removed. This was done to counteract the unphysical situation wherein the Voronoi technique allows atoms in the grain boundary to be arbitrarily close to one another. It should be noted that the exact cutoff distance is unimportant considering there are no volume constraints in the equilibration. In this case, the interatomic potential will dictate the grain boundary density for the given pressure. The final system was periodic and had an average grain size of 10 nm, system box length of 28.3 nm, and contained roughly 1.87 million atoms. The system was equilibrated for over 200 ps including a heat treatment up to 600 K. Fig. 1 illustrates a typical grain structure with each grain shown in a different color. The approximate sizes of 5 and 20 keV cascades have been projected on to the face of the simulation cell.

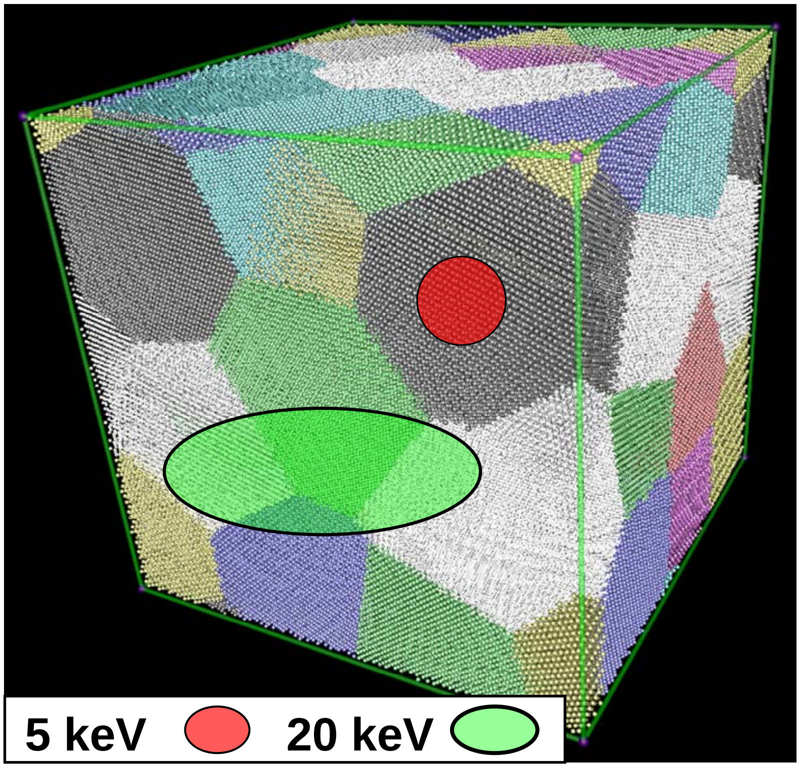

Fig. 1. MD simulation cell, 32 ~10 nm grains. Shaded red circle and green ellipse indicate approximate size of 5 and 10 keV cascades, respectively.

Analysis of nanograined material

Grain boundary atoms were distinguished from atoms in the grain interior using a coordination analysis of the 1st and 2nd nearest neighbors. Point defects were identified by comparing atom positions with the structure that existed prior to initiating the cascade simulation. Atoms displaced more than 0.3 times the iron lattice parameter from any original lattice site were flagged as interstitials, and sites with no atom within 0.3 times the lattice parameter were flagged as vacancies. Possible in-grain defects were identified as those point defects which were more than one-half a lattice parameter from the original grain boundaries. Further visual analysis was done to distinguish grain boundary reconstruction from the final, remaining in-grain defects.

The results of the cascade simulations have been evaluated using standard statistical methods. From all the simulations at each cascade energy, the mean value, the standard deviation about the mean (σ), and the standard error of the mean (ε) have been calculated. The standard error of the mean provides a measure of how well the sample mean is expected to represent the actual mean and is calculated as $\varepsilon = \sigma/n^{0.5}$, where n is the number of simulations completed.

Results

Fig. 2 compares the final defect state of typical 10 keV cascades at 100K, with the single crystal simulation shown in (a) and the nanograin simulation shown in (b). Interstitial atoms are shown as green spheres and vacant sites as red spheres. Grain boundary atoms within 3 lattice parameters of a point defect are shown as black spheres to indicate the location of the boundaries. In this case, it is clear that the cascade crossed at least one of the

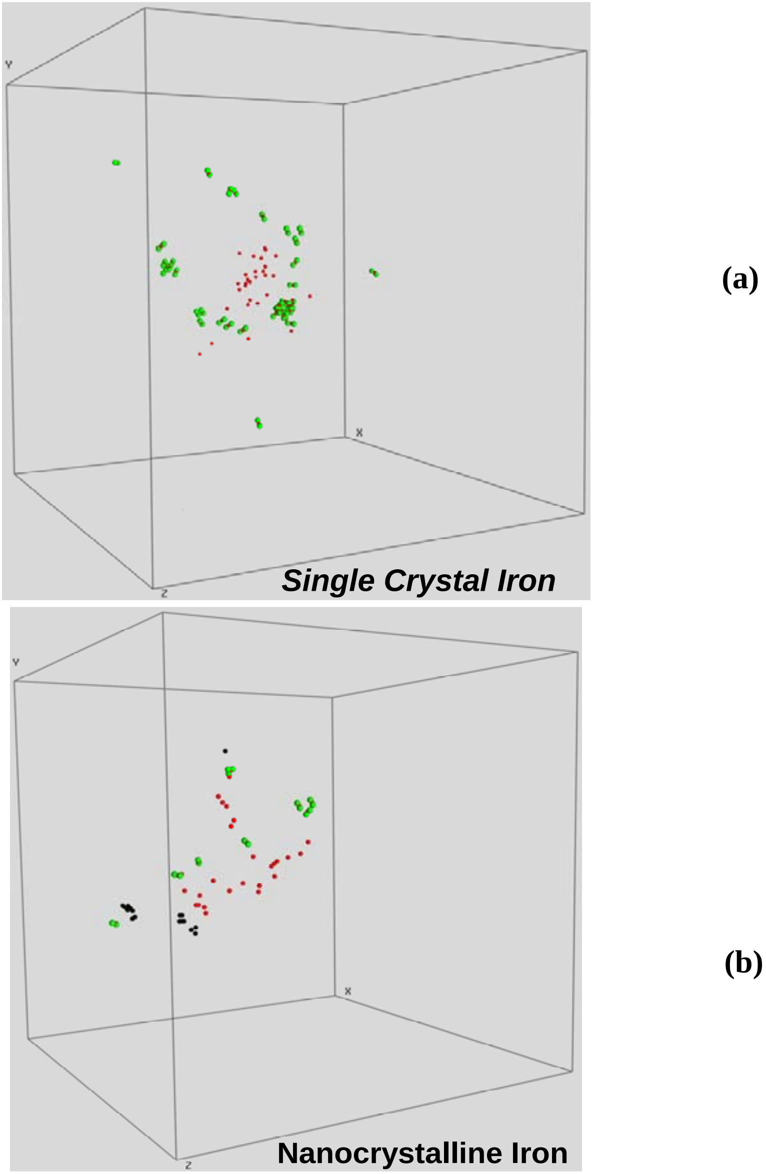

Fig. 2. Surviving point defects in 10 keV cascades at 100K for single crystal iron (a), and nanograined iron (b). Red spheres are vacant lattice sites, green spheres are atoms in interstitial positions, and black spheres are grain boundary atoms (see text).

boundaries. Even a superficial examination of these two cascades reveals dramatic differences. The total number of surviving point defects is much lower in the nanograined material, and the number of interstitial clusters is also significantly reduced. These differences are quantified in the Figs. 3 to 5.

The number of vacancies and interstitials surviving in the nanograin simulations is compared to the single crystal results in Fig. 3. A relatively wide range of cascade energies is included in Fig 3(a) to show the trend in the single crystal data, while Fig. 3(b) highlights the differences at the temperature and energy of the nanograin simulations. Mean values are indicated by the symbols in Fig. 3(a) and the height of the bars in Fig. 3(b), and the error bars indicate the standard error in both cases. The number of vacancies surviving in the nanograined material is similar to the single crystal data for 10 keV cascades, but higher at 20 keV. Much lower interstitial survival is observed in nanograined material under all conditions.

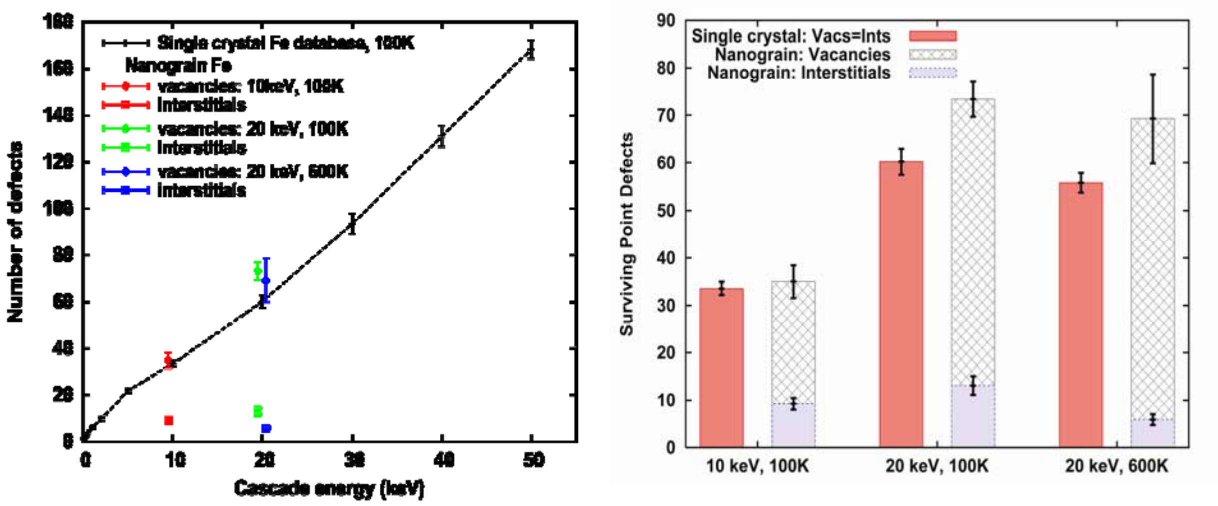

(a) (b)

Fig. 3. Number of stable interstitials and vacancies created by displacement cascades in single crystal and nanograined iron.

The number of surviving interstitials and vacancies that are contained in clusters is shown in Fig. 4(a) and 4(b), respectively. Consistent with the implications of Fig. 2 and the overall reduction in interstitial survival shown in Fig. 3(a), the number of interstitials in clusters is dramatically reduced in nanograined material for all the conditions examined. Compared to single crystal iron, the influence of irradiation temperature on interstitial clustering in 20 keV cascades appears to be reversed in the nanograined material. The influence of the nanocrystalline structure vacancy clustering appears to be more modest as shown in Fig. 4(b), which includes the results of only the 20 keV cascades. There is no significant change in the number of vacancies in clusters at 100K, but a statistically significant increase is observed at 600K. This again leads to a reversal in the temperature dependence of vacancy clustering between the single and nanograined iron, although the change is opposite of that observed for interstitial clustering.

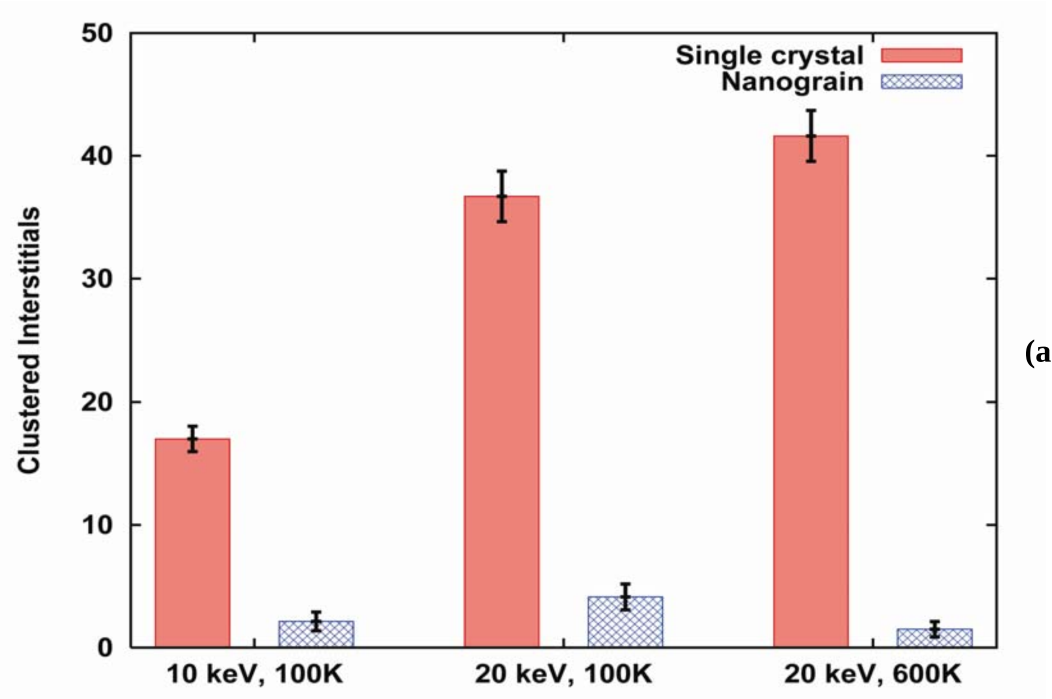

(a)

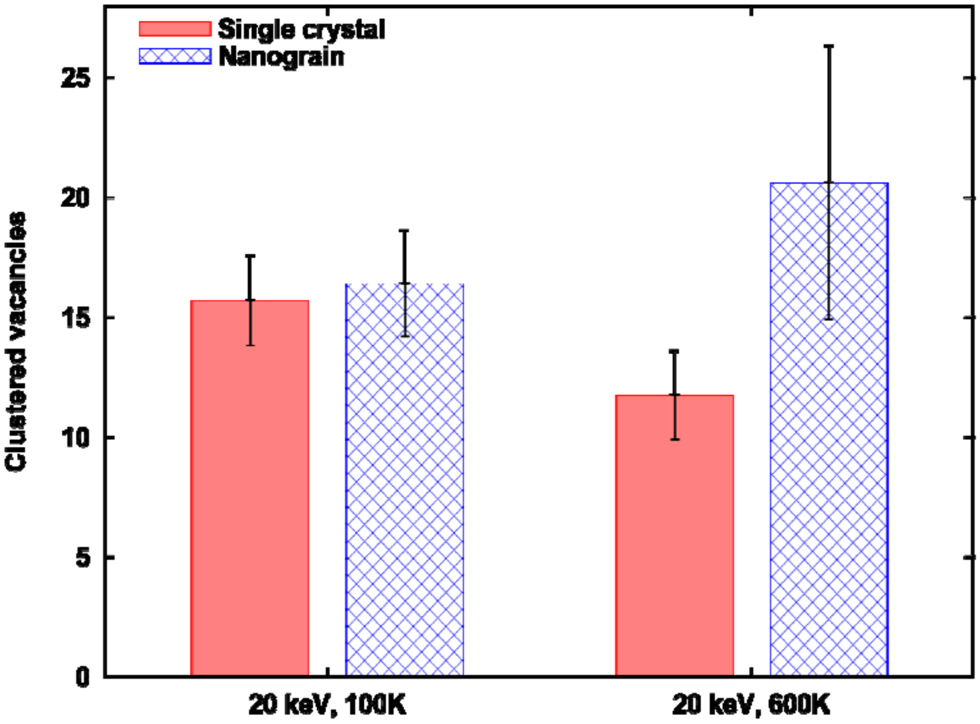

(b)

Fig. 4. Number of surviving interstitials and vacancies contained in clusters in single crystal and nanograined iron.

Since the number of surviving point defects, particularly interstitials, is so strongly reduced in the nanograin material, it is helpful to compare the fraction of defects in clusters in addition to the absolute number. Such a comparison is shown in Fig. 5 where the fractions of surviving interstitials and vacancies contained in clusters in both nanograined and single crystal iron are compared for all the conditions simulated. The changes in clustering fraction are somewhat reduced relative to the changes in the number of defects in clusters (Fig. 4), but are still substantial – particularly for interstitial defects. Notably, the reversed temperature dependence mentioned above for the number of defects in clusters in 20 keV cascades is preserved in the clustering fractions. The fraction of interstitials in clusters increases between 100 and 600K for single crystal iron but decreases for nanograined iron, while the vacancy cluster fraction decreases for single crystal iron and increases for nanograined iron.

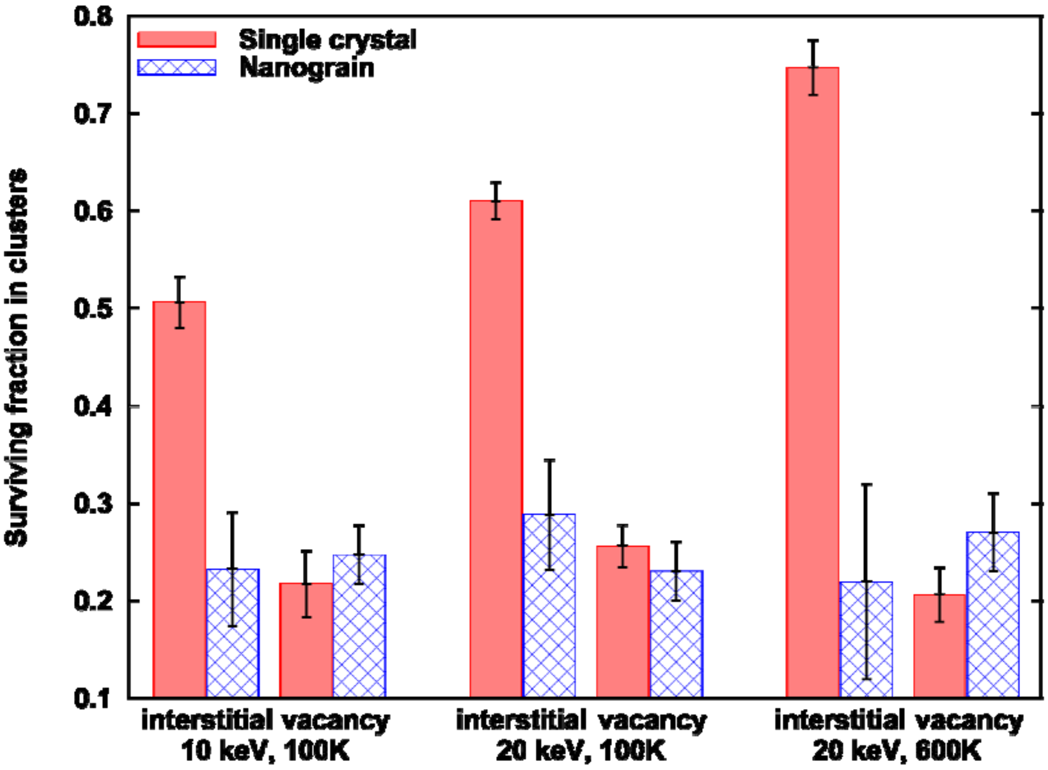

Fig. 5. Fraction of surviving interstitials and vacancies contained in clusters in single crystal and nanograined iron.

Discussion and Summary

Although the range of this study was limited in temperature and cascade energy, the results have demonstrated a strong influence of microstructural length scale (grain size) on primary radiation damage production in iron. Both the effects and the mechanisms appear to be consistent with previous work in nickel [11, 16], in which very efficient transport of interstitial defects to the grain boundaries was observed. In both iron and nickel, this leads to an asymmetry in point defect survival. Many more vacancies than interstitials survive at the end of the cascade event in nanograined material while equal numbers of these two types of point defects survive in single grain material. The nature of the residual vacancy defect clusters is different in iron than in nickel because iron does not exhibit stable stacking faults. Similar to single crystal iron [8], few of the vacancies have collapsed into compact clusters on the MD timescale. The vacancy clusters in both single and nanograined iron tend to be loose three-dimension aggregates of vacancies bound at the first and second-nearest neighbor distances [8]. The size distribution of such vacancy clusters was not significantly different between the single and nanograin material. In contrast, the interstitial cluster size distribution was altered in the nanograined iron, with the number of large clusters substantially reduced. There appears to be both a reduction in the number of large interstitial clusters formed directly in the cascade and less coalescence of small mobile interstitial clusters since the latter are being transported to the grain boundaries.

Although the differences in primary damage formation may be significant, a more important issue is the degree to which these differences alter radiation damage accumulation over much longer times. Two factors need to be considered. The first is the difference in the nature of the surviving cluster size distributions. Having fewer large clusters could delay the formation of extended defects that lead to mechanical property changes such as hardening and embrittlement. Second, and more importantly, the fact that the number of surviving vacancies is substantially greater than the surviving interstitials is likely to bias the subsequent damage accumulation toward vacancy type defects. At times long enough for vacancy diffusion, many of the mobile vacancy defects may also be lost to the grain boundaries. Alternately, the higher vacancy supersaturation could lead to the nucleation of larger, immobile vacancy defects such as voids which could promote swelling and mechanical property changes. In order to determine whether it is the more or less benign situation that prevails, the impact of altered primary damage behavior needs to be evaluated over diffusive time scale, e.g. using mean field rate theory or Monte Carlo models [21]. The higher helium levels generated in a fusion reactor environment could influence the evolution path by stabilizing vacancy defects and preventing their transport to and absorption at grain boundaries, leading to different behavior than observed under fission neutron irradiation.

The changes in defect survival observed in these simulations are qualitatively consistent with the limited available experimental observations [13-15]. For example, Rose, et al. [13] carried out room-temperature ion irradiation experiments of Pd and ZrO_2 with grain sizes in the range of 10 to 300 nm, and observed a systematic reduction in the number of visible defects produced. Chimi, et al. [14] measured the resistivity of ion irradiated gold specimens following ion irradiation and found that resistivity changes were lower in nanograined material after room temperature irradiation. However, they observed an increased change in nanograined material following irradiation at 15K. The low temperature results could be related to the accumulation of vacancy defects as mentioned above since they should be immobile at 15K.

The results of the present study, along with the previous theoretical and experimental investigations, suggest that nanograined materials may offer a path for the development of radiation-resistant materials. The potential for reduced damage accumulation is clear, at least at higher temperatures. However, it is also clear that further work is required to develop an understanding of the mechanisms involved in order to explain observation such as the increased resistivity change observed by Chimi, et al. [14] at 15K. The experimental results can be influenced by porosity in the sintered or compacted materials [13], and must consider the uncertainties associated with limited irradiation volumes in ion irradiations. As mentioned above, the results of MD cascade simulations provide only the starting point for a complex path of damage accumulation that must be investigated using other techniques.

Acknowledgments

Research sponsored by the Division of Materials Sciences and Engineering and the Office of Fusion Energy Sciences, U.S. Department of Energy, under contract DE-AC05-00OR22725 with UT-Battelle, LLC.

References

1. R. S. Averback, R. Benedek, and K. L. Merkle, Phys. Rev. B **18** (8), 4156 (1988).
2. A.J.E. Foreman, W.J. Phythian, C.A. English, Philos. Mag. A **66**, 571 (1992).
3. A. F. Calder and D. J. Bacon, J. Nucl. Mater. **207, 25** (1993).
4. D.J. Bacon and T. Diaz de la Rubia, J. Nucl. Mater. **216** (1994)
5. D. J. Bacon, A. F. Calder, F. Gao, V. G. Kapinos, and S. J. Wooding, Nucl. Instr. Meth. B **102**, 37 (1995).
6. W. J. Phythian, R. E. Stoller, A. J. E. Foreman, A. F. Calder, and D. J. Bacon, J. Nucl. Mater. **223**, 245 (1995).
7. R. E. Stoller, G. R. Odette, and B. D. Wirth, J. Nucl. Mater. **251**, 49 (1997).
8. R. E. Stoller, J. Nucl. Mater. **276**, 22 (2000).
9. R. E. Stoller and A. F. Calder, J. Nucl. Mater. **283-287**, 746 (2000).
10. C. S. Becquart, C. Domain, A. Legris, J.C. Van Duysen, J. Nucl. Mater. **280**, 73 (2000).
11. M. Samaras, P. M. Derlet, H. Van Swygenhoven, and M. Victoria, Phys. Rev. Lett. **88**, 125505 (2002).
12. M. W. Finnis and J. E. Sinclair, Phil. Mag. A **50**, 45 (1984) and Erratum, Phil. Mag. A **53** (1986) 161.
13. M. Rose, A. G. Balogh, and H. Hahn, Nucl. Instr. Meth. Phys. Res., Sect. B **127-128**, 119 (1997).
14. Y. Chimi, A. Iwase, N. Ishikawa, M. Kobiyama, T. Inami, and S. Okuda., J. Nucl. Mater. **297**, 355 (2001).
15. T. D. Shen, S. Feng, M. Tang, J. A. Valdez, Y. Wang and K. E. Sickafus, Appl. Phys. Lett. **90,** 263115 (2007)..
16. M. Samaras, P. M. Derlet, and H. Van Swygenhoven, Phys. Rev. B **68**, 224111 (2003).
17. M. W. Finnis, "MOLDY6-A Molecular Dynamics Program for Simulation of Pure Metals," AERE R-13182, UK AEA Harwell Laboratory (1988).
18. M. W. Finnis, P. Agnew and A. J. E. Foreman, Physical Review B **44** 567 (1991).
19. F. Gao, D. J. Bacon, P. E. J. Flewitt, and T. A. Lewis, J. Nucl. Mater. **249**, 77 (1997).
20. G. Z. Voronoi and J. Reine, Angew. Math. **134**, 199 (1908).
21. R. E. Stoller, S. I. Golubov, C. Domain, and C. S. Becquart, J. Nucl. Mater. **382,** 77 (2008).

TITAN TASK 2-3 SILICON CARBIDE BEND STRESS RELAXATION CREEP EXPERIMENT —

Y. Katoh (Oak Ridge National Laboratory), Y.B. Choi (Hiroshima University), and T. Hinoki (Kyoto University)

OBJECTIVE

This report provides a brief outline of the Phase-IA irradiation campaign technical plan and progress of the Task 2-3 on Dynamic Deformation of Fusion Materials, US/Japan TITAN collaboration on fusion materials and blanket technology.

SUMMARY

A study on transient irradiation creep deformation of silicon carbide is being undertaken as a part of Task 2-3 of the US/Japan TITAN collaboration on fusion materials and blanket technology. The Phase-IA program is the first of the two irradiation campaigns planned for studying the bend stress relaxation (BSR) creep of ceramics and composites under neutron irradiation. The objective of experiment is to gain understanding of the stress relaxation and transient creep behavior of SiC composites and constituents under neutron irradiation at elevated temperatures. The neutron irradiation will be performed using hydraulic and fixed rabbit facilities of the High Flux Isotope Reactor. The Phase-IA program irradiates 8 rabbit capsules; 5 in hydraulic and 3 in fixed facility. Target irradiation temperatures in the Phase-I are 300, 500, 800, and 1200ºC. The minimum number of rabbit capsules to be irradiated in entire Phase-I campaign will be 15. The present schedule assumes the initiation of irradiation in early 2009.

PROGRESS AND STATUS

Introduction

Irradiation creep is an important irradiation effect phenomenon for materials for radiation services, because it is a major contributor to potential dimensional instability of materials under irradiation at such temperatures that thermal creep is not strongly anticipated. [1] Although irradiation creep often determines irradiated lifetime of metallic structural components, it is not necessarily undesirable for brittle materials like ceramics for functional applications, because it may help relaxing or redistributing the stresses. [2] For silicon carbide (SiC)-based nuclear components, the latter function of irradiation creep may be important, in particular when a significant temperature gradient exists and the secondary stresses developed by differential swelling can be severe. Flow channel insert in liquid metal blankets of fusion energy systems is an example of such applications. [4]

Studies on neutron irradiation creep of SiC have so far been extremely limited and insufficient. Price published the result of the irradiation creep study on chemically vapor-deposited (CVD) SiC in 1977. [6] In that work, elastically bent strip samples were irradiated in a fission reactor, and the linear-averaged creep compliance was estimated to be in the order of 10^{-38} [Pa•n/m^2 (E > 0.18 MeV)]$^{-1}$, or 10^{-7} [MPa•dpa]$^{-1}$, in a temperature range 780 - 1130ºC. The experimental method of estimating the creep parameters based on the stress relaxation in elastically bent strip samples developed by Price was later adopted to examine the thermal creep behavior of refractory ceramic fibers and was named bend stress relaxation (BSR) method by Morscher and DiCalro. [5] In a recent work, Katoh et al. applied it for studying the irradiation creep of high purity, stoichiometric CVD SiC, demonstrating that the BSR technique is effective to determine the irradiation creep parameters. [3] They also revealed that the creep strains SiC were dominated by transient creep at temperatures below ~950ºC whereas steady-state creep is likely to dominate at higher temperatures with a compliance of $1.5 \pm 0.8 \times 10^{-6}$ [MPa•dpa]$^{-1}$ with the initial flexural stress magnitude ~100 MPa. However, fundamental aspects of the irradiation creep, including the effect of stress magnitude on the creep strain rate, the correlation of irradiation creep and swelling, and the responsible physical mechanism, remain to be understood.

Based on the previous demonstration of the experimental technique and the recognized importance of the irradiation creep, a more detailed study on the BSR irradiation creep of SiC ceramics and composites was planned as the Phase-I program of Task 2-3 on dynamic deformation of fusion materials in the US Department of Energy /Japan MEXT (Ministry of of Education, Culture, Sports, Science and Technology) TITAN Collaboration. The objective of the Phase-I study is to gain understanding of the transient creep and stress relaxation behavior of SiC ceramics, model composites, and composite constituents during neutron irradiation. More specifically, the study aims at determining the dose, temperature, and stress dependent BSR behavior of those materials and the correlation between the point defect swelling and the transient creep deformation.

Technical Plan Details

Irradiation Matrix

The Phase-IA irradiation program consists of irradiation of 8 rabbit capsules including 5 hydraulic rabbits and 3 fixed rabbits. The planned irradiation matrix is shown in Table 1. The irradiation conditions were chosen so that 1) the temperature range of technological interest is covered, 2) the irradiation creep – swelling coupling could be studied in a broad range of swelling magnitude, and 3) the effect of irradiation temperature may be compared both at the same dose and at the similar swelling magnitude.

Table 1 – Irradiation conditions planned for Phase-IA.

Capsule ID in Titan	Capsule Type	Target Temperature (ºC)	Target Dose ($x10^{25}$ n/m^2 fast)	Anticipated Swelling	Facility
T08-01J	Titan-BSR1	300	0.01	~0.2%	Hydraulic
T08-02J	Titan-BSR1	300	0.1	~1.0%	Hydraulic
T08-03J	Titan-BSR1	500	0.01	~0.1%	Hydraulic
T08-04J	Titan-BSR1	500	0.1	~0.6%	Hydraulic
T08-05J	Titan-BSR1	500	1	~1.2%	PTP or TH
T08-06J	Titan-BSR1	800	0.1	~0.1%	Hydraulic
T08-07J	Titan-BSR1	800	1	~0.6%	PTP or TH
T08-08J	Titan-BSR1	1200	1	~0.1%	PTP or TH

Irradiation Capsules

The standard “SiC Bend Bar” type capsule housing configuration are employed, using the existing HFIR capsule design X3E020977A325. Inside the standard sleeve, which holds two ceramic bend bar samples in the standard configuration, a rectangular casing (denoted “coffin” hereafter) is accommodated. Both the sleeves and the coffins were made of molybdenum.

Each coffin consists of a straight rectangular tube with end pillars on both ends, Fig. 1. The end pillars are for 1) fixing the internal parts and specimens in appropriate positions, and 2) retaining the internal parts and specimens during the capsule disassembly process until right before the specimen examination in the post-irradiation examination facility. The end pillars are made of the same material with the tube. The end pillars have to withstand the transient mechanical loading during the operation of the hydraulic rabbit facility.

Four BSR assembly units are accommodated in each coffin. Each BSR assembly is of size approximately 48 mm x 5.1 mm x 1 mm. The BSR assembly units are stacked together with CVD SiC liners/separator plates at the top, bottom, and between the units, Fig. 2. The CVD SiC liners/separators prevent potential undesirable reaction between the samples and the metallic parts or fixture, as well as help aligning the BSR assembly units in proper positions.

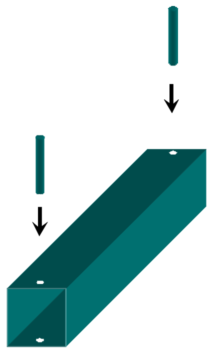

Fig.1 – A schematic illustration of the “coffin” container with retaining pillars.

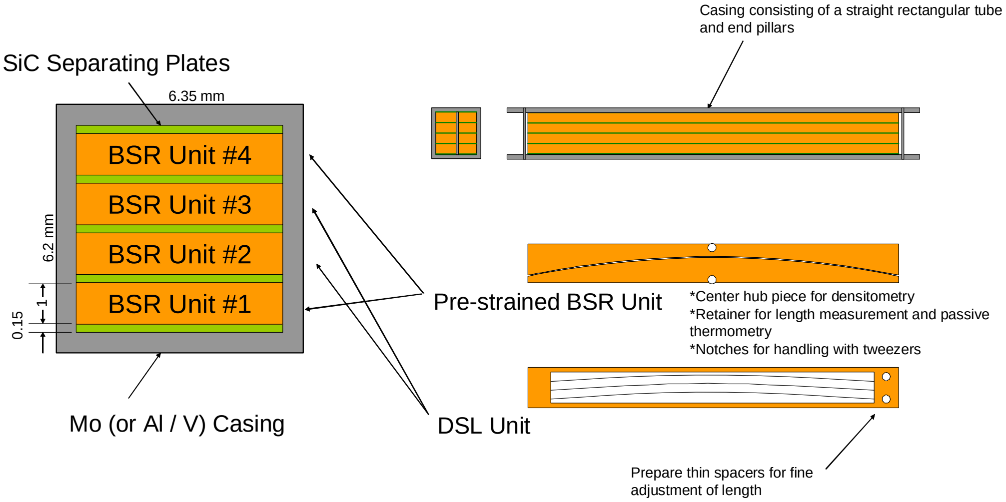

Fig. 2 – An illustration of BSR assembly units and their stacking in a metallic casing.

BSR Assembly

Two types of BSR assembly units are used: 1) conventional pre-strained (PS) BSR and 2) dynamic self-loading (DSL) BSR (Fig. 2). For each rabbit, two PS units and two DSL units are irradiated. Each unit contains several BSR strip specimens. The PS units are consisted of a pair of fixture which is made of CVD SiC. The frame for the DSL unit is made of same material with the coffin. Discussion about the DSL creep experiment is provided in a separate section.

The components of the BSR assembly and the capsule internal are shown in Fig. 3. The BSR assembly modules (fixtures of both types loaded with the specimens) are shown in Fig. 4. The assembled modules being loaded into the coffin are shown in Fig. 5.

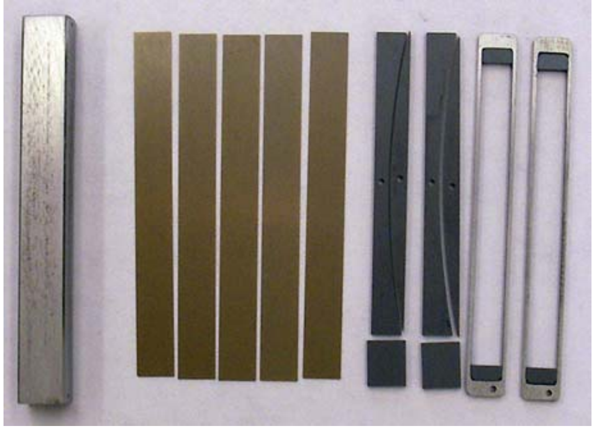

Fig.3. Components for the BSR assembly and the capsule internals. From left to right, coffin, CVD SiC lining/separating sheets, pre-strained BSR fixtures (and spacers), and dynamic self-loading fixtures.

Fig.4. Dynamic self-loading BSR fixture (middle) and pre-strained BSR fixture (bottom) both loaded with specimens. Molybdenum coffin is shown on the top.

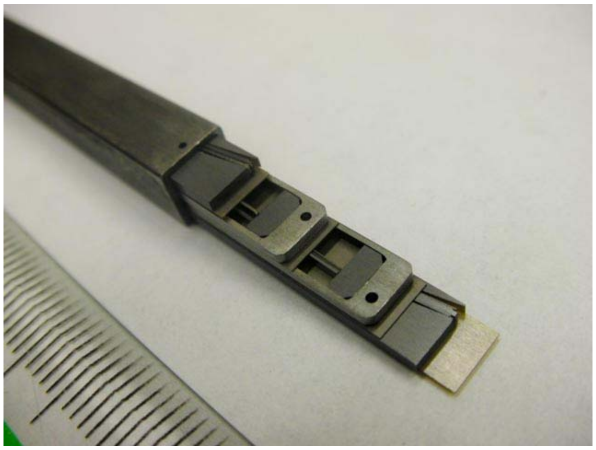

Fig.5. Loading of BSR assembly modules into the coffin. Two dynamic self-loading BSR modules are loaded in the middle and two pre-strained BSR modules are loaded on the top and the bottom. Each module and the internal wall of the coffin are separated with CVD SiC sheets.

Materials and Specimens

Materials to be studied and specimen loading to each rabbit are summarized in Table 3. The Cree 6H single crystal samples were machined for the surface parallel with {0001} and the length parallel with <1120>.

The dimensions of the BSR creep specimens are 40 mm (l) x 1 mm (w) x varied thickness. Some of the materials were machined into slightly reduced thicknesses for materials identification. The thickness was varied to allow determination of the effect of stress magnitude. Typical initial flexural stresses for the specimen thicknesses 0.05, 0.1, and 0.15 mm are ~100, ~200, and ~300 MPa, respectively.

Table 3 – Materials and specimens for the BSR creep experiment. Number of specimens per rabbit capsule. Parenthesis indicates specimens are backup.

Material ID	Material	Specimen Thickness (mm)	# of specimens in PS units	# of specimens in DSL units
RH	R&H CVD-SiC, polycrystalline beta SiC	0.05	2	
		0.10	1	1
		0.15	1	1
		0.20		1
CT	Coorstek CVD SiC polycrystalline beta SiC	0.05	1	
		0.10	1	
		0.15	1	
SX	Cree 4H SiC, W4NRF0X-0D00, Lot# FX0778-28/161430	0.05	1	
		0.10	1	
NT1	NITE matrix material, standard	0.075	1	
		0.10	1	1
		0.15		1
		0.20		1
NT2	NITE matrix material, reduced additives	0.05	2	
		0.10	1	
		0.15	1	

Dynamic Self-Loading Technique

The dynamic self-loading (DSL) is an experimental technique that makes use of the isotropic swelling of SiC strip sample to apply a flexural strain to the sample itself. When a flat strip sample mechanically constrained at both ends undergoes longitudinal expansion, the sample elastically bows out developing flexural loading. The extent of bow-out and the flexural strain are calculated and shown in Fig. 6 as a function of linear swelling. Advantages of the DSL technique include 1) flexural strain in excess of the fast fracture strain (typically <0.1% for SiC) can be applied, and 2) early stress relaxation due to the transient irradiation creep may be compensated by the additional strain application with the progress of irradiation. The DSL experiment, if successfully performed, helps determining adequacy of theory and models of irradiation creep. With a known stress exponent for the irradiation creep rate and an adequate model, irradiation creep parameter such as a swelling-creep coupling coefficient may be determined by the DSL experiment.

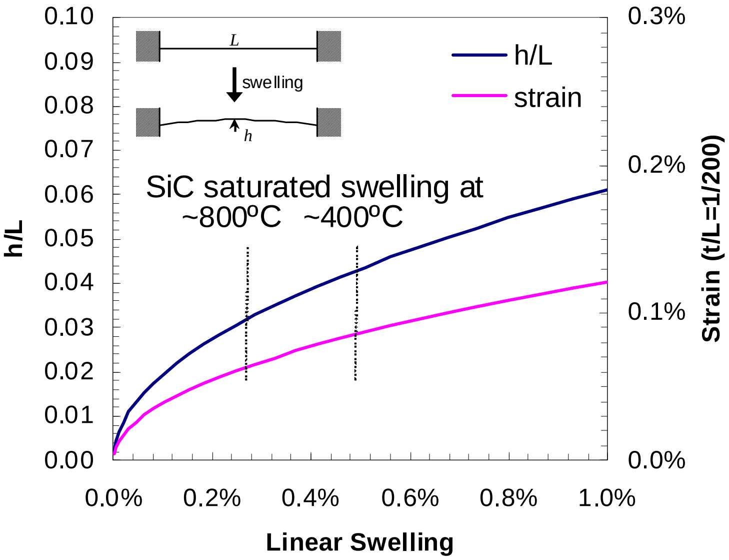

Fig.6. Calculation of bow-out magnitude (h/L) and flexural strain as a function of linear swelling. L = specimen length, h = bow-out height, and t = specimen thickness. Initial h was set to zero in this calculation.

References

[1] K. Ehrlich, Journal of Nuclear Materials 100 (1981) 149-166.
[2] Y. Katoh, S. Kondo, and L.L. Snead, Journal of Nuclear Materials 382 (2008) 170-175.
[3] Y. Katoh, and L.L. Snead, Ceramic Engineering and Science Proceedings 26 (2005) 265-272.
[4] N.B. Morley, Y. Katoh, S. Malang, B.A. Pint, A.R. Raffray, S. Sharafat, S. Smolentsev, and G.E. Youngblood, Fusion Engineering and Design 83 (2008) 920-927.
[5] G.N. Morscher, and J.A. DiCarlo, Journal of the American Ceramic Society 75 (1992) 136-40.
[6] R.J. Price, Nuclear Technology 35 (1977) 320-336.

IRRADIATION EXPERIMENT DESIGN FOR TITAN RABBITS WITH FERRITIC STEEL, TUNGSTEN, AND NICKEL SPECIMENS

—E. Popov, J. McDuffee, M. Sokolov, (Oak Ridge National Laboratory)

OBJECTIVE

The objective of this present work is to design a series of capsules for irradiation in the High-Flux Isotope Reactor (HFIR).

SUMMARY

Several designs of capsules for irradiating different specimens are described in this work. The specimens are of tensile, disk, or plate configurations from ferritic steels (FS), tungsten, and nickel. Some designs are complete, and others are still in the temperature evaluation phase. Two capsules (T9A1 and T9A2) are currently being irradiated in the hydraulic tube of HFIR as of January 2009.

Irradiation Matrix

The irradiation matrix, giving the specification for the irradiation temperatures and the numbering of the capsules is given in Table 1.

Table 1. Capsule ID and target irradiation temperatures

ID in this document	ID in request sheet	Temperature, C	Cycles (dpa)	N of rabbits	Position
DSG1	T8A1	300	2 (1.2)	1	TRH-1
DSG2	T8A2	300	TBD (9.6)	1	TBD
PER1	T9A2	56	391 hr (1.2)	1	HT-5
PER2	T9A1	56	34 hr (0.1)	1	HT-5
DSG3		300	1 (1.2)	1	TRH-3
DSG2-2		300	8 (9.6)	1	TRH-3

The original DSG 1 design provided a space at the bottom of the capsule for irradiating 3 and 6 mm diameter disks at low (80ºC) temperature. For this purpose, the standard capsule design was modified, and an insert for the disks was laid in the bottom part of the capsule under (outside) the holder. The insert serves to provide better contact with the housing thus minimizing the irradiation temperature. However, because of unsatisfactory results from a temperature calculation, the insert was removed from DSG1. Two perforated capsules were made (PER1 and 2) with the second being irradiated for 0.1 dpa in the Hydraulic Tube.

Specimen Description

The specimen material and dimensions are summarized in Table 2.

Table 2. Specimen types and sizes

Type	Material	Dimension, mm	Note
Tensile	FS	4x16x0.5	See Figure 1
Large Disk	FS or W or Ni	Ø6x0.2 or Ø6x0.3	
Small Disk	FS or W or Ni	Ø3x0.2	
TEM	FS	4x16x0.15	
APT	FS	1.25x16x0.5	See Figure 2
SANS/Hv	FS	4x8x0.5	
TD Disks	FS	Ø6x3.0	

The tensile and APT specimens are given in greater detail in Figure 1 and 2. Other specimens have simple form of round disks or plates.

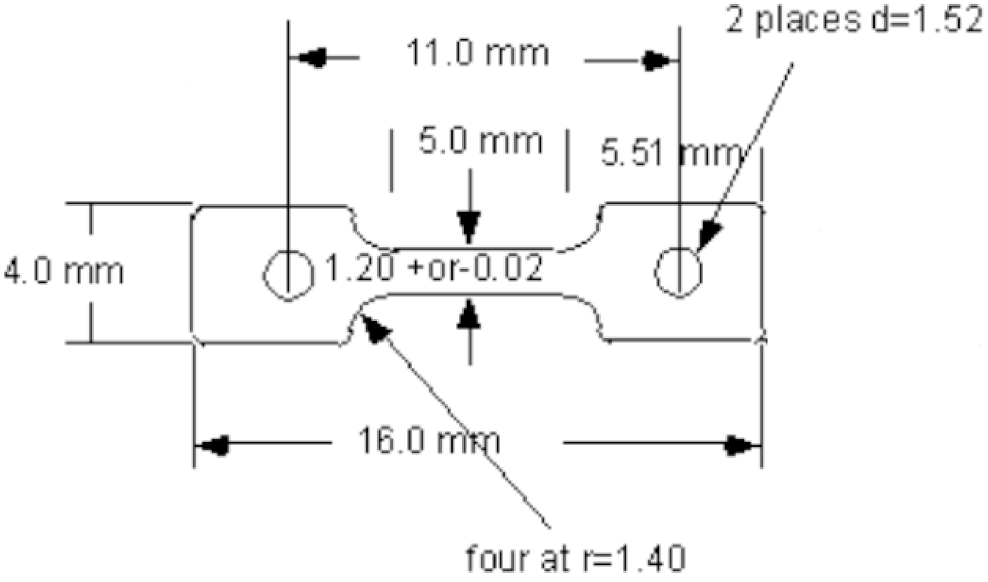

Figure 1. Tensile specimen dimensions

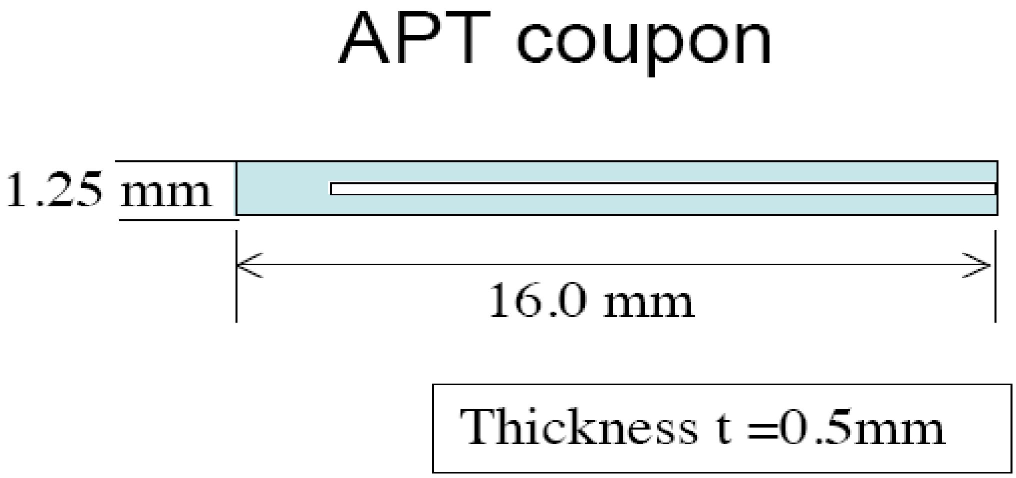

Figure 2. APT specimen dimensions

Capsule Design Technical Details

A standard capsule configuration is used consisting of a vanadium holder placed in standard aluminum housing. The required irradiation temperature is controlled by the gap size between the housing and the holder and the fill gas thermal properties.

Several designs have been developed to hold a different number and type of specimens. All of them are kept in this report for reference. Their description follows:

Design 1, v.1, (approved)

Design 1 capsules are referred as DSG1 in this document and contain specimens for irradiation at 300°C. This design was reviewed and approved and the temperature calculations are presented later in this report.

A rectangular cutout of 6.25x6.25 mm is made axially throughout the holder to place specimens in layers. Each layer is separated by the one above/below by a 3.5 mil (~0.1 mm) molybdenum disk.

The design has three vertical layers: two with tensiles and one in the middle with disks and TEM specimens. The total number of specimens per capsule in Design 1 is, as follows:

Tensiles	16
6x0.2 mm Large disks	12
3x0.2 mm Small disks	12
TEM (4x16x0.15)	8

Layers 1 and 3 contain tensiles and the arrangement is shown in Figure 3. There are 8 tensiles in this layer. A cylindrical spring pin is used to press the tensiles to the holder sides. On two of the tensiles, thermometry is provided as shown in the figure. It is wrapped around the central part of the tensiles with 0.001" Moly foil.

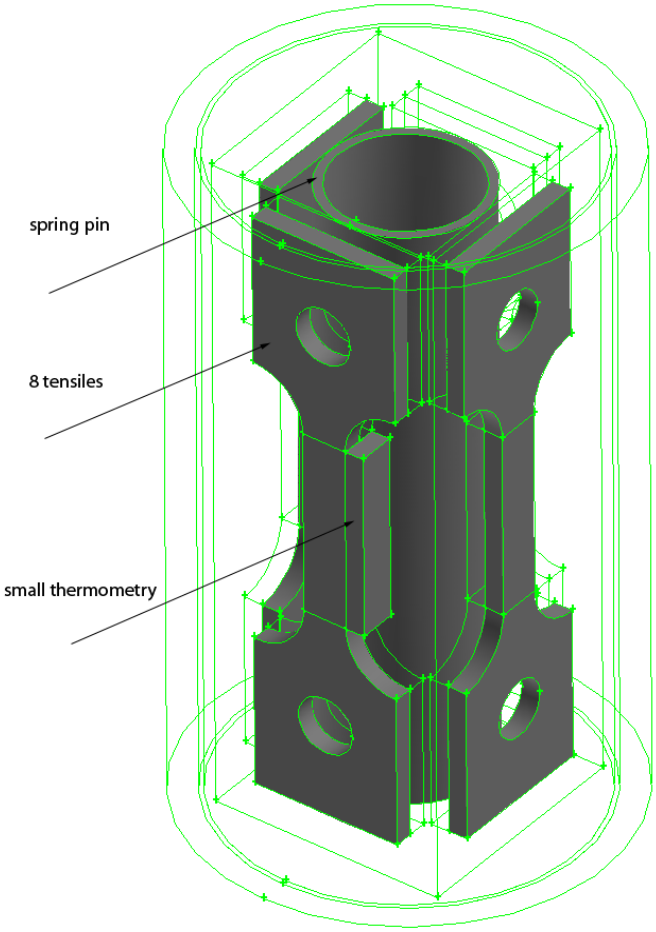

Figure 3. Tensile Layer

Layer two contains disks and TEM specimens. The arrangement is shown in Figure 4. The TEM specimens are placed behind the disks to provide better support for the pin and thus better positioning during the irradiation. Thermometry is accommodated vertically between the small disks packs as shown in the figure.

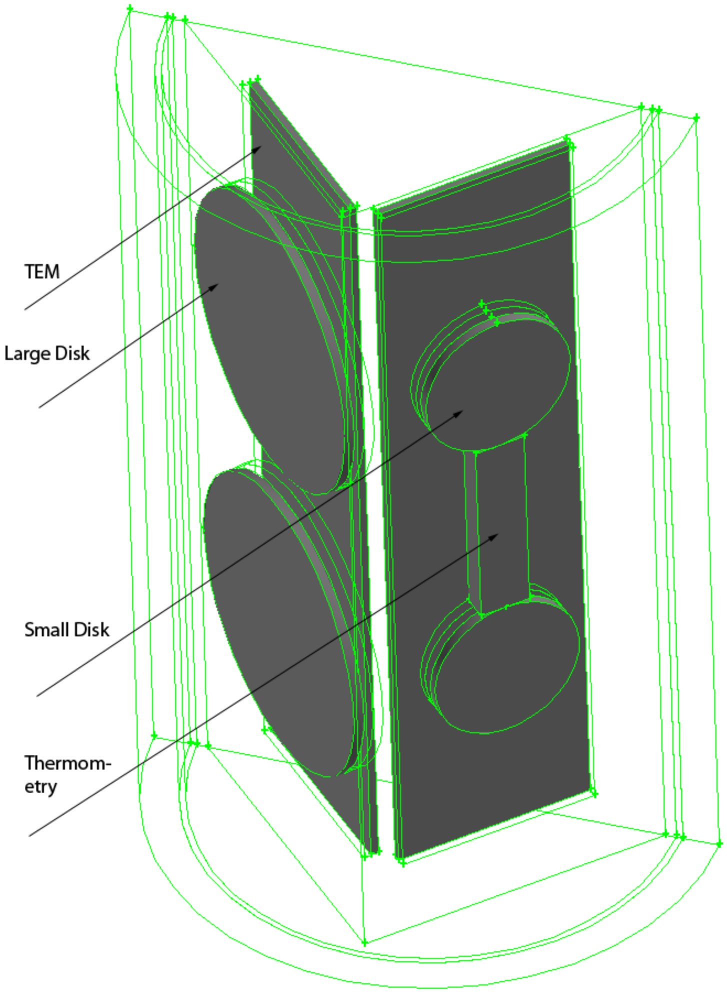

Figure 4. Layer 2 (middle) of DSG1

The disks and the TEMs are wrapped in 0.0254 mm (1 mil) molybdenum foil, but in the thermal analysis the presence of the foil is accounted only on those specimen sides that touch the cooling (holder) wall.

Design 1, v.2

During a design review meeting, Design 1 was altered both in the number of materials and material type. The short thermometry used in the original design also turned out not to be appropriate and had to be changed. The changes included the following:

- Rearrange the specimens in the tensile layers, but do not repeat the thermal analysis;
- Redesign the disk layer and perform comparative calculations with v.1;

The updated number of specimens and materials is given in Table 3.

Table 3. Number and type of specimens in Design 1, v.2

Specimen	Layer 1, 16mm	Layer 2, 16mm	Layer 3, 16mm	Material	Total
Tensile	7	-	8	FS	15
TEM	-	8	-	FS	8
Disk6x0.2	-	12	-	4-W; 8-Ni	12
Disk3x0.2	-	12	-	6-W; 6-Ni	12

Layers 1 and 3 hold tensile specimens, 7 and 8 pieces, correspondingly. In layer 1, one of the tensiles is replaced with 4 small thermometry bars 1x0.5x16mm wrapped in molybdenum foil to fill in the space. The arrangement of layer 1 is shown in Figure 6. The other tensile layer (3) has no thermometry.

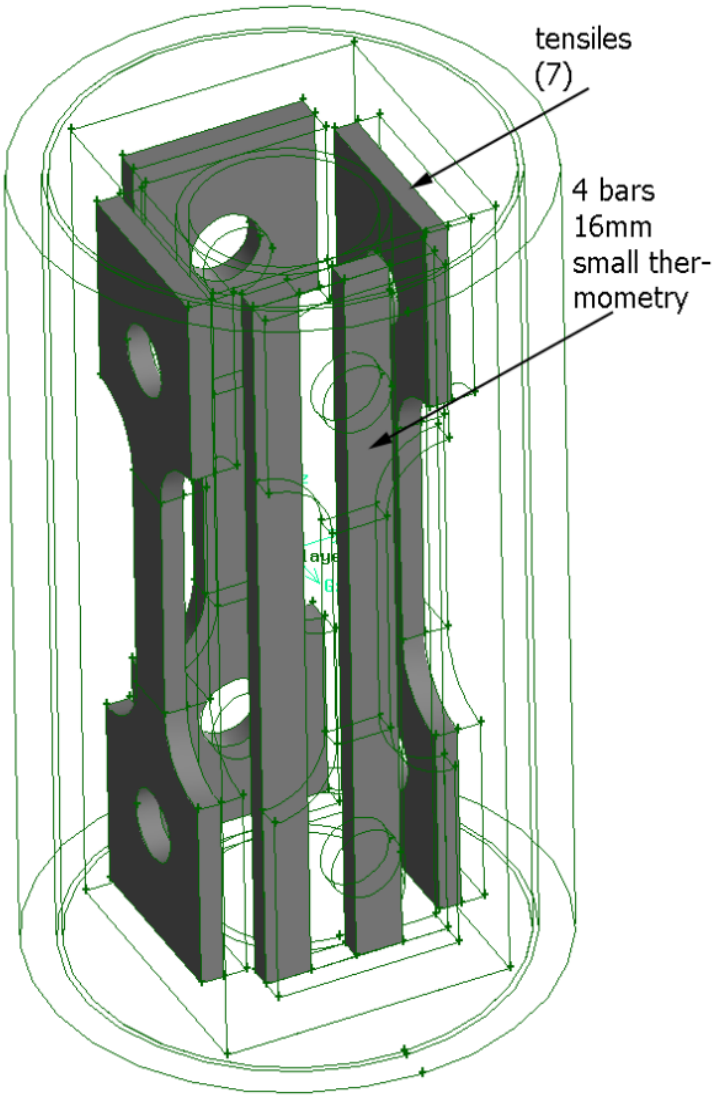

Figure 6. Design 1, v.2, tensile layer

The disk layer is rearranged to accommodate a longer possible small thermometry bar as shown in Figure 7. In order to achieve thermal symmetry (disks are out of different materials) the disks are placed as follows:

Large disks starting from the holder wall: W-Ni-Ni, top and down rows;
Small Disks: top – W-W-Ni on one side and Ni-Ni-W on the other, lower row reversed;

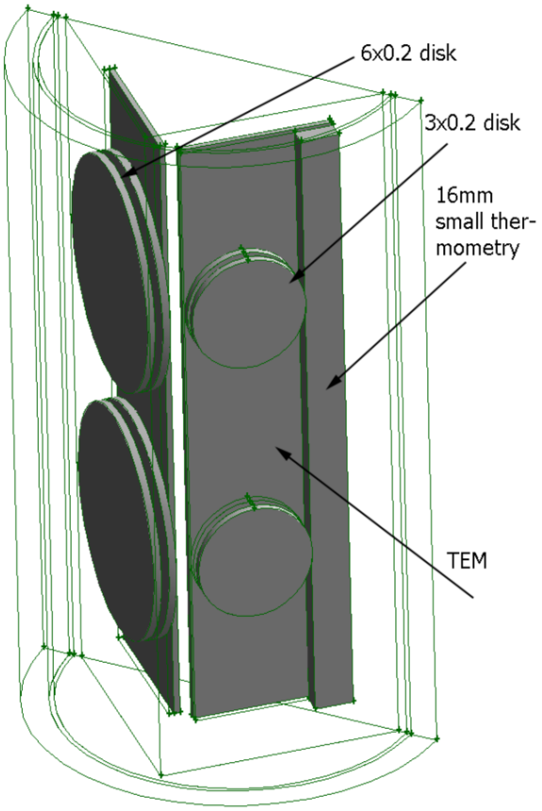

Figure 7. Design 1, v.2, disk and TEM layer

Design 2

Design 2 is similar to design 1 capsule, but with different number of disks, materials and large disk thickness. To shorten the exposure time, the capsule is designed for a higher flux position than Design 1. The specimen nomenclature is given in Table 4.

Table 4 Number and type of specimens in Design 2

Specimen	Layer 1, 16mm	Layer 2, 16mm	Layer 3, 16mm	Material	Total
Tensile	7	-	8	FS	15
TEM	-	8	-	FS	8
Disk6x0.2	-	4	-	W;	4
Disk6x0.3	-	4	-	W;	4
Disk3x0.2	-	6	-	W	6

Layers 1 and 3 are the same as in Design 1. They contain tensile specimens, and in one of the layers one tensile is replaced with 4 small thermometry bars (Figure 6).

Layer 2 is modified from design 1 and contains W disks and TEM specimens. In order to achieve even thickness on the side (holder walls), the TEMs are placed first against the wall and then the disks. All four packs are wrapped in molybdenum foil. The layer is shown in Figure 8.

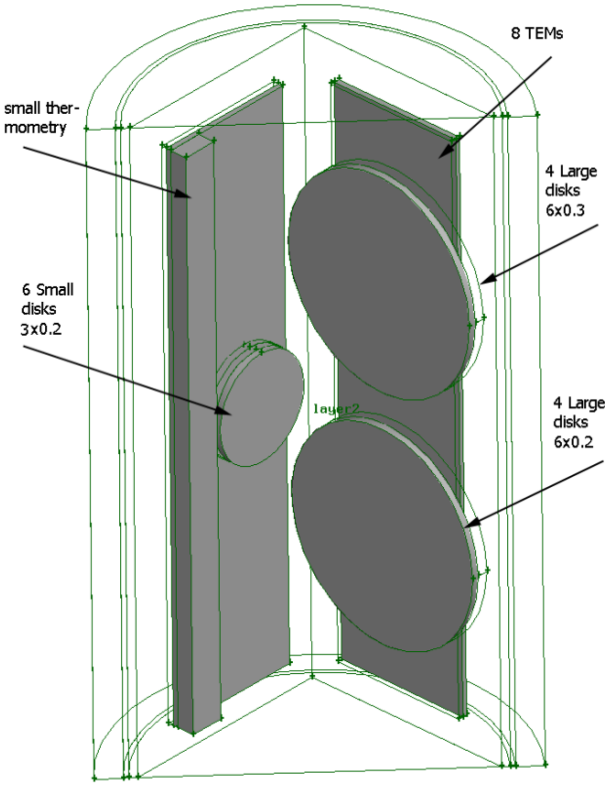

Figure 8. Design 2 Layer 2 layout

<u>Design 3</u>

Design 3 capsules are referred as DSG2 in this document and contain specimens for irradiation at 300°C, for 1 and 8 cycles. The design has four vertical layers. The number of specimens in Design 2 per layer is given in Table 5.

Table 5. Design 2 specimen arrangement per layer

Specimen	**Layer 1, 16mm**	**Layer 2, 16mm**	**Layer 3, 8mm**	**Layer 4, 8mm**	**Total**
Tensile	4	-	-	-	4
TEM	3	-	-	-	3
SANS/Hv	-	8	8	1	17
APT	4	4	-	-	8
TD disk	-	-	-	1	1

A hexagonal cutout is implemented providing larger contact surface with the holder. It allows for placement of more specimens in one row next to the holder wall, which improves the specimen temperature distribution. Layers 1-2 are 16 mm high, while Layer 3 and 4 are 8 mm high. They are separated with spacer plates.

Layer 1 is shown in Figure 9. It accommodates all of the tensile specimens and half of the APTs (four). Thermometry is provided, attached with foil to the central part of one of the tensiles.

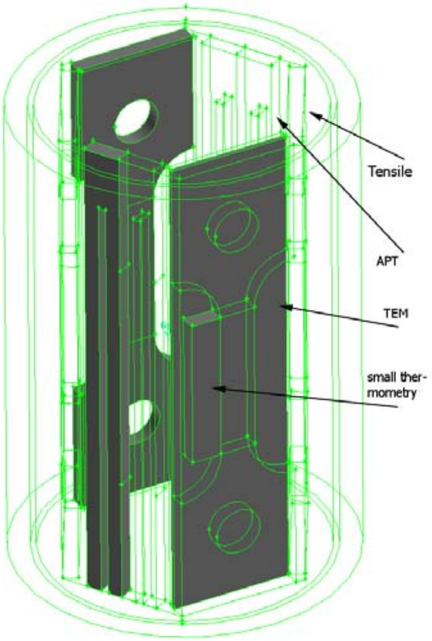

Figure 9. Design 2, Layer 1 layout

Layer 2 contains the rest of the APTs and 8 of the SANS specimens arranged by two in vertical positions (Fig. 10).

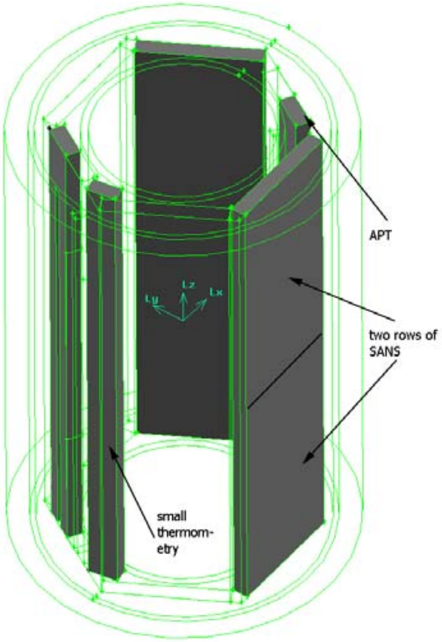

Figure 10. Design 2, Layer 2 layout

Layers 3 and 4 are shown in Figure 11 and 12, respectively. Layer 3 accommodates the rest of the SANS specimens arranged in two rows. A small thermometry is provided by two SiC (0.5x1.0) bars wrapped in foil to fill better the space.

Layer 4 is particularly designed to hold the TD disk, which is much thicker that the rest of the specimens. A SANS specimen is also contained in that layer. Spacers are designed to fill the empty space and to hold the disk in position. A molybdenum spring is used to secure the pieces on place.

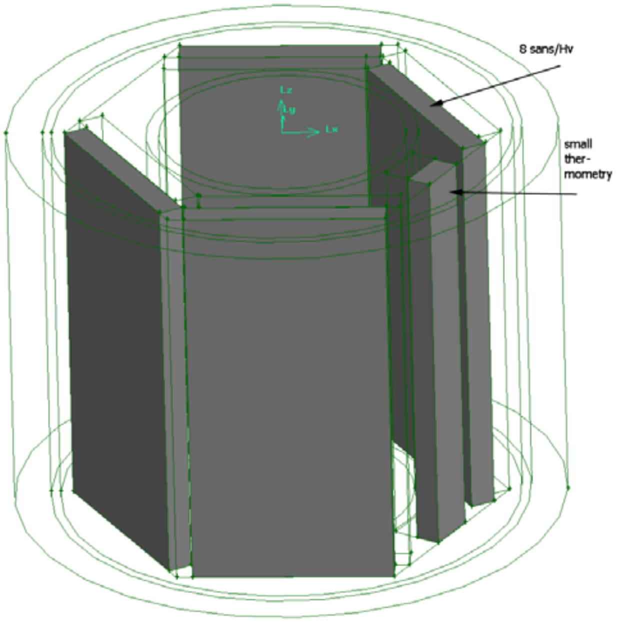

Figure 11. Design 2, Layer 3 layout

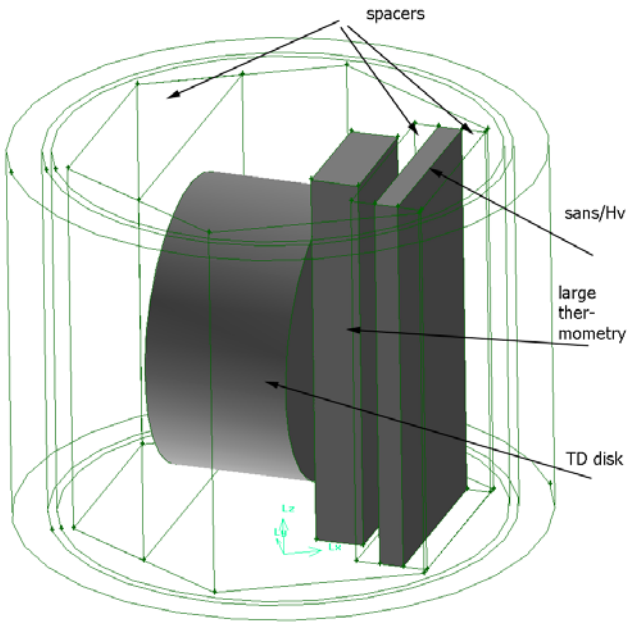

Figure 12. Design 2, Layer 4 layout

PULSED E-BEAM THERMO-FATIGUE SYSTEM (PETS)

Chad Duty, Lance Snead (Oak Ridge National Laboratory), John Sethian (Naval Research Laboratory)

OBJECTIVE:

The objective of this work is to study the effects of thermo-mechanical fatigue on various materials under consideration as first wall materials of an inertial fusion reactor. The initial phase of research focuses on the establishment of a one-of-a-kind high perveance pulsed electron beam system.

SUMMARY:

A unique pulsed electron beam system has been developed for the thermo-mechanical fatigue testing of potential first wall materials for inertial fusion energy program. The Pulsed E-beam Thermo-fatigue System (PETS) is a high perveance system that pulses a 70 kV, 74 A electron beam at rates up to 100 Hz. The pulse width ranges from 0.5 to 1.5 μs and is confined to an area of 1 cm^2. Following design and fabrication of the PETS system, it was installed at ORNL in the fall of 2007. Several technical challenges have precluded its use as a thermo-fatigue system, but plans are in place to resolve many of these issues and move toward a fully-operational system by the summer of 2009.

PROGRESS AND STATUS.

Introduction

There is a need within the inertial fusion energy (IFE) community to determine the ability of a material to withstand the extreme energy profile experienced by the first wall of an inertial fusion reactor. There are currently several systems in use to characterize various material systems, but none can accurately replicate the energy flux time history of an inertial fusion explosion. Such a reaction is expected to have pulse width on the order of a few microseconds, a penetration depth of a few microns, an energy flux of four-to-five J/cm^2, and a repetition rate of up to 100 Hz. Calculations by J. Blanchard and F. Hegeler have shown that a high perveance electron beam is capable of simulating the thermo-mechanical threat to the IFE first wall.

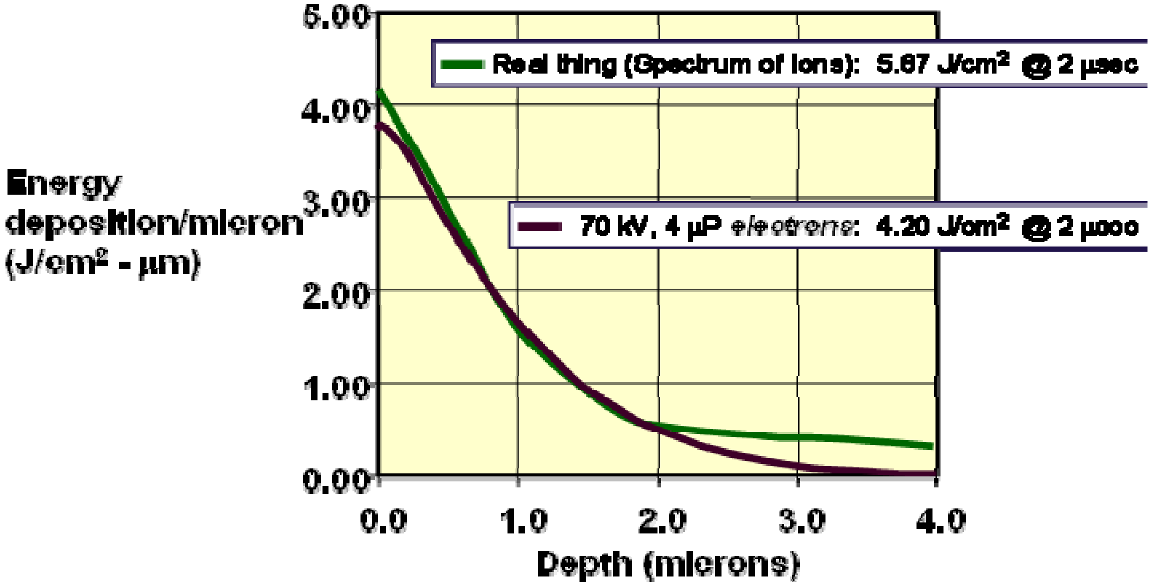

Figure 1. Energy deposition of high perveance electron beam compared to simulated inertial fusion reaction (i.e. “real thing”)

System Design

Pulsed E-beam System

The Pulsed E-beam Thermo-Fatigue System (PETS) was designed and fabricated by HeatWave Labs, Inc. out of Watsonville, CA. The system consists of an extremely high perveance electron beam gun that is designed to focus the flow of electrons to a 1 cm^2 target plane. The main system components shown in Figure 2 include a high voltage pulser unit, high vacuum system pumps and controls, the electron beam exposure chamber, and a remote control unit for the electron beam. The main chamber contains the anode and cathode stalk assembly as shown in Figure 3, which are specially designed to focus the electron beam on the target plane as shown in Figure 4.

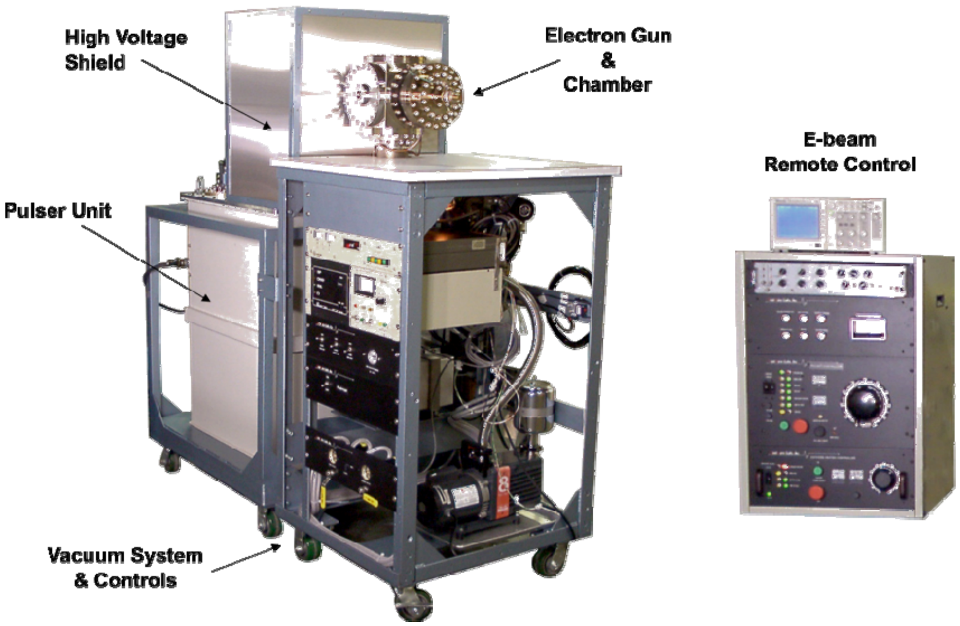

Figure 2. Main components of the PETS system.

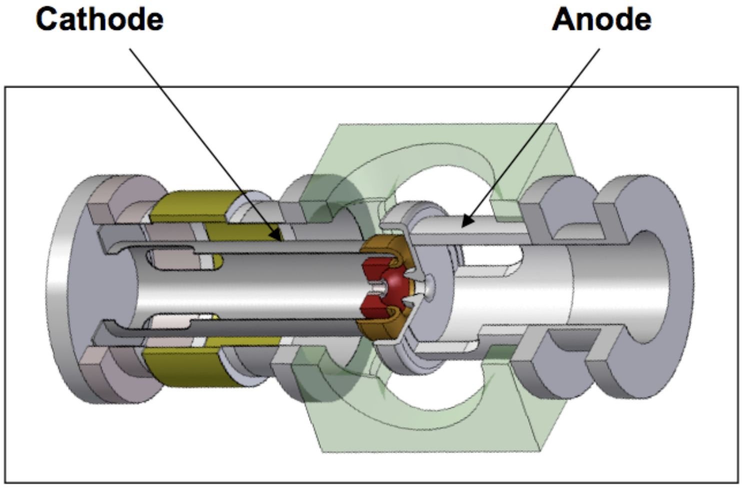

Figure 3. Anode and Cathode Stalk Assembly

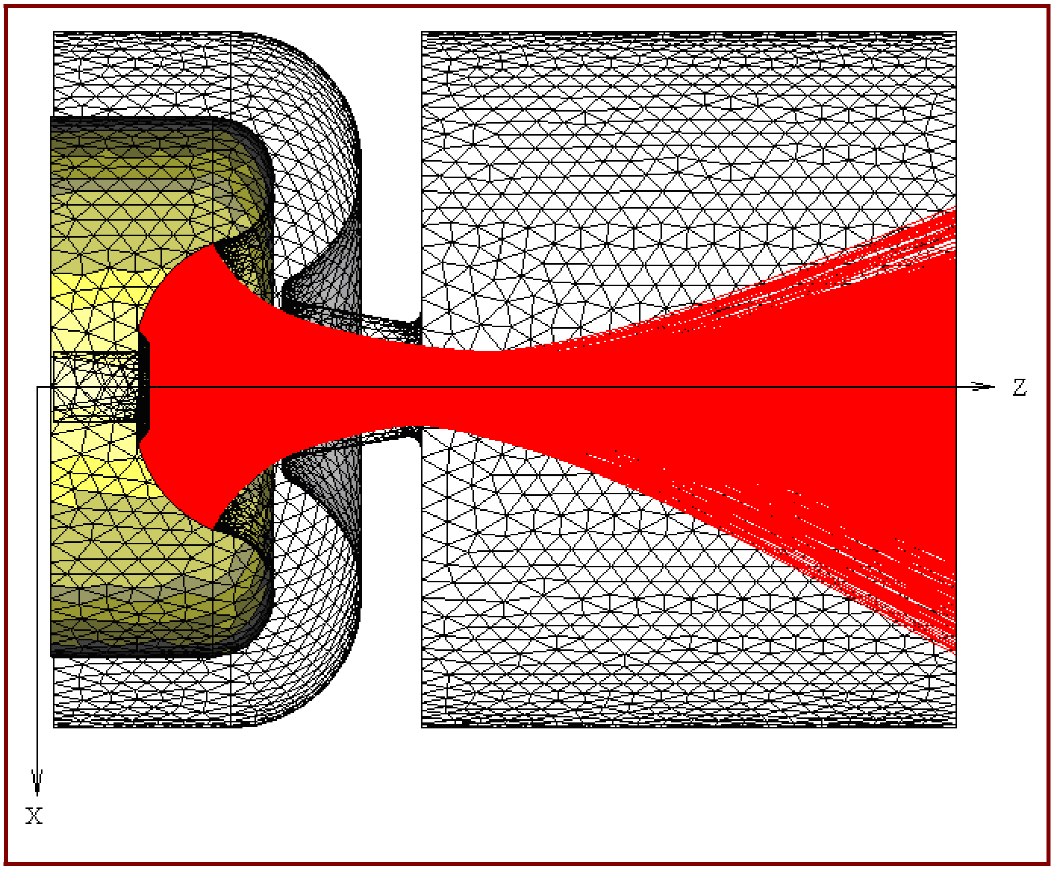

Figure 4. Beam path simulation for PETS cathode (left) and anode (right) assembly.

The pulsed electron beam has an extremely high perveance at 4μperv. Perveance (P) relates the gun anode voltage (V_a) to the space charge limited current (I) according to the equation ($I = P * V_a^{3/2}$). The specifications of the pulsed electron beam are as follows:

Voltage:	70 kV
Pulse width:	0.5 – 1.5 μs
Pulse rise & fall time:	800 ns
Peak current:	74 A
Pulse repetition rate:	up to 100 Hz
Beam spot at waist:	0.565 cm radius
Duration:	> 10 million shots

The variation of current density versus beam radius is shown below in Figure 5. It is expected that the thermal profile during the duration of the pulse will closely follow the beam density.

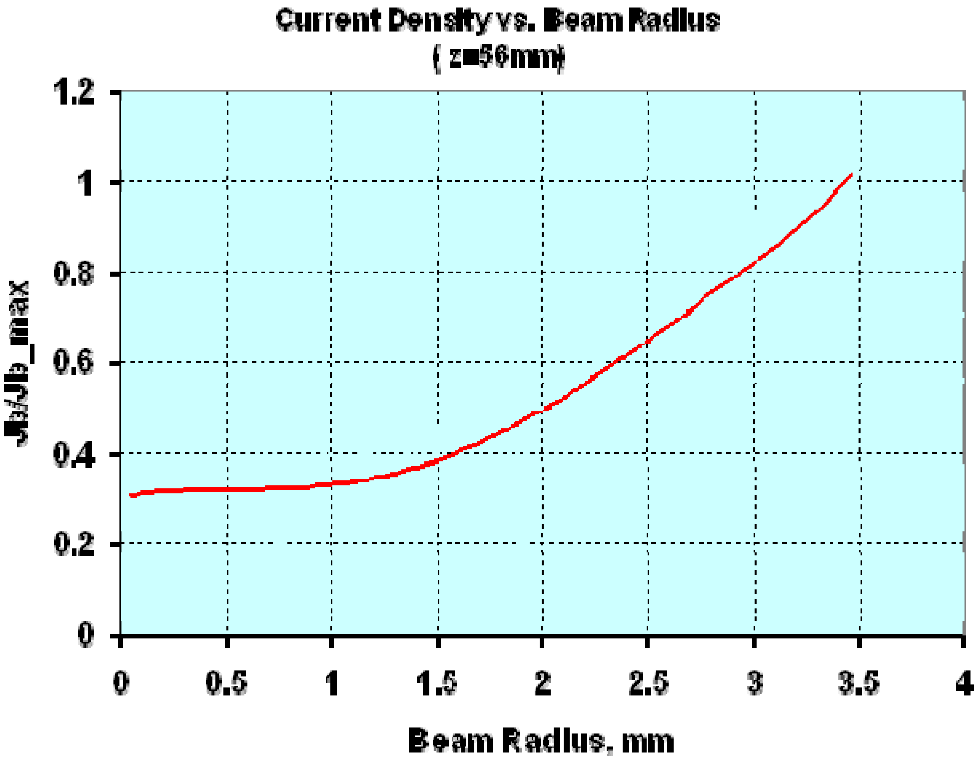

Figure 5. Beam density variation as a function of beam radius at target plane.

Water-Cooled Sample Holder

The first wall material in an IFE reactor will be exposed to severe thermal cycles. As part of the energy production process, it is necessary to quickly and efficiently transfer the heat at the front-side of the first wall material to a circulating coolant just behind the first wall. Similarly, it will be necessary to actively cool the target materials during exposure to the pulsed electron beam. Therefore, a co-axial water-cooling system was designed and fabricated to securely hold the sample material during testing. Also, since it may desirable to raise the bulk temperature of the sample material to simulate various test conditions, a resistive heater was also incorporated into the sample holder design.

Figure 6 shows a schematic of the sample holder design. The purposes of the sample holder are to 1) securely hold the sample, 2) provide line-of-sight access to the sample material from the top and side for pyrometry, 3) permit various sample geometries and thicknesses, 4) provide adequate cooling to the sample backside, 5) moderately heat the bulk sample, 6) electrically ground the sample, and 7) provide access for direct contact temperature measurement. The sample is considered to be a thin disk of material, likely a tungsten material on the order of 1-2 mm thick. The sample is secured tightly to the molybdenum base, which was selected for its high thermal conductivity (λ = 138 W/mK). Sample cooling is provided by a recirculating coaxial flow of water at the bottom of the molybdenum base. A rough heat transfer calculation indicated that a flow of 5 gallons per minute would be sufficient to remove the thermal energy of the pulsed electron beam at maximum power.

The sample holder will be electrically isolated from the remainder of the chamber, as shown in Figure 7. An electrical grounding wire will be attached to the sample holder, providing a means of monitoring the current passing through the sample in real time.

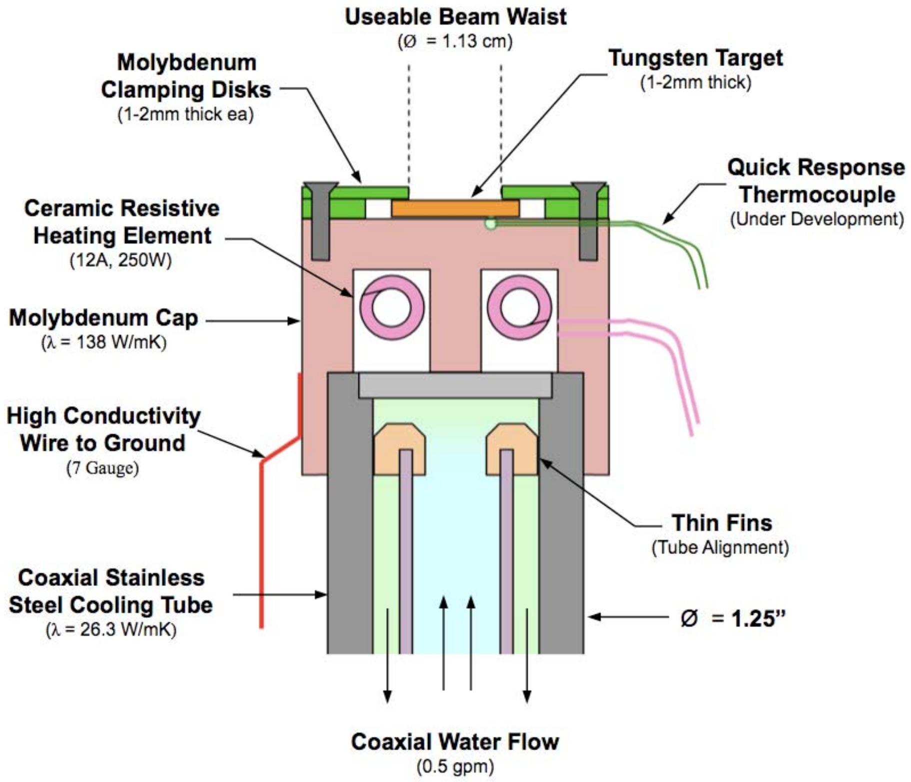

Figure 6. Water-cooled sample holder design.

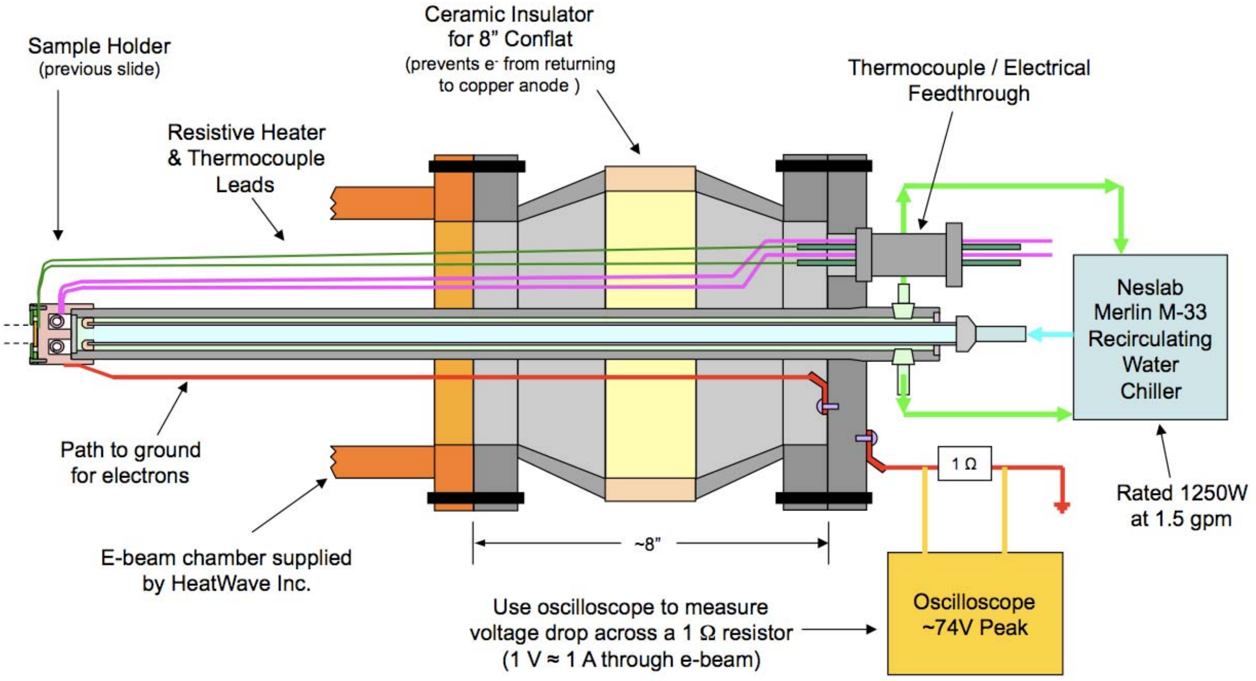

Figure 7. Cooling stalk assembly.

Thermal Modeling

In order to determine the ability of the water-cooling system to remove the heat generated by the pulsed e-beam, a preliminary thermal model was developed using the ABAQUS software package. The initial model was a steady state, two dimensional model that took advantage of radial symmetry. The electron beam was first modeled as a steady surface heat flux of up to 738 W/cm^2, time-averaged over the 1cm^2 target area. The average temperature ranged from 700 to 1000°C at the surface of the target material, depending upon the thermal output of the resistive heater (0 to 250 W) as shown in Figure 8. The radial variation in the electron beam power was also investigated – roughly estimated as a two-zone surface heat flux. The interior heat flux was 428 W/cm^2 while the outer flux was doubled to 856 W/cm^2. Figure 8 shows that the steady state temperature profiles are more uniform across the surface of the sample when approximating the electron beam as a two-zone heat flux. The heater appeared to simply raise the overall material temperature instead of directly impacting the thermal distribution.

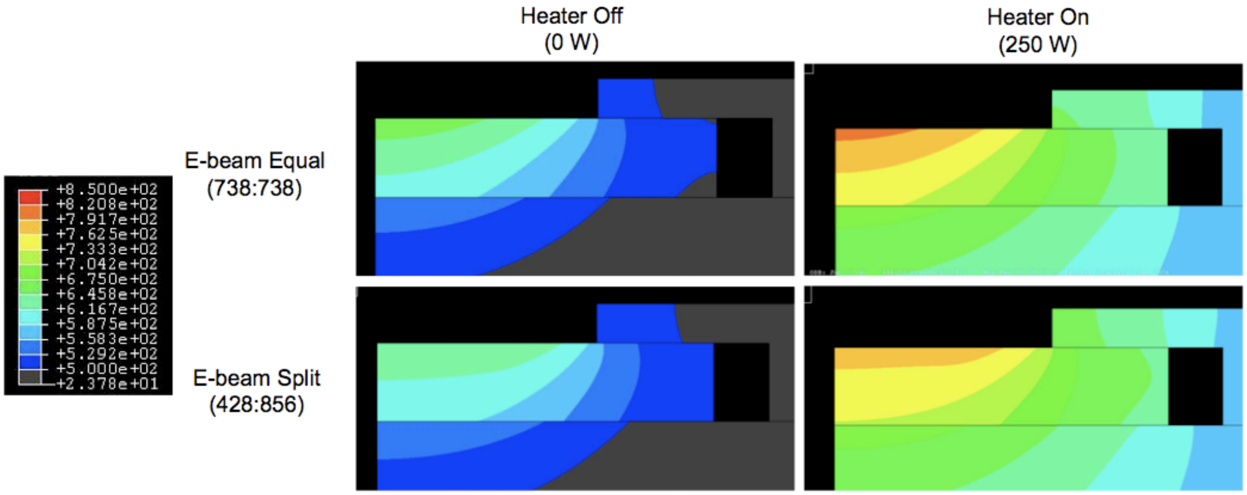

Figure 8. Thermal distribution of target material during steady state analysis. Temperatures in °C.

A transient model was also considered, during which the full power density of the electron beam was concentrated during the 1-2 μs dwell time. The maximum temperature across the surface of the target material was monitored as a function of time and is plotted in Figure 9 below. The four cases explored involve the minimum and maximum dwell time (1.5 and 0.5μs) as well as adjusting the target plane to vary the energy intensity spread across two different beam radii (3.5 and 5.6 mm). The primary observations are that 1) extremely high temperatures are achieved during the electron beam pulse and 2) the surface temperature profile mimics the energy input profile from the electron beam. Given the short time scale and the high density of energy flux, neither of these observations are surprising. Adjusting the target plane seems to be a viable means for adjusting the power distribution across the sample surface. It should also be noted that the transient model agrees well with the steady state model, in that the transient bulk material temperature was within the 700 - 1000°C range of the steady state model.

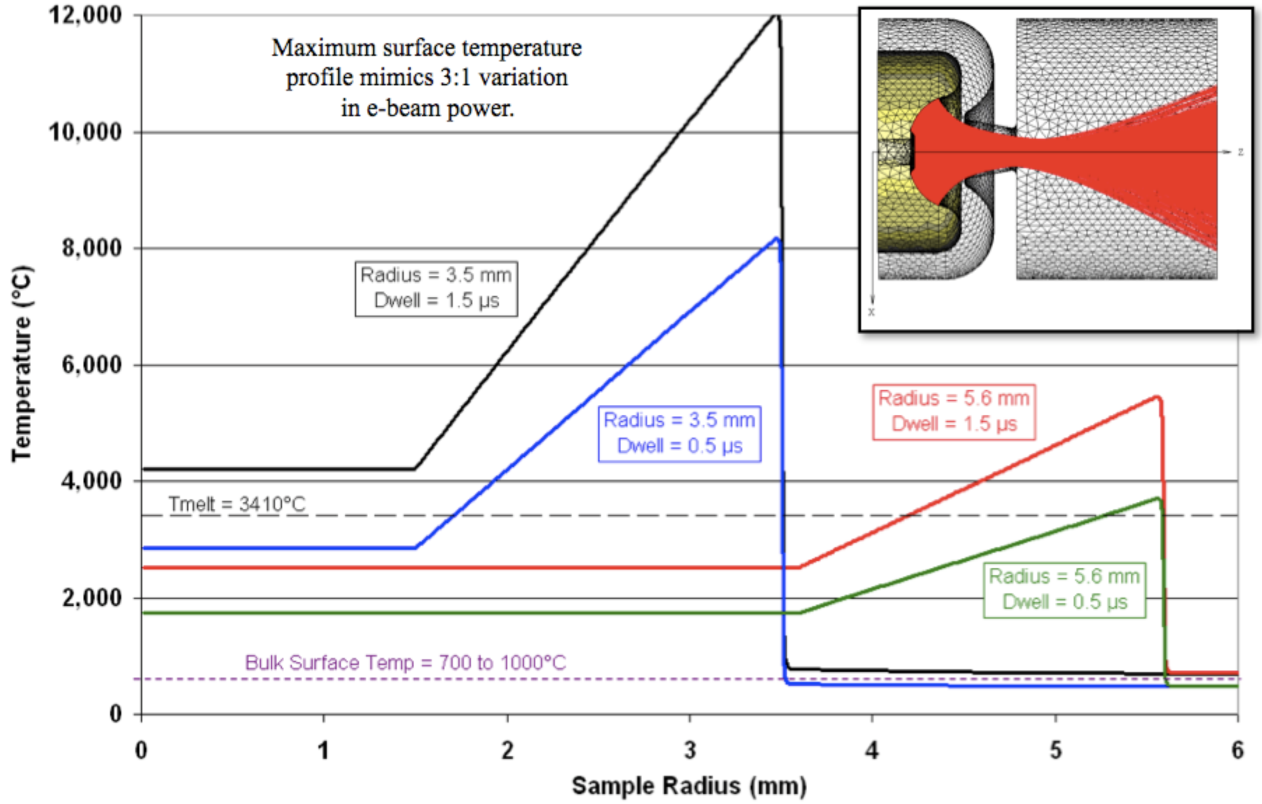

Figure 9. Maximum surface temperature during e-beam pulse.

System Installation & Qualification

The PETS system was shipped to ORNL for installation during the summer of 2007. Preliminary testing of the system was conducted off-site at HeatWave Labs in April of 2007. During this initial phase of testing, the e-beam was collected by a Faraday cup placed at the target plane with a cross sectional area of 1 cm^2. Since it was demonstrated that the toroid (generated) current was equal to the Faraday (received) current, it was confirmed that the PETS system was capable of focusing the high perveance electron beam down to a 1 cm^2 area.

The second round of acceptance testing was conducted during August of 2007 after the PETS system had been installed at ORNL. During this phase, the Faraday cup had been removed, allowing the electron beam to expand freely and be absorbed by the chamber walls. This arrangement reduced the surface flux and minimized the x-ray generation during operation, allowing the system power to be increased significantly. Over the course of a week (during which the cathode was conditioned), the PETS system achieved the maximum voltage (70 kV), the maximum repetition rate (100 Hz), and the maximum dwell time (1.5 μs). The system perveance held constant at 4.4μperv during these conditions. The maximum radiation generated during acceptance testing was 12.5 R/h measured in contact with the front viewport. It was determined that a ¼ inch steel plate provided adequate shielding, reducing the radiation levels below the detection limit of the monitor (>0.1 mR/h).

Despite a few minor complications with the vacuum integrity and the pulse signal generator, the system was accepted as fully operational.

Technical Challenges

Since the installation of the PETS system in August of 2007, there have been several technical challenges that have prevented full operation of the system. One of the primary issues has been the vacuum integrity of the PETS system during operation of the e-beam system. Without a target in place, the e-beam expands to the chamber walls, heating the walls to extreme temperatures and damaging the metal gaskets. Several leaks have resulted and much time has been dedicated to locating and fixing the leaks.

A second, but more problematic issue has been the apparent “pressure spike” during the operation of the pulsed e-beam. The pressure spike appears to occur in unison with the e-beam pulse and often results in the automatic shutdown of the system after only a few seconds of operation (there is a pressure-related interconnect that limits the vacuum pressure to below ~8×10^{-7} Torr during operation of the e-beam). It is still unclear whether the pressure spike is a true increase in the gas molecules within the chamber (possibly due to desorption from the chamber walls) or if the “pressure” spike is more appropriately a result of electrical interference from the high power e-beam pulse. A number of troubleshooting steps have been identified and we are in the process of determining the cause.

Another major issue is the time required to pump down the system from atmospheric pressures and “condition” the e-beam system for full operation. This process can often take the majority of a week and must be done between each sample run because the current configuration requires the complete removal of the cooling column in order to exchange samples. Design is currently underway for a load-lock sample exchange system that would permit us to maintain the system vacuum while remotely manipulating a sample into place through a vacuum-tight loading chamber. The load-lock system would also provide a capability for baking out sample materials before they are introduced into the main e-beam chamber.

Future work over the coming months will primarily focus on the resolution of these technical challenges and establishing full operation of the PETS system.